

UNIVERSITÉ DE MONTRÉAL

MULTIFUNCTION TRANSCEIVER ARCHITECTURE AND TECHNOLOGY FOR FUTURE
WIRELESS SYSTEMS

JABER MOGHADDASI

DÉPARTEMENT DE GÉNIE ÉLECTRIQUE
ÉCOLE POLYTECHNIQUE DE MONTRÉAL

THÈSE PRÉSENTÉE EN VUE DE L'OBTENTION
DU DIPLÔME DE PHILOSOPHIAE DOCTOR
(GÉNIE ÉLECTRIQUE)

AOÛT 2017

UNIVERSITÉ DE MONTRÉAL

ÉCOLE POLYTECHNIQUE DE MONTRÉAL

Cette thèse intitulée :

MULTIFUNCTION TRANSCEIVER ARCHITECTURE AND TECHNOLOGY FOR FUTURE
WIRELESS SYSTEMS

présentée par : MOGHADDASI JABER

en vue de l'obtention du diplôme de : Philosophiae Doctor

a été dûment acceptée par le jury d'examen constitué de :

M. CARDINAL Christian, Ph. D., président

M. WU Ke, Ph. D., membre et directeur de recherche

M. AKYEL Cevdet, D. Sc. A., membre

M. GAGNON François, Ph. D., membre externe

DEDICATION

To my Love, Hanieh

To my Family

ACKNOWLEDGEMENTS

First and foremost, I would like to express my deepest gratitude to Dr. Ke Wu who has given me the chance to join his team in the PolyGrames Research Center and study under his supervision. Prof. Wu trusted me since the first day of studies and allowed me to meet the challenge of studying directly for the highest graduate level without going through the regular procedure. He also freely agreed on a thesis subject on which I felt passionate to work. Even though I have had his insightful guidance on the main research path I have always been given enough freedom to make mistakes and learn from them and more importantly to dare to try creative paths. Throughout the time of studying, Prof. Wu has encouraged me for many opportunities including research grant applications and student competitions that helped me to build up a bright background. I would appreciate his kind supports for ever not only because of these reasons but also for his soothing smiles and inspiring speeches during my hardest days of research.

My sincere thanks go to the jury members for their time and reading my thesis and providing me with very helpful comments.

I am also very grateful to the team of technicians at the PolyGrames Research Center, i.e., Jules Gauthier, Steve Dubé, Maxime Thibault, and Traian Antonescu who helped me within all in-lab circuit fabrication and measurement processes. My gratitude extends to Mr. Jean-Sébastien Décarie and Mrs. Rachel Lortie who gave me hand in solving the IT problems and completing the administrative tasks.

I also would like to thank my love, Hanieh who has stayed by my side during the whole study. Hanieh has always had her extraordinary love and kindness for me which encouraged me to pursuit toward the complete achievements. She felt the fatigue and bores of my hard days but made her efforts to keep me motivated and have eyes open for delightful future days. I am very much indebted to her for accompanying me faithfully during these years of study. Moreover, I appreciate the kind support of my family since I was a child.

I have also had great chances to have the cooperation with our, at the time, post-doctorate fellows. I want to thank Dr. Lin Li, Dr. Tarek Djerafi, Dr. Anthony Ghiotto, and Dr. Liang Han. Furthermore, I appreciate the nice friendship of my friends at the Polytechnique Montreal, including Yangping Zhao, Kuangda Wang, Ali Doghri, Jiapin Guo, Faezeh Fesharaki, Carlos Lorenz and Sulav Adhikari.

RÉSUMÉ

Depuis la toute première transmission sans fil, les ondes radiofréquences ont été progressivement mises en valeur et exploitées dans un nombre de plus en plus important d'applications. Parmi toutes ces applications, la détection et la télécommunication sont sans doute les plus indispensables de nos jours.

Il existe un grand nombre d'utilisations des radiofréquences, incluant les transports intelligents pour lesquels les véhicules doivent être équipés à la fois de radars et de dispositifs de communication afin d'être capables de détecter l'environnement ainsi que de réaliser la communication avec d'autres unités embarquées. La technologie émergente 5G est un autre exemple pour lequel plusieurs capteurs et radios devraient être capables de coopérer de manière autonome ou semi-autonome. Les principes de fonctionnement des systèmes radars et radio sont toutefois différents. Ces différences fondamentales peuvent entraîner l'utilisation de différentes architectures de traitement du signal et d'émetteur-récepteur, ce qui peut poser des problèmes pour l'intégration de toutes les fonctions requises au sein d'une seule et même plate-forme.

En dehors de cela, certaines applications requièrent plusieurs fonctions simultanément dans un même dispositif. Par exemple, les systèmes de détection d'angle d'arrivée 2D nécessitent d'estimer l'angle d'arrivée (AOA) du faisceau entrant dans les plans horizontal et vertical simultanément. La communication radio multi-bandes et multi-modes est un autre exemple pour lequel un système radio doit être capable de communiquer dans plusieurs bandes de fréquences et dans plusieurs modes, par exemple, un duplexage en fonction de la fréquence ou du temps.

À première vue, on peut penser que l'assemblage de plusieurs dispositifs distincts n'est pas la meilleure solution en ce qui concerne le coût, la simplicité et la fonctionnalité. Par conséquent, une direction de recherche consiste à proposer une architecture d'émetteur-récepteur unifiée et compacte plutôt qu'une plate-forme assemblant de multiples dispositifs distincts. C'est cette problématique qui est spécifiquement abordée dans ce travail.

Selon les fonctions à intégrer dans un seul et unique système multifonctionnel, la solution peut traiter plusieurs aspects simultanément. Par exemple, toute solution réalisant l'intégration de fonctions liées au radar et à la radio devrait traiter deux aspects principaux, à savoir : la forme d'onde opérationnelle et l'architecture frontale RF. Cependant, dans certains autres exemples mentionnés ci-dessus, tels que le système de détection DOA 2D, une forme d'onde opérationnelle

identique peut être utilisée et le principal défi de l'intégration de fonctions concernerait l'unification des multiples émetteurs-récepteurs essentiels dans une seule unité. Par conséquent, différentes stratégies d'intégration de systèmes multiples devraient être envisagées pour ces deux catégories. Dans ce travail, les deux catégories sont étudiées et différentes solutions sont présentées.

Dans la première catégorie, les systèmes de communication radar commune (RadCom) sont développés pour des fonctionnalités plus robustes et une mise en œuvre compacte et unifiée. En outre, le schéma d'intégration du domaine en temps qui s'est révélé performant en termes de simplicité, de coût et d'efficacité par rapport à ses homologues en fréquence ou en domaine de code, a été étudié pour d'autres améliorations. Dans un premier temps, la fonction de détection d'angle a été ajoutée au schéma d'émetteur-récepteur présenté au début en améliorant l'architecture du récepteur. Un émetteur-récepteur multifonctionnel reconfigurable pour de futurs services intégrés de fusion de données de détection radar et de radiocommunication (RadCom) est étudié et développé dans ce travail. Cette alternative proposant des architectures à la pointe de la technologie présente une intégration sans précédent de toutes les fonctions de détection radar et de communication radio dans une plate-forme de division temporelle. En outre, il est capable d'offrir une fonction de positionnement à la fois des objets mobiles et statiques avec une résolution améliorée, en plus de fournir une capacité de communication de données. Les incompatibilités de conception et de performance entre les systèmes radar et radio sont explorés et étudiés. Une approche systématique de haut en bas est également présentée. Elle comprend une méthodologie étape par étape, des considérations de conception de blocs de construction et la simulation au niveau système. Dans le but de valider le schéma proposé, un prototype basse fréquence a été développé et sa performance est évaluée. Grâce à diverses mesures au niveau du système, le schéma proposé a démontré des caractéristiques intéressantes en liaison avec les fonctions radar et radio. Avec le mode radar, la capacité ajoutée de la détection d'angle et la résolution améliorée de portée par rapport à la version précédemment démontrée rend le système approprié pour des applications d'assistance. Dans le mode radio, le démonstrateur du système s'est avéré d'une bonne capacité de communication avec un débit de données de 25 Mbps.

Par la suite, ce travail s'est consacré au développement de nouvelles architectures d'émetteurs-récepteurs pouvant unifier plusieurs émetteurs-récepteurs avec des architectures et / ou spécifications essentiellement différentes. Dans cette partie, l'objectif a été la réduction des tailles et des coûts des systèmes d'émetteurs-récepteurs multifonctionnels. En raison des caractéristiques

intéressantes des architectures interférométriques, elles ont été choisies. Les architectures multiports souffrent d'une sensibilité relativement faible et d'une plage dynamique limitée, mais elles sont supérieures en termes de bande passante facilement réalisable, de coût, de simplicité, de consommation d'énergie extrêmement faible, de reconfigurabilité et de pluralité de ports disponibles. En effet, ces caractéristiques font des architectures multiports, des architectures prometteuses pour les futurs systèmes intégrés, notamment autour des bandes de fréquences millimétriques.

La technique de l'interféromètre à six ports a déjà été utilisée dans les systèmes sans fil pour diverses applications, y compris la démodulation / modulation en quadrature, la détection de petits mouvements d'objet ou même l'estimation de l'AOA du faisceau entrant. Néanmoins, à notre connaissance, un unique émetteur-récepteur multiport, capable de gérer plusieurs de ces fonctions simultanément, n'a jamais été proposé.

Dans ce travail, de nouveaux réseaux multiports avec conditionnement de phase spécifique sont développés. Ils intègrent la plupart des fonctions de systèmes six-ports précédemment rapportées. Les architectures proposées à multiports sont examinées autour de 5,8 GHz puis développées et mises en œuvre pour une exploitation autour de 77 GHz. L'intégration dans ce dernier schéma est obtenue principalement par une nouvelle configuration des signaux aux ports d'entrée, un nouveau traitement de phase des signaux d'entrée dans un réseau passif à huit ports et également un post-traitement complémentaire des signaux de sortie. Il peut être utilisé à des fins de localisation, c'est-à-dire de détection de portée et d'angle, ou de communication.

Dans la deuxième catégorie de systèmes multifonctionnels, une technique interférométrique multiport est développée pour un système de détection DOA 2D. Ce système se compose de trois parties principales, à savoir, l'antenne, le récepteur interférométrique à ondes multiples ou le discriminateur de phase et le processeur de signal. Dans ce schéma, la capacité des estimations simultanées 2D AoA est rendue possible grâce à une combinaison de configuration d'antenne spécifique et récepteur interférométrique multiport pour la discrimination de phase. L'antenne est composée de quatre éléments récepteurs situés dans le même plan, et agencé dans configuration en forme de losange. Les signaux reçus manifestent des différences de phase relatives qui contiennent des informations sur la direction d'arrivée du faisceau. Avec la topologie de jonction à huit ports proposée, l'interféromètre extrait ces différences de phase informative et les fournit à un algorithme

de traitement de signal simple permettant l'estimation des deux angles. L'analyse théorique du schéma de détection du DOA proposé est présentée ainsi que des résultats de simulation au niveau du système, afin de faire la preuve de concept. En outre, une technique d'étalonnage appropriée est formulée afin de traiter les non-idéalités et les erreurs consécutives dans la pratique. Également, la mise en œuvre du système présenté est brièvement discutée dans cette thèse pour son prototypage à plus de 60 GHz. Enfin, la performance du système prototypé est évaluée à l'aide d'un ensemble de mesures au niveau du système. D'excellents résultats sont obtenus, validant ainsi la fonctionnalité exceptionnelle du système proposé.

Dans une autre application de la deuxième catégorie, de nouvelles architectures d'émetteurs-récepteurs multi-ports sont présentées pour des applications en radios à double bande et à double mode. Dans ce travail, le concept présenté est soutenu par des simulations et des analyses au niveau du système.

De plus, plusieurs composants passifs sont présentés dans ce travail. Une structure balun à large bande est développée grâce à une combinaison hybride de guidage d'ondes intégrées au substrat (SIW) et de topologies de lignes de dérivation antipodales. La différence de phase de 180° est obtenue par la rotation de la polarisation du champ E à travers les sections de la ligne des ailettes antipodales dans deux branches non équilibrées. En raison de l'indépendance de ce déphasage par rapport à la constante de propagation et à la longueur d'onde, on obtient une différence de phase constante de 180° sur une large plage de fréquence. Le balun proposé est prototypé et démontré pour fonctionner à des fréquences d'ondes millimétriques de 70 GHz à 90 GHz. Les résultats de mesure montrent d'excellentes performances avec une perte d'insertion très faible et une différence de phase de 180° entre les ports déséquilibrés dans une large bande de fréquence.

De surcroît, une topologie simple de coupleur hybride 180° avec des entrées et des sorties non intercalées est développée dans ce travail. Cette topologie de coupleur hybride avec entrées disponibles d'un côté et sorties du côté opposé simplifient l'acheminement des signaux lorsqu'ils doivent être utilisés dans des circuits intégrés avec d'autres composants. La topologie proposée du coupleur est théoriquement analysée. Le coupleur a été démontré à 77 GHz et évalué en mesure sur wafer. Le bon accord obtenu entre les résultats de mesure et de simulations montre la fiabilité des performances du coupleur hybride 180° proposé.

ABSTRACT

Since the very early wireless transmission of radiofrequency signals, it has been gradually flourished and exploited in a wider and wider range of applications. Among all those applications of radio technology, sensing and communicating are undoubtedly the most indispensable ones. There are a large number of practical scenarios such as intelligent transportations in which vehicles must be equipped with both radar and communication devices to be capable of both sensing the environment and communication with other onboard units. The emerging 5G technology can be another important example in which multiple sensors and radios should be capable of cooperating with each other in an autonomous or semi-autonomous manner. The operation principles of these radar and radio devices are different. Such fundamental differences can result in using different operational signal, distinct signal processing, and transceiver architectures in these systems that can raise challenges for integration of all required functions within a single platform.

Other than that, there exist some applications where several functions of a single device (i.e. sensor or radio) are required to be executed simultaneously. For example, 2D angle-of-arrival detection systems require estimating the angle of arrival (AOA) of the incoming beam in both horizontal and vertical planes at the same time. Multiband and multimode radio communication is another example of this kind where a radio system is desired to be capable of communication within several frequency bands and in several modes, e.g., time or frequency division duplexing.

At a first glance, one can feel that the mechanical assembling of several distinct devices is not the best solution regarding the cost, simplicity and functionality or operability. Hence, the research attempt in developing a rather unified and compact transceiver architecture as opposed to a classical platform with assembled multiple individual devices comes out of horizon, which is addressed specifically in this work.

Depending on the wireless functions that are to be integrated within a single multifunction system, the solution should address multiple aspects simultaneously. For instance, any solution for integrating radar and radio related functions should be able to deal with two principal aspects, namely operational waveform and RF front-end architecture. However, in some other above-mentioned examples such as 2D DOA detection system, identical operational waveform may be used and the main challenge of functional integration would pertain to a unification of multiple mono-functional transceivers. Therefore, different strategies for the integration of multiple systems

should be considered for these two categories. In this work, both categories are studied and different solutions are put forward.

In the first category, joint radar-communication (RadCom) schemes are developed for more robust functionality and rather compact and unified implementation. Furthermore, the time-domain integration scheme that has been proved to outperform in terms of simplicity, cost and efficiency compared to those counterparts in either frequency or code domain, is studied for further improvements. At the first step, the function of angle detection was added to the early presented transceiver scheme by improving the receiver architecture. A reconfigurable multifunctional transceiver for future integrated data-fusion services of radar sensing and radio communication (RadCom) is investigated and developed in this work. This proposed alternative of the state-of-the-art architectures presents an unprecedented integration of all radar sensing and radio communication functions together in a time-agile scheme. Furthermore, it is capable of offering a positioning function of both moving and static objects with an enhanced ranging resolution in addition to providing the capability of data communication. The design and performance incompatibilities between radar and radio systems are explored and investigated herein. A systematic top-bottom approach is also presented, which involves step-by-step methodology, building block design considerations, and system level simulation. With the purpose of validating the proposed scheme, a low-frequency prototype is developed and its performance is evaluated. Through various system-level measurements, the proposed scheme has demonstrated attractive features in connection with both radar and radio functions. With the radar mode, the added ability of angle detection and the improved range resolution against the previously demonstrated version makes the system suitable for driving assistance applications. With the radio mode, the system demonstrator has proved a great capability of communication at a data rate of 25 Mbps.

Thereafter, the main attention in this work is drawn into developing new transceiver architectures that can unify multiple transceivers with different functions and/or system specifications. This research path is taken in this work with the purpose of reducing size, cost and complexity in the development of multifunctional transceiver schemes. Due to interesting features of the multiport interferometric based architectures, it is selected against conventional architectures for further development. Generally, the multiport architectures suffer from relatively poor sensitivity and limited dynamic range, but they outweigh in terms of easily achievable bandwidth, cost, simplicity, extremely low power consumption, re-configurability and plurality of available

ports. Indeed, these features have inspired the capability of multiport techniques as a promising architecture for future integrated wireless systems especially around millimeter-wave frequency bands.

The six-port interferometer technique has already been used in wireless systems for a variety of applications, including quadrature demodulation/modulation, small object movement detection or even estimation of the incoming beam's AOA. Nevertheless, a single multiport-based transceiver has not been reported that can handle a multitude of these functions simultaneously, in our best knowledge. In this work, a new multiport network with specific phase conditioning is introduced which integrates most of the previously reported six-port based system functions. The proposed multiport based architecture is examined first around 5.8 GHz and then further developed and implemented for millimeter-wave operation around 77 GHz. The integration within the latter scheme is mostly obtained through a new configuration of connection of input signals at the input ports, a novel phase processing of input signals in an eight-port passive network and also complementary post-processing of output signals. It can be used for AOA sensing as well as data communication. The proposed multiport receiver is modeled and implemented in a transceiver for further evaluation. The excellent functionality of the proposed eight-port receiver is proved through satisfactory system-level measurements in our laboratories.

In the second category of multifunctional systems, multiport interferometric technique is developed for a 2D DOA detection system. This system consists of three main parts, namely antenna, multiport wave interferometric receiver or phase discriminator, and signal processor. In this scheme, the capability of simultaneous 2D AOA estimations is made possible thanks to a combination of specific antenna configuration and multiport interferometric receiver for phase discrimination. The antenna is composed of four receiving elements located in the same plane, which is arranged as a diamond-shaped configuration. The received signals manifest relative phase differences that contain information about the beam's direction of arrival. With the proposed eight-port junction topology, the interferometer extracts these informative phase differences and leaves them for a simple signal processing algorithm to estimate the two angles. Theoretical analysis of the proposed DOA detection scheme is presented along with system level simulation results for the proof of concept. In addition, an appropriate calibration technique is formulated to deal with non-idealities and consecutive errors in practice. Also, implementation of the presented system scheme is briefly discussed in this thesis for its prototyping over 60 GHz range. Finally, the performance

of the prototyped system is assessed through a set of system level measurements. Excellent results are obtained, thus validating the outstanding functionality of the proposed system.

In another application of the second category, new multiport-based transceiver architectures are presented for applications in dual-band and dual-mode radios. In this work, the presented concept is supported with system level simulations and analysis.

In addition, several passive components, which are in support of our proposed system architecture developments, are presented in this work. A broadband balun structure is developed through a hybrid combination of substrate integrated waveguide (SIW) and antipodal fin-line topologies. The 180° phase difference is made by the rotation of E-field polarization through the antipodal fin-line sections in two unbalanced branches. Due to the independency of this phase shifting with respect to propagation constant and wavelength, a constant 180° phase difference is achieved over a wide range of frequency. The proposed balun is prototyped and demonstrated for operation at millimeter-wave frequencies from 70 GHz to 90 GHz. The measurement results show an excellent performance with very low insertion loss and 180° phase difference between the unbalanced ports in a broad frequency band of interest.

Moreover, a simple topology of 180° hybrid coupler with non-interspersed input and outputs is studied and developed in this work. These hybrid coupler topologies with inputs available on one side and outputs at the opposite side greatly simplify signal routing when they are to be used within integrated circuits with other components. The proposed coupler topology is theoretically analyzed that sets up some design equations and diagrams. It is also implemented for operation over 77 GHz and examined through on-wafer measurements. Good agreement of the measurement results with the simulation counterparts demonstrate the reliable performance of the proposed 180° hybrid coupler.

Table OF CONTENTS

CHAPTER 1 INTRODUCTION

1.1	Motivation and research background	1
1.2	Objectives	11
1.3	Methodology	12
1.3.1	Improvement of the state-of-the-art RadCom transceiver.....	12
1.3.2	Development of unified transceiver RadCom system through multiport technique ..	13
1.3.3	Characterization of multiport receiver and development of innovative microwave components.....	14
1.3.4	Development of millimeter-wave multifunctional multiport-based transceiver	14
1.3.5	Development of multiport-based simultaneous 2-D AOA detection system.....	15
1.3.6	Development of dual-band radio architectures for multi-standard wideband small-cell backhaul	15
1.4	Original Contributions.....	16
1.5	Thesis Organization.....	17

CHAPTER 2 FUNDAMENTALS OF TIME-AGILE INTEGRATION SCHEME AND VARIOUS TRANSCEIVER ARCHITECTURES

2.1	Time-agile integrated modulation schemes.....	19
2.2	Transceiver architectures.....	22
2.2.1	Homodyne receiver architecture	22
2.2.2	Heterodyne receiver architecture	23
2.2.3	Multiport interferometer receiver architecture	24
2.2.4	Six-port based radio receiver.....	26
2.2.5	Six-port based AOA detector	29
2.2.6	Implementation of six-port receiver	30

2.2.7	Six-port calibration.....	32
2.2.8	Pros and cons of six-port technique	32
2.3	Electromagnetic wave propagation and DOA detection	33
2.3.1	Electromagnetic wave propagation	34
2.4	DOA detection techniques	36
2.4.1	Amplitude difference of arrival technique	37
2.4.2	Phase difference of arrival (PDOA) technique	38
CHAPTER 3 MULTIFUNCTIONAL TRANSCEIVER FOR FUTURE RADAR SENSING AND RADIO COMMUNICATION DATA FUSION PLATFORM		
3.1	System concept.....	40
3.1.1	Signal modulation scheme	40
3.1.2	Operation principles	42
3.2	TFMCW radar signal analysis.....	45
3.2.1	Ambiguity intervals.....	45
3.2.2	Multi-target detection.....	46
3.2.3	Estimation accuracy	50
3.3	System architecture and analysis.....	53
3.3.1	Overview of FCC Rule Making for DSRC	53
3.3.2	Experimental RadCom system specifications	54
3.3.3	Radar-Radio incompatibilities.....	55
3.3.4	Transceiver architecture	57
3.4	Simulations.....	59
3.4.1	RF circuit simulations	59
3.4.2	System-level simulations.....	61
3.4.3	Simulation results of radar mode	62

3.4.4	Simulation results of communication mode.....	66
3.5	Prototyping and measurements	67
3.5.1	Tx Block.....	68
3.5.2	Down-converter block.....	69
3.5.3	AGC Loop	69
3.5.4	Tx and Rx antenna.....	70
3.6	System-level measurements	74
3.6.1	Radio communication	74
3.6.2	Radar sensing	80
3.7	Conclusion and discussions.....	89
CHAPTER 4 PARAMETRIC CHARACTERIZATION OF SIX-PORT INTERFEROMETER		
4.1	Noise analysis.....	92
4.1.1	NF of multi-port demodulator	93
4.2	Conversion loss improvement.....	96
4.3	Equivalent mixer model	98
4.4	Conclusion.....	101
CHAPTER 5 UNIFIED RADAR-COMMUNICATION (RADCOM) MULTIPORT INTERFEROMETER TRANSCEIVER		
5.1	System concept.....	102
5.1.1	Modulation scheme	102
5.1.2	Transceiver architecture	103
5.2	Operation principles of novel multi-port component.....	104
5.3	Prototyping and measurements	105
5.4	Conclusion.....	109
CHAPTER 6 DEVELOPMENT OF MILLIMETER-WAVE COMPONENTS		

6.1	Hybrid structure based field rotation balun for millimeter-wave applications	110
6.1.1	Concept and structure of the balun.....	112
6.1.2	Prototyping and measurements	114
6.2	Wideband planar 180° hybrid coupler with non-interspersed ports	116
6.2.1	Proposed Topology of the 180° hybrid coupler.....	118
6.2.2	Theoretical analysis.....	119
6.2.3	Design of the proposed coupler.....	128
6.2.4	Prototyping and measurements	131
6.2.5	Conclusion:.....	136
 CHAPTER 7 MILLIMETERWAVE MULTIFUNCTION MULTIPOINT INTERFEROMETRIC RECEIVER FOR FUTURE WIRELESS SYSTEMS		
7.1	Proposed multipoint architecture	139
7.2	Ambiguity in AOA detection	145
7.3	Multi-function transceiver architecture	146
7.4	Calibration technique	148
7.4.1	Calibration in sensing mode.....	149
7.4.2	Calibration in radio mode.....	150
7.5	Prototyped transceiver.....	152
7.5.1	Tx block.....	153
7.6	Antenna	155
7.6.1	Rx block	157
7.7	System-level measurements	161
7.7.1	AOA detection.....	164
7.7.2	Radio communication	165
7.8	Conclusion.....	170

CHAPTER 8 2-D DIRECTION-OF-ARRIVAL (DOA) ESTIMATION SYSTEM THROUGH MULTI-PORT INTERFEROMETRIC TECHNOLOGY

8.1	System scheme and analysis	172
8.1.1	Antenna topology and plane wave	173
8.2	Multiport interferometer topology	174
8.3	Signal processing algorithm	177
8.4	Plane wave simulations	177
8.5	Ambiguity issue and required distance between antenna elements	179
8.6	System-level simulations.....	181
8.7	Calibration technique	183
8.8	Implementation.....	187
8.9	Experimental prototyping.....	189
8.9.1	Antenna structure	190
8.9.2	Detector circuit.....	195
8.9.3	System Assembly	198
8.9.4	System level measurements	199
8.10	Conclusion.....	203

CHAPTER 9 DUAL-MODE COMMUNICATION TRANSCEIVER ARCHITECTURE FOR BACKHAUL SMALL CELL APPLICATIONS

9.1	Multiple band/mode radio	206
9.2	Proposed architecture	209
9.3	Conclusion.....	214

CHAPTER 10 CONCLUSION AND FUTURE WORK

10.1	Conclusion.....	215
10.2	Outlook and future work	218

Appendix A – List of publications and awards.....	234
---	-----

LIST OF TABLES

Table 3-1: Multi-target simulation results.....	50
Table 3-2: System specification	54
Table 3-3: Link budget analysis	55
Table 3-4: System simulation results for radio mode	65
Table 3-5: STD of range measurement	82
Table 3-6: STD of velocity measurements.....	83
Table 3-7: Measurement results	84
Table 3-8: Angle measurements.....	87
Table 3-9: Comparison of different RadCom schemes	91
Table 4-1: EVM simulation of six-port mixer	99
Table 4-2: EVM simulation of six-port mixer	100
Table 6-1: Comparison of the 180° hybrid couplers	131
Table 6-2: Comparison of measured performances of 180o hybrid couplers	136

LIST OF FIGURES

Figure 1-1: Typical scenario in the platform of ITS	1
Figure 1-2: Multiple radars with different operational zones for different applications.....	2
Figure 1-3: Antenna beam alignment application scenario.....	3
Figure 1-4: 5G network that extends to new applications.....	3
Figure 1-5: Advantages of multiple systems unification	4
Figure 2-1: Modulation scheme for integrated RadCom systems.....	20
Figure 2-2: Triangle linear FMCW	21
Figure 2-3: Homodyne receiver architecture	23
Figure 2-4: Heterodyne receiver architecture.....	24
Figure 2-5: Two different mixing processes	25
Figure 2-6: Two common topologies of passive junction for six-port receiver.....	26
Figure 2-7: Six-port radio receiver.....	28
Figure 2-8: Six-port AOA detector	30
Figure 2-9: Diode detector circuit schematic	31
Figure 2-10: Simulated (V-P) transfer function of the Schottky diode in ADS.....	31
Figure 2-11: Different DOA detection scenarios	36
Figure 2-12: DOA detection based on amplitude measurement	37
Figure 2-13: Antenna beam alignment based on amplitude measurement at two Rx elements.....	38
Figure 2-14: Wave propagation and geometrical arrangement of the receiving antenna	39
Figure 2-15: Phase difference of arrival at the antenna terminals.....	39
Figure 3-1: Spectrogram of power spectral density (PSD) of the operational signal	41
Figure 3-2: Typical application scenario.....	44
Figure 3-3: Beat frequencies along with the variation of range and velocity.	46

Figure 3-4: V-R diagram from a TFMCW radar.....	48
Figure 3-5: Multi-target simulation scenario	48
Figure 3-6: PSD of the detected beat signals from simulation in Matlab.	49
Figure 3-7: Beat frequency pairing for multi-target detection	49
Figure 3-8: Variation of velocity estimation error as a function of threshold to noise level and SNR in simulation via Matlab.....	51
Figure 3-9: Variation of angle estimation error as a function of threshold to noise level or SNR in simulation via Matlab.....	53
Figure 3-10: Proposed transceiver architecture.....	58
Figure 3-11: Chain budget simulation of Tx block.....	60
Figure 3-12: Chain budget simulation of down-converto core in Rx block	60
Figure 3-13: Block diagram of multilayer simulation at system level via Ptolemy simulator in ADS package.....	62
Figure 3-14: System simulation when operating in radar mode	63
Figure 3-15: Group delay of the RF BPF which is used in both Tx and Rx blocks in ADS	64
Figure 3-16: System-level simulation results when operating in communication mode	66
Figure 3-17: Prototyped building blocks of front-end	67
Figure 3-18: Cumulative graph of EVM spectrum of the signal at the output of Tx block.....	68
Figure 3-19: Gain and NF of down-converto block measured by NF analyzer.....	69
Figure 3-20: Gain control by two branches of AGC loop.....	70
Figure 3-21: Building blocks of Tx antenna	71
Figure 3-22: S11 of transmitter antenna.....	72
Figure 3-23: Normalized radiation pattern of Tx antenna in two planes	73
Figure 3-24: System measurement setup in communication mode.....	74

Figure 3-25: Measured constellation and EVM for different modulation schemes when system is configured to operate in radio mode	75
Figure 3-26: EVM and BER measurement results.....	76
Figure 3-27: System measurement in radio mode.....	77
Figure 3-28: Measurement results in communication mode; Received signals are match-filtered by an FIR filter with 4 taps and energy of unity.	79
Figure 3-29: Radar mode measurements with channel emulator	80
Figure 3-30: PSD of the measured beat signals with two different SNR.....	81
Figure 3-31: Measurement setup in lab.....	85
Figure 3-32: Range resolution and range profile measurement results.....	86
Figure 3-33: Angle measurement setup	87
Figure 3-34: Angle measurement results	88
Figure 3-35: Measurement results in position estimation	89
Figure 4-1: Proposed configuration for estimating the NF of a two port network.....	93
Figure 4-2: Diagram for estimating the NF of six-port mixer.....	94
Figure 4-3: Calculated NF using the proposed equations.	96
Figure 4-4: Controlling the conversion loss of the six-port mixer via LO power and DC bias	98
Figure 4-5: Platform used in ADS simulations for validating the six-port mixer model.....	99
Figure 4-6: Comparison of BER between the six-port demodulator and the mixer model with different values of P1dB in ADS simulations	100
Figure 5-1: Block diagram of the proposed transceiver architecture	104
Figure 5-2: Measurement setup.....	106
Figure 5-3: Measurement results of radio mode	106
Figure 5-4: Measured beat signals in frequency domain	107
Figure 5-5: Angle measurement results	108

Figure 6-1: Proposed balun structure	113
Figure 6-2: Prototype of the proposed balun.....	114
Figure 6-3: Measurement and simulation results of scattering parameters.....	115
Figure 6-4: The 180° hybrid coupler topologies	117
Figure 6-5: Implemented proposed topology in TEM structures	119
Figure 6-6: Four port network and T matrix	119
Figure 6-7: Comparison of the derived theoretical T parameters with the simulated ones.....	122
Figure 6-8: Comparison of the derived analytical T parameters of the Schiffman phase shifter with the simulated ones from ADS	124
Figure 6-9: Comparison of the simulation results of phase differences with the ones from analytical equations for two different values of R	127
Figure 6-10: Bandwidth control over R for two different values of phase deviations (δ)......	128
Figure 6-11: Comparison of phase differences between our proposed 180 deg hybrid topology with the one proposed by Park in race [132], and the classic rat-race.	129
Figure 6-12: Comparison of amplitude imbalance.....	130
Figure 6-13: Prototyped hybrid on ceramic die	132
Figure 6-14: Measurement setup which is hold on mmWave probing station.....	133
Figure 6-15: Measured and simulated amplitude components of S -parameters.	134
Figure 6-16: Comparison of measured and simulated phase differences.....	135
Figure 7-1: The proposed multiport network	140
Figure 7-2: The comparison of the scattering matrix relationship between the conventional and proposed multiport.	141
Figure 7-3: The unambiguous range of AOA estimation using the obtained M vector.....	146
Figure 7-4: The proposed multifunction transceiver architecture	147
Figure 7-5: Modulation scheme of the Operational waveform	147

Figure 7-6: The prototyped transceiver	153
Figure 7-7: The block diagram of the Tx block for implementing the proposed transceiver.	154
Figure 7-8: Microscopic photograph of the prototyped MHMIC SIW cavity BPF.	155
Figure 7-9: Measured and simulated S-parameters of the BPF.	155
Figure 7-10: The prototyped Tx antenna with the SIW-WR10 adaptor.	156
Figure 7-11: Measured and simulated S11 of the antenna.	156
Figure 7-12: Measured and simulated series-fed antenna pattern in two planes.	157
Figure 7-13: Fabricated multiport circuit on ceramic substrate using MHMIC process.	158
Figure 7-14: Measured S-parameter of the multiport network.	159
Figure 7-15: Measured phase difference between input and output ports of the prototyped multiport.	159
Figure 7-16: Schematic circuit of the Schottky diode for simulation in ADS.	160
Figure 7-17: Prototyped detector circuit in measurement setup.	160
Figure 7-18: Measured RF-IF conversion gain of prototyped detector at different LO powers. .	161
Figure 7-19: System level measurement setup (without absorbers).	163
Figure 7-20: Received signal at the spectrum analyzer.....	164
Figure 7-21: Measurement result of AOA detection.....	165
Figure 7-22: The block-diagram of the system-level simulation platform in ADS and MATLAB.	166
Figure 7-23: The constellation diagram of the simulated receiver with non-idealities.....	167
Figure 7-24: The EVM over different AOA. Calibration was done at angles 2 and 6 modulation of 16 QAM.....	168
Figure 7-25: Measured constellation diagram.....	169
Figure 7-26: The EVM over SNR. Calibration was done when we had noise and SNR=20 dB.	169

Figure 8-1: Receiver antenna structure with four receiving elements and their interaction with the propagation vector of an incoming plane wave	173
Figure 8-2: Proposed multiport interferometer topology for 2D DOA parameter extraction.	175
Figure 8-3: Plane wave simulation scenario in HFSS.....	178
Figure 8-4: Plane wave simulation results at 60 GHz in HFSS	179
Figure 8-5: L_{\max} values as a multiplication of free space wavelength..	180
Figure 8-6: AOA detection system level simulation results from ADS.....	181
Figure 8-7: Ptolemy Co-simulation panel of Circuit Envelop (for RF portions) and DF (data flow for DSP) simulators in ADS.....	182
Figure 8-8: System level simulation results from ADS for angle detection in two dimensions for different distances between antenna elements	182
Figure 8-9: Partitioning cells for calibration	186
Figure 8-10: Second configuration of the multiport interferometric architecture.....	187
Figure 8-11: Simulation results of amplitude component of the S-parameters of the designed eight-port interferometric network.	188
Figure 8-12: Simulation results of the phase differences (PH_{mkn}) between different pairs of input signals (m and k) at four output ports (n).....	189
Figure 8-13: Fabricated phase shifters	190
Figure 8-14: Measured phase difference	190
Figure 8-15: Designed antenna configuration	192
Figure 8-16: Fabricated antenna with input transmission lines and V-Launchers	192
Figure 8-17: Measured and simulated S-parameters of the two elements of the antenna.....	193
Figure 8-18: Measured antenna pattern in H plane	194
Figure 8-19: Measured antenna pattern in E plane	194
Figure 8-20: Detector layout with components for simulation in ADS	195

Figure 8-21: Detector circuit with EMI filter with zero-bias Schottkey diode (MZBD-9161)....	196
Figure 8-22: Return loss of the detector.....	197
Figure 8-23: Detected voltage vs input RF power at 58 GHz.....	197
Figure 8-24: The prototyped DOA detection system.....	199
Figure 8-25: Measurement setup for phase difference of arrival using the prototyped antenna..	200
Figure 8-26: Measurement results for phase difference of arrival.	201
Figure 8-27: Test bed for system level measurements.....	201
Figure 8-28: System level measurement results at 58 GHz	202
Figure 9-1: Proposed dual-band dual-mode radio architecture	210
Figure 9-2: Proposed frequency planning diagram	210
Figure 9-3: Schematic view of the simulation in ADS	213
Figure 9-4: Simulation results in FDD mode	213
Figure 10-1: Frequency-time diagram of the chirp in two units (radar mode)	219
Figure 10-2: Proposed transceiver architecture.....	220
Figure 10-3: Spectra of the de-chirped radar and communication signals.....	220

LIST OF SYMBOLS AND ABBREVIATIONS

The list of symbols and abbreviations that are used throughout the thesis is presented below:

1-D	One-dimensional
2-D	Two-dimensional
ADC	Analog-to-digital converter
AGC	Automatic gain control
ASK	Amplitude shift keying
ACC	Adaptive cruise control
BPSK	Binary PSK
CAD	Computer aided design
CMOS	Complementary metal-oxide-semiconductor
CPW	Coplanar waveguide
CTA	Cross traffic alert
CW	Continuous wave
DC	Direct current
DDS	Direct digital synthesizer
DOA	Direction of arrival
DSP	Digital signal processing
DSRC	Dedicated short range communication
DUT	Device-under-test
EIRP	Effective isotropic radiated power
EMC	Electromagnetic compatibility
EMI	Electromagnetic interference
EVM	Error vector magnitude

FCC	Federal communication commission
FDD	Frequency division duplexing
FDMA	Frequency division multiple access
FFT	Fast Fourier transform
FMCW	Frequency modulated continuous wave
FPGA	Field programmable gate array
FSK	Frequency shift keying
ISM	Industrial, Scientific and Medical
ITS	Intelligent transportation systems
LCA	Lane change assistance
LPF	Low-pass filter
LRR	Long range radar
MHMIC	Miniature hybrid microwave integrated circuits
MMIC	Multiple input and multiple output
NF	Noise figure
OFDM	Orthogonal frequency division multiplexing
OOK	On-off keying
PCB	Printed circuit board
PN	Pseudo-noise
PSD	Power spectral density
QAM	Quadrature amplitude modulation
QPSK	Quadrature phase shift keying
RCS	Radar cross section
SIC	Substrate integrated circuits

SIW	Substrate integrated (rectangular) waveguide
SNR	Signal-to-noise ration
SOLT	Short-open-load-through
SoS	System on substrate
SPR	Six-port receiver
SRR	Short range radar
TDD	Time division duplex
TDMA	Time division multiple access
TOI	Third order intercept
TRL	Thru-reflect-line
VNA	Vector network analyzer
VSWR	Voltage standing wave ration

LIST OF APPENDICES

Appendix A – List of publications and awards234

CHAPTER 1 INTRODUCTION

1.1 Motivation and research background

Rapid evolution of radio technology has brought up many related applications to further simplify the human life in a variety of aspects. Intelligent transportation system (ITS) can be a good example in which cars are equipped with multiple sensors and they are able to share the collected information with other vehicles and the related infrastructures. Figure 1-1 shows a typical scenario of ITS platform where vehicles are sensing their surroundings and communicating with each other as well. Co-existence of either sensors or radios can be mutually advantageous for both wireless functions. For instance, it helps building sensor networks with extended operational range and rather accurate estimations thanks to the redundant collected pieces of information. On the other hand, the sensory information can also help improving the communication quality by mitigating the multipath or Doppler Effect through beamforming or real time channel estimation or accurate carrier recovery, respectively.

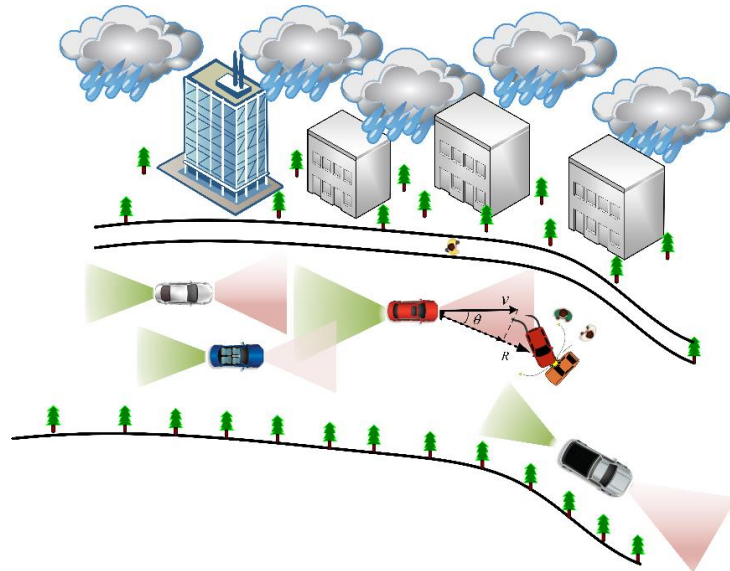


Figure 1-1: Typical scenario in the platform of ITS, on-board vehicles either sense their environment or communicate the sensory data

In addition, the majority of ITS-required functions such as cross traffic alert (CTA), adaptive cruise control (ACC) or lane change assistance (LCA) can be realized by **radio detection and ranging** (radar) sensors. Figure 1-2 shows the corresponding field of view and longitudinal zone of coverage by radars supporting these functions. Each of these desired functions demands for specific radar system's specifications such as maximum and minimum detectable range, ranging and velocity resolution, and angular area coverage or measurement accuracy. These elements specify the characteristics of each individual part of the whole radar system, i.e., from signal generator at back-end to transceiver structure at radio frequency (RF) front-end and antenna. Therefore, three types of automotive radars have emerged, namely, long range radar (LRR), middle range radar (MRR) and short range radar (SRR).

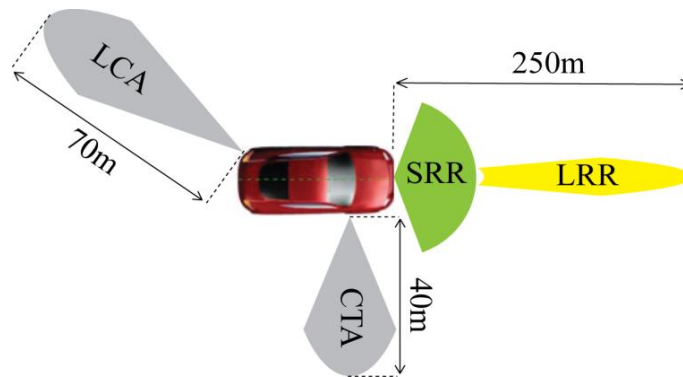


Figure 1-2: Multiple radars with different operational zones for different applications

Antenna beam alignment systems can be considered as another example which requires co-existence of multiple angle detection sensors. Within such systems, angle of arrival (AOA) detection of the incoming signal beam can help aligning the high gain antennas in high data rate point-to-point radios. In Figure 1-3, the antenna alignment and misalignment that may yield a complete communication failure is sketched. One dimensional (1-D) AOA estimation techniques have already been developed, but for very high gain antennas with pencil beams, angle estimation in two dimension is required in emerging applications such as high-speed backhaul radio links.

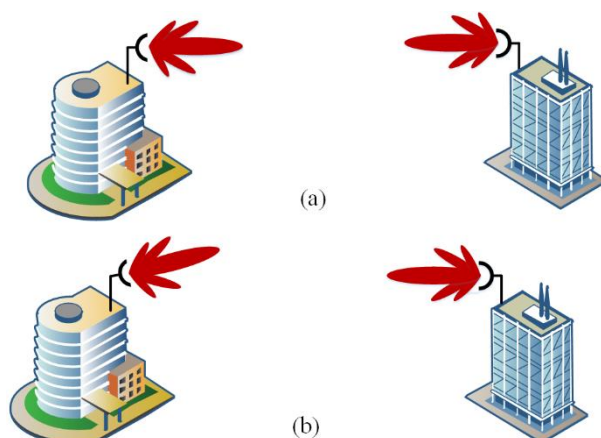


Figure 1-3: Antenna beam alignment application scenario; (a) Antennas are aligned, (b) There is a misalignment between pair of antennas

Moreover, by the advent of 5G technology, a user centric network is to be developed where people are connected to machines which are connected to the other machines and can operate in semi-autonomous manner. Figure 1-4 shows a typical scenario within future 5G network where multiple sensor and radios operate in a cooperative mode.

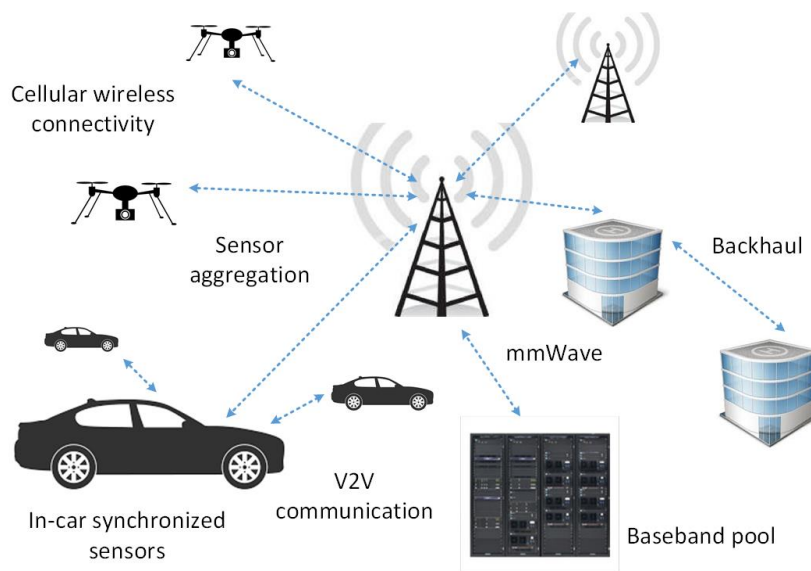


Figure 1-4: 5G network that extends to new applications

However, in all of the above-mentioned examples, assembling multiple systems for multiple applications on a single platform may end up expensive or complicated realization. Therefore, the interesting concept of integrating multiple wireless devices into a single multifunctional system

has come into view, in sake of design simplicity, better efficiency and lower cost, compact size, versatile functionality, low power consumption and shorter response time, as illustrated in Figure 1-5.

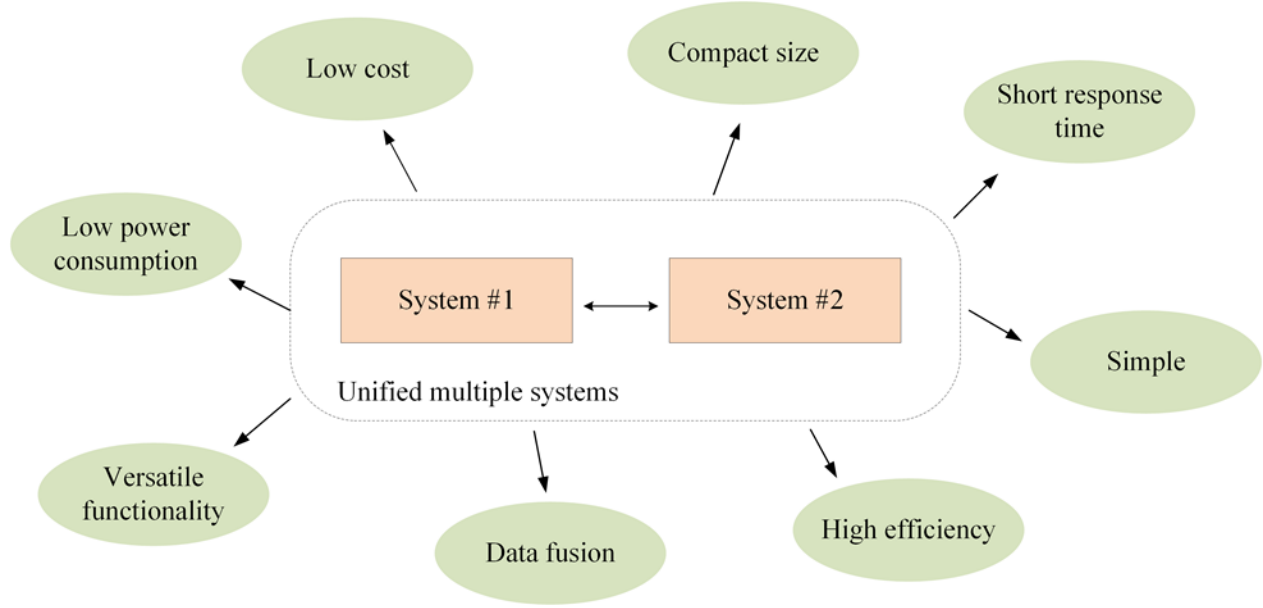


Figure 1-5: Advantages of multiple systems unification

In the framework of this thesis, our attention has been drawn into several important contexts of integrated systems, including Radar-Communication (RadCom), 2-D AOA estimation and finally dual-band and dual-mode radio architectures. The research flow in these domains is concisely reviewed next.

In the 1990s, the concept and technology of ITS was introduced and studied for the first time [1]. ITS encompasses a broad range of technologies, supporting two indispensable functionalities, namely environmental sensing and sensory-data communicating services including vehicle-to-vehicle (V2V) communications. ITS-America, ERTICO-ITS in Europe and ITS-Asia Pacific are all leading advocates and consortiums for these technologies and support ongoing research efforts that have already targeted a rapid development of ITS. Nevertheless, the ITS development has not achieved all its predefined objectives and potentials even though this concept is now more than twenty years old. That is because a successful marketing of ITS demands for low cost, highly efficient, and small form factor vehicular products while realizing a variety of required functions

also demands for utilizing different expensive sensor and radio systems. On another hand, the emerging technology of autonomous driving cars are supposed to operate based on three principles, i.e., sensing the environment, mapping the road and negotiate with other road users. Consequently, radios and radar sensors are fundamental parties of this future technology. Assembling different system modules on a single platform should not be the optimum solution. Therefore, significant research activities for developing sensor fusion techniques [2] and integrated radar and communication (radio) devices through transceiver unification [3] have come into play. The concept of radar-communication unification originates mainly from [4], which is further developed and termed as “RadCom” in this thesis for simplicity.

Interestingly, the search for the most efficient solution about multifunctional systems has progressed in a few different directions. The differentiating aspect of all reported outcomes is related to the integration scheme that involves waveform and the associated transceiver architectures. Furthermore, such a multifunctional integration may take part in frequency domain through either multicarrier or spread spectrum techniques [5-13], or in time domain through time-division technique [14-16]. To situate this work in the ongoing context of this research area, the nature and the fundamental concepts of the reported research are categorized and briefly reviewed as follows.

In [17], the mode of sensing is separated from the function of communication in frequency domain. In this case, a narrow band on the first null of spectrum of the pulsed radar between the main lobe and the first side lobe is dedicated to communication on a single carrier. This scheme would be able to sense merely the range of a detected object. Unfortunately, high data rate communications are not possible since a sharp band-pass filter (BPF) with absolute narrow communication bandwidth is required for suppressing the radar interfering signals.

Ultra-wide-band (UWB) systems are generally developed for short-range applications. They are highly capable of communication due to their large Shannon capacity and extreme immunity to Rayleigh fading, in addition to radar sensing thanks to a large capability of penetration as well as a reduced clutter. These advantages can be combined into one single design platform, using various spread spectrum techniques such as direct sequence [6, 7, 9, 12, 13], code-hopping [10], time-hopping [8] and frequency modulated (FM)-UWB [5]. In [11], both radar and communication modes make use of gated linear frequency modulated (LFM) signals but with opposite chirp slopes.

They can be combined and transmitted simultaneously through a single antenna. For data communication, the carrier can be modulated by phase shift keying (PSK) technique. At the receiver end, two separate blocks receive radar and communication signals that are distinguished by oppositely circular polarized antennas, i.e., right versus left handed.

Radar-radio integration through coding has some major advantages. Both functions can operate simultaneously with a minimum interference due to the orthogonality of pseudorandom noise (PN) codes applied in [7, 9, 12, 13] or the quasi-orthogonality of up- and down-chirps applied in [11]. In addition, these systems are highly immune against jamming and interception. However, they require considerable spectrum resources in an inefficient manner. Besides, rather limited information can be obtained through the radar mode and the overall transceiver is made expensive and complex as well.

Simultaneous radar and radio operation on the basis of a single transceiver was also realized by the amplitude modulation (AM) of an FMCW radar signal [18]. In this so-called AM-FMCW technique, information is encoded on radar signal. Therefore, radar frequency and channel are reused for data transmission without disturbing the sensing functionality. Within the sensing mode, the reflected signal from target is received and then filtered after down-conversion. The frequency component generated by modulation is suppressed by filtering and therefore, it does not impact the radar's performance. For communication, the AM data receiver synchronizes the locally generated FMCW signal with received signal so that the frequency difference is locked at a desired IF frequency. In this way, the frequency component that conveys information can be discriminated for AM demodulation. The major drawback of this integration scheme is that the operation is based on master-slave manner. In fact, the AM receiver (slave side) is not able to send data whereas the data transmitter (master side) on FMCW signal cannot receive any data from other units.

Joint or independent operation of a radio-radar fused system has also been proved to be feasible by separating those two functionalities in time domain [16]. This scheme is dedicated to applications in intelligent vehicle and highway system (IVHS). In this scheme, units in base-stations are able to sense the environment and communicate with tags that are only able to receive and transmit data. Two different modes of operation are allocated to different time-divided cycles. Furthermore, a mode-selective signal runs the VCO in transmitter to generate FMCW for radar mode and single frequency carrier for radio mode. In the radar mode, the operation principle is

identical to that of any FMCW radar. For the radio communication, base-stations operate in full-duplex mode. Carrier can be modulated by information data using amplitude shift keying (ASK) technique while for data reception from tags a pure carrier should be transmitted. Mobile tags can modulate this carrier by phase shift keying (PSK) to send data to the base stations. FMCW radar is also integrated sequentially with communication by frequency shift keying (FSK) technique [19] or even by spread spectrum scheme [20].

Radar-radio integration can also be implemented on multicarrier architectures like orthogonal frequency division multiplexing (OFDM). OFDM radar signals are not suffering from range-Doppler coupling issues. In addition, UWB-OFDM radars outperform counterparts based on UWB spread spectrum signals, due to higher spectral efficiency and pulse diversity potential. The design process of such a multifunctional system was described by [21]. In [22], the basic concept of radar and data communication fusion using OFDM signals was detailed and evaluated through simulation. For radar applications, the information of radar signal can be obtained from received signal after match filtering. On the other hand, for data communication, serial data is divided into blocks and bits on each block are mapped on sub-channels of OFDM symbol using On-Off keying (OOK). However, OFDM systems require high-peak-to-average-power-ratio (PAPR) and are sensitive to Doppler spreading. Accordingly, complex frequency synchronization and potential linearity requirement would significantly increase their system cost.

A rather complete time-domain scheme was proposed and developed in [14, 23] through an innovative waveform technique, by which all on-board units are able to either communicate or sense the environment. When radar mode comes into play, up- and down-chirp signals are separated in time with a single-frequency signal in the middle of a time division scheme. This would immune the conventional FMCW radar against interference. Radio cycle follows these three time slots and consists of a single carrier with constant frequency that can be modulated in either phase or amplitude. Using this scheme, a joint operation of radar and radio modes with minimum interference was studied and demonstrated. However, this system would be able to detect only the range and velocity of the target in sensing mode.

Either time or frequency domain based integration scheme possess specific advantages or disadvantages that may make them preferable depending on the desired functionality and tolerable cost or complexity of the system.

The main advantage of time division over frequency division is the efficient usage of frequency resources, especially around narrow available frequency bands. With the former approach, the whole band might be allocated to radar sensing in support of a good resolution during the radar cycle while the same band can be divided into several narrower segments to be used for communication between units in different cells. Moreover, the separation of distinct operational signal into different time slots would allow for avoiding the complexity of signal processing when a plurality of functions is desired to be accomplished all together.

However, the major drawback of time-domain integration scheme is the necessity of synchronization. Indeed, units in the same system cell should use the same carrier frequency, and the reference clock signal of all units in a system cell should be synchronized. This can be done, using the timing information of global positioning system (GPS) or even other techniques such as network time protocol [24].

In this thesis, the time-domain based integration scheme has been selected for further research and development with the main focus on improving RF front-end of multifunctional transceivers through unifying essentially different types of architectures for different functions. The principles of this integration scheme are discussed more in detail throughout the following chapters.

In all radio-radar integrated systems schemes, the well-known techniques of wireless sensing and communications are incorporated. The main challenge remains for the development of transceiver architectures in which techniques for RF component unification or sharing should be applied to avoid high cost and complexity. This issue becomes rather important when more functions are desired to be added to these multi-functional systems.

The radar associated functions in most reported RadCom schemes are limited to merely range and velocity estimation, and rarely a solution is presented for complete object positioning via an additional function of angle detection, while this is an indispensable function of automotive radar systems. Nevertheless, the technique of time-difference-of-arrival (TDOA) is adopted in RadCom system proposed by [25] which uses pulse-position-modulation (PPM) as operational signal and is capable of complete localization, and also the concept of incorporating OFDM RadCom systems with multiple-input-multiple-output (MIMO) architectures is discussed through simulations in [26].

Existing techniques of angle detection demand for utilizing at least two receiver channels. Hence, incorporating them in RadCom systems may undesirably augment the complexity in implementation unless every portion of the transceiver is unified or shared if possible. This research problem is explored deeply in this thesis and an improvement is made through adding a function of angle detection along with complete system characterization based upon the time-domain integration schemes and the corresponding transceiver architectures.

However, the reported transceiver schemes for integrated RadCom systems were mostly based on conventional heterodyne (low-IF) or homodyne (zero-IF) architectures [14, 15, 27, 28]. Through these architectures, integration of multiple systems can be achieved mostly through 1) time sharing of different parts of the Rx or Tx blocks between corresponding operational modes or 2) dealing with the incompatibilities between different modes regarding essential system specifications or channel characteristics. Furthermore, such architectures can be inevitably complex for implementation when additional functions such as angle detection are to be compromised with the existing functions, because multiple receiver paths would have to be added. This can eventually augment the circuit complexity especially at the final down-conversion/mixing stage in the Rx block. Thus, the strategy of unification instead of only sharing different parts of transceiver is concerned in this thesis when additional functions are to be incorporated.

Apart from the heterodyne and homodyne transceiver architectures, the technique of multiport interferometer has been applied to the design of distinct radio and sensing systems. The considerable advantages of this technique have been demonstrated for variety of applications, including modulation [29, 30] and demodulation [31-33] of carriers for communication purposes or range, velocity and angle estimation for sensing purposes [33-36].

Subsequent to the early demonstration of the multiport technique for network analyzer applications by Engen and Hoer around early 1970s [37-39], the six-port interferometer was demonstrated for the first time to be capable of quadrature demodulation when applied in the receiver (Rx) block of a communication system by [40] in early 90s. Subsequently, the same topology was employed to operate as a down-converter in the Rx block of radar systems where the FMCW signal would be de-chirped [41, 42]. Furthermore, simple, and low-cost AoA estimation systems were developed via six-port technique [43-45] with very high accuracy thanks to the excellent phase resolution in processing of the input signals within passive multiport network [46].

In addition, positioning systems with accuracy in the range of micrometer were demonstrated with this technique for small vibration detection in industrial areas [36] or patient respiration monitoring in health care centers [47]. On the other hand, it was used in the Tx block for direct modulation of the carrier signal [29, 30].

Like any other solution, six-port technique possesses pros and cons which are discussed briefly in the following. The core of the multiport interferometers is the passive network of couplers and/or phase shifters. Therefore, a wide fractional bandwidth is easily achievable. In addition, the required LO power for up/down conversion purposes is much less than the regular mixer-based up/down converters because it operates with square law diode detectors [48]. These benefits are very important for system applications around millimeter wave frequency bands [35]. Because of the very simple signal processing required in this technique, the systems based on multiport architectures do not suffer from heavy computation burdens. On the other hand, poor sensitivity of detectors restricts the dynamic range of six-port based receivers [49, 50]. In addition, such architectures demand for an appropriate calibration technique for mitigating the effects of the circuit non-idealities in practice. Therefore, various calibration techniques have been reported for six-port based systems with different applications that are categorized in [50]. In [49], a solution has been presented for diode linearization and calibration that extends the dynamic range of the receiver.

Due to the remarkable advantages of the multiport technique and the plurality of available ports, the multiport architectures can be a promising candidate for multifunction transceivers. Therefore, this interferometric architecture besides the heterodyne or homodyne ones are mainly concerned in this thesis to be further developed for the purposes of unifying the transceivers of multiple systems.

As it is mentioned, one of the challenging issues in devising an architecture for the integrated multifunctional transceiver is the intrinsic incompatibilities that either inherits from the absolute different system specifications or naturally exist in different propagation channels. For instance, the propagation path loss or required signal to noise ratio (SNR) can be significantly different for radar and radio signals that should be respected in designing the RF front-end circuitry. In other words, whatever the integration strategy would be, i.e., component sharing or unification, these incompatibilities should be dealt with which demand for complete characterization of these three types of the above-mentioned transceiver architectures.

The heterodyne or homodyne based architectures have been already characterized, whereas some aspects of multiport interferometric structures are not completely investigated yet. Therefore, multiport architectures are analyzed within this thesis in terms of noise figure (NF), conversion loss and intermodulation (IM) products that should essentially be known in transceiver design. Moreover, the capabilities of existing multiport architectures are investigated for integration of multiple functions and novel passive networks are presented that makes functional integration feasible. Furthermore, appropriate calibration techniques are presented where the existing techniques were no longer appropriate with the new proposed multiport architectures.

1.2 Objectives

The overall objective of this PhD thesis work is to propose and develop low-cost integrated multifunctional systems. Sensing and communicating as the ubiquitous application of radio technology were selected for integration. The emphasis is on radar type of sensors and on the integration of radar related functions such as range, velocity and angle detection with the function of communication. Moreover, the development of multifunction sensors and also multiband radio transceiver architectures are also considered in this thesis. Three specific objectives stem from this general objective as follows:

- 1) Improve the state-of-the-art time domain RadCom scheme and the corresponding transceiver though adding more functions such as angle detection.
- 2) Develop transceiver unification strategies for integrating multiple functions through multiport interferometric techniques.
- 3) Propose, model and characterize innovative RF components such as couplers and Baluns for millimeter wave applications which are indispensable for the transceiver unification.

The long-term objective of the projects conducted in this PhD thesis is to build up a ground for future systems-on-chip specifically for millimetre-wave applications. Transceiver unification techniques proposed in this thesis can contribute significantly to the simplification, cost and size reduction of the multifunction systems-on-chip (SoC) or systems-on-substrate (SoS). The principles of the proposed techniques in this thesis are not limited to a specific fabrication process such as printed-circuit-board (PCB) or Miniaturized-Hybrid-Microwave-Integrated-Circuit

(MHMIC) and can be realized using advanced technique of complementary metal-oxide-semiconductor (CMOS).

1.3 Methodology

The main approach in this thesis is to develop first multifunctional system concepts which may involve operational waveform schemes, RF transceiver architectures as well as signal processing techniques. The developed concepts are assessed first through system level simulations upon theoretical analysis. The systems are also prototyped and measured to prove their actual or true functionality. The latter step could inevitably include some engineering aspects which may not be explained in detail within this research thesis.

1.3.1 Improvement of the state-of-the-art RadCom transceiver

The functionality of the state-of-the-art time domain integrated RadCom transceiver has been limited to distance and velocity estimation when operating in radar mode. Moreover, such scheme has not been completely characterized in terms of required signal to noise ratio and object detection in multi-target scenarios. The ability of beam direction estimation not only qualifies system capability in individual radar mode, but is also considered as a contribution to joint mode. For example, the information about beam direction can be used in radio mode for beam forming purposes. With the main objective of incorporating the additional function of angle detection to other ones of range and velocity estimation besides communication, and also enhancing the range resolution, the RadCom system is studied, characterized and implemented to prove the concept. The following steps are taken to accomplish these goals:

- 1) Waveform scheme and the corresponding transceiver are modified for AOA estimation and higher data communication rate.
- 2) A signal processing solution is presented for multiple target detection.
- 3) The system incompatibilities in different modes of operation for different functions are completely studied.
- 4) The desired waveform is realized by a combination of software-defined direct digital synthesizer (DDS) and field programmable gate array (FPGA).

- 5) In order to validate practical functionality of the modified architecture, a low frequency prototype is realized to operate around 5.875 GHz and its performance is evaluated through the following steps:
 - 5-1) Frequency resources are studied to find valid low frequency band for our improved system.
 - 5-2) System specification is determined according to US FCC's rules and practical requirements
 - 5-3) Functionality of the unified transceiver is analyzed through a theoretical link budget analysis.
 - 5-4) RF transceiver is designed through theoretical chain-budget analysis. System specification and link budget analysis are considered as redlines for component selection.
 - 5-5) Up-converter and down-converter as the most important parts of RF transceiver are simulated by Harmonic Balance platform in a commercial package namely ADS.
- 6) The whole system including digital signal processing portion with transceiver is optimized through a multilayer and system-level simulator (i.e., Ptolemy) within ADS.
- 7) The transceiver circuits are prototyped in house and system performance is evaluated through system level measurements in our lab at the Poly-Grames research center and compared with the theoretical analysis.

1.3.2 Development of unified transceiver for RadCom system through multiport technique

As it is already mentioned, RadCom schemes involve two indispensable aspects of multifunctional systems, i.e., operational signal and RF transceiver. With the already proposed time-domain integration of distinct operational signal, the first aspect is studied. However, and on the second aspect, further improvement should be made toward cost and size reduction of such multifunction transceivers along with incorporating additional functions with the former ones. Therefore, the main emphasis of the research in this thesis is on the second aspect to develop rather unified multifunctional transceiver as an effective method to reduce their complexity and size. Because of the interesting features of the multiport technique, it is considered as an excellent candidate for developing rather compact transceiver architectures. Due to the plurality of available

ports and the possibility of analog signal processing through phase conditioning, multiport-based transceiver architectures are more capable of unification of the architecturally different transceivers of integrated systems than the conventional heterodyne and homodyne based multifunctional transceiver architectures.

It should be highlighted that with the conventional six-port configuration, multiport based receivers were already developed that were capable of accomplishing all those functions distinctly. However, to have all functions in one single multiport receiver the conventional six-port should be further developed. Therefore, a novel multiport architecture with specific phase conditioning is proposed that can handle all functions of range, velocity and angel detection as well as data communication.

1.3.3 Characterization of multiport receiver and development of innovative microwave components

Although the concept of six-port receiver has been used extensively for many applications since its advent, some aspects have not yet been characterized which are indispensable to know in the design process. Therefore, the multiport receiver is studied to formulize its characteristics in comparison to conventional mixers. In addition, several passive components including balun and 180° hybrid coupler are developed and characterized for applications around millimeter-wave frequency bands. The developed components can be used within the newly proposed passive multiport networks for implementation in high frequencies.

1.3.4 Development of millimeter-wave multifunctional multiport-based transceiver

The proposed multiport receiver is further completed with the intention of simplification of signal processing and preserving the inherent range resolution within multiport technique. The proposed multiport architecture can unify both six-port based AOA detection systems and communication receivers. An appropriate calibration technique is also developed to deal with the non-idealities in practice for both modes of AOA sensing and data communication. An appropriate calibration technique is also developed to deal with the non-idealities in practice for both modes of AOA sensing and data communication. A system demonstrator at around millimeter-wave

frequency bands, i.e., 77 GHz, is also implemented based on this multiport receiver and its performance is assessed through system level measurements, for concept validation purposes.

1.3.5 Development of multiport-based simultaneous 2-D AOA detection system

Other than integrated radar communication transceivers, the multiport interferometric receiver is developed for estimation of incoming electromagnetic beam's direction of arrival, i.e., both horizontal and elevation angles. With the existing six-port receiver only one angle can be estimated, and two identical systems should be assembled for detection of both angles provided that the complexity of implementation can be overcome. An eight-port passive network with appropriate phase conditioning is proposed that unifies two distinct six-port based systems. The main application of such systems is antenna beam alignment in point to point radios and therefore the proposed receiver is implemented along with the newly proposed antenna configuration at around 60 GHz. Furthermore, a calibration technique along with appropriate signal processing is presented. Finally, the performance of the prototyped system is evaluated through system-level measurements.

1.3.6 Development of dual-band radio architectures for multi-standard wideband small-cell backhaul

The dramatic growth in the demand for bandwidth in mobile wireless communication systems along with the rapid development of 5G technology, has brought the backhaul technology for small cells into view. The technology of choice for the small cells that are being deployed at the street level has been millimeter wave radio technology. V-band (57-66 GHz) and E-band (71-76, and 81-86 GHz) are the preferred spectral regions for implementing small-cell backhaul solutions because of their available large bandwidths as well as the fact that they are still sparsely occupied. V-band has unstructured channelization favoring time division duplexing (TDD), whereas E-band is structured around frequency division duplexing (FDD). Interference in the mobile wireless communication systems should be avoided while maximizing the data communication throughput and availability. Therefore, a combined V/E-band radio architecture in one flexible product would be the ideal solution.

In this thesis, some solutions are presented by putting forward several dual-band and dual-mode radio transceiver architectures using multiport technology. The proposed schemes within this thesis can be potentially used to map out the technical solutions for next generation V/E band radio architecture.

1.4 Original contributions

In this thesis, a thorough development of multifunction transceivers in several contexts of integrated systems is presented through a systematic study and a top-down approach. The scientific contributions lie not only on the development of transceiver architectures but also the corresponding signal processing techniques as well as innovative RF components if needed for implementation of the proposed multifunctional transceivers. On the ground of the original idea of function integration of multiple distinct systems in time domain, the state-of-art RadCom system is further improved by incorporating the additional function of AOA detection to the existing ones of range and velocity estimation besides communication. The time domain RadCom scheme with the improved system and transceiver architecture is completely analyzed and implemented in 5.8 GHz to evaluate its performance and the presented system analysis.

Moreover, a new configuration of multiport network is put forward and adopted in receiver block of RadCom transceiver that makes substantial size reduction through transceiver unification. The functionality of the proposed RadCom system based on the multiport receiver is proved with the developed system demonstrator at 5.8 GHz.

The proposed multiport receiver is improved further, with the focus on two functions of AOA sensing and data communication, by making use of additional port that helps angle estimation in time domain, while within our first multiport-based multifunction receiver, angle estimation was feasible through FFT in frequency domain. As such, the extraordinary phase resolution within multiport technique is preserved. The improved multiport receiver with novel passive phasing network is theoretically analyzed and enriched by an appropriate calibration technique. This novel multiport receiver is adopted in a complete multifunction transceiver and implemented at around 77 GHz.

Additionally, several passive components, including balun and 180° hybrid coupler with non-interspersed ports are also developed, analyzed and prototyped at very high frequency bands.

Moreover, the technique of multiport is improved through proposing a new configuration of passive network and receiving antenna as well as signal processing algorithm. Indeed, with the proposed multiport scheme, two distinct AOA detection receivers are unified for the purpose of two dimensional angle detection.

Several multiport-based radio transceiver architectures are presented that can handle two different schemes of full duplex operation in two distinct bands, as well as sensing the spectrum to keep the system aware of the unused channels in unlicensed frequency bands. The operation principles of the presented transceiver architectures are analyzed and proved through system level simulations.

In addition, the multiport interferometric receivers are studied and characterized for some aspects including noise figure, conversion loss and LO power requirements. These characteristics of multiport based receivers should be essentially known prior to transceiver design especially when multiport receivers for multiple functions or integrated systems are used.

All in all, major scientific contributions that are made throughout this PhD thesis project cover a wide range of transceiver architectures, i.e., from heterodyne and homodyne to multiport and diverse applications, from RadCom integrated systems to 2D DOA detection systems. The subjects are addressed in either system or component level and are studied deeply in various aspects including theory, modelling and signal processing to electronics and electromagnetics, from CAD simulations and design to fabrication and measurements. Our research outcome is reported in several peer-reviewed scientific conference, journal and transaction articles as well as patents.

1.5 Thesis organization

This thesis is organized as follows. In chapter 2, some fundamental concepts that are addressed throughout the whole thesis are briefly reviewed to make this thesis self-complete and stand alone for the interested reader. In chapter 3, the improved time-domain integrated RadCom system is analyzed and the 5.8 GHz prototyped system is presented. Chapter 4 covers the multiport based RadCom transceiver and the discussion around the system demonstrator at 5.8 GHz. In chapter 5

discussions about the parametric characterization of the six-port receiver are provided, and the development of various passive components are discussed in chapter 6. In chapter 7, the development of the multifunctional multiport transceiver at around 77 GHz is given while chapter 8 deals with multiport based 2D DOA detection systems. Chapter 9 discusses dual-band and dual-mode radio architectures, and finally chapter 10 concludes this thesis with discussion on future prospective on the relevant research topics.

CHAPTER 2 FUNDAMENTALS OF TIME-AGILE INTEGRATION SCHEME AND VARIOUS TRANSCEIVER ARCHITECTURES

As it is already mentioned in Chapter 1, throughout this thesis, among various integration techniques, the time-domain integration of distinct operational signals [51] forms the basis of developing multifunction transceiver architectures for joint radar-radio operations. Therefore, the principles of this simple technique is introduced in the following section. Since the main emphasis has been made in examining new RF transceiver architectures within this thesis research, the fundamentals of the existing wireless transceiver architectures are also reviewed. Additionally, in this chapter, electromagnetic wave propagation and the existing AOA detection techniques are discussed in a nutshell in order to provide the reader with sufficient related background.

2.1 Time-agile integrated modulation schemes

As it is discussed in the previous chapter, the integration of different operational signals associated with distinct systems, each for specific application, in successive time slots provides an excellent and simple solution for devising suitable modulation schemes for multifunctional systems. Principally within the technique of time domain integration, appropriate duration of a single time slot is allocated to the essential waveform of the desired function. For example, if a radar associated function such as object detection and ranging is to be integrated with the capability of communication, an up-chirp frequency sweeping signal can be integrated with single frequency carrier in distinct time slots (Figure 2-1(a)). The single frequency carrier can be modulated by data bits using a variety of modulation techniques such as QAM or PSK. Furthermore, if the additional function of measuring the velocity of mobile object is to be integrated, the up-chirp signal can be followed by a down-chirp signal in the subsequent time slot with identical duration (Figure 2-1(b)). Moreover, if range and velocity measurements of multiple targets are desired the triangular shape of up-down chirp signal can be transformed to trapezoidal FMCW (TFMCW) by adding a constant frequency (equivalent to the maximum frequency of the up-chirp) between the up and down chirps (Figure 2-1(c)). The important parameters such as sweeping bandwidth and time can be determined in accordance with the required range and velocity resolution. The essential phase continuity condition for preventing the out-of-band spectrum growth was discussed in [51]. Other waveform

design parameter determination and essential signal processing technique for sensory data extraction are discussed in detail in Chapter 3.

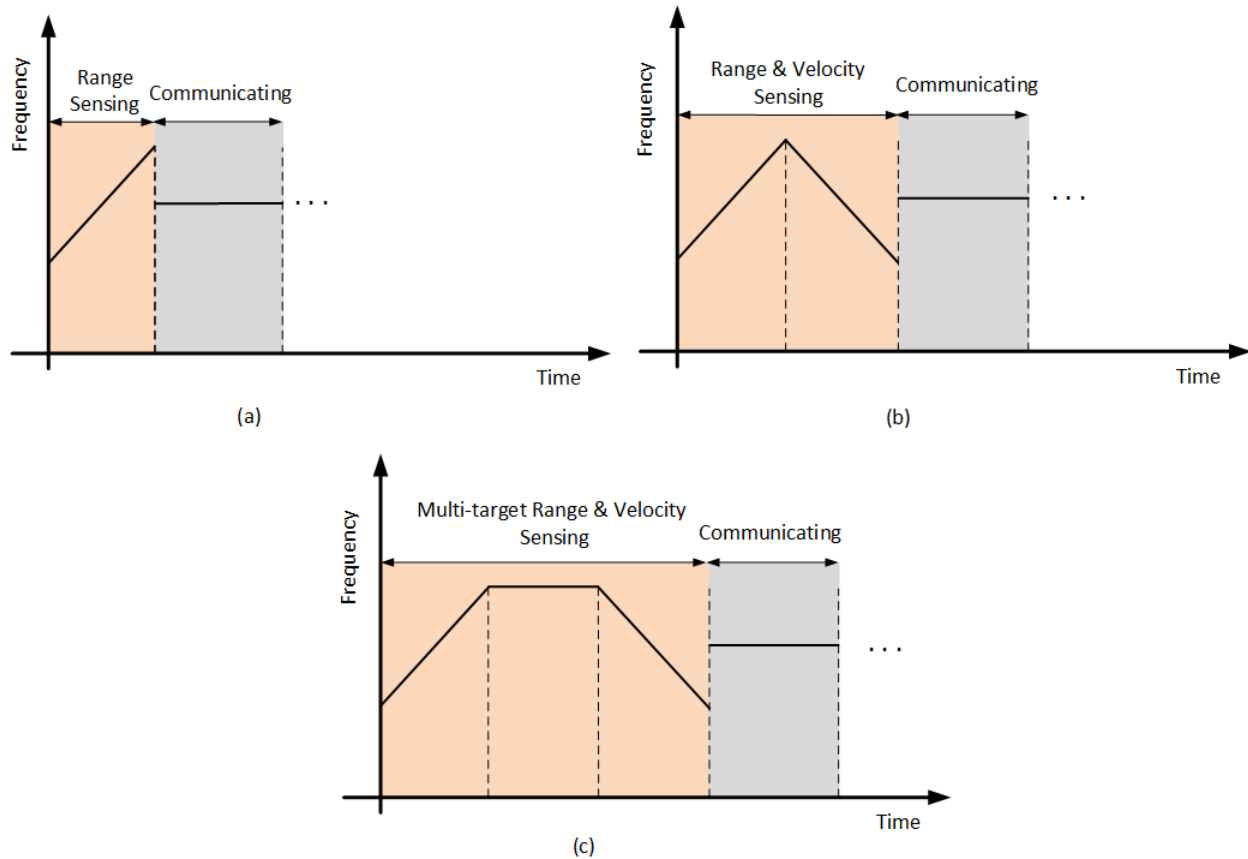


Figure 2-1: Modulation scheme for integrated RadCom systems

Such time-agile modulation scheme presents a simple technique for multi-system integrations and has a number of attractive features. First, the mutual interference between radar and communication functions is minimized when they are allocated to different time slots. Second, it can be utilized in multi-user environment thorough assigning a specific time slot to each user based upon the technique of time-division-multiple-access (TDMA). Third, the staggered radar and radio modes allows for data fusion and consequently improving the functionality in each mode. For example, different units exchange sensory information and extend the operational range within a radar network. Likewise, the obtained information of velocity of motion can help compensating the effect of Doppler spread in radio communication. Fourth, the time agile waveform is reconfigurable in different application scenarios and the sensing/communicating time cycle

duration or repetition laps can be easily changed, using a reconfigurable waveform generator. The operation principles of integrated RadCom system based on such time-agile scheme is explained more in detail in Chapter 3.

Since the time-agile modulation scheme uses the FMCW radar signal, the fundamental theory of this radar sensing technique is concisely introduced in the following.

FMCW has a very long history [52] and is widely adopted in existing radars especially in long-range radars [53]. The fundamental features of this technique are discussed in [54]. Figure 2-2 shows the time-frequency diagram for FMCW radar signal. The frequency is actually swept back and forth between f_1 and f_2 linearly and therefore, phase is a quadratic function of time. The transmitting signal can be expressed as

$$S_t(t) = \begin{cases} S_u(t) = \cos\left(f_1(t - nt) + \frac{(f_2 - f_1)}{T}(t - nT)^2\right) & nT \leq t < \frac{(2n+1)T}{2} \\ S_d(t) = \cos\left(f_2\left(t - \left(\frac{(2n+1)T}{2}\right)\right) - \frac{(f_2 - f_1)}{T}\left(t - \frac{(2n+1)T}{2}\right)^2\right) & \frac{(2n+1)T}{2} \leq t < nT \end{cases} \quad (2-1)$$

The phase of the received signal is a delayed version of the one in the transmitted signal. Assuming that the target is located at a distance R which is moving with velocity of v , this phase delay is a function of time, i.e., $\tau = 2(R + vt)/c_0$. Therefore, on the contrary to doppler radar, both upchirp and downchirp beat signals contain information about both velocity and range of the detected object.

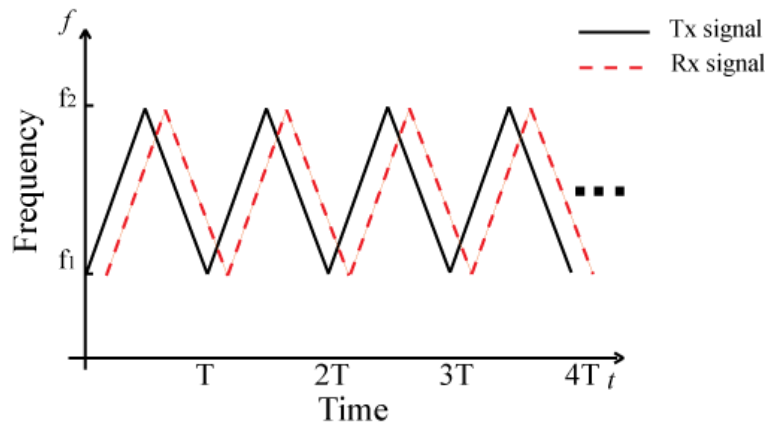


Figure 2-2: Triangle linear FMCW

The functionality of a triangle FMCW can be readily interpreted as follows. Let's assume that the target is stationary. Hence, the Doppler frequency is zero. However, the beat frequency (f_b) is non-zero (i.e., the waveform is shifted by τ along the time axis) and can be expressed by

$$\frac{f_b}{(f_2 - f_1)} = \frac{2\tau}{T} = \frac{2 \times 2R}{c_o T} \Rightarrow f_b = \frac{4(f_2 - f_1)R}{c_o T}. \quad (2-2)$$

Now, for a moving target the Doppler effect shifts the diagram of the received signal vertically by $f_d = 2f_2 v/c_o$. This shift is upward or downward for approaching or receding target, respectively, and consequently:

$$\begin{cases} f_{uc} = f_b \pm f_d \\ f_{dc} = f_b \mp f_d \end{cases} \quad (2-3)$$

It should be remarked that time domain integrated waveform is not limited to the ones presented above and it can be devised based on the functions which are desired to be integrated. Phase continuity and compatibility between the waveforms should be respected within the waveform schemes. Another time-agile waveform scheme is also proposed and used for another multifunctional transceiver within this thesis which is presented in Chapter 7.

2.2 Transceiver architectures

The main task of RF transceivers is to prepare the signal for transmission over the propagation channel or dispose the received signal for extracting the desired information. The signal preparation is mostly the filtering, amplification besides frequency up or down conversion for transmission and reception, respectively. Frequency conversion is done by mixing the incoming RF signal with either another RF signal or a local oscillator. This can be conducted within different architectures. The fundamentals of the three most common types of architectures are concisely reviewed in the following.

2.2.1 Homodyne receiver architecture

The homodyne architecture which is also known as “zero-IF” in the literature is shown in Figure 2-3. The main feature of the homodyne architecture that differentiates it from other type of

architectures is the single stage down conversion using LO signals with an angular frequency equivalent to that of the received RF carrier. Therefore, it is less complex and more compact as opposed to the heterodyne architecture [55]. However, it suffers from other disadvantages. For example, small portions of LO can leak into the RF port in the mixing stage, and get converted into DC upon self-mixing that can either distort the demodulated signal or saturate the ADC chips. In addition, the RF signal fluctuations impacts directly the amplitude of the baseband signals which is usually compensated by means of automatic gain control (AGC) loops that requires complex RF variable gain amplifiers (VGA). Moreover, the essential LO synchronization demands for phase locked loops (PLL) circuitries whose design complexity would be augmented at higher frequencies. Nevertheless, quadrature homodyne receivers are widely used especially in software defined radio systems, because many of these problems are resolved through baseband signal processing [56] as well as high data rate transceivers [57].

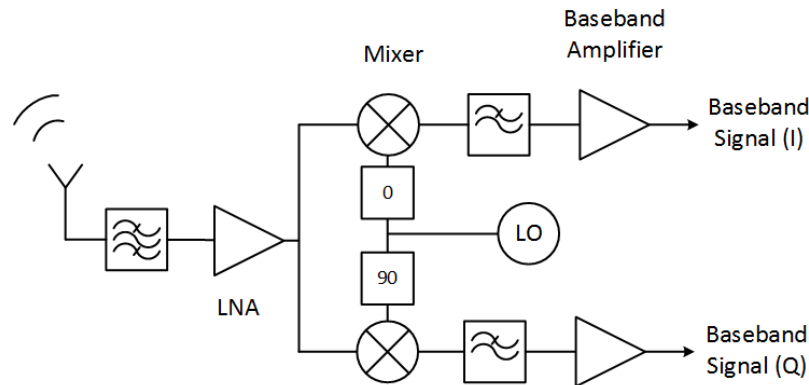


Figure 2-3: Homodyne receiver architecture

2.2.2 Heterodyne receiver architecture

Figure 2-4 shows the typical schematic block diagram of a heterodyne or “low-IF” architecture. Two separate stages of down conversion are used in this architecture. The modulated carrier is down-converted first to an intermediate frequency (IF) signal when mixed with a LO with unequal frequency. Subsequently, the IF modulated carrier is demodulated into baseband signal. Image rejection techniques should be applied to the first stage of mixing to prevent interference and SNR reduction due to side band conversion into the desired IF band. The complex RF AGC and PLL circuitry can be substituted by IF counterparts with low complexity and cost. These

benefits are achieved at the expense of more complex transceiver circuitry with more required components.

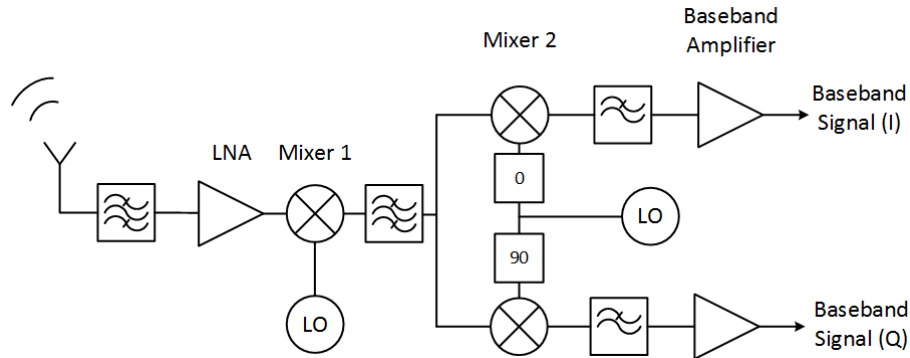


Figure 2-4: Heterodyne receiver architecture

2.2.3 Multiport interferometer receiver architecture

Mixers are the key component in the wireless transceivers in which the RF and LO signals are mixed together within a nonlinear device. The output of the mixers includes variety of products including the fundamentals of the input signal and their harmonics and intermodulation products. All mixers are multipliers, indeed. However, mixers can be categorized into additive and multiplicative ones from their implementation standpoint. In multiplicative mixers the RF and LO signals are applied to separate input ports of the nonlinear device, while in additive mixers they are applied to the same input port [58]. The block diagram of two different procedures through which the signals can be mixed are sketched in Figure 2-5. This structural difference in implementation yields different characteristics for these two types of mixer implementation. For example, the isolation between LO, RF and IF ports are more than that in additive mixers.

In addition to the heterodyne and homodyne receiver architectures, multiport interferometer based receiver architectures has been developed that operates based on the additive diode mixing [59].

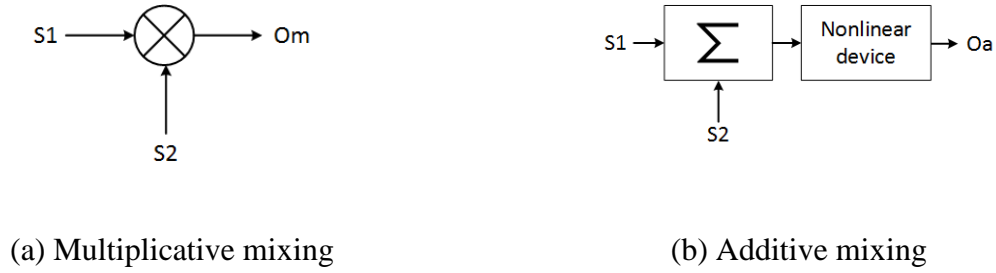


Figure 2-5: Two different mixing processes

If signals S_1 and S_2 are single tone sinusoidal signals with angular frequencies of f_1 and f_2 , and amplitudes of A_1 and A_2 , the output of the ideal mixer can be mathematically treated as:

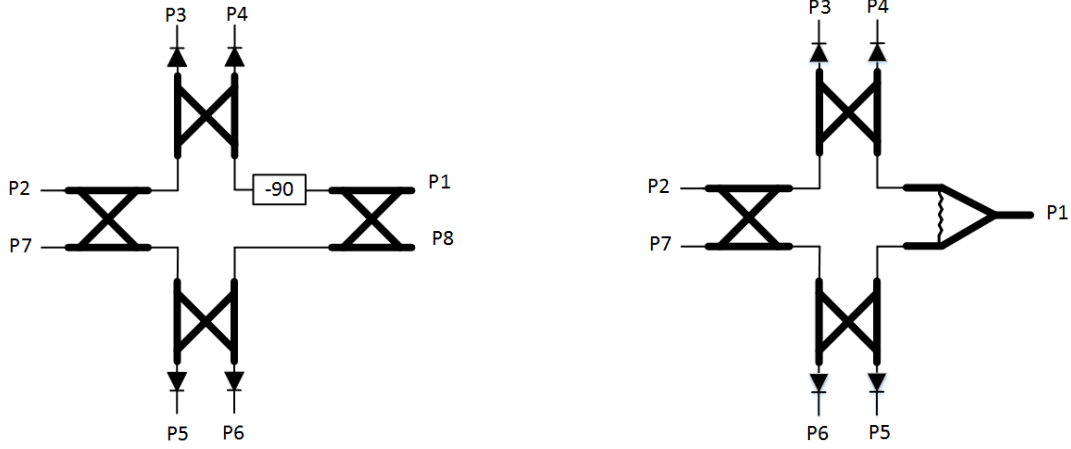
$$O_a = \sum_{q=1}^{\infty} a_q (S_1 + S_2)^q \quad (2-4)$$

which include all nonlinear products with the weighting factor of a_q . In multiport receivers, the input signals are superposed throughout a passive multiport component and applied to diode mixers. Diode mixers in multiport receivers operate in their square-law region to produce the desired multiplication in the squared term. Taking only the quadratic term ($q=2$) with the strongest weighting factor, we can express the output product with

$$O_m = \frac{1}{2} A_1 A_2 \{ \cos(2\pi(f_1 - f_2)t + \varphi_1 - \varphi_2) + \cos(2\pi(f_1 + f_2)t + \varphi_1 + \varphi_2) \} \quad (2-5)$$

The unwanted frequency contents are usually filtered out of mixing product.

The conventional six-port based receiver is comprised of a passive structure consisting of a network of quadrature hybrid couplers, power dividers or phase shifters with two input and four output ports [60] and also four diode detectors. Figure 2-6 shows two most common formats of the six-port interferometers which are widely used in the development of six-port based receivers. The additional available ports are terminated with matched loads if more than six ports are available.



(a) Quadrature hybrids and phase shifter

(b) Quadrature hybrids and power dividers

Figure 2-6: Two common topologies of passive junction for six-port receiver

In this interferometric architecture, the input signals superimpose throughout the passive junction upon experiencing a specific relative phase shift. The relative phase shifts of the input signals at the four output ports are $0, \pi/2, \pi, 3\pi/2$ for the conventional six-port network depicted in Figure 2-6. It should be emphasized that these relative phase shifts are indispensable for six-port operation and should be preserved in any other variants of network designed for six-port receiver. In other words, the output signals are fundamentally dependent on the S -parameters of the multiport network. The output signals are obtained from the linear combination of the detected powers at the output of diode detectors where the superimposed signals are mixed together.

As it is already mentioned, six-port architecture has been used in a variety of circuits with different application, such as modulators, demodulators, DOA detection receivers and highly accurate ranging sensors. Since six-port based radio receivers and DOA sensors are addressed for further development throughout this thesis, the fundamental theories of them are briefly explained next.

2.2.4 Six-port based radio receiver

Figure 2-7 shows the schematic architecture of a six-port based radio receiver (SPR). Two input ports are fed by LO and received RF signals. The detector outputs are converted to digital

domain upon filtering and amplification to be further processed and used in synthesizing the complex in-phase and quadrature components. The complete demodulation is conducted provided that the following conditions are satisfied on passive junction [48]:

$$\begin{aligned}
 1) \quad & |S_{41}| = |S_{31}| \quad \& \quad |S_{42}| = |S_{32}| \\
 2) \quad & |S_{51}| = |S_{61}| \quad \& \quad |S_{52}| = |S_{62}| \\
 3) \quad & \angle S_{41} = \angle |S_{31}| + 90^\circ \quad \& \quad |S_{32}| = |S_{42}| + 90^\circ \\
 & \angle S_{51} = \angle |S_{61}| + 90^\circ \quad \& \quad |S_{62}| = |S_{52}| + 90^\circ \\
 5) \quad & \angle S_{42} - \angle |S_{31}| - \theta_{LO} = 2n\pi, \quad n=0,1,2\dots \\
 6) \quad & \angle S_{52} - \angle |S_{61}| - \theta_{LO} = \left(2n + \frac{1}{2}\right)\pi, \quad n = 0,1,2\dots
 \end{aligned} \tag{2-6}$$

In addition, the diode detectors should operate in their square law region where the detected voltage is in linear relation with the detector's input power, i.e., $P_i = K_i V_i$, and all the detector's coefficients should be identical. Given the ideal conditions, I and Q symbols are obtained through subtracting the outputs of port 3 from that of port 4 and the output of port 5 from that of port 6, respectively. The complex I and Q symbols are calculated out of a linear combination of output detected voltages through the following expressions, where the coefficients can be obtained through suitable calibration techniques [50]:

$$I = \sum_{i=3}^6 \alpha_i P_i \quad \text{and} \quad Q = \sum_{i=3}^6 \beta_i P_i \tag{2-7}$$

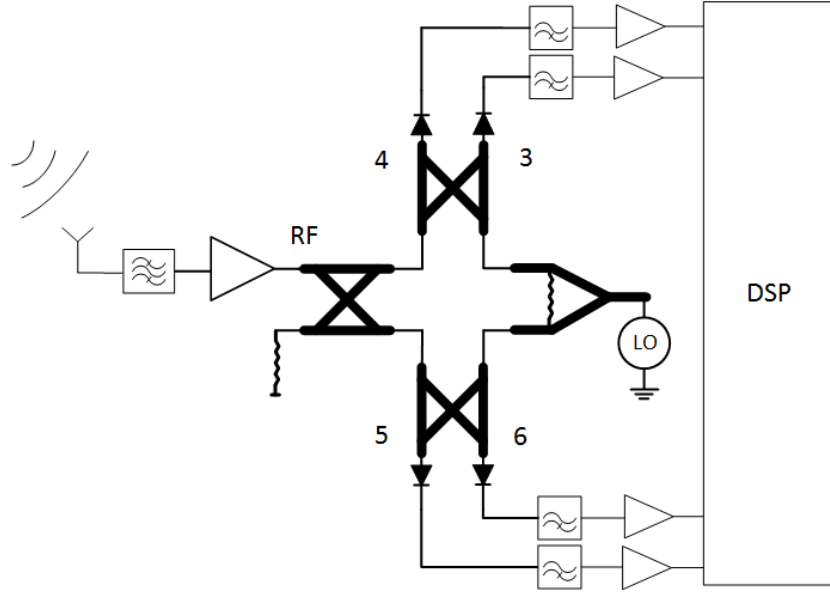


Figure 2-7: Six-port radio receiver

In order to analyze the operation of the SPR, we assume the phasor expressions of the input RF and LO signals:

$$\begin{aligned} a_{LO} &= |a_{LO}| e^{j(\omega_{LO}t + \theta_{LO})} \\ a_{RF} &= |a_{RF}| \sqrt{I^2 + Q^2} e^{j(\omega_{RF}t)} \end{aligned} \quad (2-8)$$

The output detected power (P_i), considering the quadratic term of the nonlinear outputs of the diodes, can be expressed as

$$P_i = |S_{i2}a_{LO} + S_{i1}a_{RF}|^2 \quad i=3, 4, 5, 6 \quad (2-9)$$

$$P_i = |S_{i2}|^2 |a_{LO}|^2 + |S_{i1}|^2 |a_{RF}|^2 + |S_{i2}||S_{i1}||a_{LO}| \left[a_{RF}^* e^{j((\omega_{LO} - \omega_{RF})t + (\theta_{i1} - \theta_{i2}) + \theta_{LO})} \right] \quad (2-10)$$

Subtracting two pairs of detectors' outputs would result in

$$P_i - P_j = -2K_1 I \sin \left(\frac{\sigma + 2(\omega_{LO} - \omega_{RF})}{2} \right) \sin \left(\frac{\delta}{2} \right) + 2K_1 Q \cos \left(\frac{\sigma + 2(\omega_{LO} - \omega_{RF})}{2} \right) \sin \left(\frac{\delta}{2} \right) \quad (2-11)$$

where

$$\begin{aligned}
\sigma &= \theta_{i1} - \theta_{i2} + \theta_{j1} - \theta_{j2} + 2\theta_{LO} \\
\delta &= \theta_{i1} - \theta_{i2} - \theta_{j1} + \theta_{j2}
\end{aligned}
\tag{2-12}$$

If the above mentioned conditions are fulfilled, and $w_{RF} = w_{LO}$ the differentiated outputs of detectors can be expressed as

$$\begin{aligned}
P_3 - P_4 &= -2K_1 I \\
P_5 - P_6 &= +2K_1 Q
\end{aligned}
\tag{2-13}$$

2.2.5 Six-port based AOA detector

Figure 2-8 shows the schematic architecture of a DOA detection receiver, where both input ports are fed by RF received signals from two antenna elements separated at a distance of d . The AOA of the incoming RF signal can be readily calculated from the detector outputs through

$$\text{AOA} = \sin^{-1} \left[\frac{\lambda \tan^{-1} \left(\frac{P_5 - P_6}{P_3 - P_4} \right)}{2\pi d} \right]
\tag{2-14}$$

which is obviously much simpler than other algorithms such as MUSIC or ESPRIT. Also, measurements with very high accuracy can be achieved, due to the interferometric nature of six-port based systems through which RF signals are processed in analog domain, and with excellent phase resolution. However, the application of such systems for AOA detection is limited to LOS scenarios and mostly limited to the detection of AOA of the incoming signal originating from single radiator.

The unambiguous range of angle detection depends on the distance between antenna elements. For $d/\lambda > 0.5$, the phase difference would wrap that can cause ambiguity in the angle detection. As this ratio becomes larger than 0.5, the phase resolution would improve, because a smaller range of angles should map between $-\pi$ to π , while the phase difference wraps for values of AOA larger than a specific limit and causes ambiguity. In other words, systems with different ratios of d/λ can detect angles within different unambiguous ranges. The largest unambiguous range (-90° to 90°) belongs to the ratio of 0.5 and it would be smaller for antennas placed in larger distances. In

practice, the design of antennas in shorter distances apart is difficult because of a stronger coupling that can deform the radiation pattern of each antenna element. The minimum distance that can guarantee the desired unambiguous range of angles can be determined from the following equation

$$\frac{2\pi}{\lambda} d_{\min} \sin(\theta_{\max}) = \Delta\varphi_{\max} \quad (2-15)$$

where θ is the AOA and the maximum detectable phase difference between received signals at two antenna elements is π .

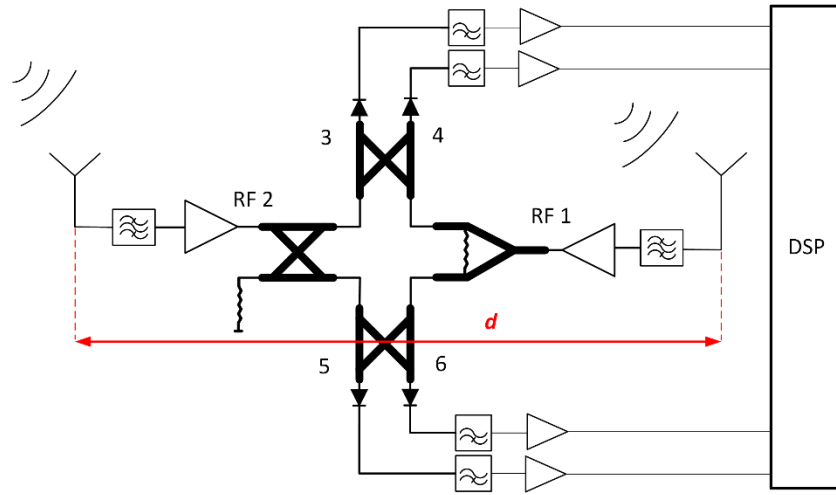


Figure 2-8: Six-port AOA detector

2.2.6 Implementation of six-port receiver

Passive six-port wave correlator and diode detectors are the most critical parts of the six-port receiver for implementation. Implementation of the passive junction using a variety of the transmission lines including microstrip or substrate integrated waveguide (SIW) have been already reported. The six-port junction comprises couplers and phase shifters which are already characterized, and the design of a six-port junction follow the same rules. Therefore, the basic design rules are not repeated here and the reader is encouraged to refer to the dedicated references [61]. However, the principles of the diode detector are briefly explained in the following and the design procedure of detectors at very high frequencies is explained further in detail through the next chapters.

Figure 2-9 shows the typical circuit of a diode detector which basically converts the RF input signal to DC signal at the output. The common nonlinear devices in these detectors are Schottky or tunnel diode [62]. With the nonlinear I-V transfer function of the diode, the detector rectifies the input RF signal power to single polarization current through the device that can be transformed to rectified voltage passing through a resistor, namely video resistor. The range of input power where the detected voltage has a linear relationship with the input power, i.e. $V=kPin$, is called the square-law region. Figure 2-10 shows these different operational regions of a simulated diode detector which is designed using the SPICE model of the MZBD-9161 Schottky diode.

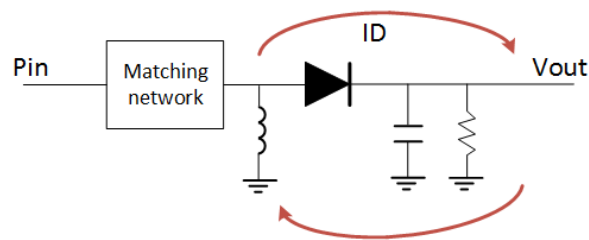


Figure 2-9: Diode detector circuit schematic

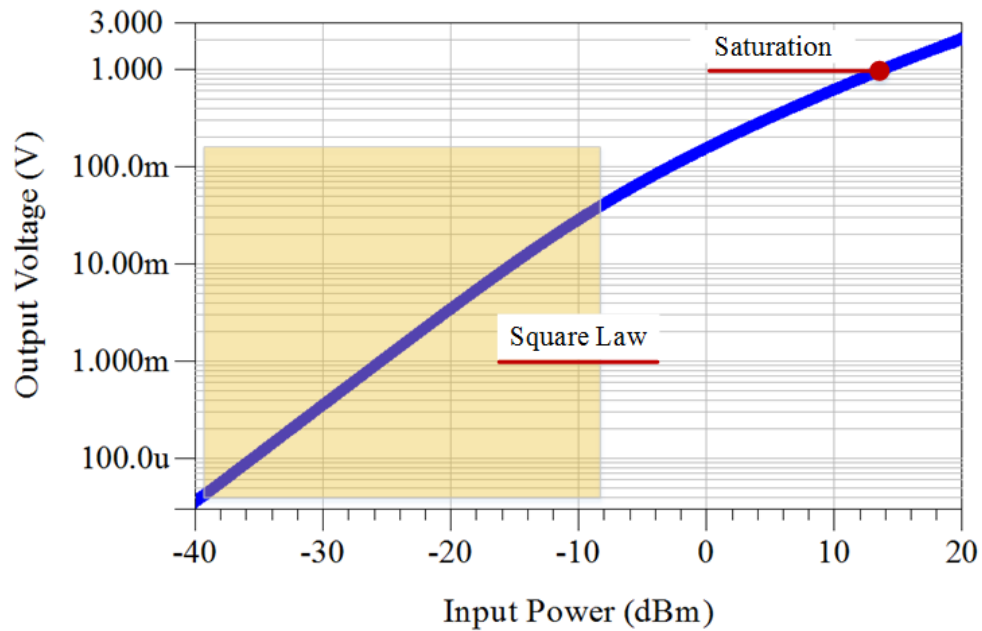


Figure 2-10: Simulated (V-P) transfer function of the Schottky diode in ADS using the developed MZBD-9161 zero-bias Gallium-Arsenide (GaAs) beam lead diode model

The capacitor at the output filters out the RF signal, and the RF choke completes the DC current path and blocks the RF input signal. If the diode detector is not matched, suitable matching circuit should be used.

2.2.7 Six-port calibration

In order to account for the imperfections in practice, appropriate calibration technique should be applied to the systems based on six-port technique. Since the advent of the six-port technique, a variety of calibration methods have been developed for different six-port based systems [49, 50, 63-65]. In linear six-port calibration techniques, both RF and LO signals are superposed throughout the passive six-port network and appear at the input ports of all detectors. The I and Q signals are extracted from a linear combination of them with weighting coefficients that depend on the S-parameter of the passive six-port junction, and conversion loss of the detectors. Unfortunately, the diode power detectors have a limited square-law region which constraints the dynamic range of the detector. In order to open up this region, diode linearization techniques can be used [49, 65]. A comparative analysis of the existing calibration and linearization methods is provided by [50].

2.2.8 Pros and cons of six-port technique

The interesting features of the six-port based direct conversion architecture have made it a competitive alternative of the conventional transceiver architectures for microwave and millimeter-wave frequencies [35]. Simplicity of passive circuit implementation, large achievable bandwidth capability and low cost diode detectors are some of the exceptional features of this type of architectures. In addition, the complex and expensive nonlinear mixer based circuits are substituted by simple passive diode based circuits. More importantly, the operation in square-law region allows for using low power LO (below 0 dBm) signals which draws a lot of attention for applications around millimeter wave frequency bands. Benchmarks on comparison of this newly introduced receiving technology against the conventional ones have been reported in [59, 66, 67].

Undesired leakage and input reflections in direct conversion receivers can cause self-mixing of the input RF and LO signals that can increase DC offset level, whereas the impact of DC offset in SPRs would be mitigated through the applied calibration technique.

The dynamic range of the SPR depends mainly on the detector sensitivity (i.e. the ratio of detected voltage to the input power), the minimum detectable signal above noise and also the applied calibration technique, which is typically around 40 dB [68, 69], which is much less than the dynamic range of other types of architecture. It has been demonstrated that the dynamic range of the SPR can be improved by extending the operation region beyond the square-law region, using suitable linearization technique [49].

To our best knowledge, no straightforward technique for calculating the noise figure (NF) of the SPRs based on the designed wave correlator, detector and baseband amplifier have been reported in the literature, and are mostly approximated based on the general circuit characteristics. The NF of six-port receiver is determined by the loss of the wave correlator which can be more than 7 dB and the noise of the detector [70]. Hence, the resulting NF of the SPRs is much more than that of other architecture types. Through this research thesis the six-port receivers are characterized further in detail which are discussed in chapter 5.

2.3 Electromagnetic wave propagation and DOA detection

The main objective in estimating the AOA of a radio signal at a receiver terminal is to find the direction of propagation or the relative angle of the electromagnetic wave propagation vector with respect to a specific coordinate system. The wave can be either emitted from a source or reflected from a target. The information about the AOA along with the one about the distance of the source can be used for complete localization that has been broadly investigated for various applications [71]. A broad range of advanced angle detection techniques, including MUSIC or ESPRIT have been reported [72] that are mostly based on baseband signal processing. The overall basics of the classical and modern angle detection techniques can be found in [73] which presents a reasonable insight about the wide topic of AOA estimation. It is worth mentioning that in this thesis, we have focused on the line-of-sight AOA detection technique which is mostly based on phase or amplitude difference of arrival at one, two or several receiving nodes. Therefore, the fundamentals of DOA detection from physical point of view are explained concisely in the following without dealing with the advanced associated signal processing algorithms.

2.3.1 Electromagnetic wave propagation

Before discussing the angle detection techniques, a summary of the theory of electromagnetic field propagation is given next. The real component of a time harmonic complex wave propagating in a specific medium (with dielectric permittivity of ϵ and magnetic permeability of μ) can be formulized as

$$\vec{\Psi}(\vec{r}, t) = A(\vec{r}) \cos(\vec{k} \cdot \vec{r} - \omega t + \varphi) \quad (2-16)$$

where \vec{r} is the unity three dimensional direction vector, A is the amplitude of the wave, ω is the angular frequency of oscillation and φ and \vec{k} are the phase and wave vector, respectively. The direction of wave vector identifies the direction of propagation and its magnitude is inversely proportional to the wavelength (λ), i.e., $|\vec{k}| = 2\pi/\lambda$. The parameter that describes the rate that the wave-fronts of a wave progress in space is called the phase velocity which represents the proportionality between angular frequency (ω) and the angular wave number [74] through

$$v_p = \frac{\omega}{k} = \frac{1}{\sqrt{\mu\epsilon}} \quad (2-17)$$

On the other hand, the envelope of the wave's amplitude propagates with the velocity called group velocity (\vec{v}_g) which is equivalent to the phase velocity only in the non-dispersive mediums where ϵ and μ are not functions of frequency.

The electric field (\vec{E}) and magnetic field ($\vec{B} = \mu\vec{H}$) of an electromagnetic wave can be described from (2.13) with simplified sinusoidal solutions to the general electromagnetic wave equation as

$$\begin{aligned} \vec{E}(\vec{r}_E, t) &= \vec{E}_0(\vec{r}_E) \cos(\vec{k} \cdot \vec{r}_E - \omega t + \varphi) \\ \vec{B}(\vec{r}_B, t) &= \vec{B}_0(\vec{r}_B) \cos(\vec{k} \cdot \vec{r}_B - \omega t + \varphi) \end{aligned} \quad (2-18)$$

This electromagnetic wave equation can be simplified to Helmholtz equations for \vec{E} and \vec{B} with single angular frequency using Maxwell equations

$$\begin{aligned}
(\nabla^2 + k^2) \vec{E} &= 0 \Rightarrow \nabla^2 \vec{E} + \omega^2 \mu \epsilon \vec{E} = 0 \\
(\nabla^2 + k^2) \vec{H} &= 0 \Rightarrow \nabla^2 \vec{H} + \omega^2 \mu \epsilon \vec{H} = 0
\end{aligned} \tag{2-19}$$

General solutions for Maxwell equations can be found in the dedicated literature [75] and the interested reader may refer to them.

The direction of propagation of a wave is the direction of \vec{v}_g or mainly the one in which the wave flows. The average power density can be obtained from the time average Poynting vector \vec{P} :

$$\vec{P}(r) = \frac{1}{2} \Re \left\{ \vec{E} \times \vec{H}^* \right\}. \tag{2-20}$$

It should be highlighted that the wave vector (\vec{k}) is oriented in the direction of phase velocity as long as the propagation takes place in lossless isotropic media, implying that (\vec{k}) is orthogonal to the wave-fronts i.e., surfaces with constant phase. We consider finding the direction of \vec{k} as the direction of wave propagation, because propagation of the plane-wave (with TEM properties) over the air, which is lossless medium, is assumed for all applications discussed throughout this thesis. It should also be remarked that the wave properties and the applicability of the DOA detection techniques strongly depend on the electric distance from the source and the source dimensions. Accordingly, three different regions from the emitter can be generally specified including: near-field (non-radiative), Fresnel (radiating near-field) and Fraunhofer (far-field). In the latter one only, the spherical phase front approximately deforms into ideal plane phase fronts of a TEM wave. The distance from the radiator where the far-field properties can be observed depends on the radiation aperture and accordingly to the maximum dimension of the antenna (D) through [62]

$$R_f = 2 \frac{D^2}{\lambda}. \tag{2-21}$$

It should also be remarked that the discussions throughout this thesis is under the assumption that the observer is located in the far-field region with respect to the radiator of the wave with linear polarization, unless it is clearly specified.

2.4 DOA detection techniques

Generally, in line-of-sight DOA estimation, two different scenarios should be distinguished:

- 1) Detection of the incoming angle of a wave from a radiator whose location is unknown for the observer: As it is depicted in Figure 2-11(a), the position of the source is unknown for the observer and the DOA is detected with respect to a reference coordinate system.
- 2) Misalignment detection of an antenna: This case is shown in Figure 2-11 (b). The observer is located in the same reference axis and the misalignment angle of the main radiation beam from the reference axis is estimated.

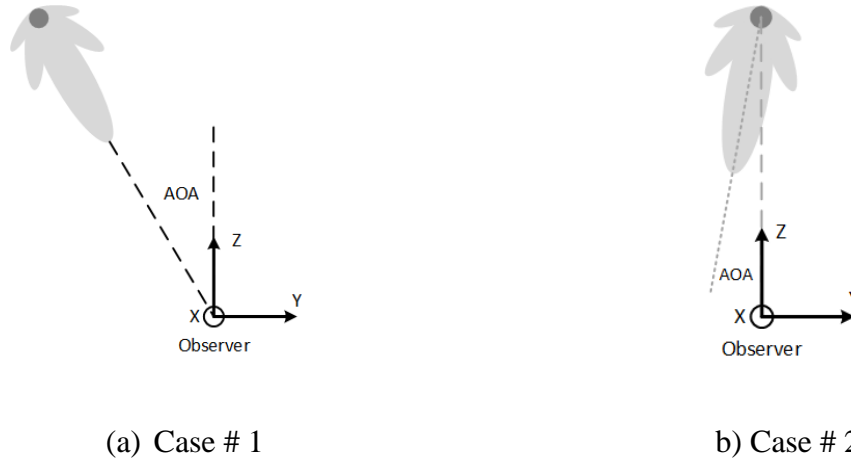


Figure 2-11: Different DOA detection scenarios

Considering the electric field of the propagating wave as the detected signal at the receiver, one can express it with the complex quantities as:

$$\vec{E} = A e^{j\phi} = A \cos(2\pi ft + \phi) + jA \sin(2\pi ft + \phi) \quad (2-22)$$

where A is the amplitude and ϕ is the phase at the receiver terminal. The direction of the Poynting vector or equivalently the DOA can be extracted from these two characteristics using two different techniques which are explained next.

2.4.1 Amplitude difference of arrival technique

In this very primitive technique of angle detection, two different configurations of Rx antenna are used for different scenarios of DOA detection. For the case of DOA detection with unknown angular location of radiator, Rx antenna with single receiving element can be rotated around its local axis and correct DOA would be detected where the maximum power is received [76]. Obviously, the Rx antenna should have directive radiation pattern so that changes in receiving power in different rotation angles can be observed. Therefore, for measurement with high resolution a Rx antenna with narrow main lobe width should be used so that small variation in amplitude with small angle rotation can be monitored. Initially, mechanical techniques were used for rotation which gradually evolved into digital beam forming techniques [77]. However, systems with mechanical rotation suffer from poor mechanical tolerance and long sweeping time, whereas the systems with digital scanning techniques should go through heavy computation burden to achieve precise measurements. Figure 2-12 shows the DOA detection setup with this technique.

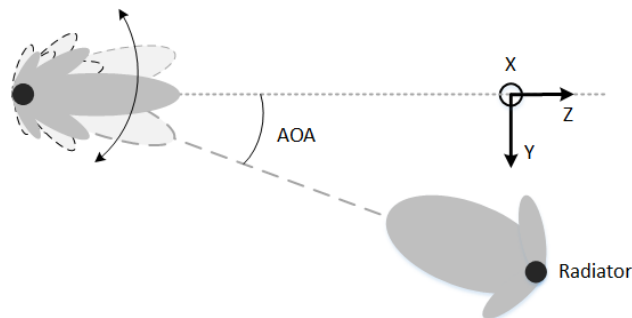


Figure 2-12: DOA detection based on amplitude measurement

On the other hand and for misalignment angle detection, two identical Rx antenna elements are used as this scheme is depicted in Figure 2-13. This technique is mostly used for aligning a high gain Tx antenna in the orientation of the axis perpendicular to the straight connecting lines between two antenna elements, rather than accurate misalignment angle detection. Given the high gain Tx antenna with highly symmetric main radiation lobe, the alignment happens when the same power is received at both Rx elements, i.e. $A_{Rx1} = A_{Rx2}$.

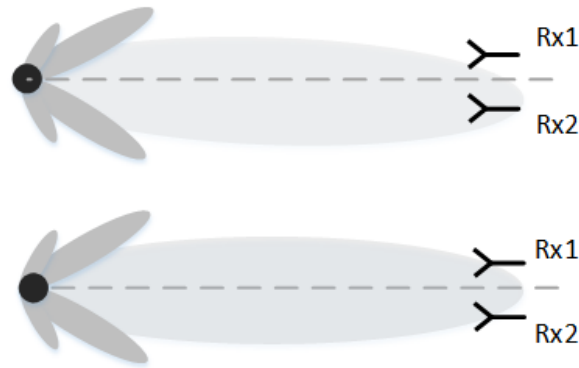


Figure 2-13: Antenna beam alignment based on amplitude measurement at two Rx elements

2.4.2 Phase difference of arrival (PDOA) technique

In addition to the amplitude based DOA measurement, phase of the incoming signal also conveys information about the relative direction of the Poynting vector. The phase of a propagating wave at a specific point varies periodically from $-\pi$ to π if compared to an absolute reference. Since, the phase of the Tx is not available as reference, at least two receiving nodes would be considered when making use of this technique. Figure 2-14 illustrates the phase fronts of a wave emitted from a directive antenna and travel toward two receiving elements. It can be seen that if the Poynting vector is orthogonal to the connecting axis of the two receiving elements, the phase of the received signal would be identical, whereas the phase difference would be non-zero when the Poynting vector deviates from the orthogonal direction. Different receiver architectures that are explained above can be used to extract the phase difference between the received signals. The main advantage of this technique compared with the amplitude based technique is that the exact value of DOA can be calculated from the extracted phase difference of arrival.

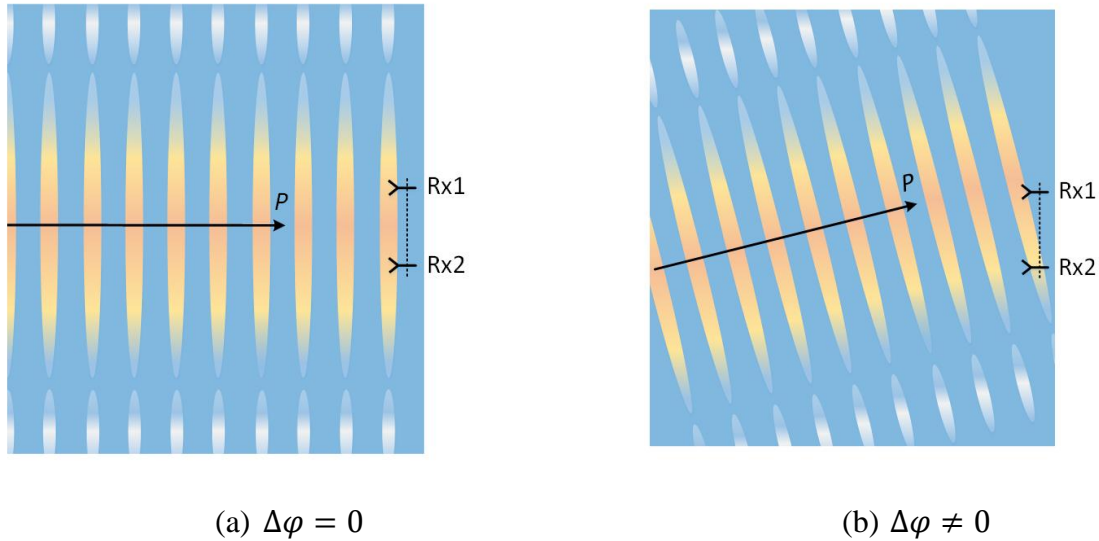


Figure 2-14: Wave propagation and geometrical arrangement of the receiving antenna elements with respect to the propagation direction

The phase difference observed at the two receiving elements depends on the distance between elements, the wavelength and also the incoming angle. Figure 2-15 shows the geometrical representation of the Poynting vector when making a nonzero angle with the normal vector of connecting axis. It can be seen that the phase difference is due to the additional path that wave-front should travel to arrive at the second antenna terminal. This path length depends on the wave's incoming angle that can be expressed simply as:

$$\Delta\varphi = \frac{2\pi}{\lambda} d \sin(\theta) \quad (2-23)$$

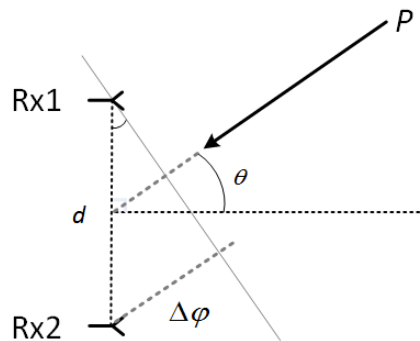


Figure 2-15: Phase difference of arrival at the antenna terminals

CHAPTER 3 MULTIFUNCTIONAL TRANSCEIVER FOR FUTURE RADAR SENSING AND RADIO COMMUNICATING DATA-FUSION PLATFORM

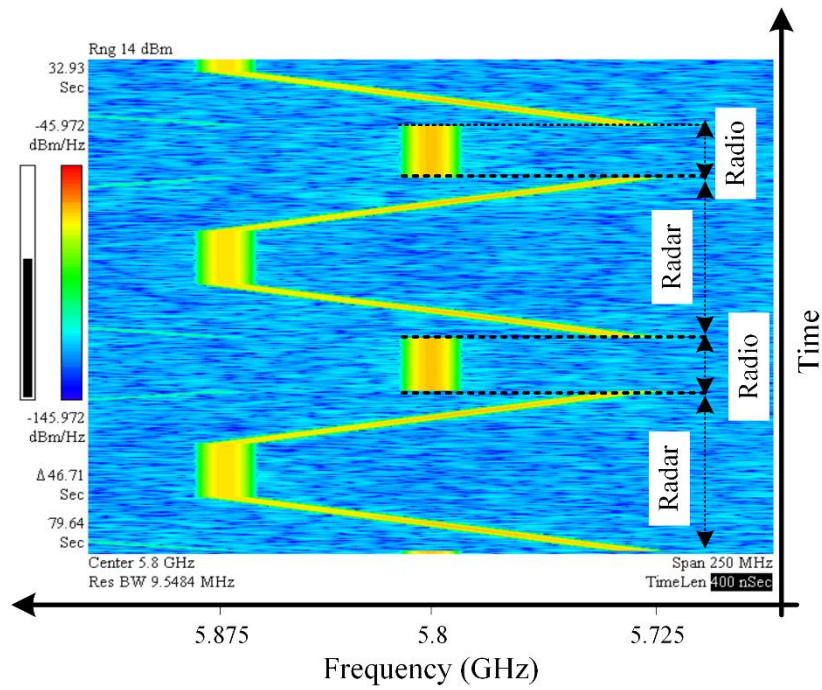
In this work, our focus is on the development of in-time-domain integrated RadCom systems with an intended application around dedicated short range communication (DSRC) band where a very narrow bandwidth is available. The function of angle detection is added by employing the Doppler and beat signal's phase-difference of arrival. Therefore, a new transceiver architecture is proposed. To address the simplicity and compactness, some essential portions in the Tx block are implemented in a software manner and a switching technique is applied to share the components in Rx block.

Additionally, the features of the in-time-domain integrated RadCom waveform is studied further in detail and the techniques that can be applied to meet the intended specifications of the proposed RadCom transceiver are re-examined concisely. The severe incompatibility of radar and radio channels and systems are also analyzed and accordingly a new transceiver architecture is proposed and prototyped. The functionality of the whole transceiver is validated through both system-level simulations and measurements. Early results of this effort have been presented by authors in [27] and a comprehensive discussion was presented in [28] along with extensive measurement results and details which are brought in this chapter. In the end, the limitations of current systems along with the capabilities of further research and developments of RadCom systems are concluded.

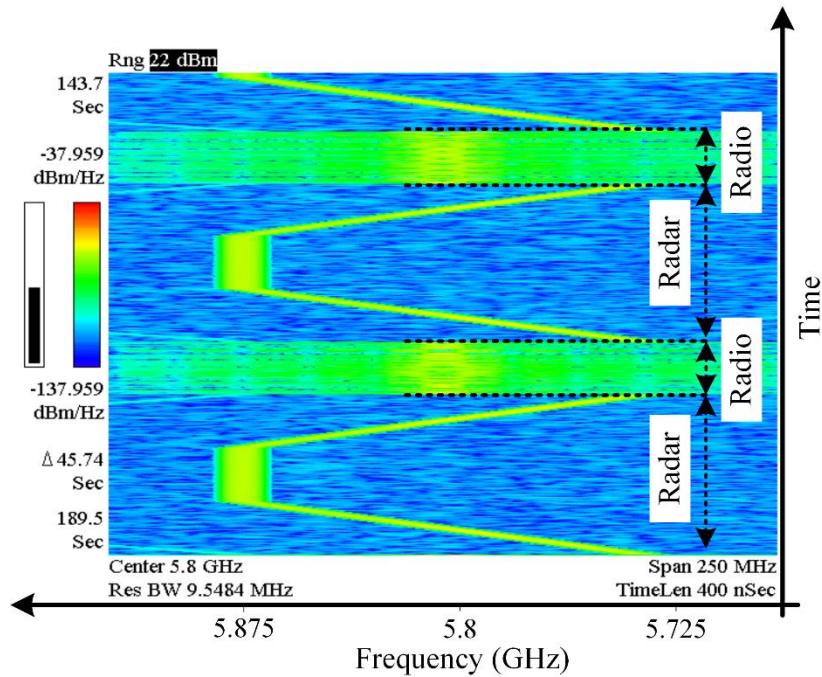
3.1 System concept

3.1.1 Signal modulation scheme

Figure 3-1 shows the spectrogram of power spectral density (PSD) of an operational signal of our time-domain RadCom system that was probed using a digital oscilloscope (Agilent-DSO81204B) and analyzed by a commercial software of vector signal analyzer (Agilent-VSA89600). The signal is generated by a combination of field programmable gate array (FPGA) and direct digital synthesizer (DDS).



(a) Single carrier for communication is not modulated



(b) Single carrier for communication is modulated in phase

Figure 3-1: Spectrogram of power spectral density (PSD) of the operational signal for the proposed RadCom system for two modes of operation.

The frequency-versus-time diagram of the signal in Figure 3-1(a) shows that it consists of a trapezoidal FMCW (TFMCW) that is followed by a single frequency carrier in the middle of the band. The TFMCW may appear occasionally as radar cycle for sensing the environment while the single frequency carrier pertains to communication cycle and can be phase-modulated by information data as it is shown in Figure 3-1(b). This waveform can be considered as a function of time within the following expression.

$$S^{Tx}(t) = \text{Re} \left\{ \begin{array}{ll} A e^{j2\pi(0.5\Gamma t^2 + f_1 t)} & 0 \leq t \leq T_c \\ A e^{j2\pi(f_2(t-T_c))} & T_c \leq t \leq 2T_c \\ A e^{j2\pi(-0.5\Gamma(t-2T_c)^2 + f_2(t-2T_c))} & 2T_c \leq t \leq 3T_c \\ \sqrt{I^2 + Q^2} e^{j2\pi\left(f_c(t-3T_c) + \tan^{-1}\left(\frac{Q(t)}{I(t)}\right)\right)} & 3T_c \leq t \leq 4T_c \end{array} \right\} \quad (3-1)$$

where Γ is the chirp's slope, T_c is the time slot duration, and f_1 and f_2 are lower and upper sides of chirps, respectively. It should be noted that the carrier position for communication may vary along the frequency axis and thereby onboard units may use a frequency division multiple access (FDMA) technique and hence increase the network capacity.

3.1.2 Operation principles

With this time-agile waveform scheme and the use of a software-defined signal source, the system is able to operate as either radar or radio in a reconfigurable manner. A typical scenario is shown in Figure 3-2. All on onboard units must be synchronized and operate within the identical mode, i.e., radar or radio ones. As a radio for communication, onboard units must work through time division duplexing (TDD) and it may not transmit and receive data, simultaneously. Hence, any single unit may not receive data from other units while it is sending information data to others. Indeed, in order to communicate as a receiver, the unit must sustain the carrier intact and use it as LO for the quadrature demodulator in receiver. Let's take an example of the two onboard units which intend to communicate. If unit 1 wants to transmit data, it should modulate its carrier while unit 2 keeps the carrier un-modulated and uses it for quadrature demodulation of the received signal from unit 1. The minimum communication time slot duration should be equal to the Tx/Rx

switching interval in the adopted TDD scheme. In multiuser environments, TDMA techniques may be applied to allocate different time slots to each unit

As a radar, the system can estimate the position of either a mobile or stationary object. Furthermore, echo signal arrives at receiver with a frequency difference (beat frequency) associated with time delay that corresponds to object's range and velocity of motion with respect to receiver's reference point. Since the waveform is a combination of the triangle FMCW and single frequency Doppler radar, the information may be obtained through similar analysis of these waveforms [78]. Range (R) and velocity (v) can be obtained from beat frequencies (f_b) through the following expressions:

$$\begin{cases} f_{bu} = \frac{2\Gamma R}{c_0} + \frac{2f_2 v \cos \theta}{c_0} \\ f_{bd} = -\frac{2\Gamma R}{c_0} + \frac{2f_2 v \cos \theta}{c_0} \\ f_{bc} = \frac{2f_2 v \cos \theta}{c_0} \end{cases} \quad (3-2)$$

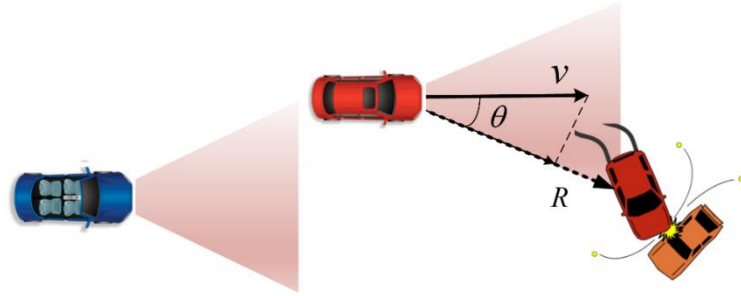
where θ is the angular position of target that equals the angle of arrival (AOA) of the echo beam. The sign of the velocity of an approaching target is assumed to be negative and vice versa.

In order to make the beat signal to convey information about AOA, the echo signal can be received with a phase difference ($\Delta\phi$) by two separate elements of receiver (Rx) antenna. For this RadCom system, the low-cost two-elements receiving array technique [79] is adopted, as opposed to conventional beam steering technique that demands for several receiver channels [80].

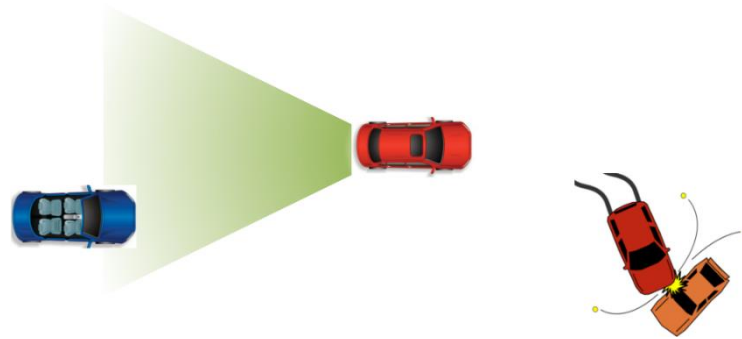
In a coherent FMCW radar, $\Delta\phi$ can be preserved even after down conversion, provided that the RF paths of two branches are identical in terms of electrical length. This phase difference appears in beat signals and can readily be estimated after frequency transform. With the assumption of an infinite integration time, AOA and subsequently angular position of n th detected object can be found through the following expressions:

$$\begin{cases} S_{bi}^2(f) = S_{bi}^1(f) e^{j\Delta\varphi(f)} = \sum_{k=1}^N \delta(f - f_k) e^{j\Delta\varphi(f_k)} \\ \theta_k = \sin^{-1}\left(\frac{\Delta\varphi_k}{2\pi d/\lambda}\right) = \sin^{-1}\left(\frac{\psi_{bi}^2 - \psi_{bi}^1}{2\pi d/\lambda}\right) \\ i = u, c, d \end{cases} \quad (3-3)$$

where d is the spacing between antenna elements, and N is the number of detected objects. ψ_b^1 and ψ_b^2 are the phase of the detected beat signals from the first and second channels, respectively. Unlike the time domain correlation of received signals from Rx antenna with two separate elements, the estimation of angle through (3-3) allows discrimination of several targets in angle, provided that the beat signals are discriminated in PSD spectrum.



(a) Radio mode



(b) Communication mode

Figure 3-2: Typical application scenario; in radar time cycle all on-board units are sensing the environment while they can communicate and exchange the sensory data in radio time cycle.

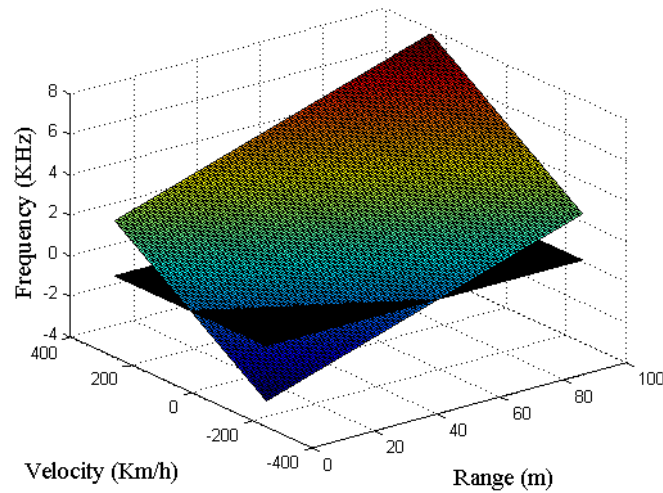
3.2 TFMCW radar signal analysis

The radar cycle in the in-time-domain integrated RadCom system can be reconfigurable, depending on the scenario of operation. Furthermore, the operational signal may be configured to either triangle or trapezoidal FMCW. The latter one is the preferable solution in the context of RadCom systems as it may outweigh especially in multi-target environments. We have re-examined the fundamental features of this radar signal throughout simulations in terms of 1) ambiguity intervals, 2) multi-target detection and 3) estimation accuracy. The results of this study are discussed concisely next, which brings in a quick reference for this multi-functional transceiver design.

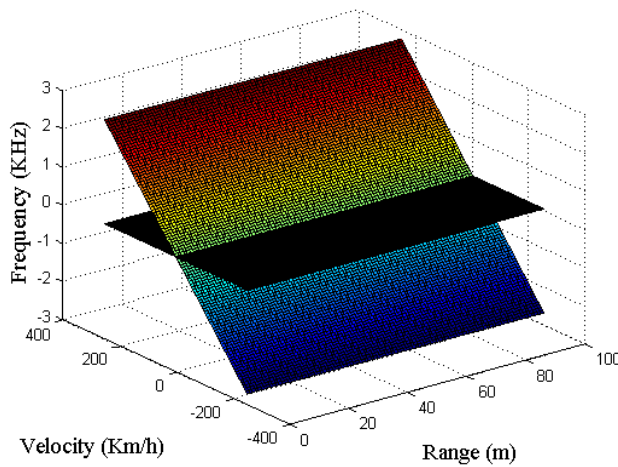
3.2.1 Ambiguity intervals

In order to determine the essential type of demodulation of the radar signal, whether quadrature or in-phase, the range of variation of beat frequencies should be studied. Figure 3-3 shows all possible values of the beat frequencies along with the variation of the range from 0 m to 100 m and the velocity from -250 km/h to 250 km/h.

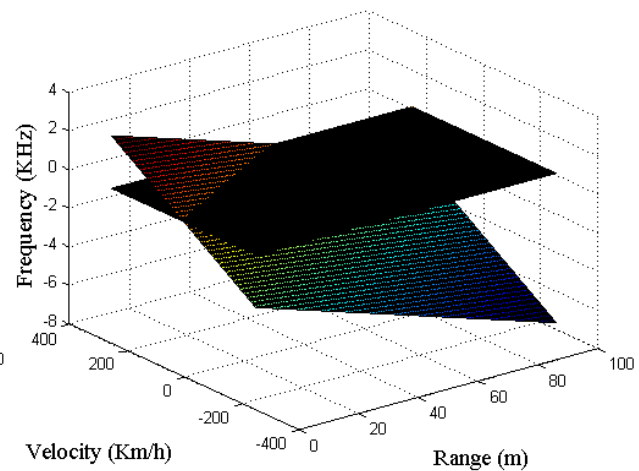
Beat frequencies which are obtained from (3-2) experience both negative and positive signs. Hence, the calculations of the range and velocity must be done with the true sign in order to avoid any ambiguity. This requires obtaining the spectrum of the beat signals using the complex data that may be obtained through quadrature demodulation via de-chirping mixer. Also, the quadrature component of the received in-phase signal can be obtained through its Hilbert transformed signal [81]. Replacing the quadrature demodulator with the in-phase mixer reduces the complexity of the radar RF front-end but at the expense of a heavier computation burden.



(a) Up-chirp beat



(b) Constant beat



(c) Down-chirp beat

Figure 3-3: Beat frequencies along with the variation of range and velocity.

3.2.2 Multi-target detection

FMCW radars may readily estimate the range and the relative velocity of a single detected target through a pair of up or down-chirp beat signals. However, this estimation gets complicated when several targets exist as any pair of the beat signals is possible that may yield ghost target

detection or incorrect parameter estimation. This problem can be solved by repeating triangle FMCW with different rates or sending an unmodulated signal besides up-chirp and down-chirp [82-84]. A similar technique may be applied for this RadCom scheme.

Figure 3-4 shows the Range-Velocity diagram of TFMCW radar when detecting three beat signals. This plot can be obtained by reforming (2) as

$$\begin{cases} v_u = \alpha f_{bu} - \alpha \beta R \\ v_d = \alpha f_{bd} + \alpha \beta R \\ v_c = \alpha f_{bc} \end{cases} \quad (3-4)$$

where $\alpha = c_0/(2f_2 \cos\theta)$ and $\beta = 2\Gamma/c_0$. Parameter estimation should be obviously made at the intersection points in the R-V diagram which may yield ghost target detection in triangle FMCW radars. In the typical example of Figure 3-4, one can see that the radar system may detect two extra targets mistakenly given using only up and down chirp beat signals.

In order to find the correct group of beat signals, a vector of beat frequencies can be made for each up-chirp beat frequency using all constant beat frequencies by

$$\bar{P}_{di} = 2 \bar{f}_c - f_{ui} \quad (3-5)$$

where, f_{ui} is the i^{th} beat frequency in the up-chirp time slot, \bar{f}_c is the vector of all detected constant beat frequencies and \bar{P}_{di} is a vector of all possible down-chirp beat frequencies. For each up-chirp beat frequency one vector of \bar{P}_d should be made. Then each element of \bar{P}_d that agrees with the one of the true detected down beat frequencies must be used with the associated constant and up-chirp beat frequencies in group for further calculations. The technique is explained further in the following example.

Figure 3-5 shows the multi-target scenario with three moving targets which is simulated in Matlab. The radar signal after de-chirping mixer is simulated [81] and the chirp time slot is selected long enough so that it covers the maximum unambiguous range as well as the velocity resolution, i.e. maximum value between $(10 \times 2 \times R_{max})/c$ and $\lambda/(2 \times V_{res})$.

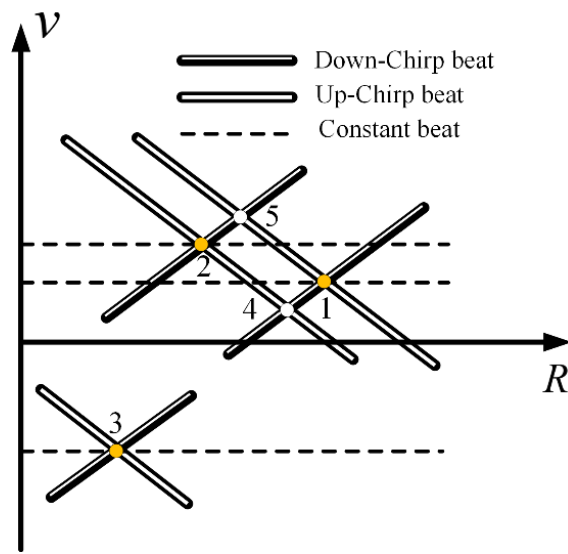


Figure 3-4: V-R diagram from a TFM CW radar; Nodes 4 and 5 are ghost targets which may not be distinguished from real targets if the constant beats do not exist. Unlike targets 1 and 2, target 3 is approaching the radar.

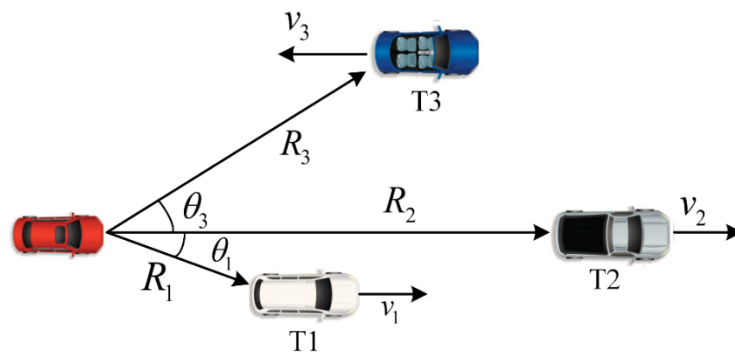


Figure 3-5: Multi-target simulation scenario; $R_1=45$ m, $R_2=100$ m, $R_3=60$ m, $V_1=70$ km/h, $V_2=150$ km/h, $V_3=-30$ km/h, $\theta_1 = 23^\circ$, $\theta_2 = 0^\circ$ and $\theta_3 = 40^\circ$.

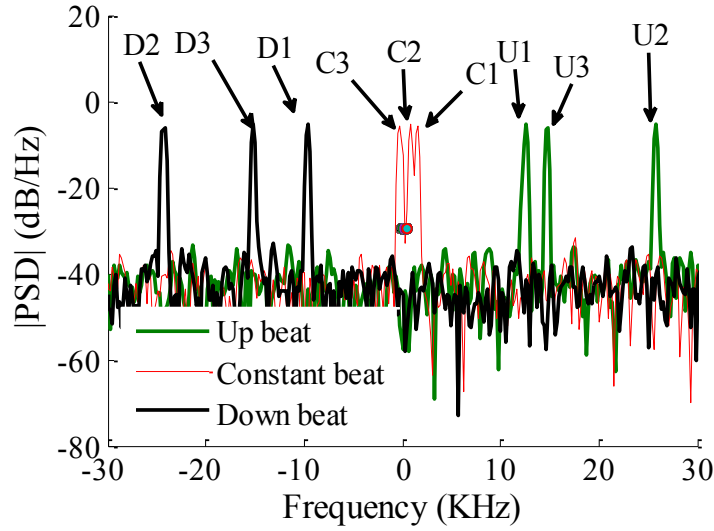


Figure 3-6: PSD of the detected beat signals from simulation in Matlab. Three beat frequencies are detected at each time slot. D, C and U denote the peaks in down-chirp, constant and up-chirp time slots, respectively. In multi-target scenario, all peaks appear together and it is unknown which peak pertains to which target which makes correct target detection complicated.

	f_{u1}	f_{u2}	f_{u3}		T1	T2	T3
p1		f_{d2}		f_u	1	2	3
p2			f_{d1}	f_c	3	1	2
p3	f_{d3}			f_d	3	2	1

(a)
(b)

Figure 3-7: Beat frequency pairing for multi-target detection; (a) Table of comparison of \bar{P}_{di} with f_d ; three matches are found, hence three targets exist (b) Group of beat frequencies that should be used for calculations; the numbers indicate the indices of the detected beat frequency vectors.

The maxima above the threshold in the periodogram shown in Figure 3-6 are detected in each time slot and three vectors are made including the detected beat frequencies. It is still not clear how many targets exist and also which group of beat frequencies must be used for calculations. Using

(5), three vectors of \bar{P}_{di} are made, and then compared with the down beat frequencies. Figure 3-7(a) shows p1, p2 and p3 as the first, second and third elements of each of the vector of \bar{P}_{di} .

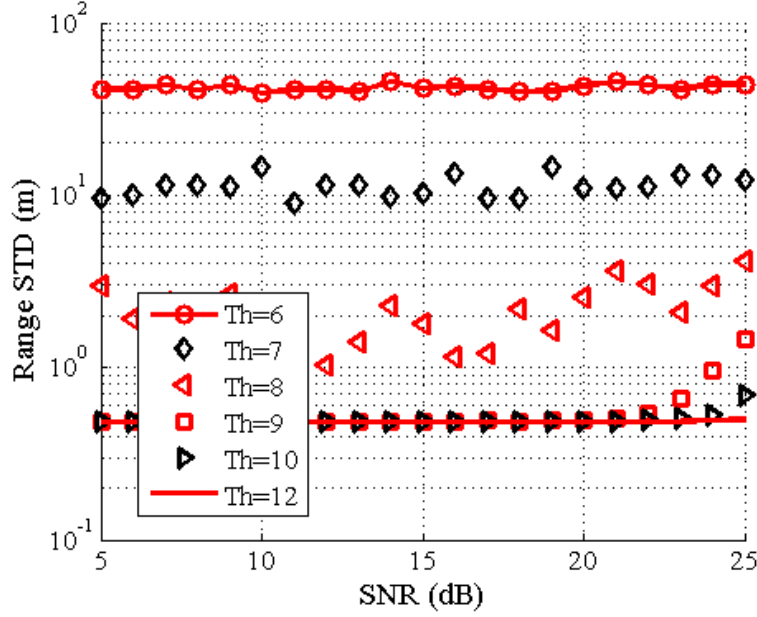
Table 3-1: Multi-target simulation results

Simulation Parameters				
Target	Range (m)	Angle (°)	Velocity (km/h)	
T1	45	23	150	
T2	100	0	70	
T3	60	40	-30	
Simulation Results				
Target	Range (m)	Angle (°)	Velocity (km/h)	
			v	$v/\cos(\theta)$
T1	45	23.265	137.872	150.051
T2	100	0.131	68.936	68.936
T3	60	-39.917	-22.979	-29.960

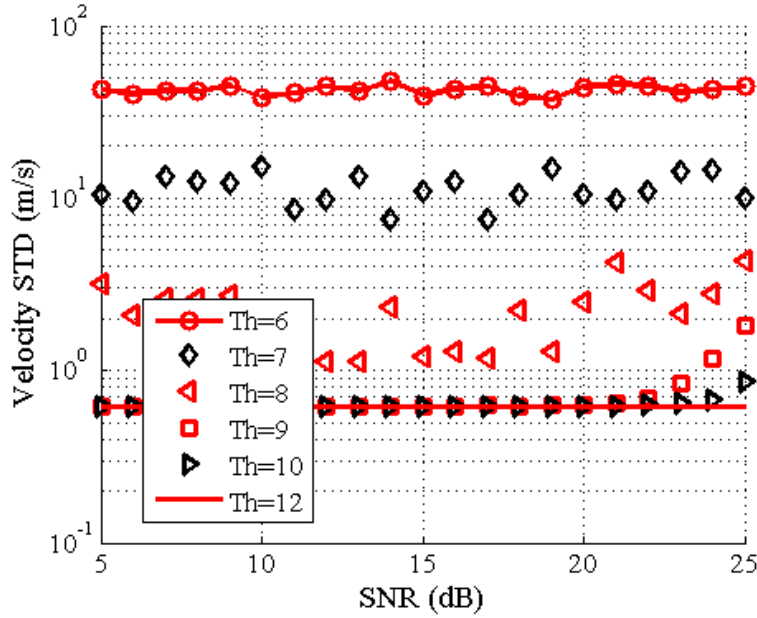
One can observe that three targets are detected and the appropriate group of beat frequencies for each target is found as it is shown in Figure 3-7(b). The calculation results are listed in Table I. One can see that the targets are detected correctly. The importance of the angle detection in true estimation of the real target's velocity is also noticeable.

3.2.3 Estimation accuracy

In order to find out the minimum required SNR of the received beat signals for estimations of the range, velocity and angle with enough accuracy, a statistical analysis is carried out with a few set of simulations of a scenario with only one-point target in Matlab. This preliminary information can be used in transceiver design.



(a) Standard deviation of the range estimation



(b) Standard deviation of the velocity estimation

Figure 3-8: Variation of velocity estimation error as a function of threshold to noise level and SNR in simulation via Matlab; the chirp length is selected to be 20 ms that sweeps 150 MHz bandwidth around 5.8 GHz. Beat frequencies occur in the middle of the two adjacent spectrum resolution points. Sampling frequency is 50 kHz and the STD is obtained out of 10000 runs for each point

In practice, the SNR varies mainly because of the changes in signal level for targets with different RCS in different distances if the background noise level remains constant. However, to keep the analysis independent of any additional processing technique for detection, the signal level is assumed to be constant, but the noise level is tuned to change the SNR. Signal detection occurs when the signal in PSD crosses the threshold level [82].

Figure 3-8 shows the standard deviation (STD) of error in range and velocity estimation for different values of SNR and threshold to mean noise level. One can observe that the main reason of error in range estimation is the wrong detection and when a correct detection happens (with threshold level around 12 dB) the calculation would be correct and remains constant for a range of SNR. The STDs of errors in range and velocity converge to 0.488 m and 0.63 m/s which are half of the estimation error in range (e_r) and velocity (e_v), respectively. These values correspond to the frequency resolution of PSD with selected FFT length (N), i.e. $e_r/2 = c_o f_s T_c / (4NBW)$ and $e_v/2 = c_o f_s / (4Nf_c)$ where f_s is the sampling frequency and BW denotes the sweeping frequency bandwidth.

The minimum threshold level of around 12 dB from our simulations is associated to the false alarm rate under 10^{-6} that requires a threshold-to-noise ratio (TNR) of at least 11.4 dB from $TNR = \ln(1/P_{fa})$ [84].

For practical applications and in the presence of clutter or multiple targets, appropriate constant-false-alarm-rate (CFAR) technique must be applied [85]. Range operational curve (ROC) of FMCW radar based on target detection from periodogram may also be obtained, using the same analysis [82].

The same analysis is carried out for angle estimation when the threshold to noise ratio is considered to be identical to SNR. Two different cases are considered, i.e., beat frequency occurs in an integer or fractional multiplication of frequency resolution. The STD results demonstrated in Figure 3-9, confirm that the accuracy of angle estimation improves with the larger values of SNR for both cases as it depends directly on the phase.

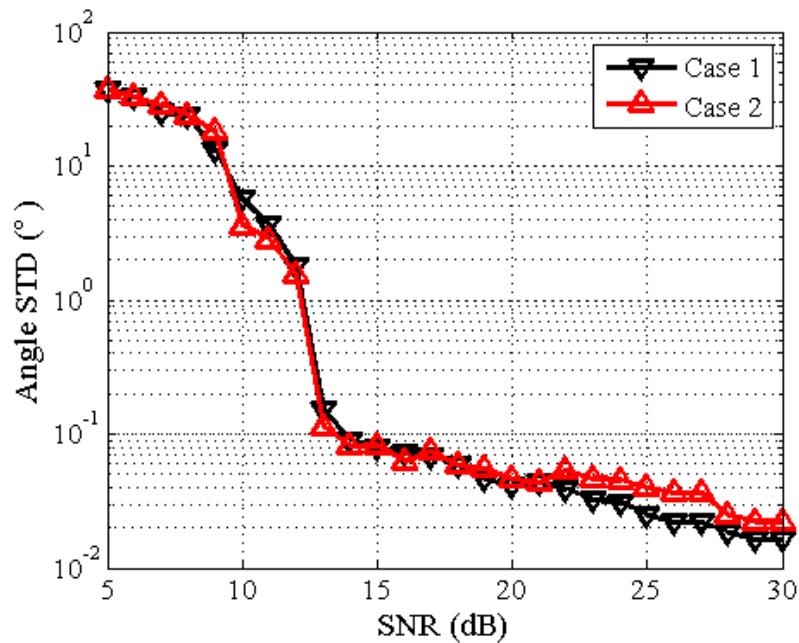


Figure 3-9: Variation of angle estimation error as a function of threshold to noise level or SNR in simulation via Matlab; Case 1: Beat frequencies occur at the spectrum resolution points. Case 2: Beat frequencies occur in the middle of the two adjacent spectrum resolution points.

Abrupt drop of STD occurs at SNR and also TNR of around 13 dB where a false detection would not take place. Consequently, a minimum SNR value of around 12 dB to 15 dB should be considered if correct estimation of all three parameters of range, velocity and angle is desired.

3.3 System architecture and analysis

3.3.1 Overview of FCC Rule Making for DSRC

In 1997, FHWA and ITS filed their petition for 5.85-5.925GHz as the DSRC band. Therein, among three categories of 1) current, 2) emerging, and 3) future DSRC-applications, collision warning system was pinpointed in third category [86]. Therefore, radar sensing in intelligent transportation platform must be viewed as a substantial objective that was considered even during the early actions of rulemaking for future developments of DSRC [86-88].

According to the FCC's Part-15 ruling, the maximum transmitter output power, fed into the antenna, is 30 dBm while maximum Effective Isotropic Radiated Power (EIRP) is 36 dBm. If the transceiver is used in a fixed point-to-point link, there is an exception. The maximum EIRP can be

53 dBm, i.e., 30 dBm output power with 23 dBi antenna gain. According to FCC's DSRC ruling, the maximum transmit power and EIRP is 28.8 dBm and 44 dBi respectively. It should be mentioned that radio-communication services operating within this band must accept harmful interferences that may be caused by ISM applications.

3.3.2 Experimental RadCom system specifications

According to the FCC rules [89] and desired specifications of middle range automotive radar [80] and mobile radio for DSRC applications, we have defined the whole system operational specification that is listed in Table 1. 150 MHz between 5.725-5.875 GHz around DSRC band is considered for prototyping in order to have a desired range resolution which is in inverse relationship with bandwidth i.e., $\Delta R = c_o/(2BW)$.

Table 3-2: System specification

Mode	Specification	Values
Radar	Frequency band	5725-5875 MHz
	Channel bandwidth	150 MHz
	Max. power (EIRP)	41 dBm
	Min. & Max. detectable range	1 m & 100 m
	Range resolution	1 m
	Max. detectable velocity	250 km/h (64.44 m/s)
Radio	Velocity resolution	5 km/h (1.29 m/s)
	Angular area coverage	$\pm 45^\circ$
	False alarm rate	1e-6
	Probability of detection	0.9
	Max. communication range	1000 m
	Max. data rate	75 Mbps
	Bit error rate for BPSK	1e-6

3.3.3 Radar-Radio incompatibilities

Apart from the differences in the operational signal, the design and performance incompatibilities between radar and radio systems are indeed the main factors that make a RadCom transceiver design not straightforward. These incompatibilities come into view upon initial budget analysis, which is summarized in Table III. The following observations in Table III are worthwhile to mention.

Table 3-3: Link budget analysis

Characteristics	Radar Mode	Radio Mode
Operational Range	100 m	1000 m
Total Cycle	60 ms	20 ms
Receiver video Bandwidth	400 kHz	50 MHz
Transmitting Power	22.34 dBm	22.34 dBm
Transmitter's Antenna Gain	19 dBi	19 dBi
Friis Path Loss	175.42	107.71
Radar Cross Section Gain	36.83	----
Receiver's Antenna Gain	7 dBi	7 dBi
Signal Power at the Receiver Input	-90.25 dBm	-59.37 dBm
Thermal Noise Power at the Rx Input	-117.98 dBm	-96.85 dBm
SNR at the Receiver Input	27.73 dB	37.48 dB
Receiver Noise Figure	7 dB	7 dB
SNR at the Receiver Output	20.73 dB	30.14 dB
Roll-off Factor	----	1
Data Rate-BPSK	----	25 Mbps
E_b/N_o	----	33.14 dB
Required SNR (E_b/N_o in Radio mode)	15 dB	10.5 dB
Link Margin	5.73 dB	22.64 dB

First, the required video bandwidth in relation with noise bandwidth for radar mode is much less than that in radio mode.

Furthermore, for a radio system, the required SNR originates from the desired BER which depends on the energy-per-bit to noise-power-spectral-density ratio (E_b/N_0). It is related to SNR by

$$SNR = \frac{R_s}{BW_{radio}} \times \frac{E_s}{N_0} = \frac{\log_2 M}{\beta + 1} \times \frac{E_b}{N_0} \quad (3-6)$$

where BW_{radio} is the bandwidth of radio signal which depends on the roll-off factor (β) of the Nyquist filter, and the symbol rate R_s . M denotes the order of modulation which is 4 for QPSK as an example [88].

In stretch processing or “de-ramping” the energy of the signal would remain the same before and after the process. However, it is congested in a narrow temporal pulse, i.e., ($T_p = 1/BW$), and hence it is more than the one before compression. This processing gain is the chirp’s “time-bandwidth” product indeed, i.e. $T_c BW$. However, the random noise power does not change as it is not correlated to the transmitted signal. Hence, the SNR would change and this gain in SNR may be considered in radar equation. Alternatively, this can be viewed as the noise power in the beat signal is less than the one in the chirp as in

$$SNR = \frac{P_b}{P_n} = \frac{P_s \times T_c \times BW}{N_0 BW} = \frac{P_s}{N_0 \times \frac{1}{T_c}} \quad (3-7)$$

where P_b and P_s are the beat and chirp signal power, respectively [86, 87]. Hence, the receiver noise bandwidth in radar mode may be assumed to be the beat signal video bandwidth which can be determined based on the maximum detectable range and velocity and also the chirp slope. The duration of the chirp-slot (T_c) should be selected large enough in order to have the desired resolution in velocity measurement ($\lambda/(2T_c)$). Thus, the radar receiver bandwidth at the output can be much smaller than the one of radio receiver and should be controlled in order to suppress the excessive noise in radar mode.

Second, the propagation channel behaves differently in terms of path loss. In fact, the received radar signal power can be viewed as

$$P_r^{Rad} = P_t G_t G_r G_{rcs} P_{loss}^{Rad} = P_t G_t G_r \left(\frac{4\pi\sigma}{\lambda^2} \right) \left(\frac{\lambda^2}{(4\pi)^2 R^2} \right)^2 \quad (3-8)$$

where P_t is the transmitted power, G_t is the Tx antenna gain, G_r is the Rx antenna gain, G_{rcs} is the RCS gain and P_{loss}^{Rad} is the path loss in radar mode. Received power in communication mode (P_r^{Com}) can be obtained from (8) by eliminating G_{rcs} and taking the root-square of P_{loss}^{Rad} as path loss of communication channel. From this standpoint, the received radar signal power would be much less than the radio one given the same transmitter output power. The RCS gain may vary among the ITS related objects, but in this initial calculation σ is considered to be unity, i.e. $\sigma = 1$, which yields RCS gain of 36.82 dB for a non-fluctuating target.

The radio signal level should be fixed at a specific value before the symbol decision-making device, therefore using an AGC (automatic gain control) loop in the receiver block is a common solution. On the other hand, the radar signal level varies from -10 dBm to -90 dBm for a typical target with $\sigma = 1$. The difference can be even larger when large and small objects are detected at short and long distances, respectively. This high dynamic range requires an excellent linearity of both receiver front-end and the ADC. If the dynamic range of the ADC is not sufficient (72 dB for our 12-bit ADC), an AGC loop can be used for desensitizing the receiver through attenuating the large returned signals.

3.3.4 Transceiver architecture

According to all the above mentioned observations related to system requirements, a heterodyne transceiver architecture is proposed, as shown in Figure 3-10 which is explained next.

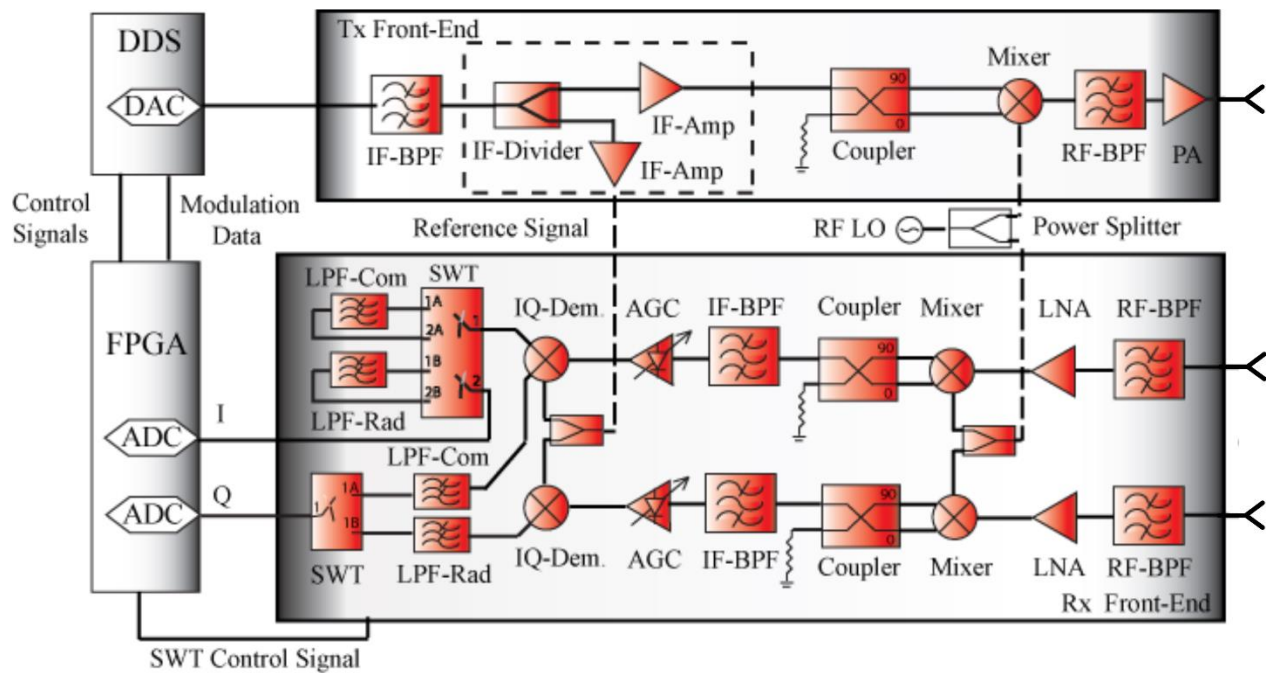


Figure 3-10: Proposed transceiver architecture

Combination of DDS (AD9858) and FPGA (Altera-Stratix) boards in the back-end forms a software-defined signal generator which is capable of reconfiguration. The FPGA is able to control the DDS for either frequency sweeping or phase shifting in an absolute timing manner with output carrier at intermediate frequency (IF).

In the transmitter front-end, an active in-phase divider is positioned between the low-pass filter (LPF) and the up-converter. Using this divider a branch of the IF signal is taken as a reference signal to be used as the carrier of the Quadrature demodulator in receiver in radar mode and also in radio mode when receiving signal from other unit. The combination of 90° hybrid coupler and I-Q mixer forms a single side-band (SSB) up-converter. Heterodyne products are first filtered out by a band-pass filter (BPF) and then the desired RF component is amplified in power amplifier (PA) block before going to the Tx-antenna.

The Rx-antenna is a low-gain antenna and is separated from the transmitting antenna to have a better isolation. This antenna must capture two samples of the arriving beam with a phase difference that represents the AOA. The receiver front-end consists of two identical channels, each connecting to a single element on Rx-antenna. The received signal in each channel is amplified in low-noise amplifier (LNA) block and then down-converted in frequency by image rejection

mixing. A wide range of fluctuations at the IF signal level can be compensated by an AGC loop. Thereby, two quadrature demodulators are fed at a fixed signal level.

Switching technique is used for three purposes. First, it helps preserve the sensitivity of the receiver in two modes by controlling the bandwidth. Second, the quadrature mixers are shared between two channels in two modes. Indeed, both quadrature (Q) and in-phase (I) components of a single demodulator are allocated to the communication signal whereas at least one component from each demodulator is required for eliciting all desired radar information. And third, the required number of ADCs is minimized by multiplexing I and Q components of the two channels. In radio mode, I and Q components of one channel go to ADC to be sampled, whereas in the radar mode at least one component from each channel is required and therefore out of four, only two of them, i.e., one from each mixer, go to ADC to be sampled and further processed. This does not disturb the necessity of coherent and simultaneous radar signal receiving from the two channels.

3.4 Simulations

3.4.1 RF circuit simulations

Based on the above analysis and the proposed architecture, both transmitter and receiver circuitries are designed using commercial off-the-shelf components. With the purpose of optimization, the circuits are carefully simulated via Harmonic-Balance (HB) and Chain-Budget platforms in the commercial simulation package of Advanced Design Systems (ADS). In these sets of simulation, either S- or X-parameters of RF chips, provided by manufacturers in datasheets, are used for characterization of the corresponding simulation components. Two design aspects are considered for optimum chip selection and configuration.

First, the minimum number of amplifiers is used and second, the interference from spurs is minimized by moving third-order-intercept (TOI) point away from 1dB-compression point (P1dB). Figure 3-11 shows the up-converter block accompanying the results of a chain-budget analysis. With nominal input power of -15 dBm, an input matching of around -14 dB is achieved and the TOI point is also around 11 dB higher than the compression point.

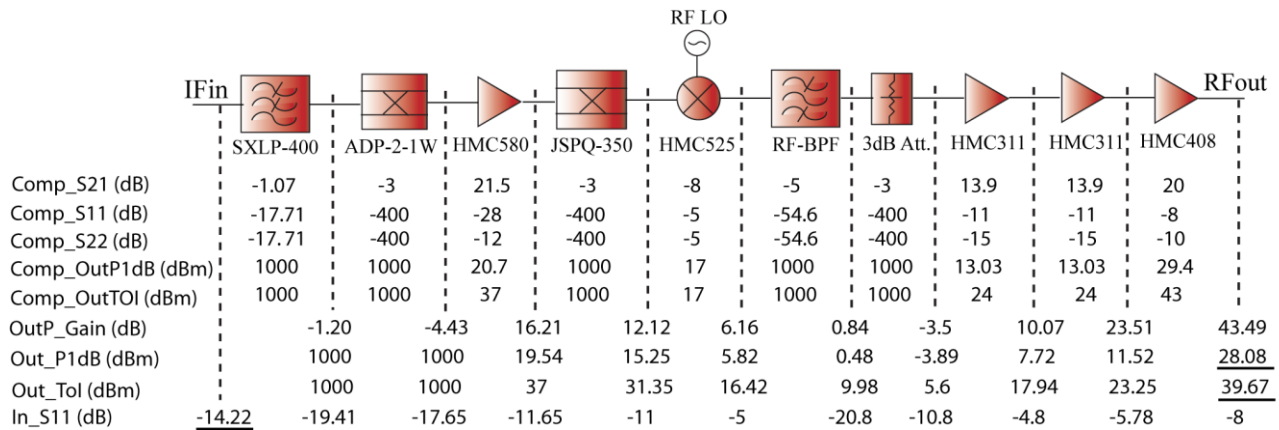


Figure 3-11: Chain budget simulation of Tx block

Figure 3-12 shows the down-converter block with all building components. A perfect input matching of 21.8 dB and TOI of 10.2 dBm at the output is achieved that is around 10 dB larger than the compression point.

The noise figure (NF) of 7.79 dB is slightly more than the specified one in the link budget analysis. This is due to the loss of the RF BPF, which is considered to be 5 dB in simulation. The same filter with 1 dB bandwidth of 150 MHz is used in the up-converter for suppressing the LO, which is only 225 MHz away from the center frequency of 5.8 GHz. Given at least 20 dB rejection at LO frequency, 5 dB loss could be inevitably anticipated in practice.

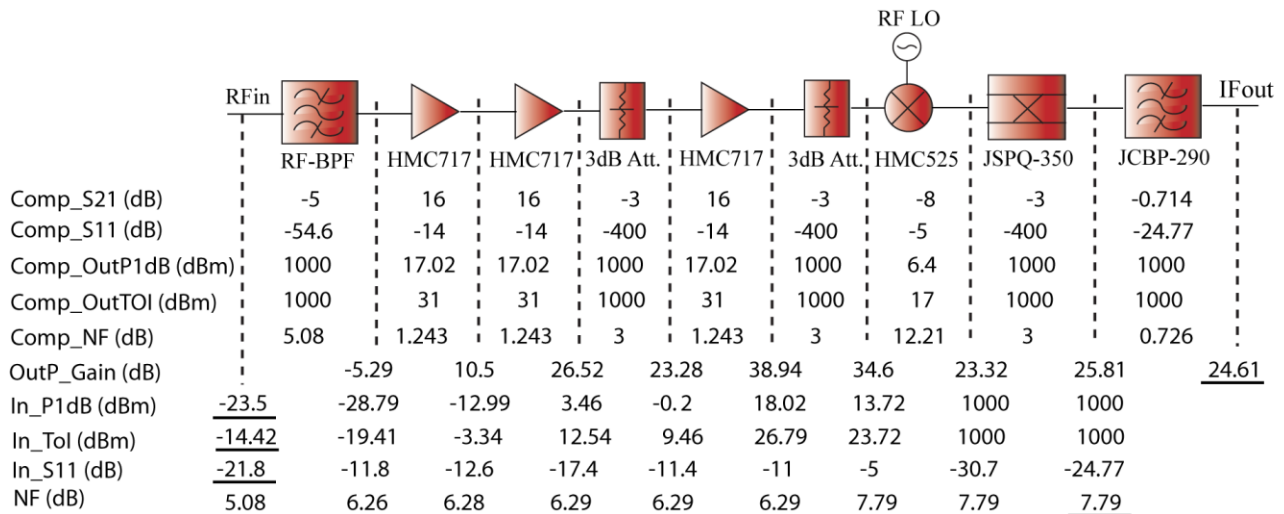


Figure 3-12: Chain budget simulation of down-converter core in Rx block

3.4.2 System-level simulations

In order to investigate a proper operation of the whole system, a series of simulations are carried out at the system-level via Ptolemy simulator in ADS. In this platform, various aspects from nonlinear effects in RF circuitry to fading in propagation channel or even sampling noise in ADC can be taken into account. Figure 3-13 shows the block diagram of this type of multi-layer co-simulation. Indeed, the signal flow in RF circuits is controlled by the Circuit-Envelope simulator at the bottom layer while Dataflow simulator controls all signal processing as well as signal flow in propagation channel at the top layer. The characteristics of each off-the-shelf component in both Rx and Tx blocks are taken from datasheets and the propagation is modeled in a free-space channel with AWGN.

The desired modulated signal in (1) is generated by a combination of discrete signal processing DSP blocks in discrete time domain and then transformed to continuous time domain. For instance, the up-chirp signal that enters the bottom layer is made in the form of,

$$S_{upchirp}(t) = A e^{j2\pi(0.5\Gamma(T_{step}^2 n^2) + f_1 T_{step} n)} \times e^{j2\pi f_c t} \quad (3-9)$$

where f_c is the carrier, n is the discrete time index and T_{step} is the simulation time step. Note that the chirp slop and the chirp starting frequency are denoted by ΓT_{step}^2 and $f_1 T_{step}$, respectively.

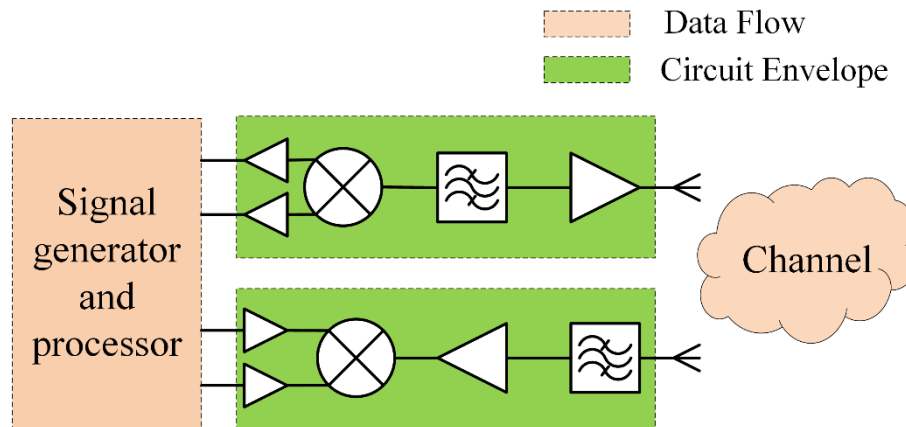
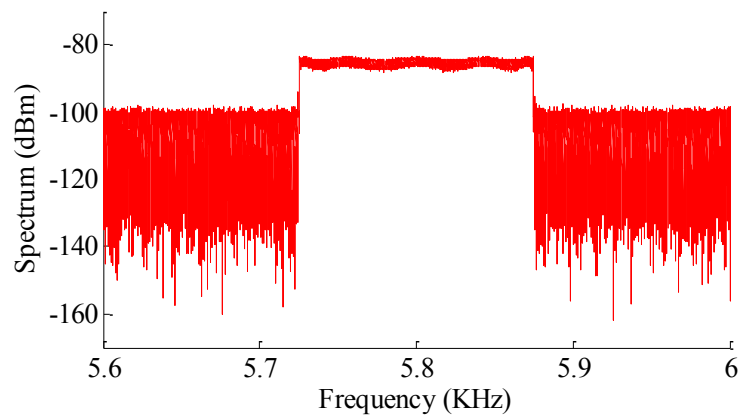


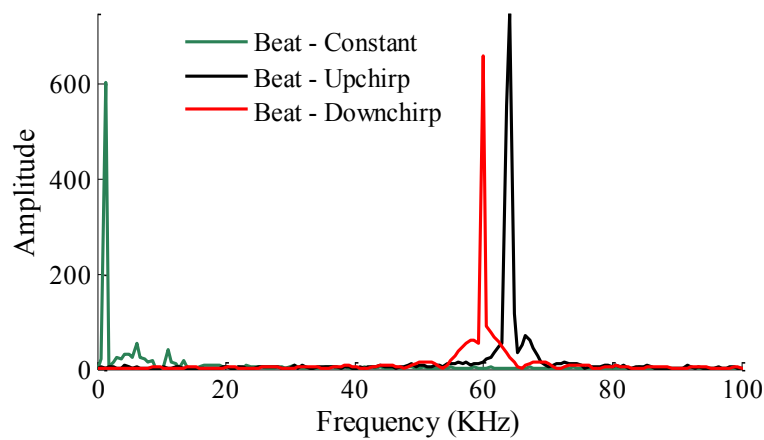
Figure 3-13: Block diagram of multilayer simulation at system level via Ptolemy simulator in ADS package.

3.4.3 Simulation results of radar mode

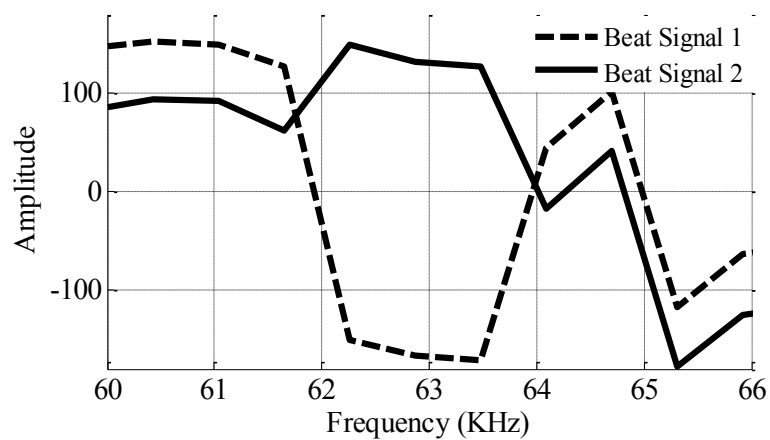
Figure 3-14 (a) shows the spectrum of a radar signal arriving at the receiver input. The AWGN channel is configured to resemble the existence of a target which is 100 m away from the receiver. Beat signals are sampled by the ADC blocks at sampling rate of 10 MHz and then transformed to frequency domain through 8192-points discrete Fourier transform (DFT) algorithm with around 1.22 kHz frequency resolution. Doppler-Effect is taken into account through appropriate I-Q frequency up or down conversion with the corresponding Doppler frequency. Amplitude and phase of the resulting signals are shown in Figure 3-14 (b) and (c).



(a) Power spectrum of the radar signal at the receiver input



(b) Spectrum of the detected beat signals



(c) Phase of the Up-chirp beat signals after DFT

Figure 3-14: System simulation when operating in radar mode; The distance of the target from Rx antenna and its angular position is 100 m and 20° , respectively.

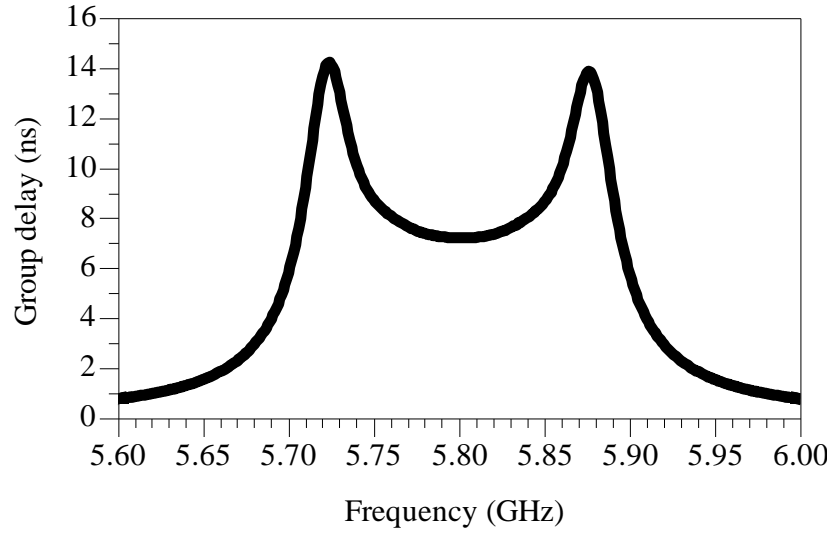


Figure 3-15: Group delay of the RF BPF which is used in both Tx and Rx blocks for simulation in ADS; In-band group delay of around 9 ns causes a constant error in parameter estimations.

The existence of a peak in amplitude notifies the detection of an object at a distance that corresponds to the frequency in which peak appears. For estimating the AOA, the phase difference should also be read at this frequency. The results are summarized in Table IV. Note that the deviation in simulation results is mainly attributed to the intrinsic time delay in RF circuitry at the bottom layer and also the low resolution of the DFT in simulation.

Figure 3-15 shows the group delay of the employed band-pass filter (BPF) both at the transmitter output and the receiver input. The received signal at the de-chirping mixer experiences this delay twice which yields a constant offset in range measurement. This is expected to occur in practice and therefore, the system requires calibration.

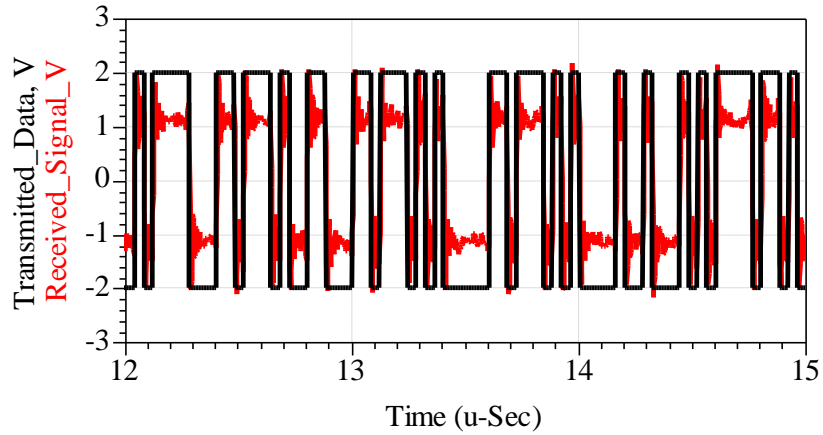
The simulation is repeated with the BPFs bypassed and the obtained up, down and constant beat frequencies were 62.255289 kHz, 1.202703 kHz and 59.814453 kHz, respectively. Consequently, the estimated range was exactly 100 m.

Table 3-4: System simulation results for radio mode

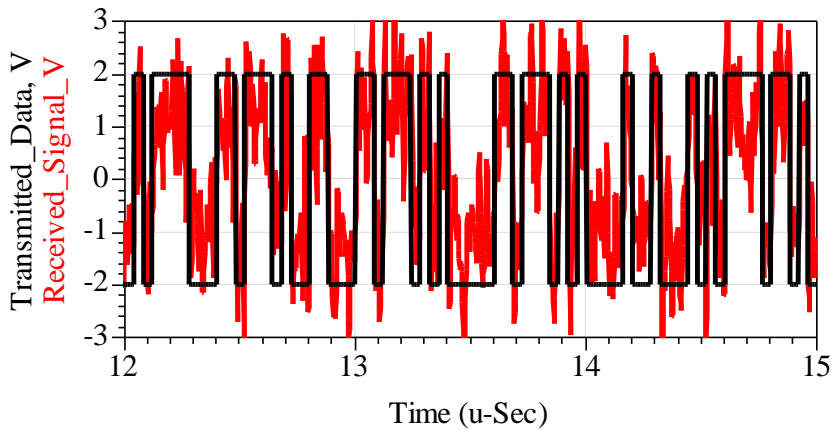
Simulation Parameters		
Chirp duration	1.6384 ms	
Center freq.	5.8 GHz	
Bandwidth	150 MHz	
SNR	15 dB	
Sampling freq.	10 MHz	
DFT length	8192	
Number of samples	$0.9 \cdot F_s \cdot T_s$	
Simulation Scenario	# 1	# 2
Target's range	100 m	100 m
Target's velocity	119 km/h	119 km/h
Radar velocity	0 km/h	0 km/h
Target's angle	20°	20°
Relative velocity	112 km/h	112 km/h
Direction	Receding	Approaching
Simulation Results	# 1	# 2
f_{bu}	64.089 kHz	61.645 kHz
f_{bd}	61.645 kHz	64.089 kHz
f_{bc}	1.2207 kHz	1.2207 kHz
R	103 m	103 m
v	119 km/h	119 km/h
θ	20.027°	20.01°

3.4.4 Simulation results of communication mode

For system simulation in radio mode, the carrier in radio cycle is modulated by BPSK scheme. Depending on a desired E_b/N_0 , the noise power spectral density of the propagation channel can be controlled by $10\log_{10}\left(\frac{P \times T_s}{\log_2 M}\right) - \frac{E_b}{N_0}$, where P is the signal power at the output of the Tx antenna, T_s is the symbol duration and M denotes the order of modulation. Figure 3-16 shows the results of simulation for two different cases of $E_b/N_0=12$ dB and 3 dB, where we can observe the system capability to communicate with a high data rate.



(a) $E_b/N_0=12$ dB

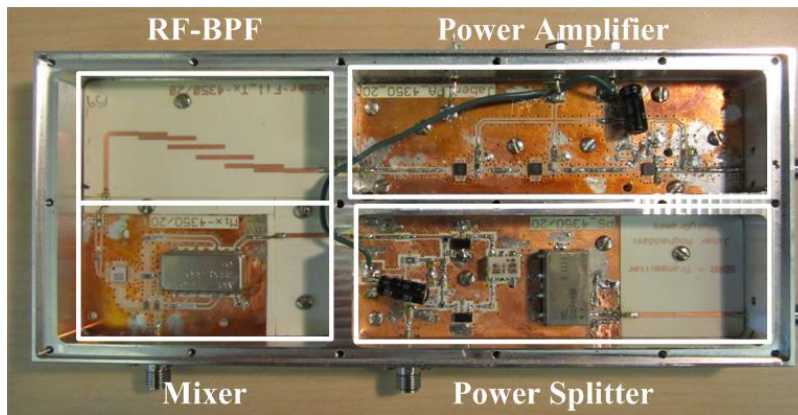


(b) $E_b/N_0=3$ dB

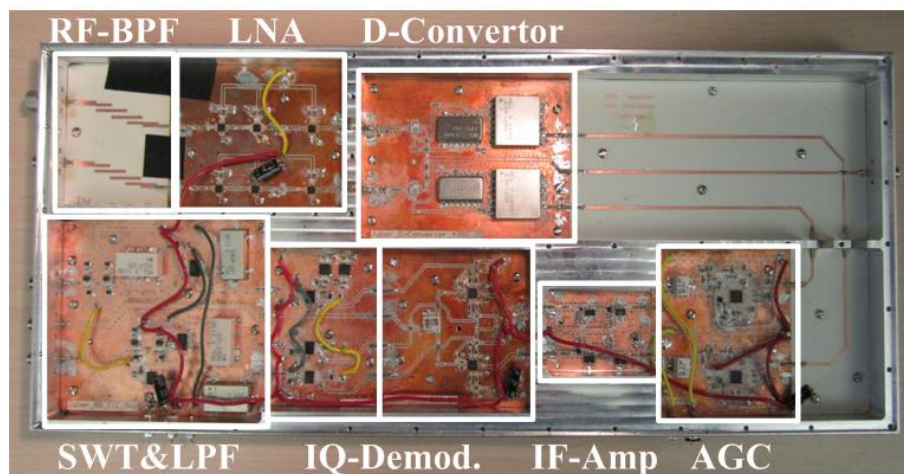
Figure 3-16: System-level simulation results when operating in communication mode

3.5 Prototyping and measurements

All individual circuits in the front-end of the low-frequency demonstrator of our proposed system are fabricated in-house using low-cost printed circuit board (PCB) process on substrate Rogers-4350B with thickness of 0.508 mm. Grounded coplanar waveguide (CPWG) topology is preferred as transmission line in the PCB layout due to its low radiation loss and leakage as well as enhanced isolation because of a larger ground plane between RF lines. Upon the evaluation of each circuit, all are assembled in two separate aluminum housings as transmitter (Tx) and receiver (Rx) blocks considering electromagnetic compatibility issues. Figure 3-17 shows the Tx and Rx blocks indicating each functional unit.



(a) Transmitter block



(b) Receiver block

Figure 3-17: Prototyped building blocks of front-end

The performance of the proposed transceiver is evaluated through different tests in either individual circuit or system level and some measurement results are presented next:

3.5.1 Tx Block

In order to test the performance of the proposed signal transmitting unit in terms of linearity, output of the transmitter block is probed using DSO and then analyzed further in VSA. Our signal source is configured at radio mode and generates a BPSK modulated signal by 25 Mbps pseudorandom bit sequence (PRBS) with a maximum length of $2^{11}-1$.

The measured error vector magnitude (EVM) is around 2.25 %rms with IQ phase error of 512.88 mdeg, magnitude error of 2.068 %rms and IQ-offset of -40 dB. In addition, the parameter that can evaluate the linearity of the transmitter front-end is the error vector spectrum. Furthermore, small in-band inter-modulation spurs that may not appear in spectrum of the demodulated signal can show up in error vector spectrum and thereby the magnitude and frequency offset of the spurs can be observed [90]. The cumulative graph of error vector spectrum of the demodulated carrier is shown in Figure 3-18. Inexistence of any in-band spurs proves that up-converter and PA units are highly linear.

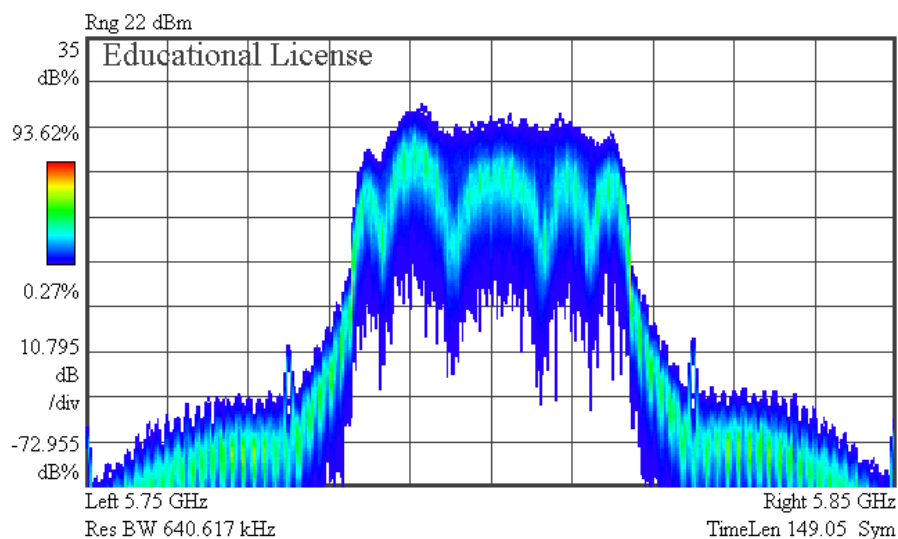


Figure 3-18: Cumulative graph of EVM spectrum of the signal at the output of Tx block. Error vector spectrum can monitor the small in-band intermodulation spurs that may not appear in the spectrum of the signal [90].

3.5.2 Down-converter block

Down-converter block which includes two channels of RF BPF, LNA and image rejection mixer is examined for NF and gain by NF analyzer (Agilent N8975A) and hot noise source (Agilent SNS-4002A). Measured results of both channels are shown in Figure 3-19.

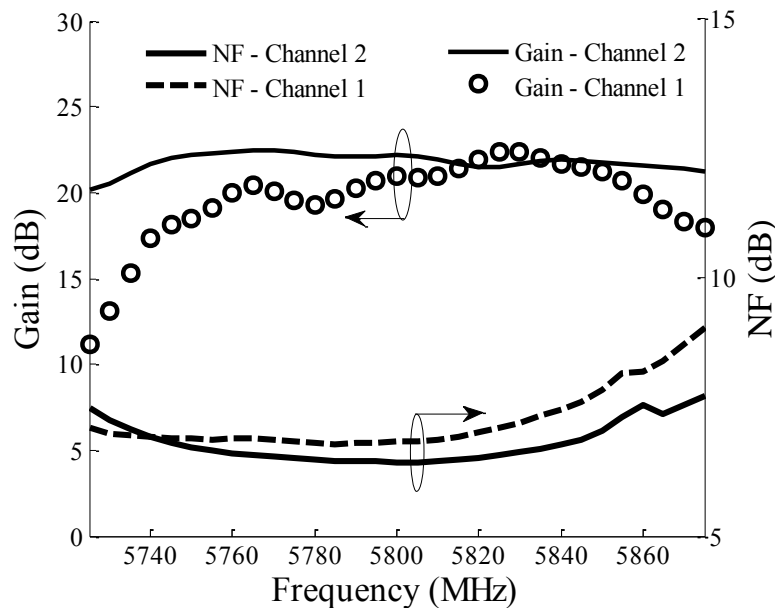


Figure 3-19: Gain and NF of both branches of down-converter block measured by NF analyzer (Agilent N8975A) and hot noise source (Agilent SNS-4002A).

It can be seen that NF for both channels is almost around 7 dB as was anticipated according to chain budget simulations. Gain is also around 22 dB that is 2 dB less than the HB simulation results. This attributes to the loss in PCB and connections between three circuits. The variation in measured gain of channel-1 is caused by mismatch and cross-coupling in PCB.

3.5.3 AGC Loop

The Principal cores of an AGC loop are a variable gain amplifier (VGA), an RF detector and a directional coupler. Among three different types of RF detectors, logarithmic detector as opposed to RMS and envelope detector gives the fastest response to recover from large abrupt decreases in signal level thanks to the steep slope of logarithmic curve for low inputs [91, 92]. This features the AGC loop with a high response time and therefore it is appropriate for the RadCom system that

experiences large collapse in input power transferring from communication mode to radar mode. For our system demonstrator, this loop is realized by a 7 dB directional coupler, two IF amplifiers (GVA-82 and GVA-62) and an IC package (HMC992LP5E) which houses VGA and log-detector cores. Figure 3-20 shows measured results of output power from coupler versus control voltage. One can observe that 40 dB linear dynamic range in both channels enables the receiver to deal with minimum signal level from -68 dBm in radar mode to -38 dBm in radio mode at the output of down-converter. While the control voltage is set to be 0.78 V, by 30 dB gain of IF amplifiers the signal is fed into quadrature demodulator (HMC597LP4) at fixed signal level of 12 dBm.

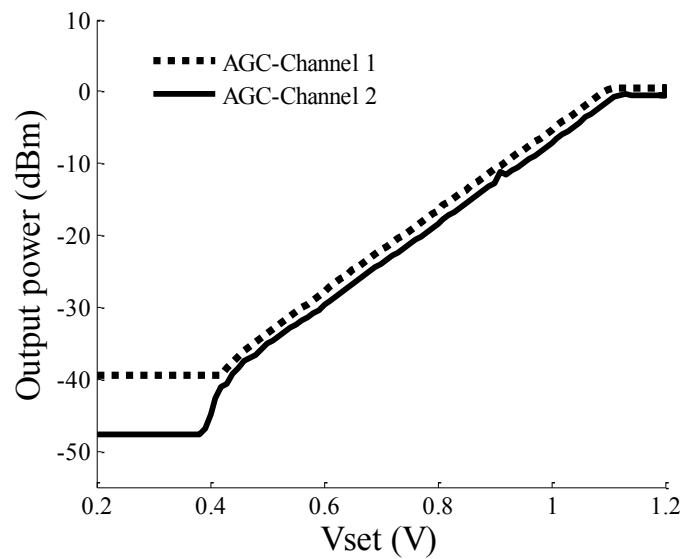


Figure 3-20: Gain control by two branches of AGC loop; Input power is -37.8 dBm in this measurement. The output of AGC loop is around -18 dBm for around 40 dB dynamic range of input power, provided that the V_{set} is fixed at 0.78 V.

3.5.4 Tx and Rx antenna

High gain Tx-antenna is adopted for this system on purpose. First, it can compensate the excessive path loss in radar propagation channel and give a sufficient range of coverage and second, it prevents unwanted ground-reflected echo due to its narrow beam in either horizontal or vertical planes. This antenna is realized by a 4×4 array of inset-fed patch elements as it is shown in Figure 3-21. Feeding network encompasses 3 dB-splitters and distributes the transmitting signal with equal amplitude.

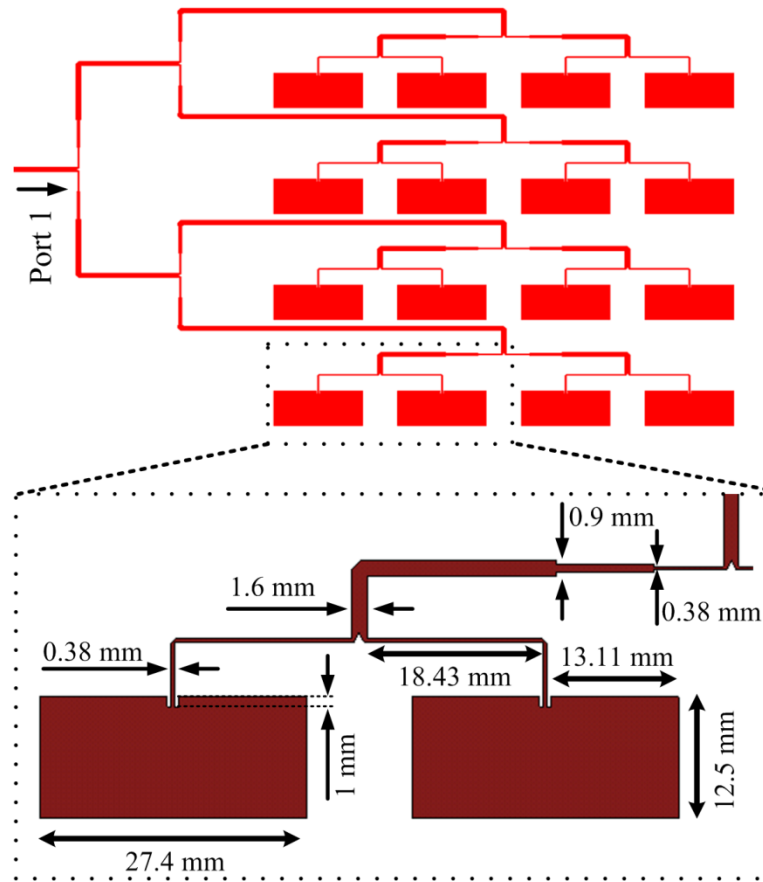


Figure 3-21: Building blocks of Tx antenna

The layout is printed on Rogers-4350B substrate with 0.762 mm thickness. Antenna is optimized by 3D electromagnetic simulation software of computer simulation technology (CST). Figure 3-22 shows that return loss is more than 10 dB for the whole specified band.

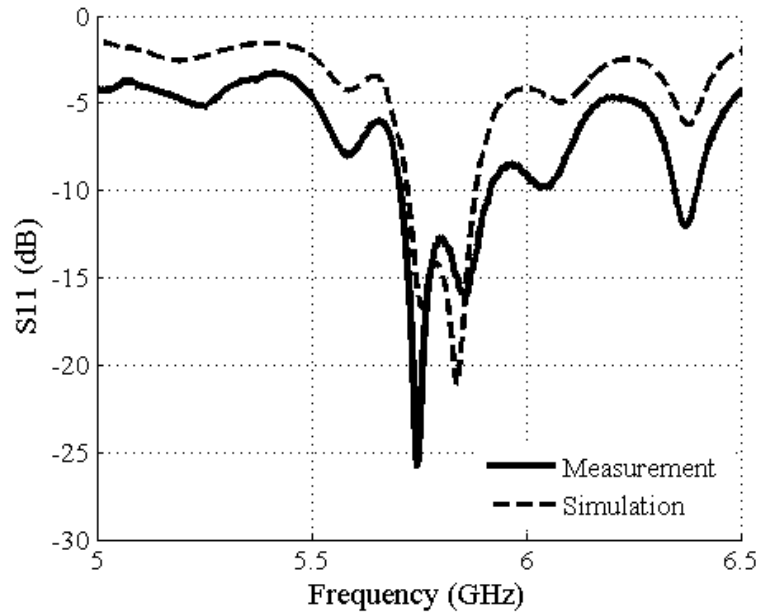


Figure 3-22: S11 of transmitter antenna

Measured and simulated radiation patterns in both E- and H- planes are sketched in Figure 3-23(a) and (b), respectively. Half power beam width (HPBW) of 20° along with 10 dB side lobe level in both planes isolates Tx antenna from the Rx antenna. The radar signal analysis in section III.C demonstrates that a minimum SNR of around 13 dB is required in order to guarantee the error variation of less than 1° . Therefore, the 10 dB side lobe level may not be enough and must be improved as it causes erroneous angle estimation. Nevertheless, this antenna is acceptable for system-level measurement for this prototype.

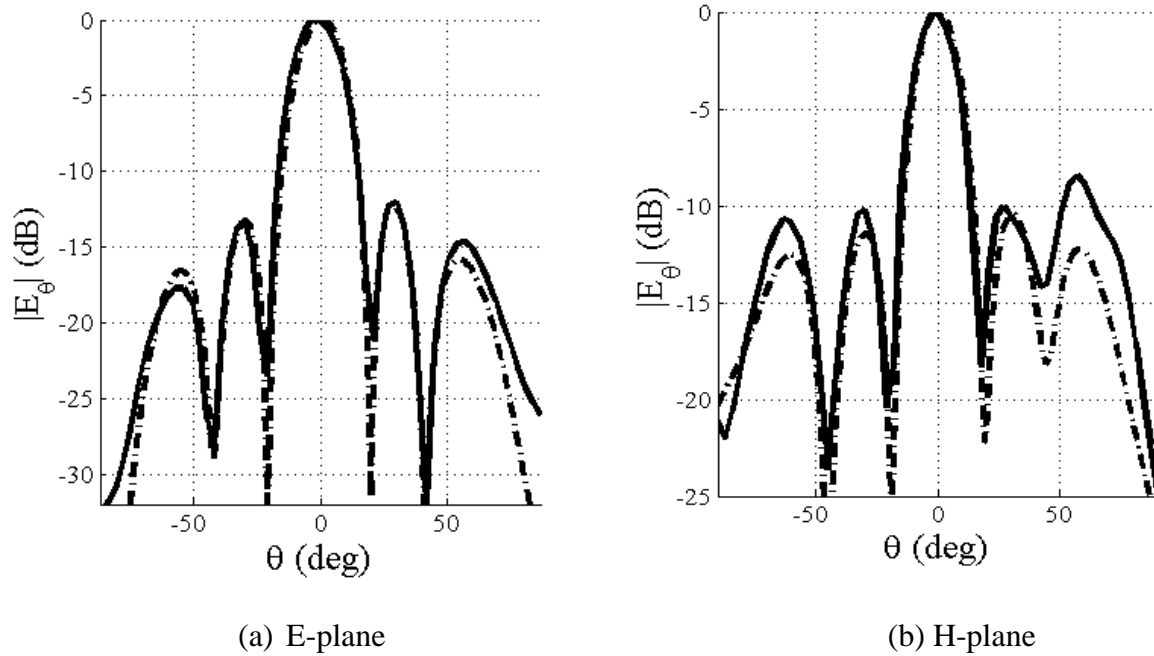


Figure 3-23: Normalized radiation pattern of Tx antenna in two planes; Solid line: measurements, dashed line: simulation

Rx antenna is purposefully separated from Tx antenna to enhance the isolation and has a low gain in order to have sufficient angular range of coverage. This antenna is built up of two $15 \text{ mm} \times 12.5 \text{ mm}$ patch elements that are fed by two separate SMA connectors from its backside. The layout is printed on Rogers-5870 with thickness of 3.175 mm. Both channels of antenna are matched to 50 Ohm and isolated from each other with measured return loss and isolation of more than 20 dB. According to the radiation patterns of one of the channels in both E- and H- planes the antenna demonstrates HPBW of 90° that satisfies the specified angular range of coverage, i.e. $\pm 45^\circ$. In addition, back-lobe level is less than -15 dB that immunizes the system from undesired echo from backside.

3.6 System-level measurements

3.6.1 Radio communication

Figure 3-24 shows the measurement setup for evaluating the performance of our transceiver when operating in radio mode. The IF modulated signal is generated using a vector signal generator (VSG) and is up-converted and transmitted using our prototyped Tx block and antenna.

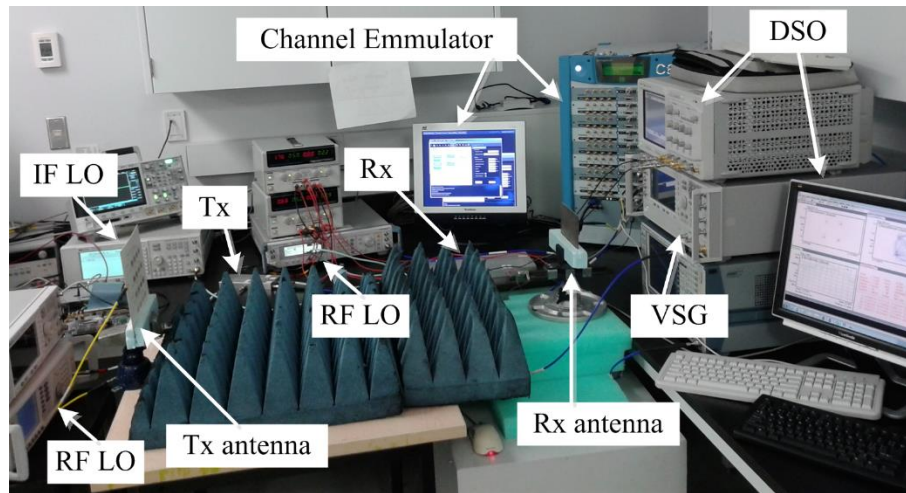
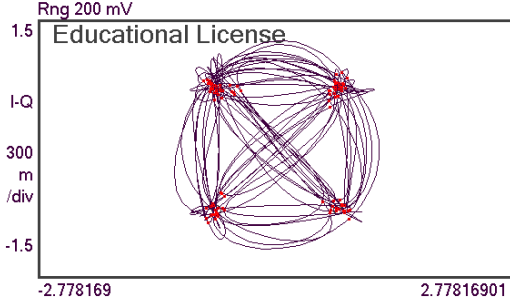
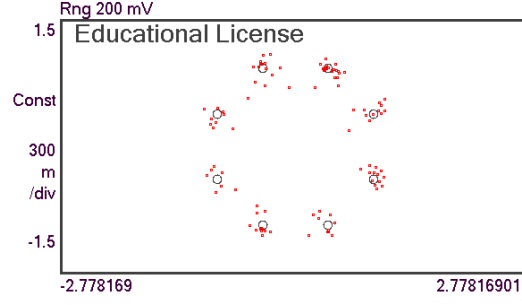


Figure 3-24: System measurement setup in communication mode; Channel emulator is used for SNR adjustment and the received SNR and EVM is measured using VSA in DSO

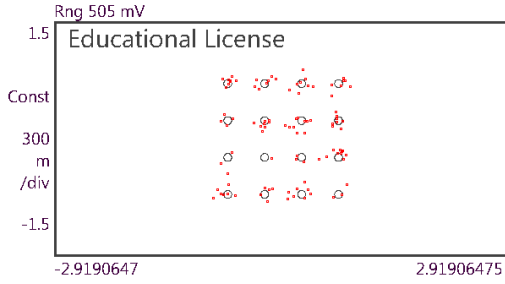
The transmitted signal goes through a channel emulator (EB Propsim C8) by which the SNR of the received signal can be tuned before going through the Rx block. The demodulated signal at the output of the Rx is connected to a VSA that can plot the constellation diagram and also measure the SNR and EVM. Figure 3-25 shows the constellation diagram of the demodulated signal for different types of modulation along with the measured EVM values. This measurement validates the successful performance of our prototyped RadCom transceiver when operating in radio communication mode.



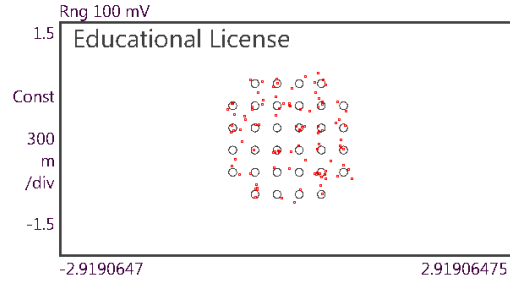
(a) QPSK, EVM= 9.75%



(b) 8PSK, EVM= 14.56 %



(c) 16 QAM, EVM= 10.9 %



(d) 32 QAM, EVM= 8.83 %

Figure 3-25: Measured constellation and EVM for different modulation schemes when system is configured to operate in radio mode

The theoretical EVM for QPSK signal can be expressed as a function of SNR by

$$EVM_{4QAM} = \left[\frac{1}{SNR} - 4 \sqrt{\frac{1}{2\pi \times SNR}} e^{\frac{-SNR}{2}} + 2 \operatorname{erfc}\left(\sqrt{\frac{SNR}{2}}\right) \right]^{1/2} \quad (3-10)$$

from [93]. Both measured and theoretical EVM, plotted in Figure 3-26 proved to be in excellent agreement.

EVM is actually the normalized error magnitude between measured constellation and the standard constellation [94] and in the Gaussian noise model has inverse relation with the root square of SNR, i.e., $EVM = 1/\sqrt{SNR}$. This helps building a relation between measured EVM to BER.

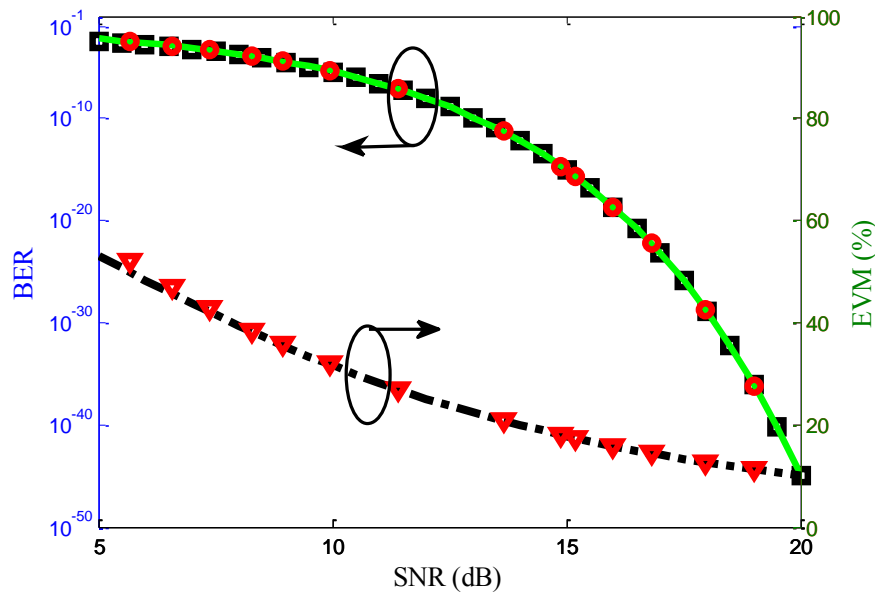


Figure 3-26: EVM and BER measurement results; -: BER (theory), square: BER converted from EVM (theory), o: BER converted from EVM (measurement), -.-: EVM (theory), triangle: EVM (measurement)

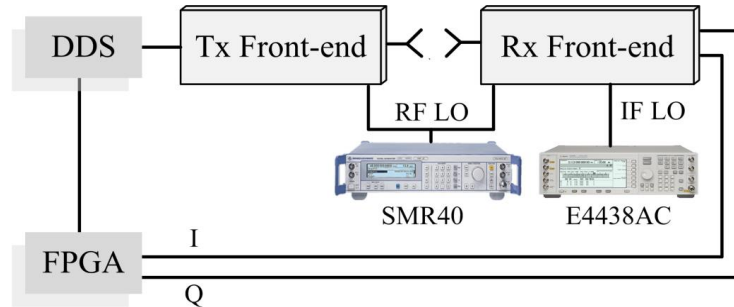
Figure 3-26 shows the BER values converted from measured EVM agree very well with the well-known theoretical BER for QPSK signal as a function of SNR that proves our system excellent capability in communication.

In another measurement for radio mode, the performance of the whole proposed transceiver is tested within a line of sight (LOS) communication setup shown in Figure 3-27(a).

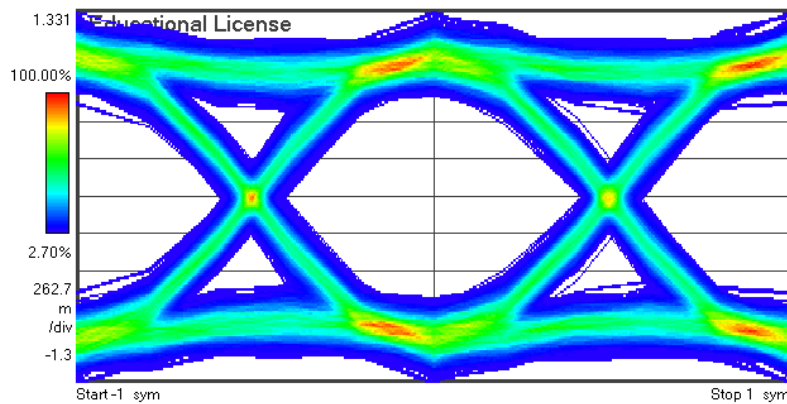
The Tx and Rx blocks of a single prototyped unit are playing the role of Tx and Rx blocks of two different on-board units which are supposed to communicate with each other. As in the previous measurement, the Tx block in this setup may also not share its IF carrier with the RX block as it is modulated in the back-end. Therefore, a separate signal generator is used as IF carrier for demodulating mixer in Rx block. In addition, RF LO is not prototyped in our system. So, another signal generator is used as a carrier for down-converting mixer.

Since the carrier recovery is not implemented devices are synchronized by sharing a single reference clock signal. Output of the transmitter is attenuated before radiation in order to emulate the received power of -59 dBm that associates to maximum communication range.

The test signal is a BPSK modulated carrier with a data rate of 25 Mbps. Discriminated I and Q signals are probed by DSO and the measured eye-diagram is illustrated in Figure 3-27(b). A wide eye opening along with a low distortion of symbols at zero crossing points demonstrates wide noise margin and safe sampling area.



(a) Measurement setup



(b) Measured eye-diagram in VSA89600

Figure 3-27: System measurement in radio mode.

In addition, the signals are sampled by ADCs at sampling rate of 100 MHz in order to have four samples per symbol. Since phase recovery algorithm is not implemented the carrier phase alignment is done by a phase shifter.

The sampled signals as well as transmitted data are probed in FPGA via Signal-Tap2 software in Altera Quartus II package. Given the proper operation of the whole system, the received signal must be a delayed version of the transmitted one. This can be readily observed in Figure 3-28(a).

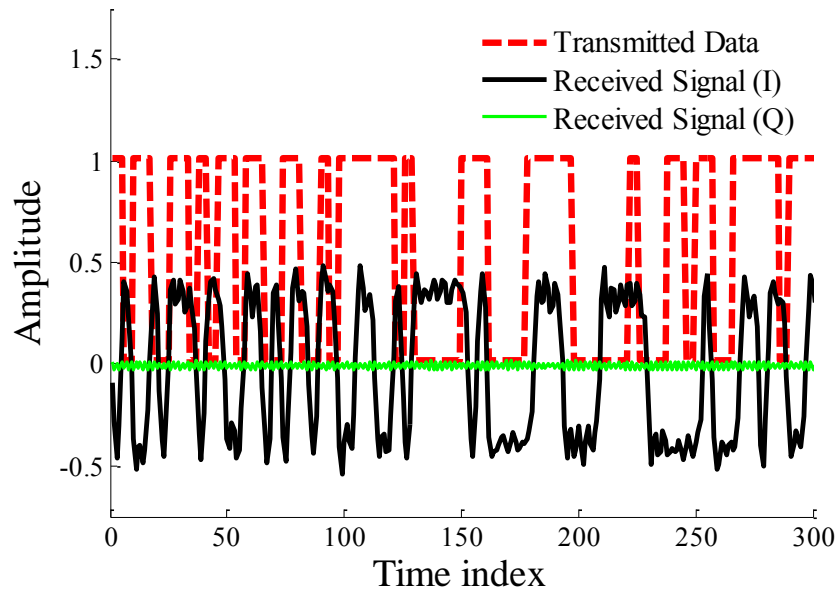
Then, the received signal is match-filtered with a finite impulse response (FIR) filter of 4 taps and energy of unity. We can see a very good agreement between the transmitted and recovered symbols in Figure 3-28(b). In order to measure the SNR of the received symbols, the signal is processed further as follows: First, noise power in I and Q channels are calculated as P_{nI} and P_{nQ} by,

$$\begin{aligned} P_{nI} &= \sigma^2(|I(k)|) = \frac{1}{N} \sum_{k=1}^N (|I(k)| - m(|I(k)|))^2 \\ P_{nQ} &= \sigma^2(|Q(k)|) = \frac{1}{N} \sum_{k=1}^N (|Q(k)| - m(|Q(k)|))^2 \end{aligned} \quad (3-11)$$

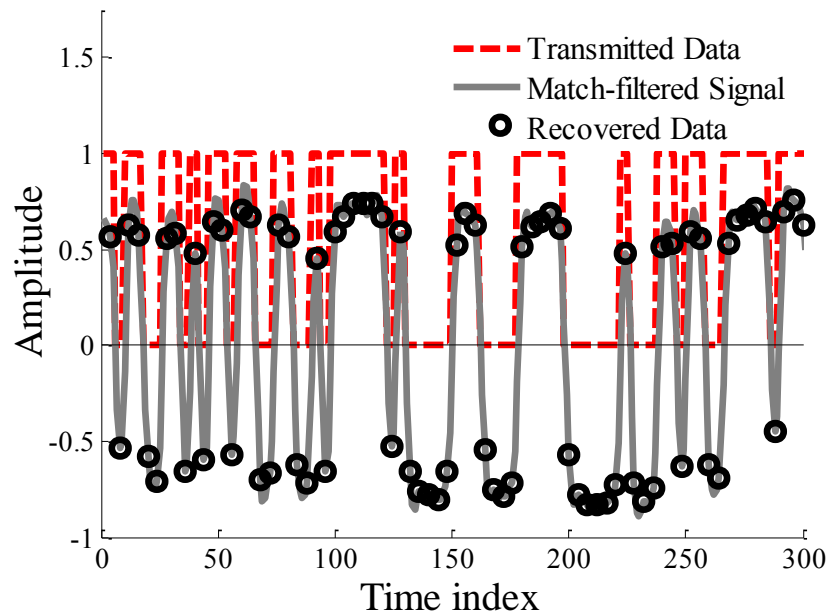
where $\sigma^2(x)$ and $m(x)$ are variance and mean values of x , respectively. N is the total number of symbols which is 8184 in this measurement. The signal power per symbol is calculated by

$$P_s = \frac{1}{N} \sum_{k=1}^N I^2(k) - P_{nI}. \quad (3-12)$$

Measured $SNR = P_s / (P_{nI} + P_{nQ})$ is 14.36 dBm, which satisfies the predefined system specifications on BER very well.



(a) Received signal and transmitted data



(b) After recovery

Figure 3-28: Measurement results in communication mode; Received signals are match-filtered by an FIR filter with 4 taps and energy of unity.

3.6.2 Radar sensing

Several measurement setups are compromised on purpose as each of them addresses a specific parameter for which a contribution is made throughout this research.

Figure 3-29 shows the measurement setup of radar function which is built up to evaluate our simulated analysis of threshold detection. The channel emulator can emulate a pure-Doppler radar channel that resembles round trip propagation time and Doppler frequency shift with added interference noise at any desired SNR. Furthermore, mobile targets may be defined to move at constant velocity and positioned at a distance (R) that associates with propagation time (τ) by $R = c_0\tau/2$.

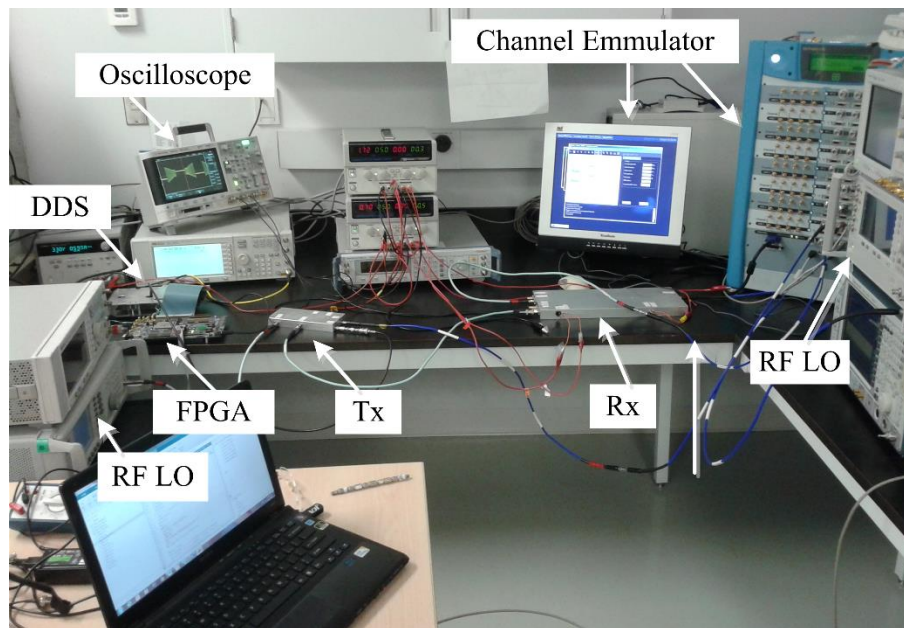


Figure 3-29: Radar mode measurements with channel emulator

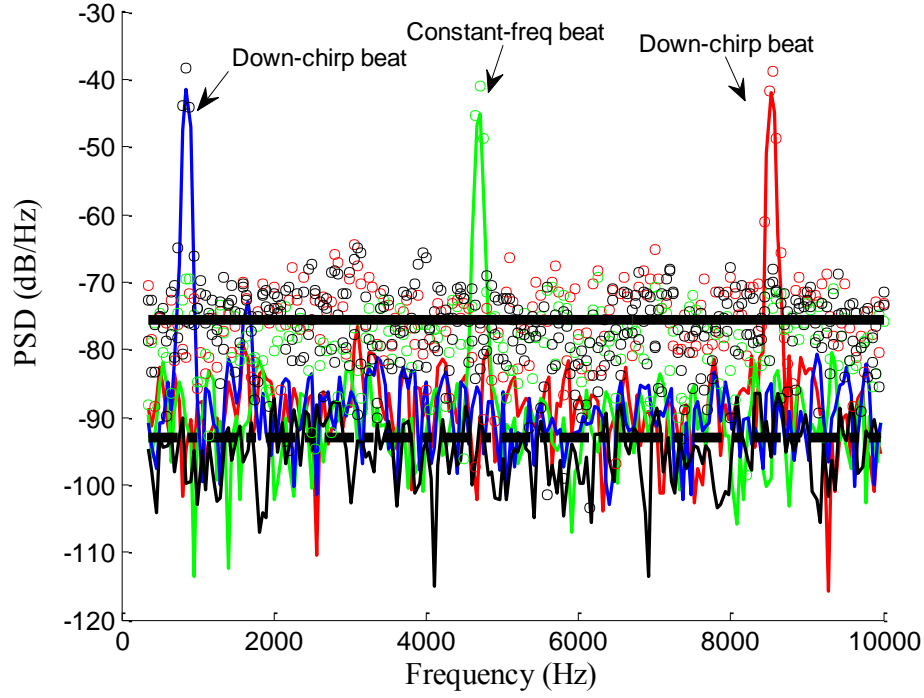


Figure 3-30: PSD (with Hanning window) of the measured beat signals with two different SNR; - : SNR=29.94 dB (case 1) o : SNR=15.04 dB (case 2), -.- : average noise level for case 1, -- : average noise level for case 2

The SNR from PSD can be calculated as follows. Defining $S_1 = \sum_{j=0}^{N-1} w_j$ and $S_2 = \sum_{j=0}^{N-1} w_j^2$, the RMS value of PSD from N -point FFT of a signal with windowing (w_j) is known to be [83]

$$PSD_{rms}(f) = \frac{PS(f)}{ENBW} = \frac{\frac{|FFT(S_b w)|^2}{|S_1|^2}}{N \frac{S_2}{|S_1|^2} \times \frac{f_s}{N}} \quad \left(\frac{V^2}{Hz} \right) \quad (3-13)$$

where PS is the power spectrum and the $ENBW$ is the effective noise bandwidth. Thus, SNR can be calculated by comparing the signal and noise power obtained from PSD

$$SNR(f_b) = \frac{PSD(f_b) \times ENBW}{E[PSD(N_o)] \times f_s} \quad (3-14)$$

where $E[.]$ and N_o denote the expectation function and the background noise, respectively.

Within the first measurement, the noise density is tuned for a single value of propagation time delay and Doppler in the emulator. One can observe the different noise levels in Figure 3-30 that shows the PSD of beat signals for two cases with SNR of around 15 dB and 30 dB.

More measurements were done with several distinct values of SNR keeping the value of time delay and velocity unchanged. Indeed, around 50 sets of beat signals for each value of SNR were saved for further processing. Then the STD of range and velocity was estimated with several values of threshold for each set of signals. It can be concluded from the results, tabulated in Table 3-4 that a minimum threshold of around 12 dB is essential to ensure correct detection which is in good agreement with our simulation results. Convergence of STD to half of range and velocity resolution validates our RadCom system ability in radar mode. It should be noted that the system in this measurement setup is first calibrated by measuring the internal delay when the Rx and Tx blocks are connected directly.

Table 3-5: STD of range measurement

SNR (dB)	Threshold (dB)					
	1.5	4.5	6.5	8.5	11.5	16.5
10.3	94.8	-	1.48	-	1.48	
14.5	101.6	32.89	1.37	-	1.37	
21.7	-	-	91.11	39.17	1.42	1.42
24.7			102.81	59.12	1.47	1.47

Table 3-6: STD of velocity measurements

SNR (dB)	Threshold (dB)					
	1.5	4.5	6.5	8.5	11.5	16.5
10.3	34.85	-	1.26	-	1.26	
14.5	42.6	1.22	1.21	-	1.22	
21.6	-	-	17.6	1.24	1.24	1.24
24.7			9.03	1.26	1.26	1.26

Another measurement in radar mode is carried out within the same testbed in order to assess our system's consistency in radar mode. Therefore, a few radar channels with different propagation time delay and Doppler shifts are set using the channel emulator. For this measurement, the data is collected from sampled signal provided by onboard ADCs by probing from FPGA. Subsequently, captured signals are processed by FFT with zero padding in order to obtain desired information. FFT with length of 512 K is selected with the purpose of relaxing the error in estimation due to frequency resolution even though lower order of FFT may be used if the computation burden imposed by this high order FFT is not feasible in some practical applications.

The measurement results are presented in Table 3-7. As it was already observed in simulations and also the previous measurement, there is an almost constant error in estimated time delay due to the inherent delay between received and reference signals. The measured results after calibration agree very well with the defined values. This can fairly prove the consistency in radar functionalities.

Table 3-7: Measurement results

Defined values		Measured values			
Delay (ns)	Velocity (m/s)	Delay (ns)			Velocity (m/s)
-----	-----	Before calibration	Error	After calibration	Without calibration
1500	30	1526	25.6	1499.2	30
1500	40	1526	25.8	1496.4	40.06
1500	50	1526	26	1499.6	50.12
2000	30	2026.4	26.4	2000	30
2000	40	2026.4	26.4	2000	40.06
2000	50	2026.4	26.4	2000	50.12
2750	30	2777.2	27.2	2750.8	30
2750	40	2777.2	27.2	2750.8	40.06
2750	50	2777.2	27.2	2750.8	50.12
3500	30	3527.6	27.6	3501.6	30
3500	40	3527.6	27.6	3501.6	40.06
3500	50	3528	28	3501.6	50.12

With the purpose of evaluating the achievable range resolution, several targets are arranged in an indoor test-bed as it is shown in Figure 3-31. Targets 3 and 4 as well as targets 5 and 6 are placed in a distance around the range resolution. The received beat signal is sampled by ADCs and read out of FPGA.

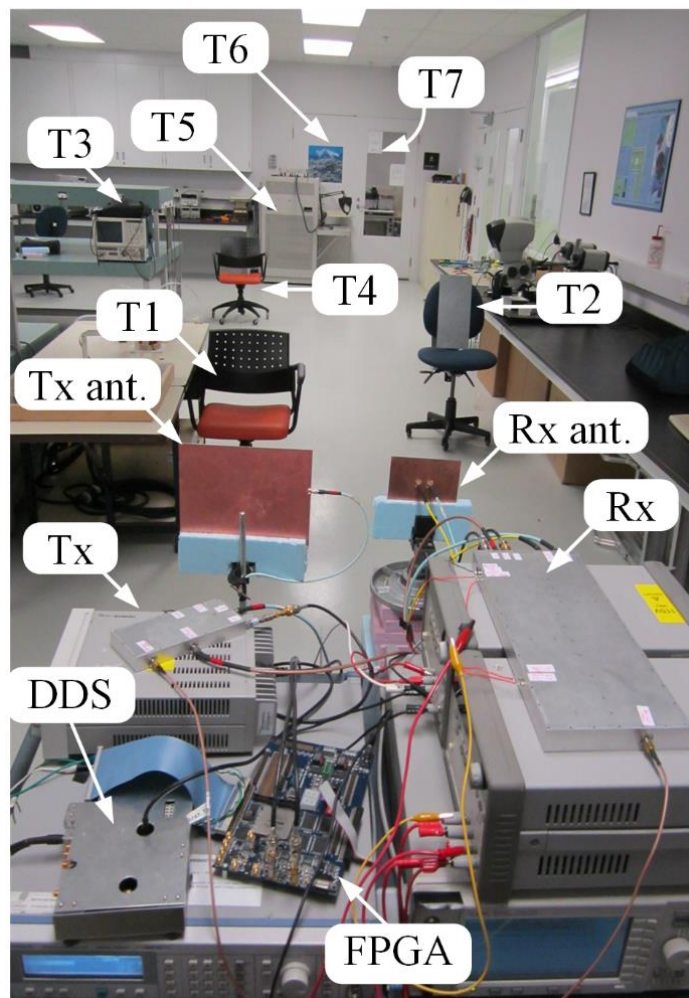


Figure 3-31: Measurement setup in lab Targets 3 and 4 as well as targets 5 and 6 are deliberately positioned so close to each other to evaluate resolution in range estimation

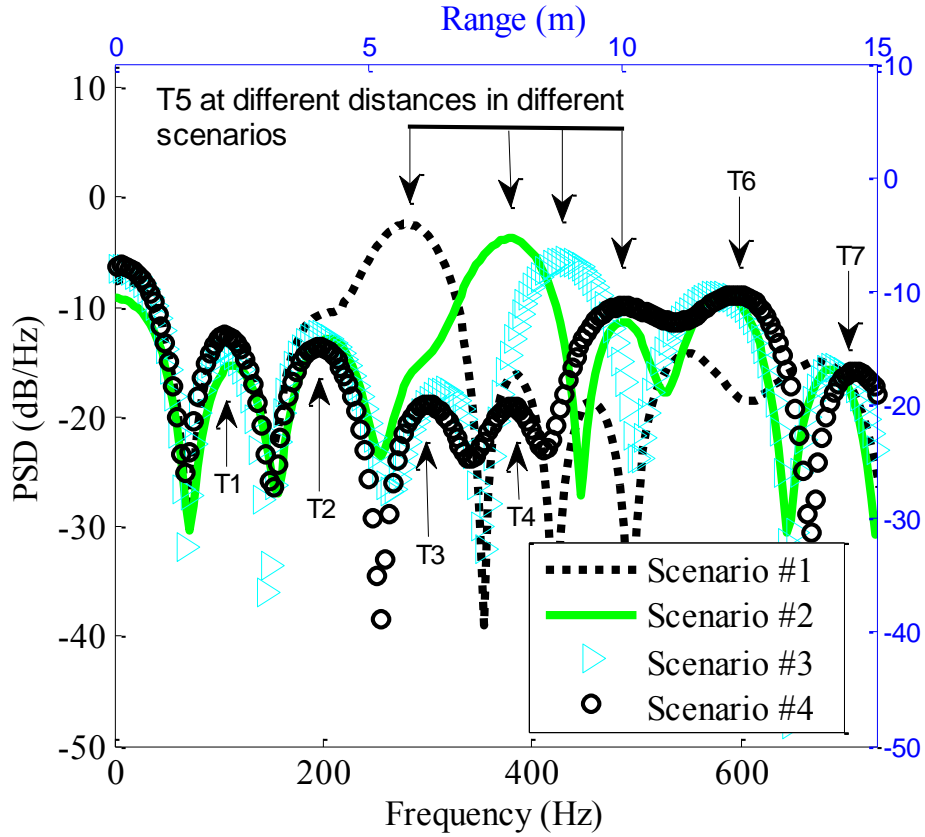


Figure 3-32: Range resolution and range profile measurement results; Scenario #1 (dot line) with T5 located at 5.5 m, Scenario #2 (solid line) with T5 located at 7.5 m, Scenario #3 (triangles) with T5 located at 8.5 m, Scenario #4 (circles) with T5 located at 9.5 m., Labels T_i ($i=1:7$) indicate the detected targets in Scenario #4 which is shown in Figure 3-29. Measured range resolution between T3 and T4 is 1.526 m.

The range profile is estimated through FFT with zero padding as it is shown in Figure 3-32. One can readily see that all targets are discriminated from each other. The range values shown in top x-axis in Figure 3-33 is actually mapped from the frequency axis by solving the system functional equations in (2). Furthermore, since the targets are stationary no Doppler contribution is made to the beat frequencies, i.e. $f_{bu} = 2\Gamma R/c$. Hence, the range profile can be directly obtained from the frequency axis of the spectrum of the received beat signal in the up-chirp time slot. The measured range resolution for the minimum distinguishable range of target is 1.52 m.

Additionally, in the same test-bed only T5 is placed in 4 different known distances in scenarios 1-4 and the range profile is obtained and added to Figure 3-32. One can see as the target is placed further the corresponding peak appears in larger frequency.

In order to evaluate the system capability in estimating the angular position of detected stationary objects, a special setup (sketched in Figure 3-33) is arranged in our lab. True angular position with respect to the Rx antenna phase center can be roughly expected to be $\tan^{-1}(y/x)$. The target is a small piece of metal and is located in an appropriate distance respecting Fresnel near field zone.

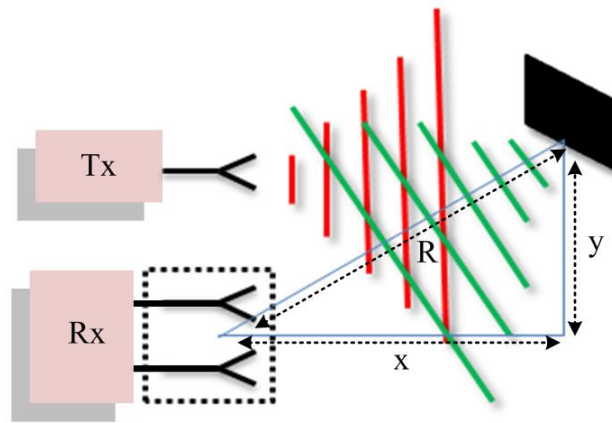
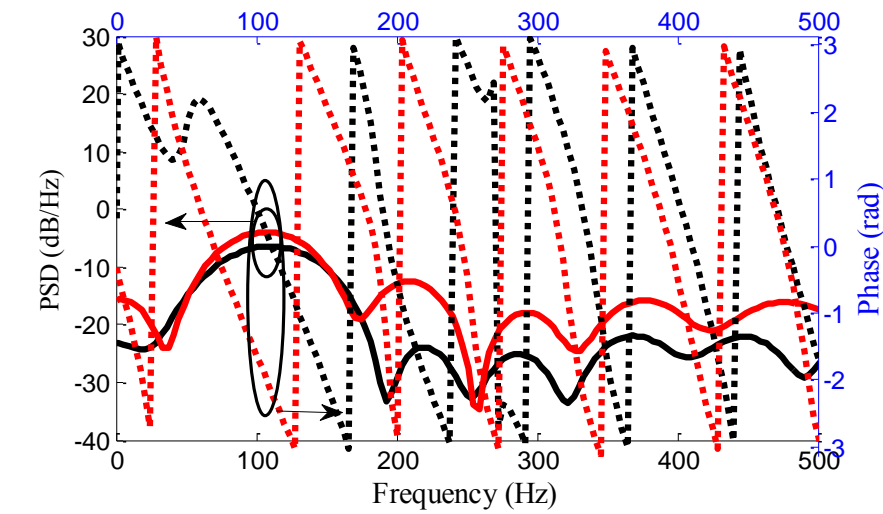


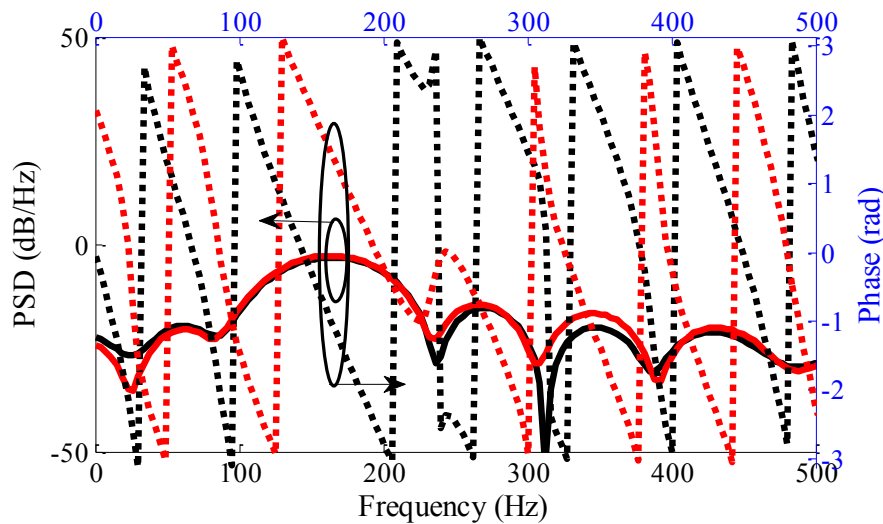
Figure 3-33: Angle measurement setup

Table 3-8: Angle measurements

Target's angle (deg)	Frequency bin (Hz)	Targets detected range (m)	Phase difference (rad)	Measured angle (deg) before & after calibration	
15°	95.03	1.900	1.0376	19.28°	14.11
30°	102.07	2.041	1.8151	35.21°	30.04
45°	159.9	3.198	2.4428	51.03°	45.86



(a) Angle=30°



(b) Angle= 45°

Figure 3-34: Angle measurement results; PSD (solid) and angle (dashed) of beat signals after FFT for two different positions of target. Red: channel 1, black: channel 2.

Phase and amplitude of the received beat signals after FFT for two different cases are plotted in Figure 3-34 for reference. It should also be mentioned that the test is not carried out in anechoic chamber and the existence of adjacent in-lab objects increased the clutter level. One can see that as angle increases the distance of the target from Rx antenna increases and this makes the peak in

amplitude to occur in larger values of frequency. Angles and distances are estimated through (3) and the results are listed in Table V. The estimated range and angle can give us the position of the detected target as it is shown in Figure 3-35. As we can see, there is around 5° of error between our estimated results and the true value. This can be attributed to a few reasons. First, the low SNR (measured roughly around 10 dB) or the possible small amount of inherent phase delay caused by PCB layout or cables can offset the phase difference.

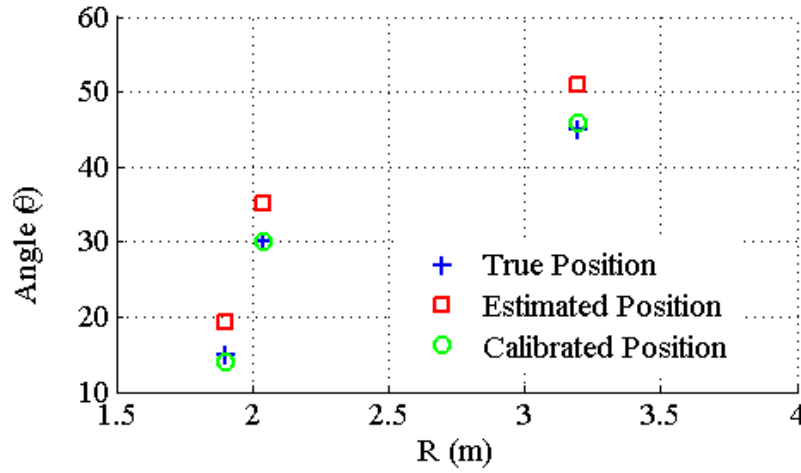


Figure 3-35: Measurement results in position estimation

Second, the exact expected value of angle in this test can only be determined with rough approximations because the reflected signal from a metal surface is a multipath signal [95]. In fact, depending on the position of the node along the surface with strongest angular reflection, the angle estimation value by our prototyped system may change. This pinpoints a limitation of the system in exact angle detection when targets with large metal surface are present in the scenario. However, subtracting the average error from measured values yields rather accurate calibrated results.

3.7 Conclusion and discussions

We have proposed and demonstrated a multifunctional system architecture taking all incompatibilities between radar and radio systems into account. It is capable of integrating the radar and communication functions required for future mobile data-fusion platform. In comparison to previous architectures, our system is improved to be capable of angle detection besides velocity and range estimation with enhanced resolution and accuracy. Our proposed multifunctional

transceiver is prototyped and true multiple functionalities of the system are validated through several system-level simulations and measurements with the support of numerous results. Using an FPGA in back-end has made out system rather compact and capable of a flexible functional reconfiguration upon data fusion.

In Table VI, this work is compared with the state of the art reported works for different integration schemes of time and frequency in terms of the variety of functions that was integrated with their proposed scheme. We can see that our work outweighs because it detects angle and also the measured range resolution is around 1.5 m, utilizing only 150 MHz. It should be noted that our system performance in communication with data rate of up to only 25 MSPS is verified due to limited maximum clock frequency of our onboard ADC's (i.e. 100 MHz). Among the references, localization technique proposed by [18] which is capable of complete positioning demands for larger bandwidth resources and is mostly appropriate for short range applications.

Nevertheless, the proposed transceiver scheme is still subject to further developments. For example, the proposed interferometry approach for angle detection might have some limitations in a real scenario with multiple targets especially when two close targets are moving with identical speeds and the beat frequencies may not be discriminated.

Despite these limitations, angle detection based on Doppler phase difference was considered as the best candidate at this stage of research for multi-functional transceivers, due to its simplicity. Evolving phased-array or digital beam forming (DBF) technique has demonstrated reliable performance when applied to automotive radars, [80, 96, 97]. However, a considerable improvement on further unification of the RF front-end of RadCom transceivers, the Rx in particular, should first be made if the undesired complexity of beam forming systems is to be avoided. In addition, a significant research effort can be anticipated on the antenna part by developing a reconfigurable antenna with variable gain. Furthermore, the RadCom system needs a high gain antenna when functioning as radar while a low gain with wide beam-width is desirable in the radio mode.

Therefore, the proposed architecture can ignite the further developments of future sensor-fused automotive and vehicular radars with the full ability of high-speed communication [2] as well as DSRC devices with an expanded ability of collision avoidance and other functionalities.

Table 3-9: Comparison of different RadCom schemes

Reference	Integration domain	Bandwidth (MHz)	Radio signal	Radar signal	Range estimation	Velocity estimation	Angle estimation	Range resolution (measured)	Maximum data rate
[98] 5.9 GHz	Frequency	90	OFDM	OFDM	Yes	Yes	No	1.7 m (Theory)	27 Mbps
[16] 10 GHz	Frequency	500	PM-LFM	FMCW	Yes	Yes	No	63 cm	1 Mbps
[99] 7.5 GHz	Frequency	1000	OFDM	OFDM	Yes	Yes	No	34 cm	57 Mbps
[25] 60 GHz	Frequency	3000	PPM	PPM	Yes	Yes	Yes	12.4 cm	200 Mbps
[100] 1.75 GHz	Time	60	ASK	FMCW	Yes	Yes	No	2.5 m (Theory)	1 Mbps
[23] 24 GHz	Time	100	PM	TFMCW	Yes	Yes	No	1.65 m	50 MSPS
[14] 5.8 GHz	Time	20	PM	TFMCW	Yes	Yes	No	7.5 m (Theory)	10 MSPS
This work [28] 5.8 GHz	Time	150	PM	TFMCW	Yes	Yes	Yes	1.53 m	75 MSPS

CHAPTER 4 PARAMETRIC CHARACTERIZATION OF SIX-PORT INTERFEROMETER

Despite the wide applications of six-port interferometric technology and its extended research activities which have been reported in the literature, not all aspects of this technique were completely investigated. In [59], the operation principles of a black-box model of six-port interferometers were theoretically analyzed a bit further in detail while they were compared with other types of Rx through experimental evaluations in [101]. Moreover, it was concluded that the multi-port interferometers function as an additive mixer. In [25], the intermodulation products of a six-port demodulator were studied through circuit-level simulations. One drawback of the six-port demodulator is its high conversion loss. To determine an appropriate LO power level for optimum operation, a procedure that was mostly based on simulations was reported in [102]. For the considered detector diode model, it was demonstrated that a LO power of around 8 dBm, which pushed the power detector operation out of the well-known square law region, should be selected to minimize the conversion loss. However, the main benefit of low LO power operation of the six-port cannot be preserved in this case. In [102], the performance of the multi-port and in particular six-port demodulator in terms of noise was studied. The effect of different noise sources was compared, indeed. However, a closed-form equation for calculating the noise figure (NF) of the demodulator that is required especially in system analysis has never been reported so far. In this chapter, a method of computing the NF of six-port demodulators is proposed, and the detector biasing for optimizing the conversion loss is studied. Moreover, the six-port demodulator is characterized as a conventional mixer model in terms of systematic parameters. In order to avoid any secondary issue that may appear due to non-idealities in measurements, all analyses are validated through circuit simulations in commercial software of the advanced design system (ADS).

4.1 Noise analysis

In order to estimate the NF of any two port network, the noise power at its input and output terminals must be compared. Figure 4-1 shows the diagram which is used for NF calculation of any two-port device under test (DUT).

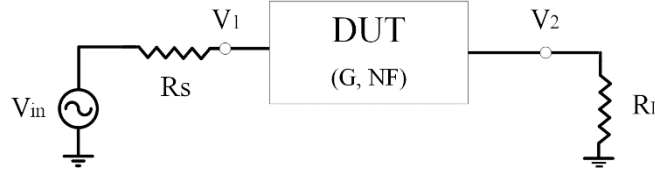


Figure 4-1: Proposed configuration for estimating the NF of a two port network

If R_s is assumed to be a noiseless resistor, the noise voltage that is generated by the noisy DUT and transferred to the input terminal at the node V_1 can be expressed by

$$V_n^{in} = \frac{V_n^{out}}{G_v} = V_1 \frac{V_n^{out}}{V_2} \quad \text{V} / \sqrt{\text{Hz}} \quad (4-1)$$

where G_v is the voltage gain of the DUT. This noise voltage can be assumed to be generated by thermal noise of R_s which is matched to input resistance of DUT, and hence equivalent noise temperature T_{eq} is

$$T_{eq} = \frac{(\sqrt{2} \times V_n^{in})^2}{4 \times K \times R_s} \quad \text{K} \quad (4-2)$$

4.1.1 NF of multi-port demodulator

Among the thermal noise and shot noise, the latter may have a more significant contribution to the total noise power [8]. The shot noise depends on the diode junction current and can be expressed as:

$$I_{nd}^2 = 2q(I_d + 2I_s) \quad \text{A}^2 / \text{Hz} \quad (4-3)$$

where q is the unit charge and equal to $1.6 \times 10^{-19} \text{ C}$. I_s and I_d are the saturation current and the DC current passing through the diode junction, respectively.

Usually a six-port junction is terminated by a set of four power detector circuits where the combined RF and LO signals are multiplied with each other. However, the four outputs are usually transformed to two in-phase (I) and quadrature (Q) components of a down-converted signal using differential amplifiers [34]. Therefore, the whole architecture of six-port demodulator which consists of a coupler network, detectors and differential amplifiers can be viewed as a single three-port network, i.e. one RF input and two I and Q output ports. Since the NF of the demodulator with

reference to either of the output ports is identical, it can be viewed as a two-port network. Figure 4-2 shows the diagram in which the six-port demodulator substitutes the DUT in Figure 4-1.

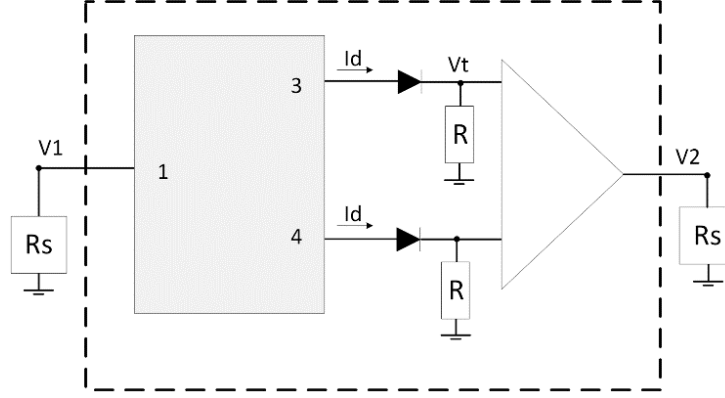


Figure 4-2: Diagram for estimating the NF of six-port mixer

For the NF calculation, two different approaches of noise power and voltage comparison at the input and output terminals are presented as follows. By connecting the terminals with matched noiseless loads, assuming all parts are in thermal equilibrium and all of the noise sources are uncorrelated, the noise power at port 2 can be simply estimated through the superposition of noise powers from detectors and differential amplifiers through

$$\begin{aligned}
 P_n^{amp} &= \frac{2(V_n^{amp})^2}{R_s} & \text{W / Hz} \\
 I_{nd}^2 &= 2q(I_d + 2I_s) & \text{A}^2 / \text{Hz} \\
 V_n^D &= R \times \sqrt{I_{nd}^2} & \text{V} / \sqrt{\text{Hz}} \\
 P_n^D &= \frac{2(V_n^D)^2}{R_s} & \text{W / Hz} \\
 N_2 &= P_n^D + P_n^{amp} & \text{W / Hz}
 \end{aligned} \tag{4-4}$$

where V_n^{amp} and V_n^D are the noise voltage of the video amplifier at its input port and that of the Schottkey diode. The value of diode current (I_d) depends on the input LO power level and can be obtained from circuit simulation with SPICE models of the diode. When the junction capacitance is infinitesimal or the operation frequency is very low, one can assume that the whole noise current passes through the video resistance. The noise power is to be transferred to the input port using the

power gain of the DUT (G_{DUT}) so that the equivalent noise temperature at the input port can be estimated by

$$T_{eq} = \frac{N_2}{G_{DUT}^P \times K} \quad \text{k}^\circ \quad (4-5)$$

where K is the Boltzman constant.

NF can also be estimated through the noise voltage and its equivalent noise temperature. The noise voltage of the amplifier, transferred to the input of the two-port network can be expressed by

$$V_{in}^i = \frac{\sqrt{2} \times V_n^i}{G_{DUT}^V} \quad (4-6)$$

where G_{DUT}^V is the voltage gain of the DUT and V_n^i denotes either the noise voltage of the amplifier or the shot noise voltage of the diode. The equivalent noise temperature of the resistor R_s with equal noise voltage at the input port is

$$T_{eq}^i = \frac{(\sqrt{2} \times V_{in}^i)^2}{4 \times K \times R_s} \quad (4-7)$$

Hence, using the superposition principle, the total equivalent noise temperature is

$$T_{eq} = T_{eq}^{amp} + T_{eq}^D \quad (4-8)$$

Noise temperature can be readily converted to NF using the well-known equation of $NF = 10\log(1 + T_{eq}/T_o)$ from [61].

The equations are validated through a set of simulations in ADS and the results are presented in Figure 4-3. First, the NF calculation is done for a conventional mixer with a predefined NF. One can observe that our estimated value agrees very well with the predefined NF of the mixer. Subsequently, a six-port demodulator is built up using HSCH-9161 diodes as detectors and ideal couplers. Then using the option of Noise Contribution (NC) with Harmonic Balance (HB) simulation in ADS, the noise voltage is obtained and processed further in the above-mentioned equations. It can be observed that the NF varies between 17 dB to 20 dB if the noise of the video resistance is also considered. In addition, it is shown that the effect of video amplifier on the noise performance can be considerable.

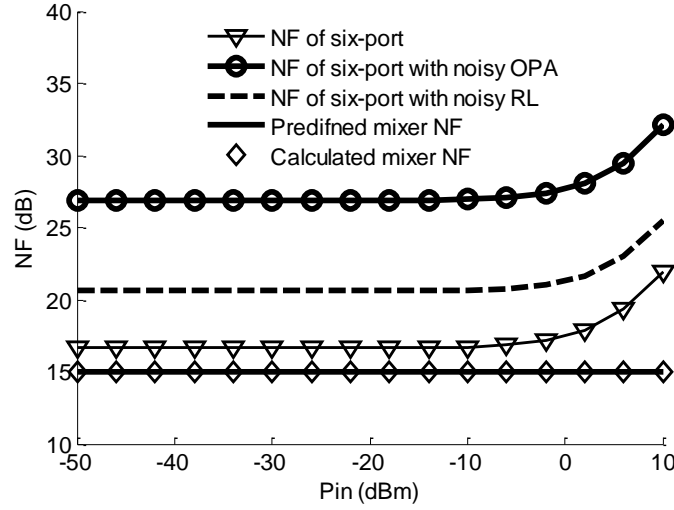


Figure 4-3: Calculated NF using the proposed equations; noise voltage of video amplifier is assumed to be $2.5 \text{ nV}/\sqrt{\text{Hz}}$.

4.2 Conversion loss improvement

The I-V characteristics of a diode can be expressed by the following exponential equation [8]

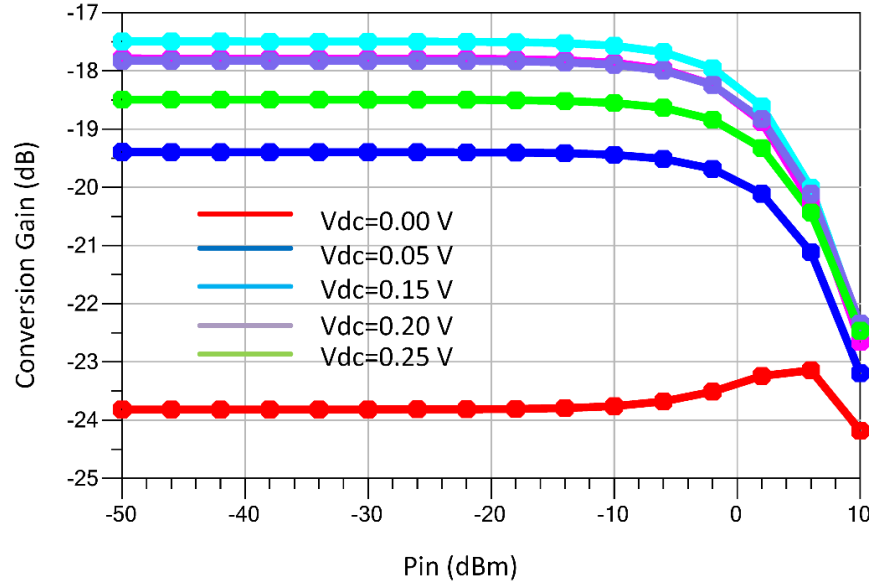
$$I = I_s (e^{\frac{qV}{n k T}} - 1) \quad (4-9)$$

Assuming $V = V_{RF} \cos(\omega_{RF} t + \varphi_{RF}) + V_{LO} \cos(\omega_{LO} t + \varphi_{LO})$ and expanding (4-9) into Taylor series up to second power, one can have

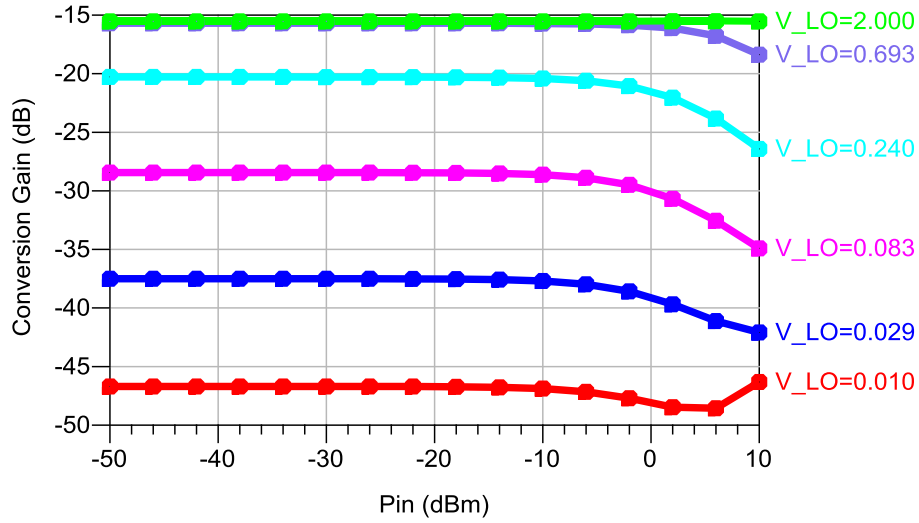
$$I = \zeta + \frac{\partial I}{\partial V} V + \frac{\partial^2 I}{\partial V^2} V^2 + \zeta \zeta = \chi + \frac{q^2 (I_B + I_s)}{2(n k T)^2} (2V_{LO} V_{RF}) (\cos((\omega_{RF} - \omega_{LO}) t)) \quad (4-10)$$

where I_B is the diode bias current and χ denotes all other products of expansion which can be filtered using either high or low pass filters. One can observe in (4-10) that the amplitude of the mixing product of interest depends on both of the LO power and the bias current, and hence the zero-bias detectors may suffer from high conversion loss when supplied with low LO power. Therefore, it gives us a freedom of selecting between none-zero bias current or high LO power for multi-port demodulator. The interesting feature of low LO power requirements has made the multi-port techniques an excellent candidate for application on circuits operating at millimeter-wave

frequency bands where a high power LO signal is not always available. However, with a low LO power, the conversion loss and consequently the NF would be very high. Therefore, picking up the second choice and biasing the diode that compensates the effect of low LO power on conversion loss comes into view. It should be mentioned that the video bandwidth of the detectors decreases by increasing the bias current [103], and therefore a compromise should be made between video bandwidth and conversion loss. The effect of biasing on the conversion loss of six-port demodulators is investigated via simulations in ADS and the results are demonstrated in Figure 4-4 (a). One can observe that for a bias around 0.15 V, the conversion loss reduces down to 17.5 dB which is around 6.5 dB less than that with zero bias. The detector is still in the square-law region and the compression point decreases along with the increase of conversion gain. Also, the variation of conversion gain with the changes in LO power is demonstrated in Figure 4-4 (b). The movement from the square-law region to mixer region with the increase of LO up to around 2 V is noticeable. Selecting a low LO power of -4 dBm with DC bias of 0.15 V makes the detector to remain in the square-law region.



(a) Effect of V_{dc} : PLO= -4 dBm or VLO=0.397 V



(b) Effect of LO power with $V_{dc}=0.15$ V

Figure 4-4: Controlling the conversion loss of the six-port mixer via LO power and DC bias

4.3 Equivalent mixer model

In order to validate the parameters of the modeled six-port mixer, a simulation platform is used as it is shown in Figure 4-5. The 3dB power gain ideal amplifier followed by a power divider is used such that the voltage gain of the entire demodulator constructed by two mixers is identical to

each of the single mixer. Moreover, the voltage gain definition is selected as $V_{out-over-open-circuit}-V_{in}$ such that the gain of the six-port demodulator is consistent with that of the mixer model for a fair comparison.

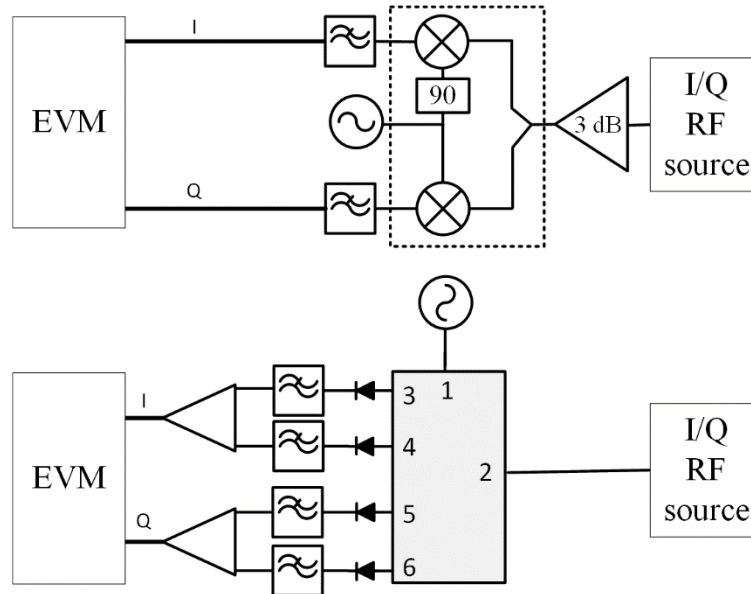


Figure 4-5: Platform used in ADS simulations for validating the six-port mixer model

Table 1 shows the EVM of the six-port with detectors biased at 0.15 V and LO power of -4 dBm at different RF input power. The NF of the mixer component in ADS, i.e. Mixer-2, is swept and the EVM is estimated for a range of input power level from -50 dBm to -25 dBm, within co-simulation of Envelope and Data Flow. Comparing the results with the values of the six-port demodulator, we can find the EVM corresponding to the NF of around 18 dB in a good agreement with that of the six-port demodulator. This implies that the NF of the six-port demodulator can be assumed to be around 18 dB which agrees well with the calculated value of around 17 dB.

Table 4-1: EVM simulation of six-port mixer

Pin (dBm)	EVM (%)
-50	7.9
-45	4.5
-40	2.6
-35	1.5
-30	1
-25	0.7
-20	0.7

Table 4-2: EVM simulation of six-port mixer

Pin (dBm)	-25	-30	-35	-40	-45	-50
NF	EVM (%)	EVM (%)	EVM (%)	EVM (%)	EVM (%)	EVM (%)
17	0.4	0.8	1.3	2.2	4.0	7.0
17.5	0.5	0.8	1.4	2.4	4.2	7.4
18	0.7	0.8	1.5	2.6	4.4	7.8
18.5	0.7	0.9	1.5	2.7	4.7	8.3
19	0.6	0.9	1.7	2.8	5	8.6
19.5	0.6	1.0	1.8	3	5.4	9.1
20	0.8	1.0	1.9	3.2	5.6	9.5
20.5	0.7	1.1	2.0	3.4	5.9	10

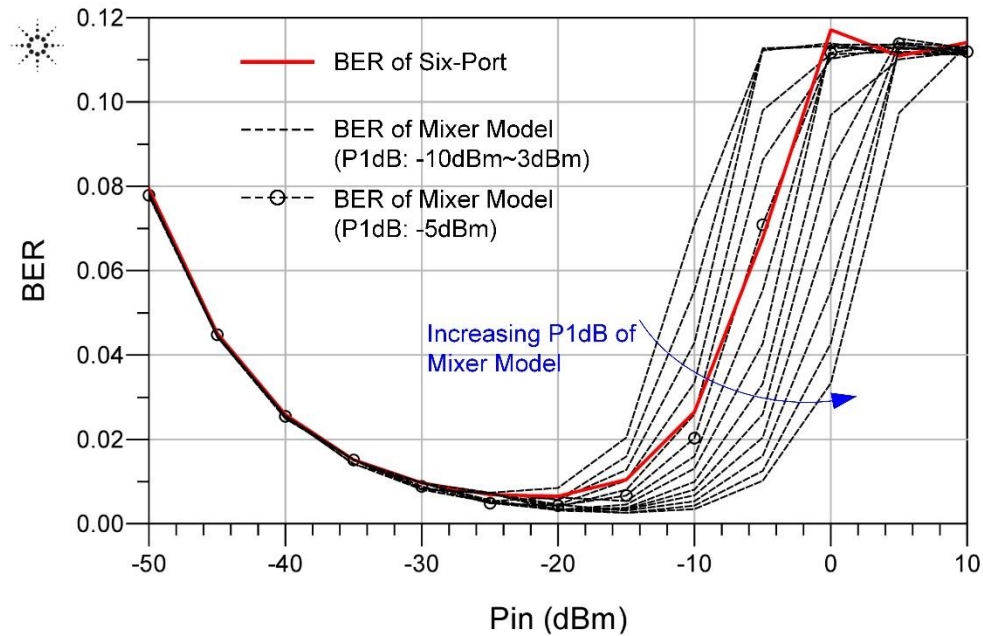


Figure 4-6: Comparison of BER between the six-port demodulator and the mixer model with different values of P1dB in ADS simulations

In addition, the BER of both six-port demodulator and the mixer model are compared for different values of P1dB of the mixer model. Figure 4-6 compares the result of simulation. From the agreement of the curves around the P1dB of -5 dBm, one can conclude this value as the

compression point of the six-port demodulator which is consistent also with the previous results, shown in Figure 4-4.

4.4 Conclusion

Six-port demodulators are re-examined with the purpose of modeling their characteristics with mixer counterparts in terms of characteristic parameters. The presented results give a good understanding of the main specification of multiport demodulator and can be used readily in system design such as chain budget calculations.

CHAPTER 5 UNIFIED RADAR-COMMUNICATION (RADCOM)

MULTI-PORT INTERFEROMETER TRANSCEIVER

So far, all proposed RadCom transceivers have been developed based on the conventional architectures of heterodyne or homodyne which impose some limitations along with increasing the number of desired functions that should be integrated. Because of interesting features of the technology of multiport interferometry which can be remarked through previous chapters, we have considered developing multiport based multifunctional transceivers. The conventional six-port topology, which is shown in Figure 2-6, is not capable of handling radar and communication functions, simultaneously. Therefore, new schemes of phasing networks have been examined through this research. First, multifunctional multiport based transceiver is introduced along with a low frequency system demonstrator in the context of RadCom systems within this chapter. Subsequently the proposed architecture is developed further for theoretical analysis and practical assessment through mathematical modeling and implementation in millimeter-wave frequency bands, respectively. The details of the latter one are reported in chapter 7.

In this chapter, according to the operation principles of the time-agile waveform scheme which is explained in the previous chapters, the six-port topology is improved and adopted in the receiver design. The early results for concept demonstration purposes have been reported in [104] which are discussed in this chapter, as well. First, a modified transceiver architecture is presented which is based upon the operation principles of our time-agile multifunction scheme. Then, a novel six-port is theoretically analyzed and finally its performance is evaluated through a preliminary system-level measurement.

5.1 System concept

5.1.1 Modulation scheme

The modulation scheme that was proposed in Figure 3-1 was again used herein with the new multiport based transceiver architecture which is introduced next.

5.1.2 Transceiver architecture

Figure 5-1 shows the block diagram of the proposed transceiver architecture that operates based on our waveform scheme. The signal generator consists of a field programmable gate array (FPGA) and a direct digital synthesizer (DDS) board. The FPGA is supposed to control the DDS by sending the frequency sweeping signal in radar cycle and phase shift keying signal in radio cycle. In radio cycle, a quadrature modulation is realized in digital domain. Therefore, only one digital to analog convertor (DAC) is enough to feed the transmitter with intermediate frequency (IF) signal.

The transmitter up-converts the IF signal after initial amplification and filtering. Using a directional coupler, a branch of the RF signal is sent to the receiver as a reference signal for down-conversion. The receiver antenna has two identical patch elements on the same substrate in connection with two separate channels. Through this topology, two distinct beams of arriving signal are captured with a phase delay corresponding to the arriving beam direction, i.e., $\sin(\theta) = x/d = \Delta\phi/\beta d$.

At the receiver side, a multiport component with three input ports is used for combining input signals with specific phase relationship. The operation principle of this novel multiport scheme will be briefly discussed in section III. The Schottky diode detector circuits operate as additive “mixers” and down-convert the received signal. Note that the receiver does not need any RF local oscillator and the reference signal coming from the transmitter is used for mixing. Two out of the four outputs of detectors are enough. Therefore, they are differentially amplified and injected into two onboard ADCs for further processing in the FPGA.

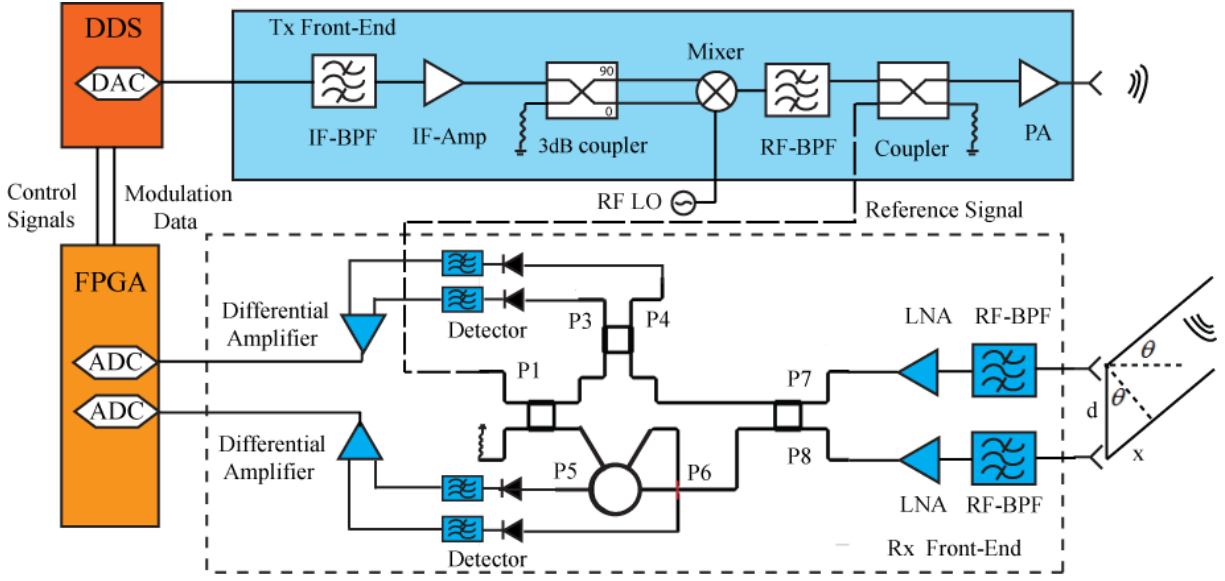


Figure 5-1: Block diagram of the proposed transceiver architecture

5.2 Operation principles of novel multi-port component

The layout of the proposed multiport interferometer circuit is sketched in Figure 5-1. It consists of three quadrature hybrids and one rat-race coupler. In order to investigate the performance of this component, let us assume S_{LO} , S_7^r and S_8^r with the following expressions as the input signals to P1, P7 and P8, respectively

$$\begin{aligned}
 S_{LO}(t) &= \text{Re} \left\{ r_{LO} e^{j\varphi_{LO}(t)} \right\} \\
 S_7^r(t) &= \text{Re} \left\{ r_7 e^{j\varphi(t)} \right\} \\
 S_8^r(t) &= \text{Re} \left\{ r_8 e^{j\varphi(t) - \Delta\varphi} \right\}
 \end{aligned} \tag{5-1}$$

where $\Delta\varphi$ is the phase difference corresponding to the direction of a received beam. Although this information is needed for estimating θ , this phase difference can cause interference in communication signals. Compensation of this interference from the output of conventional six-port demodulator cannot be made straightforwardly [105]. However, it can be readily dealt with thanks to the scattering matrix of the six-port topology. Equation (5-2) shows how two outputs of the whole receiver are created. Note that either amplification or conversion gains are assumed to be unity in (5-2).

$$\begin{aligned}
\begin{bmatrix} S_3^{bb} \\ S_4^{bb} \\ S_5^{bb} \\ S_6^{bb} \end{bmatrix} &= \begin{bmatrix} -r_{LO} r_7 & -r_7 r_8 & -r_{LO} r_8 \\ r_{LO} r_7 & -r_7 r_8 & r_{LO} r_8 \\ r_{LO} r_7 & r_7 r_8 & -r_{LO} r_8 \\ -r_{LO} r_7 & r_7 r_8 & r_{LO} r_8 \end{bmatrix} \begin{bmatrix} \sin(\varphi_{LO}(t) - \varphi(t)) \\ \sin(\Delta\varphi) \\ \cos(\varphi_{LO}(t) - \varphi(t) + \Delta\varphi) \end{bmatrix} \Rightarrow \\
\begin{cases} S_4^{bb} - S_3^{bb} = 2r_{LO} r_7 \sin(\varphi_{LO}(t) - \varphi(t)) + 2r_{LO} r_8 \cos(\varphi_{LO}(t) - \varphi(t) + \Delta\varphi) \\ S_5^{bb} - S_6^{bb} = 2r_{LO} r_7 \sin(\varphi_{LO}(t) - \varphi(t)) - 2r_{LO} r_8 \cos(\varphi_{LO}(t) - \varphi(t) + \Delta\varphi) \end{cases} \quad (5-2) \\
\Rightarrow \begin{cases} S_4^{bb} - S_3^{bb} = Q_7 + I_8 \\ S_5^{bb} - S_6^{bb} = Q_7 - I_8 \end{cases}
\end{aligned}$$

Both I and Q components can be readily discriminated in the FPGA by simple subtraction and addition of the sampled outputs of the receiver. In radar mode, they are actually beat signals received by the two antennas antenna elements. So, the signals should be processed by fast Fourier transform (FFT) to obtain the frequency bins. These frequencies can be used for estimating R and v . Since the phase of I and Q is preserved after transformation to the frequency domain, $\Delta\varphi$ in (5-1) can be obtained by differentiating the phase at exact beat frequency bins, i.e., $\Delta\varphi = \angle I_8 - \angle Q_7 - \pi/2$.

In radio mode, both I and Q components in the output pertain to the received signal at different channels P8 and P7, respectively. The signals arrive with a phase difference if the other onboard unit is not exactly in front of the receiving antenna. Hence, this would lead to a phase imbalance in the constellation diagram. This phase imbalance can be corrected out of the data fusion. Furthermore, the information about $\Delta\varphi$ that is obtained in radar mode can be used to compensate the imbalance through the following expression.

$$\begin{bmatrix} I \\ Q \end{bmatrix} = \frac{1}{\cos(\Delta\varphi)} \times \begin{bmatrix} 1 & \sin(\Delta\varphi) \\ 0 & \cos(\Delta\varphi) \end{bmatrix} \begin{bmatrix} I_8 \\ Q_7 \end{bmatrix} \quad (5-3)$$

5.3 Prototyping and measurements

In order to prove and demonstrate the functionality of the proposed concept and scheme, the whole transceiver is prototyped at 5.8GHz ISM band and its performance is evaluated through

preliminary system level measurements. It should be noted that in the receiver circuitry, low noise amplifiers (LNAs) and bandpass filters (BPFs) are not included.

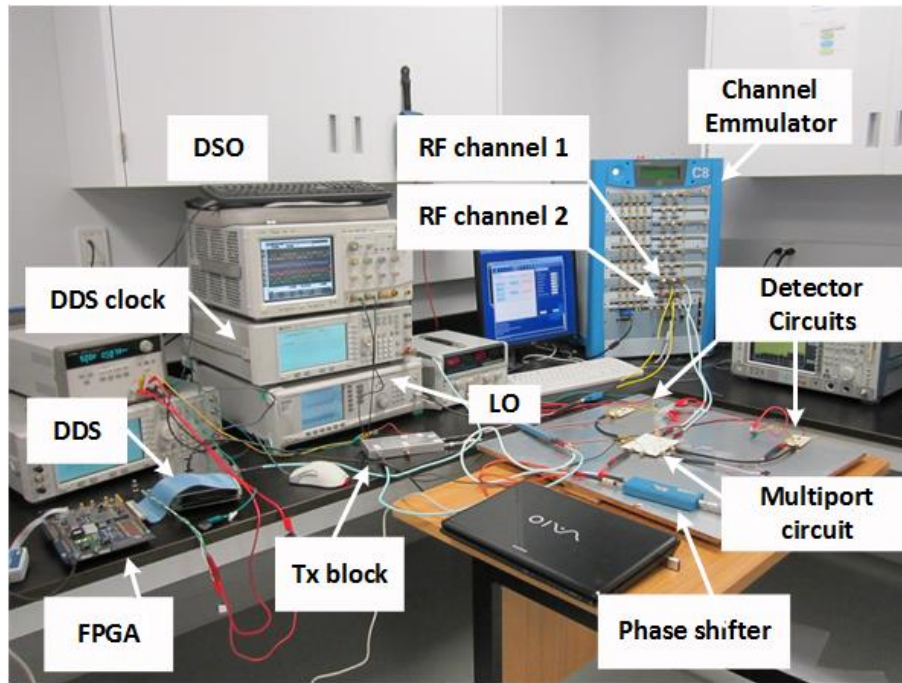


Figure 5-2: Measurement setup

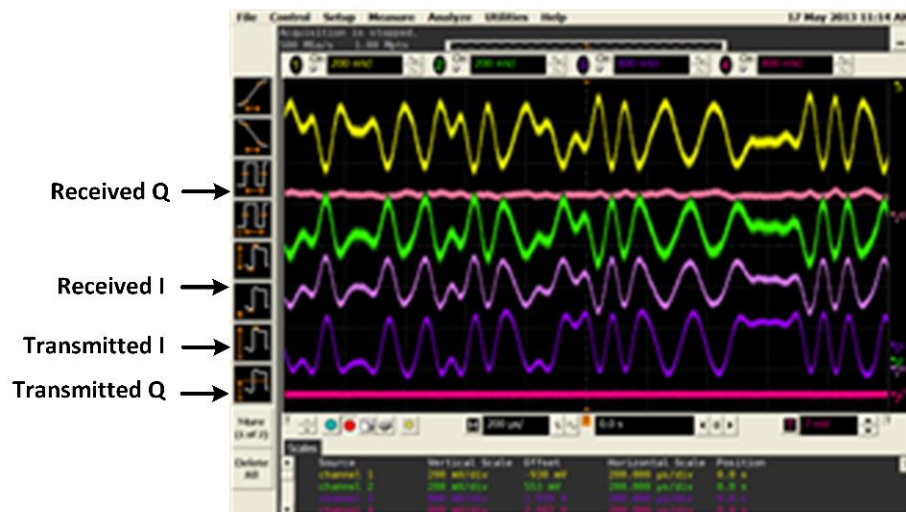


Figure 5-3: Measurement results of radio mode

Figure 5-2 shows the test bed which is set up for the purpose of evaluation. In this test bed, the transmitting signal is split into two branches and goes through a channel emulator (EB Propsim

C8) with the configuration of two AWGN channels by which an interference noise with desired signal to noise ratio (SNR) can be added. To take path loss into account, the internal attenuator can also be used. In addition, any desired time delay can be imposed. This feature of emulator is useful especially for the radar mode. The outputs of the emulator are fed into the six-port block for detection

To test the system in radio mode, a binary phase shift keying (BPSK) signal with a roll-off factor of 0.35 is used. The output power of the transmitter is 15dBm and the channel emulator is configured at 15dB SNR with -35dBm output power. The detected signals are probed by our digital oscilloscope (Agilent DSO infiniiium) which is able to implement signal addition and subtraction. Discriminated I and Q components as well as transmitted ones are demonstrated in Figure 5-3. A nearly perfect agreement between them proves the data reception capability of the receiver.

For the radar mode, the FPGA and DDS are programmed to generate TFMCW with 50MHz bandwidth. The emulator is configured at pure-Doppler channel by which the target's mobility can also be emulated, besides the propagation time delay. Thereby, the defined delay can be considered as $2R/c_o$.

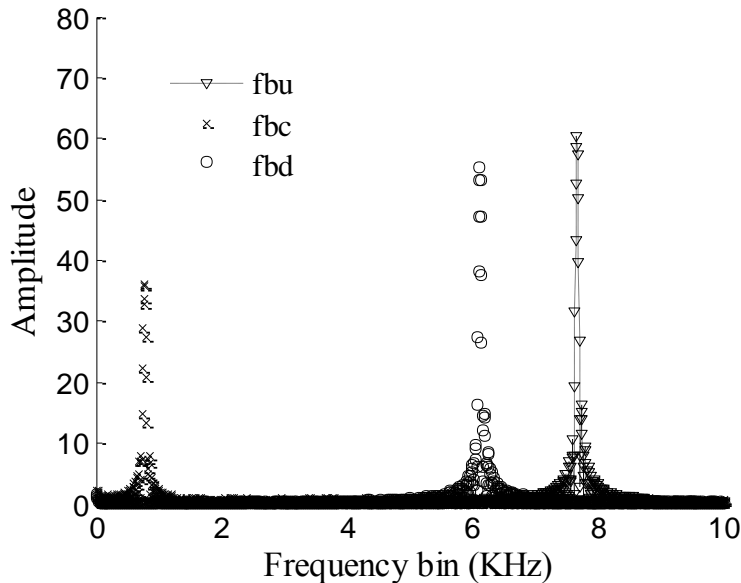


Figure 5-4: Measured beat signals in frequency domain

Table 4.1: Range and velocity measurement results

Defined delay (ns)	Defined velocity (m/s)	Measured delay (ns)	Measured velocity (m/s)
2750	20	2758.96	19.93
2750	50	2755.6	50.12
3250	30	3259.2	30

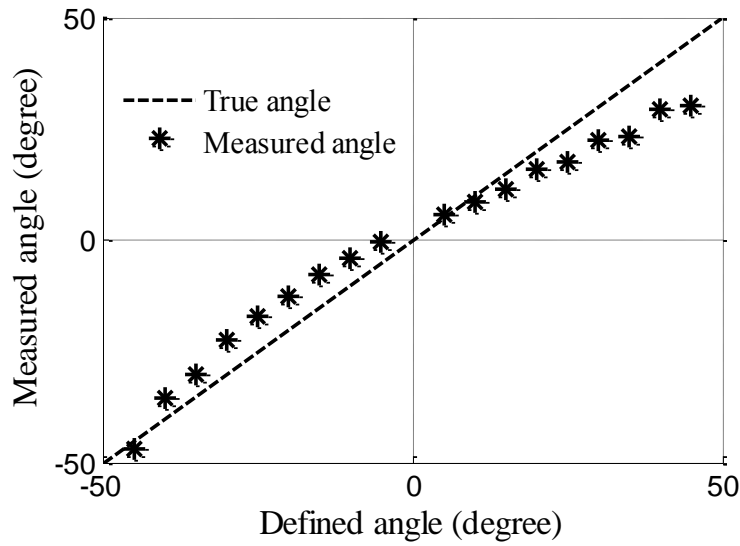


Figure 5-5: Angle measurement results

The outputs of the receiver are sampled by two onboard analog-to-digital converter (ADCs) with the sampling rate of 100MHz. Upon down sampling to 1MHz, the beat signals in each time slot are processed separately through FFT with zero padding. Figure 5-4 shows the beat frequencies of a typical defined case of $\tau = 3750ns$ and $v = 20m/s$. Additionally, the results of three other cases are listed in Table I. The measured and defined velocities are in a very good agreement, while an offset can be observed in time delay measurements. This is due to the inherent delay between the reference signal and the received signal that originates from the group delay in RF circuits. Therefore, the system should be calibrated for range measurements with regard to the average value of this offset. For angle measurements, two identical pure Doppler channels are again used. However, in order to emulate the desired AOA, the signal in one of the channels is delayed in phase with any desired value ($\Delta\phi$) that corresponds to target's angular position (θ). Figure 5-5 shows the

measured angle versus the defined angle ranging from -45° to $+45^\circ$. This is obtained by comparing the phase of constant-frequency beat signals after FFT processing. The deviation of a few degrees is observed which is almost constant for either positive or negative angles. This attributes to the undesired phase imbalance between different output ports of the multiport circuit layout. Thus, the system should be calibrated after the initial angle measurement.

5.4 Conclusion

A multifunctional transceiver architecture has been proposed and demonstrated which operates based on the fusion and integration of radar and radio systems in the time domain. The main difference of this work with previous works is the use of a multiport interferometer technique in the receiver block. The conventional topology of a six-port interferometer circuit is modified and the RF front-ends of radar and radio systems are unified in a robust manner. Therefore, an extreme size reduction is realized. In this work, the operation principles of this new scheme are analyzed and the whole system is fabricated in-house and then validated by examining its performance in an indoor test-bed.

CHAPTER 6 DEVELOPMENT OF MILLIMETER WAVE COMPONENTS

Our proposed multiport-based multifunction transceiver which was introduced in chapter 5 encompasses a 180° hybrid coupler as a key part that discriminates this new topology from the conventional that of the six-port passive junction. It was used to realize the essential phase difference within the phasing network of the proposed passive junction. One can observe in Figure 5-1 that the configuration of input-output ports in rat-race coupler does not allow for laying out the connection traces in the multiport network without interception. Therefore, a jumper was used in the prototype at 5.8 GHz which was shown in Figure 5-2. However, this solution would fail if the proposed multiport receiver is to be implemented in very high frequencies. The interesting features of the multiport technology such as large bandwidth, low LO power requirement or simplicity make it very suitable for applications around millimeter-wave frequency bands. We have also developed the proposed concept in chapter 5 and implemented the multiport based transceiver for operation around 77 GHz which is demonstrated in chapter 7. Therefore, two essential millimeter-wave components including 180° hybrid coupler and a balun have been developed throughout this PhD research. Our structure-based balun is frequency independent thanks to field rotation that takes part within the proposed hybrid structure. On the other hand, the proposed 180° hybrid coupler is a simple topology with non-interspersed input and outputs, as oppose to that of conventional rat-race. Such hybrid coupler topologies with inputs located on one side and outputs at the opposite side simplify the design of signal routings when integrated with other circuits and components. It also relaxes the necessity of using auxiliary compensating components such as tapers, jumpers and cross-overs. The corresponding results of these two innovative component developments are already reported in [106] and [107], which are presented in this chapter, as well.

6.1 Hybrid structure based broadband field rotation balun for millimeter-wave applications

Balun transformers have found wide applications as a critical part in the design of many microwave circuits such as balanced mixers, antenna feeding circuits, push-pull amplifiers and other building blocks of wireless communication systems [108, 109]. Furthermore, a proper design

of balun with a simple way of transferring the signal from an unbalanced line into two balanced transmission lines is essential in order to guarantee the desired performance of these microwave circuits. As a challenging research topic in the past few decades, several types of baluns have been reported based on microstrip transmission lines in connection with satisfactory performance or design specification-related parameters including low insertion loss, high return loss, good amplitude balance and 180° phase difference between the balanced ports [110-112].

However, at very high frequency bands, for example, V or E bands, obtaining acceptable parameters over a broad band is a challenge task and in some cases not even feasible with some conventional planar balun topologies. The well-known Marchand balun [113] may fail to operate favorably at such high frequencies since the tight edge coupling may not be easily realized through simple printed circuit board (PCB) process at those higher frequencies. Improved versions of Marchand baluns were also reported for mixer applications at millimeter-wave frequencies using MMIC process [114].

Also, non-planar baluns may not be an appropriate solution because their use may also raise some difficulties in integrating with other surface mount components. In [115], a combination of substrate-integrated-waveguide (SIW) and microstrip transmission line was used to develop a wideband balun operating at around 24 GHz. Using an SIW 3-dB power divider and a double-sided PCB process, the signal is divided into two branches and transferred into microstrip lines at the far end of each line in different manners. The principal background concept in the balun proposed by [115] is to consider the opposite broad walls of SIW lines for transition to ground plane of the following microstrip lines and then to share a common ground with the other line through a transition which consists of a co-planar waveguide (CPW) and a metallized via hole. However, realizing the same concept at higher frequencies, i.e. E-band, may not be feasible because of a much smaller wavelength of higher frequency signals and inevitable fabrication limits through PCB process.

We have proposed an SIW-based balun for E-band applications. The key part of our proposed balun is the phase inverter which is realized through field rotation using antipodal fin-lines. Fin-lines with different schemes have been applied as antennas [116] and some other microwave components such as waveguide-to-microstrip transition [117]. Furthermore, antipodal fin-line antennas might be fed by a parallel strip line or SIW with the vertical polarization of E-fields within

the transmission line but transmit it in the horizontal polarization by its gradual rotation. This feature is used in a small section of SIW line in that the signal rotates 180° , regardless of its phase change along transmission line. In order to compensate the effect of difference in propagation constant between SIW and fin-line, an almost identical section is applied in the other balanced branch, but somehow the polarization remains the same at both ends. Indeed, the field is rotated by 90° in one direction and then gets rotated back in the opposite direction. Therefore, the signals at two outputs must be out-of-phase.

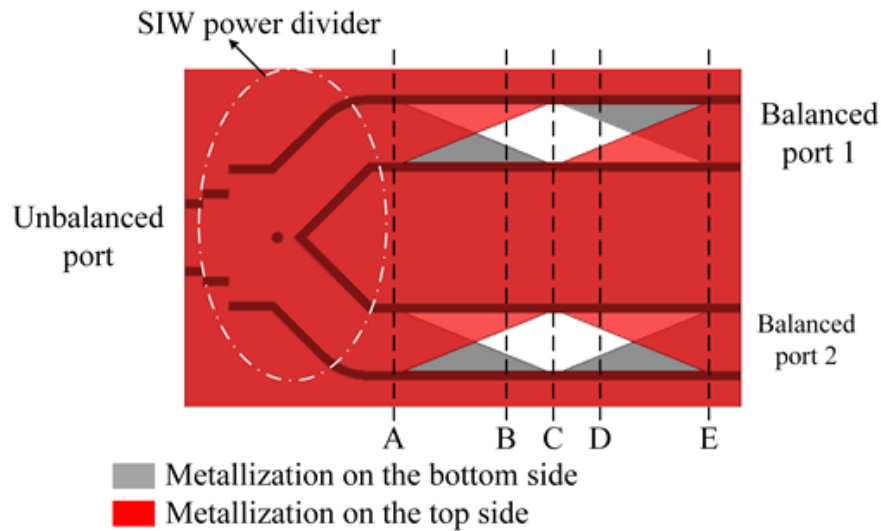
This concept is first evaluated using a commercial software package of high frequency structure simulator (HFSS) and then validated through prototyping and measurements.

6.1.1 Concept and structure of the balun

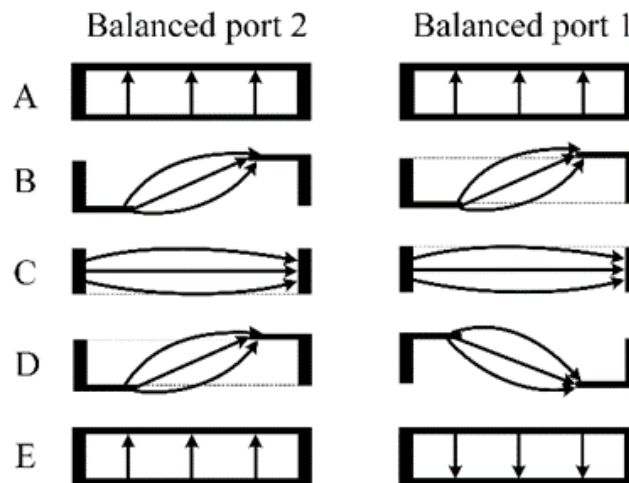
Figure 6-1(a) shows the structure of the proposed balun. One can observe that it consists of an SIW three port power divider [117] that splits the signal at the unbalanced port into two output branches. The signal at each branch is then transferred to planar antipodal fin-line that rotates the E-field smoothly from vertical into horizontal polarization so that the E-field leaves the fin-line tips with 90° rotation with respect to its initial polarization at its input. In order to bring the detached field back into the waveguide, another fin-line section is required that may gradually transform the polarization from horizontal into vertical. However, this should not be done at the same manner in two branches should an 180° phase difference be desired. In fact, the first fin-line section in one branch is mirrored twice; one with respect to the axial plane which is parallel to the narrow wall of the waveguide, and the other with respect to the one perpendicular to the narrow wall of the waveguide. On the other hand, the second fin-line section in the second branch is mirrored only once, i.e. with respect to the plane perpendicular to the narrow wall of the waveguide.

The manipulation of the E-field through this topology in two different branches is depicted in Figure 6-1(b). At the end of the SIW power divider, the E-field arrives with the same phase and rotates gradually along the fin-line section within identical directions in both branches. At the fin-line tips, the field becomes detached when its polarization is shifted by 90° as it is shown in plane C. The field then re-enters the following fin-line section as shown in plane D. The opposite metallization in two branches yields a reverse polarization of the E-field when it arrives at the balanced ports. It should be mentioned that the phase change along the length of fin-line section

remains the same as the propagation constant is identical in both branches. Also, the smooth tapered fin-line with a length of one wavelength at the center frequency provides appropriate matching and reduces radiation loss. Continuation of the SIW metallic walls along the fin-line section also prevents current leakage out of the line.



(a) Topology of the Balun



(a) Changes in E-field polarization along the waveguide

Figure 6-1: Proposed balun structure; it consists of an SIW power divider and fin-line sections which invert the phase polarization

6.1.2 Prototyping and measurements

The proposed SIW balun is simulated via commercial simulation package of HFSS and prototyped on RO6002 with permittivity of 2.94 through our PCB process. The balun is optimized for functionality at E-band, i.e. 70 GHz to 90 GHz.

Figure 6-2 shows the photo of the fabricated balun along with its critical dimensions. The balanced ports in the fabricated prototype are placed at the opposite sides in order to make measurements easier.

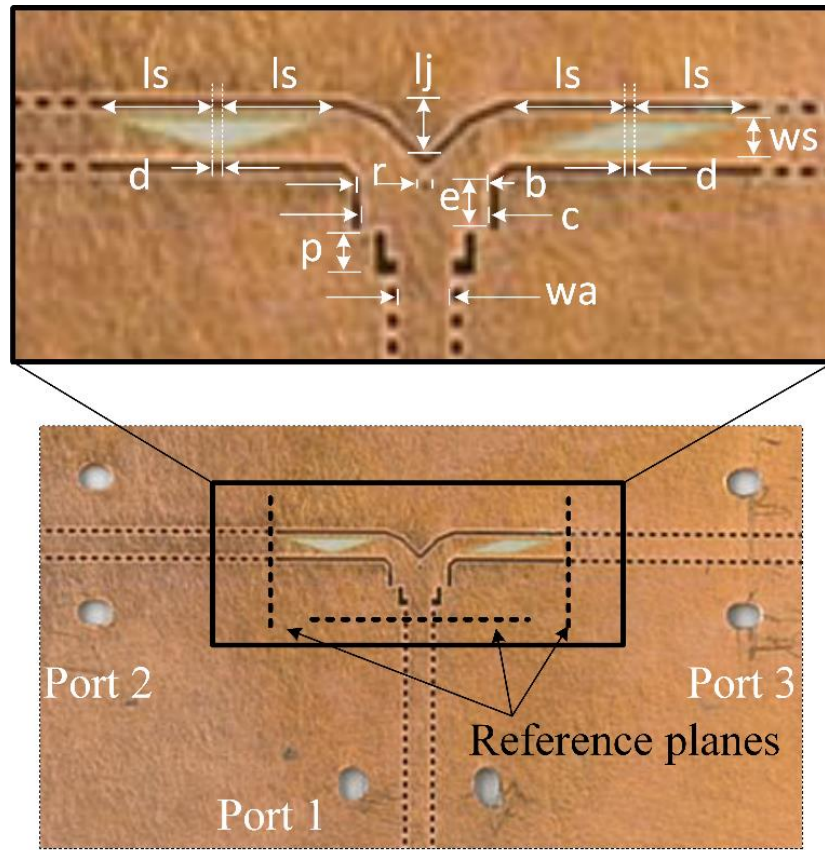
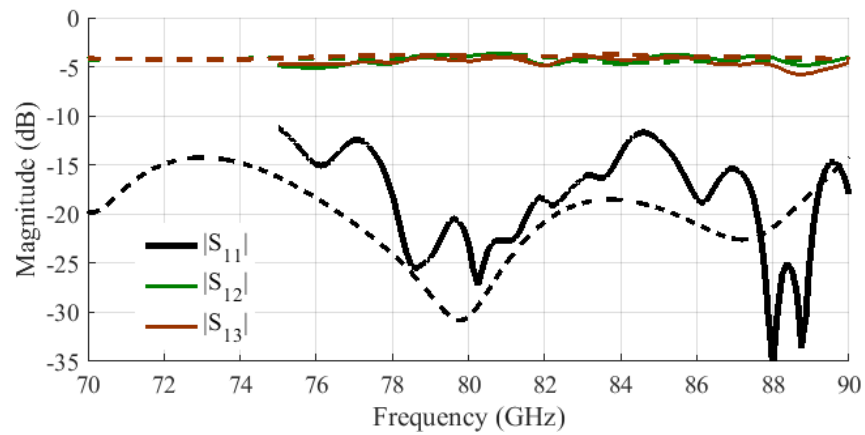
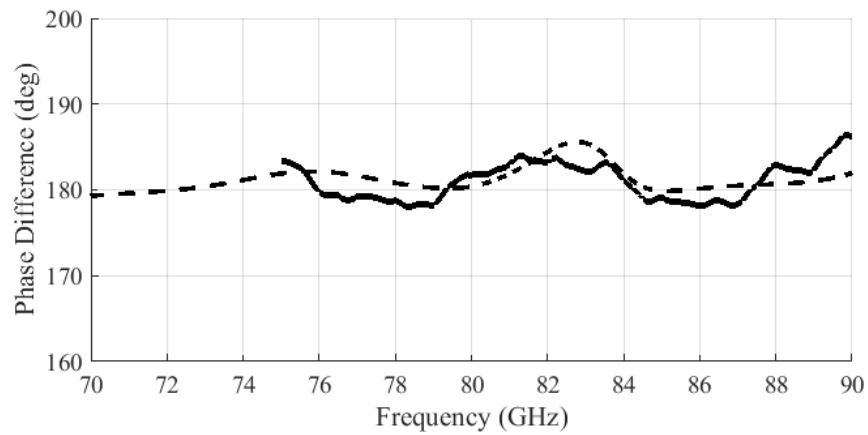


Figure 6-2: Prototype of the proposed balun; $w_a=1.511\text{mm}$, $p=1.267\text{mm}$, $c=3.674\text{mm}$, $e=1.491\text{mm}$, $l_s=2.972\text{mm}$, $d=0.545\text{mm}$, $l_j=1.622\text{mm}$, $w_s=1.003\text{mm}$, $r=0.152\text{mm}$

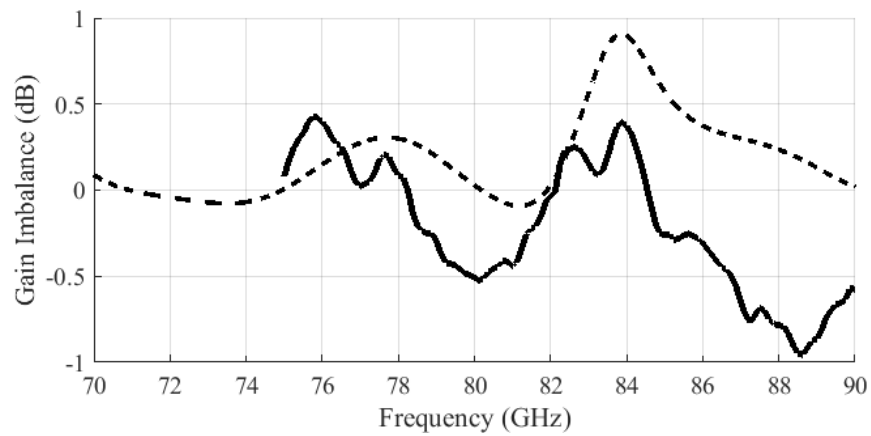
Scattering parameters of the prototyped balun are measured using SIW-to-WR10 waveguide transition and Agilent PNA-X vector network analyzer (VNA). Since three-ports measurements were not feasible, one port was match-loaded when measuring the two other ports. The measurement and simulation results are described in Figure 6-3.



(a) S-parameters



(b) Phase difference between two balanced ports



(c) Gain imbalance

Figure 6-3: Measurement and simulation results of scattering parameters; measurements (solid line) and simulations (dashed line)

The simulation result is shown in a wider range of frequency, i.e. 70 GHz to 90 GHz, while the measurement could only be made from 75 GHz up to 90 GHz with WR10 waveguides. In order to avoid the effect of transitions on the return loss and also to compensate the insertion loss of the additional SIW line from VNA ports to input ports of the balun, TRL calibration technique is applied. As such, the reference planes are defined as depicted in Figure 6-2. Within the band where measurement is made, a good agreement between simulation and measurement results is observed, implying the reliability of the simulation results in the rest of band. A slight shift in return loss could be expected as the permittivity of 2.94 from substrate datasheet is considered during design and optimization which should be slightly different at higher frequencies. In addition, both measured and simulated phase differences of 180° in a broad bandwidth prove the functionality of the proposed concept of field rotation. The gain imbalance between the balanced ports which is defined to be $||S_{21}| - |S_{31}||$ is demonstrated in Figure 6-3(c).

6.2 Wideband planar 180° hybrid coupler with non-interspersed ports

The 4-port Rat-Race (or ring hybrid which is a form of 180° coupler) and 180° hybrid couplers provide the sum and difference operations of two input signals at two isolated ports. In other words, they create 180° relative phase difference between the signals at the output ports for a signal arriving at one input port and zero-degree relative phase difference for a signal arriving at the other input port. This relative phase difference between the output signals is 90° for the 90° hybrid coupler. But, with the 180° hybrid coupler, if two distinct signals are incident at two input ports, two equally divided portions of each input signal appear at the two output ports. One pair of output signals, each including two portions from the two input signals, is out of phase while the two other output signals are in phase. The principle and the S-matrix of the conventional 180° hybrid coupler (rat-race) are described in [61]. This hybrid coupler with its specific phasing network between all ports has found application in many types of RF and microwave integrated circuits such as balanced mixers [118], multiport interferometers [104], and in-phase/quadrature mixers [119].

The 180° hybrid couplers have been investigated for different aspects including bandwidth enhancement using coupled lines [120], broadband phase inverter [121-126], size reduction using shunt open stubs [127, 128], spurious suppression [129] and arbitrary power division [130, 131].

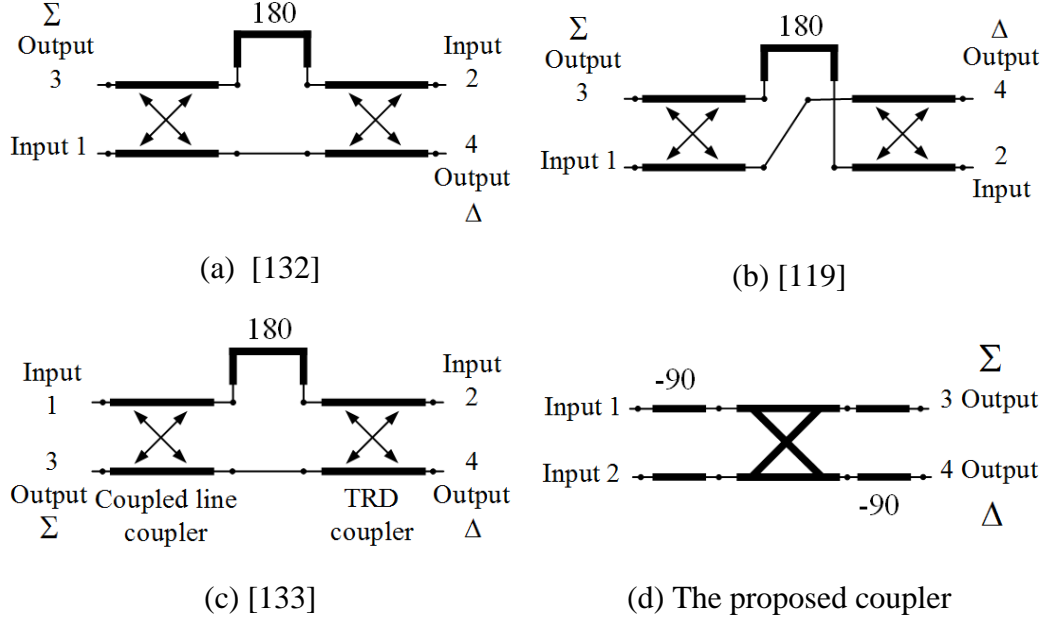


Figure 6-4: The 180° hybrid coupler topologies

A different 180° hybrid coupler was introduced by [134] in which non-interspersed ports were obtained by two section hybrids using cascaded hybrid rings. Another configuration of a pair of cascaded microstrip coupled line couplers and one 180° phase shifter was reported by [132] that was realized with broadside microstrip coupled line couplers. This topology that still suffers from the location of input output ports is shown in Figure 6-4(a) for reference. Based on this topology, multilayer hybrid couplers were developed and implemented using the multilayer low-temperature co-fired ceramic (LTCC) technology [119]. Within multilayer implementation of the topology in Figure 6-4(a), a pair of input and output were implemented in one layer and the other pair in the other layer. To position the pair of input in one layer and the pair of outputs in another layer, the interconnections between three sections were rewired in an improved topology as it is shown in Figure 6-4(b). However, this solution becomes ineffective should the coupler be used in single layer circuits.

A near-TEM Lange hybrid was also reported in [135]. However, the use of vias for interlayer connection or bond-wires limits the frequency of operation and increases the gain and phase imbalances due to the parasitic inductance in vias. Another topology comprising of a weak-coupling parallel coupled line and a strong-coupling trans-directional (TRD) coupler connected with 180° phase shifter was proposed by [133]. This topology is depicted in Figure 6-4(c). The use of periodic shunt capacitor components in TRD relaxes the necessity of tightly coupled lines and allows for the use of single layer printed circuit board (PCB) technique without any vias or bond wires. However, the capacitors may fail to operate at very high frequencies and also increase the cost.

In this section, an alternative topology of rat-race with non-interspersed ports is proposed, which is briefly sketched in Figure 6-4(d). The proposed topology does not require any vias, bond-wires or lumped components and can be implemented in a single layer of substrate. The principles of this topology are discussed along with analytical solutions in the next sections. This coupler is also implemented in this work using our in-house technology of Miniaturized Hybrid Microwave Integrated Circuit (MHMIC) to demonstrate its performances around 77 GHz. The prototyped 180° hybrid coupler is assessed through on-wafer measurements whose results are presented, at the end.

6.2.1 Proposed Topology of the 180° hybrid coupler

The proposed topology of 180° hybrid coupler is comprised of one quadrature coupler and two 90° phase-shifters. With this configuration, two input ports can be located on one side and outputs on the other side. As opposed to the previously reported structures, which were mainly based on backward-coupled line couplers the quadrature coupler in the proposed topology is a forward coupler. This configuration can be implemented with both TEM- or quasi-TEM mode structures such as microstrip and non-TEM structures such as substrate integrated waveguide (SIW). In this work, TEM-mode based structures are developed and demonstrated for the proposed 180° coupler topology.

Figure 6-5 shows a TEM-mode based topology of the 180° hybrid coupler which consists of wideband Schiffman phase shifters [136] and a quadrature branch coupler [61]. The phase difference within the Schiffman phase shifter can be set to a desired value over a wide bandwidth by appropriate selection of the length of lines and coupling coefficients [136, 137]. The original

configuration of the Schiffman phase shifter requires tightly coupled lines that are difficult to implement. Several improved topologies of this differential phase shifter have been put forward that can be used to design this phase shifter with loosely-coupled lines [138, 139] or for wider bandwidth [140-143].

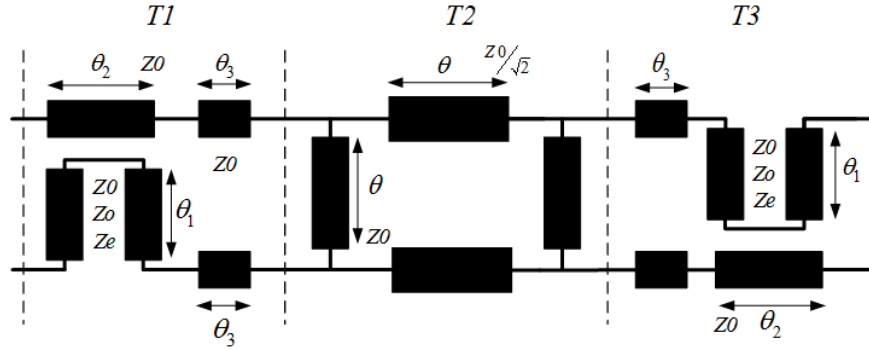


Figure 6-5: Implemented proposed topology in TEM structures

6.2.2 Theoretical analysis

To theoretically analyze the proposed 180° hybrid coupler, a transfer T -matrix is derived that relates the output port power wave variables to the input port power wave variables of a network [144]. It should be highlighted that the standard definition of multiport T -matrix from [145] is used throughout the whole discussion in this paper. Figure 6-6 shows the standard four-port network along with port numbers that agrees with the general standard N -port network from [145]. Symbols a_i and b_i denote the incoming and outgoing power wave variables at the i^{th} port.

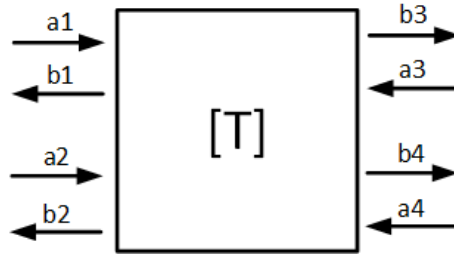


Figure 6-6: Four port network and T matrix

The standard T matrix of the four-port network in Fig. 3 is defined in accordance with equation (8) in [145] as:

$$\begin{bmatrix} b_1 \\ b_2 \\ a_1 \\ a_2 \end{bmatrix} = \begin{bmatrix} T_{11} & T_{12} & T_{13} & T_{14} \\ T_{21} & T_{22} & T_{23} & T_{24} \\ T_{31} & T_{32} & T_{33} & T_{34} \\ T_{41} & T_{42} & T_{43} & T_{44} \end{bmatrix} \begin{bmatrix} a_3 \\ a_4 \\ b_3 \\ b_4 \end{bmatrix} \quad (6-1)$$

The reference port impedances in our analysis are considered to be identical. In view of the above, the structure shown in Figure 6-5 is first divided into three distinct segments, namely two Schiffman phase shifters and one branch quadrature coupler, to derive the overall T -parameters from a multiplication of three matrices, i.e., $T_1 \times T_2 \times T_3$. The T -matrix of each part can be derived as it is explained next.

6.2.2.1 T-matrix of branch quadrature hybrid coupler (T2)

To obtain the matrix T_2 , the whole branch-line quadrature hybrid can be subdivided into three T-matrices T_{21} , T_{22} , and T_{23} . T_{21} and T_{23} are identical and denote the T-matrix of one branch of a branch line directional coupler with characteristic impedance of Z_0 and electrical length of θ . T_{22} is the T-matrix of a pair of transmission lines with characteristic impedance of $Z_0/\sqrt{2}$ and identical electrical lengths of θ .

The T-matrix of the branch line with electrical length of θ and impedance of Z_0 is

$$T_{21} = T_{23} = \begin{bmatrix} 1-Q & P & -Q & P \\ P & 1-Q & P & -Q \\ Q & -P & 1+Q & -P \\ -P & Q & -P & 1+Q \end{bmatrix} \quad (6-2)$$

where $Q = j0.5\cot(-\theta)$ and $P = j0.5/\sin(-\theta)$ [144]. The matrix T_{22} when the reference impedance is Z_0 can be expressed as in

$$T_{22} = \begin{bmatrix} B_{11} & 0 & B_{12} & 0 \\ 0 & B_{11} & 0 & B_{12} \\ B_{21} & 0 & B_{22} & 0 \\ 0 & B_{21} & 0 & B_{22} \end{bmatrix} \quad (6-3)$$

where $B_{11} = \cos(\theta) - j3\sin(\theta)/2\sqrt{2}$, $B_{12} = -j\sin(\theta)/2\sqrt{2}$, $B_{21} = j\sin(\theta)/2\sqrt{2}$, and $B_{22} = \cos(\theta) + j3\sin(\theta)/2\sqrt{2}$.

The matrix $T2$ can then be obtained through multiplying the submatrices (i.e., $T21 \times T22 \times T21$) and expressed as

$$T2 = \begin{bmatrix} Th_{11} & Th_{12} & Th_{13} & Th_{14} \\ Th_{12} & Th_{11} & Th_{14} & Th_{13} \\ -Th_{13} & -Th_{14} & Th_{33} & Th_{34} \\ -Th_{14} & -Th_{13} & Th_{34} & Th_{33} \end{bmatrix} \quad (6-4)$$

$$\begin{aligned} Th_{11} &= \cos(\theta)(1 - j \cot(-\theta)) + \\ &\quad \frac{\sin(\theta)(\sin^2(-\theta)(0.5 j \cot^2(-\theta) - \cot(-\theta) - 1.5 j) + 0.5 j)}{\sqrt{2} \sin^2(-\theta)} \\ Th_{12} &= \frac{\sin(\theta)(1 - j \cot(-\theta)) + j \cos(\theta)\sqrt{2}}{\sqrt{2} \sin(-\theta)} \\ Th_{13} &= -j \cot(-\theta) \cos(\theta) + \frac{\sin(\theta)(\sin^2(-\theta)(0.5 j \cot^2(-\theta) - 0.5 j) + 0.5 j)}{\sqrt{2} \sin^2(-\theta)} \\ Th_{14} &= \frac{-j \cot(-\theta) \sin(\theta) + j \cos(\theta)\sqrt{2}}{\sqrt{2} \sin(-\theta)} \\ Th_{33} &= \cos(\theta)(1 + j \cot(-\theta)) + \\ &\quad \frac{\sin(\theta)(\sin^2(-\theta)(-0.5 j \cot^2(-\theta) - \cot(-\theta) + 1.5 j) - 0.5 j)}{\sqrt{2} \sin^2(-\theta)} \\ Th_{34} &= \frac{\sin(\theta)(1 + j \cot(-\theta)) - j \cos(\theta)\sqrt{2}}{\sqrt{2} \sin(-\theta)} \end{aligned} \quad (6-5)$$

The derived T -matrix of the branch line hybrid is validated through comparison with simulations in ADS which is demonstrated in Figure 6-7.

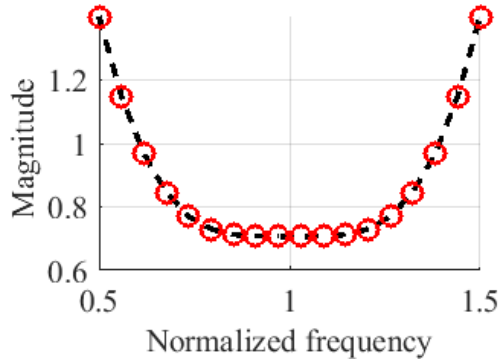
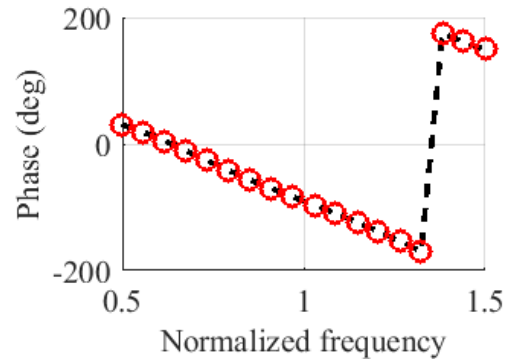
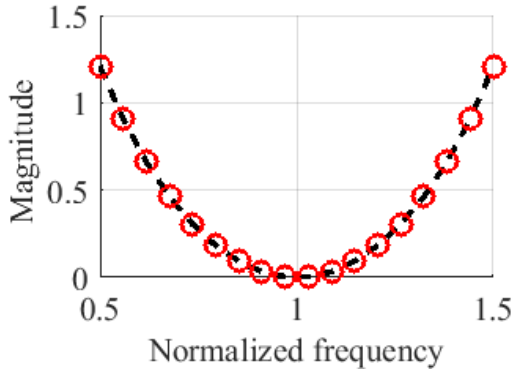
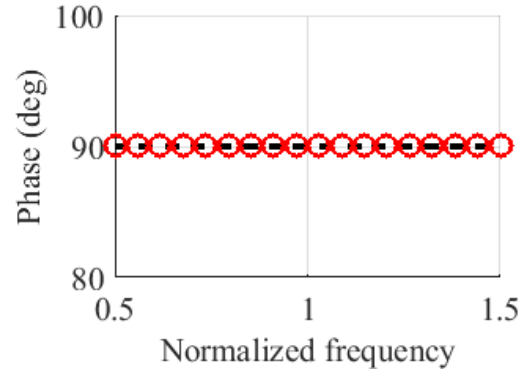
(a) Th_{11} (b) Th_{11} (c) Th_{13} (d) Th_{13}

Figure 6-7: Comparison of some of the derived theoretical T parameters with the simulated ones from ADS; --: simulation, -o-: analytical calculations from (6-5).

6.2.2.2 T -matrix of Schiffman phase shifter

The T -matrix of the Schiffman phase shifter can be obtained by converting the ABCD parameters of coupled-line with connected end-ports that were reported by [146] into T -parameters using the equations from [147]. The T -matrix of the phase shifter, cascaded with a transmission line with electrical length of θ_3 can be expressed as in (6-6) where Z_e and Z_o denote the even and odd mode impedances of the coupled-line in the phase shifter part and Z_0 is the characteristic impedance of the transmission line.

$$T1 = \begin{bmatrix} T1sh_{11} & 0 & 0 & 0 \\ 0 & T1sh_{22} & 0 & T1sh_{24} \\ 0 & 0 & T1sh_{33} & 0 \\ 0 & T1sh_{42} & 0 & T1sh_{44} \end{bmatrix} \quad (6-6)$$

$$\begin{aligned} T1sh_{11} &= (\cos(\theta_3) - j \sin(\theta_3))(\cos(\theta_2) - j \sin(\theta_2)) \\ T1sh_{22} &= \frac{(\cos(\theta_3) - j \sin(\theta_3))(Z_0 Z_e \cot(\theta_c) - j(Z_0^2 + Z_e Z_o - jZ_0 Z_o \tan(\theta_c)))}{Z_0(Z_e \cot(\theta_1) + Z_o \tan(\theta_c))} \\ T1sh_{24} &= \frac{(Z_0^2 - Z_e Z_o)(-j \cos(\theta_3) + \sin(\theta_3))}{Z_0(Z_e \cot(\theta_1) + Z_o \tan(\theta_1))} \\ T1sh_{33} &= (\cos(\theta_3) + j \sin(\theta_3))(\cos(\theta_2) + j \sin(\theta_2)) \\ T1sh_{42} &= \frac{(Z_0^2 - Z_e Z_o)(j \cos(\theta_3) + \sin(\theta_3))}{Z_0(Z_e \cot(\theta_c) + Z_o \tan(\theta_1))} \\ T1sh_{44} &= \frac{(\cos(\theta_3) + j \sin(\theta_3))(Z_0 Z_e \cot(\theta_1) + j(Z_0^2 + Z_e Z_o + jZ_0 Z_o \tan(\theta_1)))}{Z_0(Z_e \cot(\theta_1) + Z_o \tan(\theta_1))} \end{aligned}$$

where T matrix elements of the line with length of θ_i ($i = 2, 3$) and impedance of Z0 is considered to be

$$\begin{aligned} TL_{11} &= \cos(\theta_i) - j \sin(\theta_i); \quad TL_{12} = 0 \\ TL_{22} &= \cos(\theta_i) + j \sin(\theta_i); \quad TL_{21} = 0 \end{aligned} \quad (6-7)$$

The derived analytical T parameters are compared with the simulated ones in ADS and demonstrated in Figure 6-8 for validation.

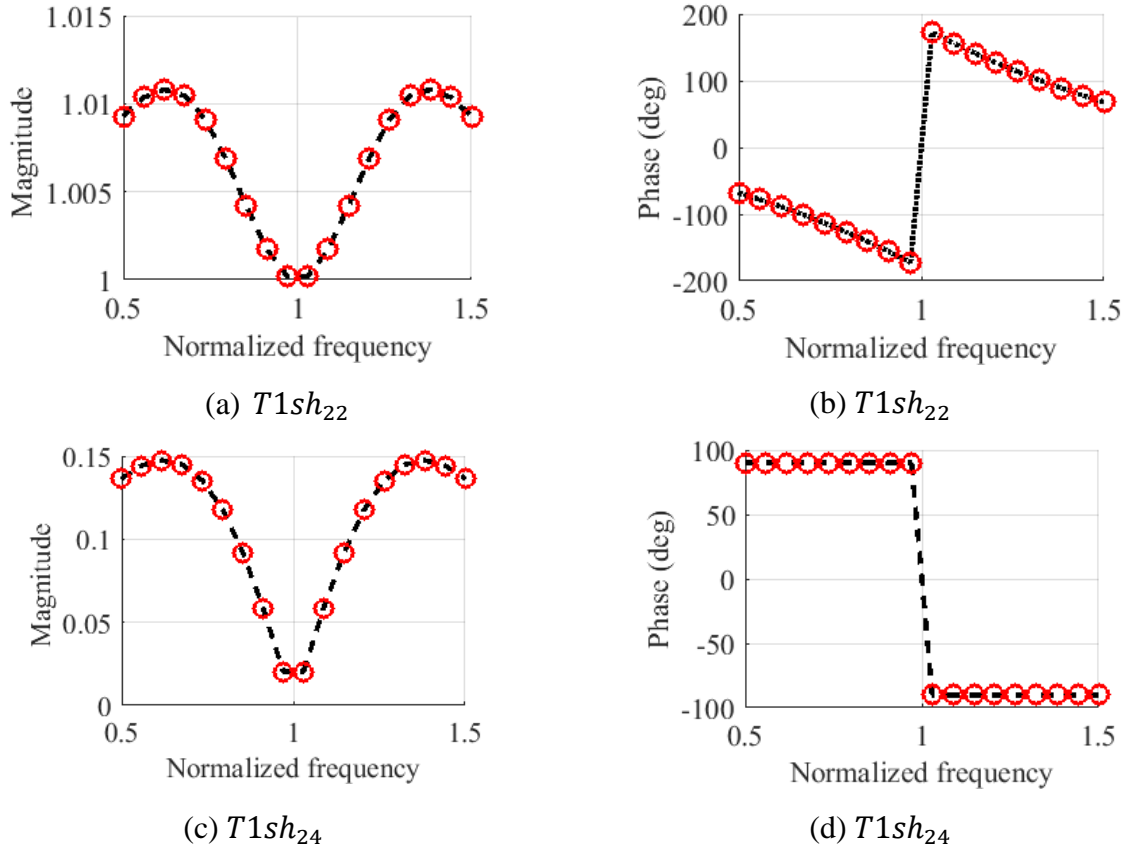


Figure 6-8: Comparison of the derived analytical T parameters of the Schiffman phase shifter with the simulated ones from ADS; --: simulation, -o-: analytical calculations.

6.2.2.3 T-matrix of the Schiffman phase shifter (T3)

The matrix $T3$ pertains to another phase shifter which is connected at the input port to the branch-line hybrid coupler via a transmission line with length of θ_3 . The matrix $T3$ can be expressed as

$$T_3 = \begin{bmatrix} T2sh_{11} & 0 & T2sh_{13} & 0 \\ 0 & T2sh_{22} & 0 & 0 \\ T2sh_{31} & 0 & T2sh_{33} & 0 \\ 0 & 0 & 0 & T2sh_{44} \end{bmatrix} \quad (6-8)$$

$$\begin{aligned}
T_{2sh_{11}} &= \frac{(\cos(\theta_3) - j \sin(\theta_3))(Z_0 Z_e \cot(\theta_1) - j(Z_0^2 + Z_e Z_o - j Z_0 Z_o \tan(\theta_1)))}{Z_0 (Z_e \cot(\theta_1) + Z_o \tan(\theta_1))} \\
T_{2sh_{22}} &= (\cos(\theta_3) - j \sin(\theta_3))(\cos(\theta_2) - j \sin(\theta_2)) \\
T_{2sh_{13}} &= -\frac{j(Z_0^2 - Z_e Z_o)(\cos(\theta_3) - j \sin(\theta_3))}{Z_0 (Z_e \cot(\theta_1) + Z_o \tan(\theta_1))} \\
T_{2sh_{31}} &= \frac{j(Z_0^2 - Z_e Z_o)(\cos(\theta_3) + j \sin(\theta_3))}{Z_0 (Z_e \cot(\theta_1) + Z_o \tan(\theta_1))} \\
T_{2sh_{33}} &= \frac{(\cos(\theta_3) + j \sin(\theta_3))(Z_0 Z_e \cot(\theta_1) + j(Z_0^2 + Z_e Z_o + j Z_0 Z_o \tan(\theta_1)))}{Z_0 (Z_e \cot(\theta_1) + Z_o \tan(\theta_1))} \\
T_{2sh_{44}} &= (\cos(\theta_3) + j \sin(\theta_3))(\cos(\theta_2) + j \sin(\theta_2))
\end{aligned}$$

Finally, the overall T matrix of the proposed 180° hybrid coupler can be formulated by multiplying three matrices via arithmetic tools such as Mathematica. Due to complexity of the resulting equations, they are not brought in here. However, the derived T matrix would be helpful for computer aided design (CAD) when the conditions of 90° phase shifters and branch-line couplers are applied.

The phase difference between signals at the output ports of the Schiffman phase shifter was formulated in [136], which reads as

$$\Delta \varphi = K \theta_1 - \cos^{-1} \left(\frac{R - \tan(\theta_1)^2}{R + \tan(\theta_1)^2} \right) \quad (6-9)$$

where $K = \theta_2/\theta_1$ and $R = Z_e/Z_o$. For 90° phase shifter, θ_1 and K are selected to be $\pi/2$ at the center frequency and 3, respectively. At the center frequency where θ and θ_1 are $\pi/2$ and θ_2 is $3\pi/2$ the T matrix of the 180° hybrid coupler would be

$$T = \frac{1}{\sqrt{2}} \begin{bmatrix} -e^{-2j\theta_3} & e^{-2j\theta_3} & 0 & 0 \\ -e^{-2j\theta_3} & -e^{-2j\theta_3} & 0 & 0 \\ 0 & 0 & -e^{2j\theta_3} & e^{2j\theta_3} \\ 0 & 0 & -e^{2j\theta_3} & -e^{2j\theta_3} \end{bmatrix}. \quad (6-10)$$

Substituting the T matrix elements into the T -to- S parameter conversion equations in [145], one can conclude

$$[S] = \frac{-e^{-2j\theta_3}}{\sqrt{2}} \begin{bmatrix} 0 & 0 & 1 & -1 \\ 0 & 0 & 1 & 1 \\ 1 & 1 & 0 & 0 \\ -1 & 1 & 0 & 0 \end{bmatrix} \quad (6-11)$$

which confirms the hybrid is matched at input ports 1 and 2. Moreover, (7) shows that at output port 4 there is 180° phase difference between the input signals from ports 1 and 2, whereas this phase difference is zero at output port 3. The S -matrix in (7) is almost the same as that of the classic ring hybrid. The only difference is that the signals at the output ports are either in-phase or out-of-phase with respect to the input signals, whereas the output signals in the classic ring hybrid are in quadrature phase with the input signal [61].

The derived T matrix can be converted to S matrix via arithmetic tool of Mathematica. At frequencies other than the center frequency, the condition of $\theta_1 = \theta$ and $\theta_2 = 3\theta$ remains valid. In addition, the coupled line is matched when $Z_0 = \sqrt{Z_o Z_e}$ [136]. Under these conditions the phase difference at output ports 3 and 4 can be formulated from the S -matrix of the proposed hybrid as in the following:

$$\begin{aligned} \Delta &= \angle S_{13} - \angle S_{14} \\ \angle S_{13} &= \angle \left[\frac{(-0.54582 + j1.31773 \cot(\theta)) Csc(\theta)^2}{(\Phi_1 + \Phi_2 + \Phi_3)(\cos(3\theta) + j \sin(3\theta))^2} \right] \\ \Phi_1 &= 0.614047 + j2.52241 \cot(\theta)^3 + \cot(\theta)^4 - 0.136455 Csc^2 \\ \Phi_2 &= 0.0682275 Csc(\theta)^4 + \cot(\theta)^2 (-3.15786 - 1.06823 Csc(\theta)^2) \\ \Phi_3 &= \cot(\theta) (-j1.97659 - j0.658863 Csc(\theta)^2) \end{aligned} \quad (6-12)$$

$$\angle S_{14} = \angle \left[\frac{jZ_0 (Z_o + Z_e \cot(\theta)^2) Csc(\theta) (\Psi_1)}{(\Psi_2) (\Psi_3 + \Psi_4 + \Psi_5) (\cos(3\theta) + j \sin(3\theta))} \right]$$

$$\Psi_1 = -0.783612 + j1.2612 \cot(\theta) + \cot(\theta)^2 + 0.261204 Csc(\theta)^2$$

$$\Psi_2 = -Z_o Z_0 + j2Z_e Z_o \cot(\theta) + Z_e Z_0 \cot(\theta)^2$$

$$\Psi_3 = 0.614047 + j2.52241 \cot(\theta)^3 + \cot(\theta)^4 - 0.136455 Csc(\theta)^2$$

$$\Psi_4 = 0.0682275 Csc(\theta)^4 + \cot(\theta)^2 (-3.15786 - 1.06823 Csc(\theta)^2)$$

$$\Psi_5 = \cot(\theta) (-j1.97659 - j0.658863 Csc(\theta)^2)$$

It can be observed in (6-12) that the bandwidth of the 180° phase difference depends on the ratio of even to odd mode impedances, i.e., $R = Z_e/Z_o$.

In Figure 6-9, simulation results of the proposed hybrid with ideal components through the commercial package of ADS is compared with the analytical equations concluded in (6-12). The excellent agreement between simulation and analytical results for two different values of R validates the theoretical analysis throughout this section.

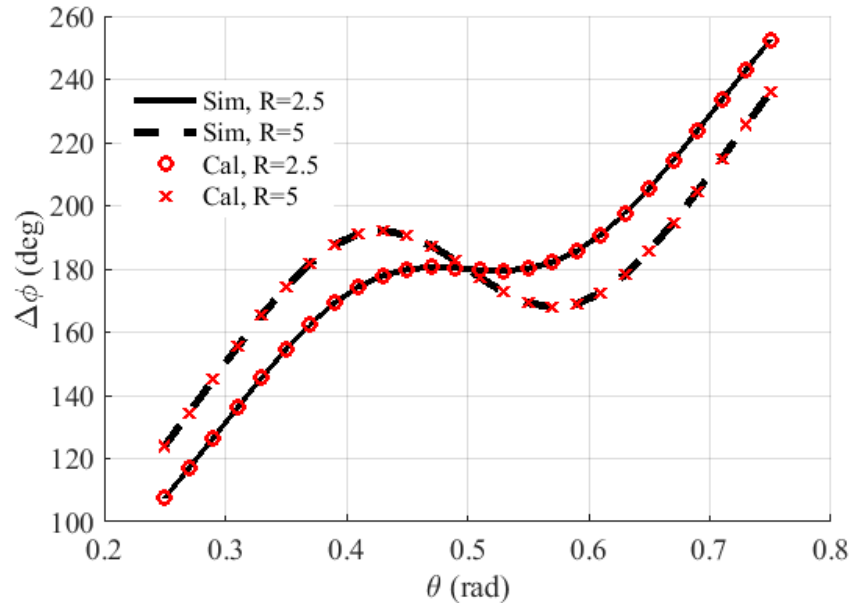


Figure 6-9: Comparison of the simulation results of phase differences with the ones from analytical equations for two different values of R

Figure 6-10 shows the change of bandwidth versus different values of R which is helpful in the design of proposed coupler. The abrupt changes in bandwidth is due to exit of maximal and minimal points from the desired range of phase difference with tolerable phase deviations of either 2° or 5° .

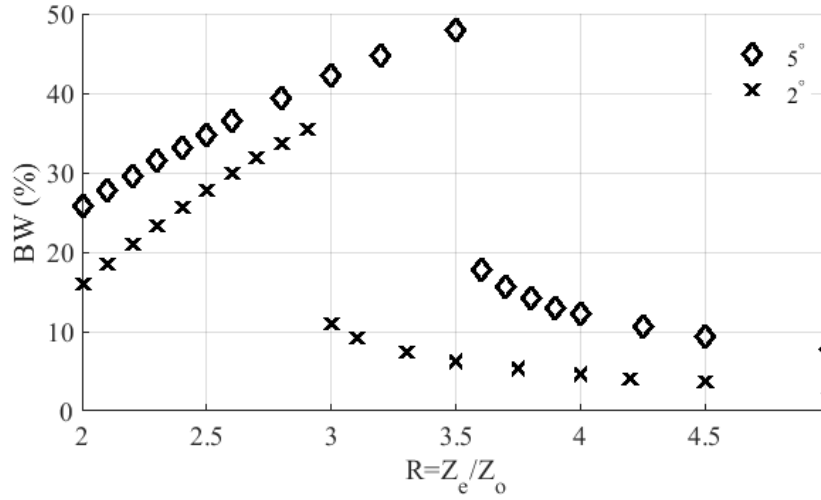


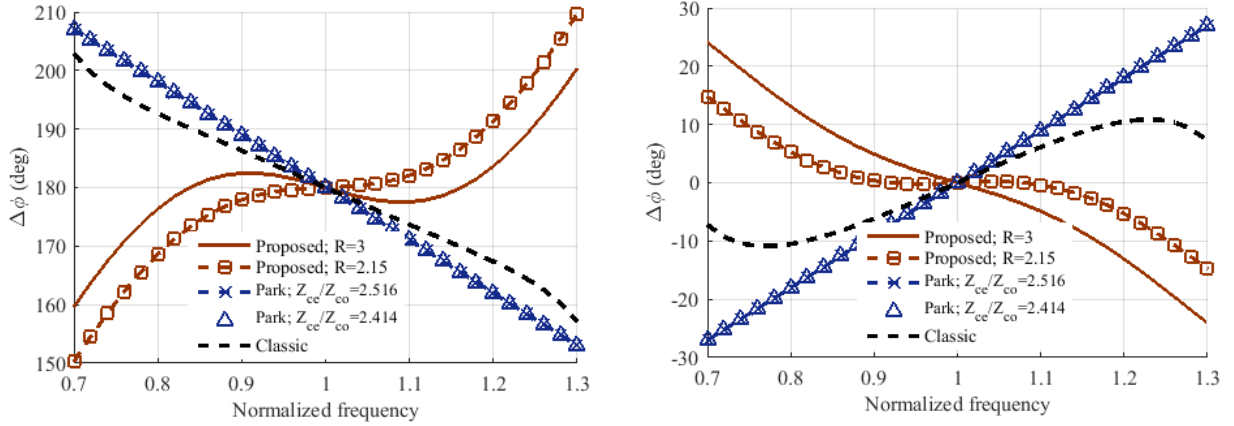
Figure 6-10: Bandwidth control over R for two different values of phase deviations (δ) of $\pm 2^\circ$ and $\pm 5^\circ$. This is obtained from the result of analytical analysis in (6-12).

6.2.3 Design of the proposed coupler

The proposed coupler has fairly a simple design procedure. To design the proposed coupler, the even and odd mode impedances of the coupled line should be determined per the desired bandwidth of the maximum tolerable deviation from the 180° phase difference. Figure 6-10 can be used to find a suitable ratio of even to odd mode impedances to achieve the desired bandwidth. On the other hand, a matching condition to the reference impedance (i.e. $Z_0 = \sqrt{Z_o Z_e}$) provides the second equation to determine the even and odd mode impedances and accordingly the coupling factor (C) of the coupled line (i.e., $C = -20 \log[(R - 1)/(R + 1)]$). The electrical lengths of θ_1 and θ are 90° and θ_2 is 270° .

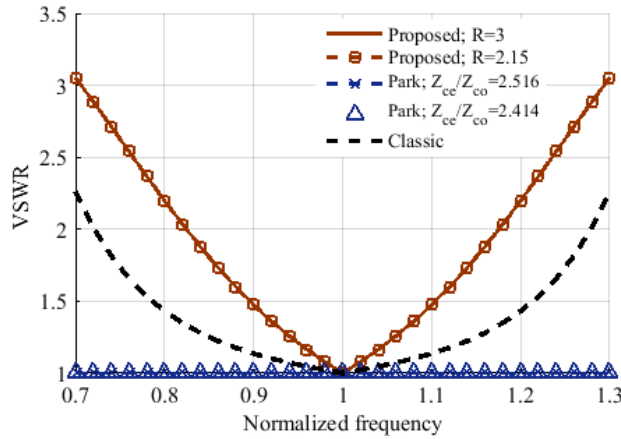
To discuss the characteristics of the proposed hybrid coupler, they are compared with those of the counterparts of classic rat-race and coupled-line from [132], based on simulations which are carried out using ideal blocks in ADS. Two different values of the ratio of even to odd mode impedances for each of the proposed hybrid (R) and the coupled-line hybrid (Z_{ce}/Z_{co}) from [132]

are considered for simulations and results are plotted in Figure 6-11 and Figure 6-12. It can be observed in Figure 6-11 (a) and (b) that the phase differences between output signals in the hybrid proposed by [132] are not affected by changes in the ratio of (Z_{ce}/Z_{co}).



(a) phase difference (Out-of-phase)

(b) Phase difference (in-phase)



(c) VSWR

Figure 6-11: Comparison of phase differences between our proposed 180 deg hybrid topology with the one proposed by Park in race [132], and the classic rat-race.

Moreover, the bandwidth in which the maximum phase deviation of 5° occurs for both in-phase and out-of-phase components is slightly less than that of the rat-race hybrid coupler. However, the proposed hybrid has considerably larger bandwidth for both phase difference components with the same amount of deviation of 5° . This bandwidth can be controlled by

changing R .

In Figure 6-11(c), the hybrid couplers are compared in terms of matching at the input ports. One can see that the proposed hybrid has narrower bandwidth of VSWR with the value less than 1.22 (i.e. return loss > 20 dB), while the hybrid coupler in [132] is completely matched given the condition $Z0^2 = Zce \times Zco$ is satisfied for any non-zero coupling factor, regardless of the length of the coupled lines. It should be pointed out the latter consequences can be concluded given the coupled line hybrid circuit of [132] is lossless.

Figure 6-12 demonstrates the performance of the hybrids in terms of amplitude imbalance for the output signals. The proposed hybrid coupler has less bandwidth of 0.5 dB amplitude imbalance when compared to the classic rat-race hybrid. This remains unaffected by changes in R , whereas the amplitude imbalance of the output signals in hybrid coupler of [132] can be controlled by changing the ratio (Zce/Zco). This ratio in hybrid coupler of [132] can be set for a larger bandwidth of 0.5 dB amplitude imbalance than that of the classic rat-race hybrid.

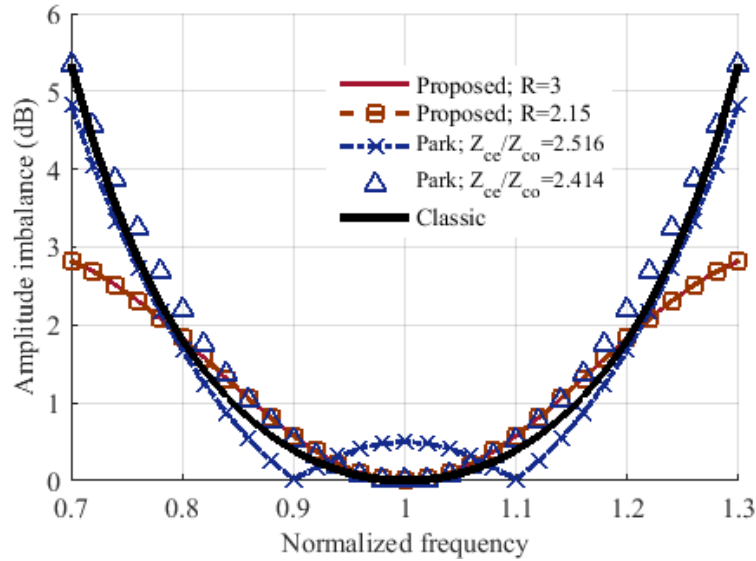


Figure 6-12: Comparison of amplitude imbalance; -.- classic rat-race hybrid, -o- proposed hybrid, : coupled-line hybrid in [132].

These characteristics of studied hybrids are summarized in Table I in terms of fractional bandwidth for comparison purposes. One can observe that the proposed hybrid can have a larger

bandwidth of desired phase differences even though it has a poor performance in terms of matching and amplitude imbalance in comparison to the other hybrid topologies.

Table 6-1: Comparison of the 180° hybrid couplers

Hybrid topology	Fractional BW (%)			
	VSWR < 1.22	Amplitude imbalance < 0.5 dB	Phase deviation < $\pm 5^\circ$ (180°)	Phase deviation < $\pm 5^\circ$ (0°)
Rat-race	27.75	22.44	15.8	16.03
Coupled-line [132] ($\frac{Z_{ce}}{Z_{co}} = 2.414$)*	100	19.57**	11.16	11.16
Coupled-line [132] ($\frac{Z_{ce}}{Z_{co}} = 2.516$)*	100	27.56***	11.16	11.16
Proposed hybrid ($R=2.15$)	10.4	18.56	28.77	39.19
Proposed hybrid ($R=3$)	10.4	18.56	42.22	20.35

* Z_{ce} and Z_{co} are the even and odd mode impedances of the coupled-line couplers in hybrid topology of [132], and $Z_0^2 = Z_{ce} \times Z_{co}$

** Under-coupled

*** Over-coupled

6.2.4 Prototyping and measurements

As it has already been mentioned, the proposed topology can outperform other existing counterparts as the design frequency increases, because no via, wire-bonding or lumped elements are essentially used that can affect matching, phase and amplitude imbalance. Therefore, the proposed hybrid was designed and implemented for operation around 77 GHz, using our in-house MHMIC fabrication process on an Alumina ceramic substrate with permittivity of around 9.9 and thickness of 0.254 mm. The prototyped MHMIC die is displayed in Figure 6-13. Small modifications in the original configuration at the input of phase shifter are made within optimization process in the commercial 3D EM simulation package of HFSS.

To measure the S -parameters through 2-port VNA, a few circuits are fabricated on the same die. The microscopic view shows one of the circuits with details. The measuring ports are connected to the designed coplanar adaptor while the unused ports are loaded with integrated matched resistors and RF grounds. The quadrature round shaped coupler with branch-line impedance of 70.7 ohm was designed for this frequency of operation. To minimize the radiation loss of the microstrip transmission line, the reference characteristic impedance was selected to be 70.7 ohm.

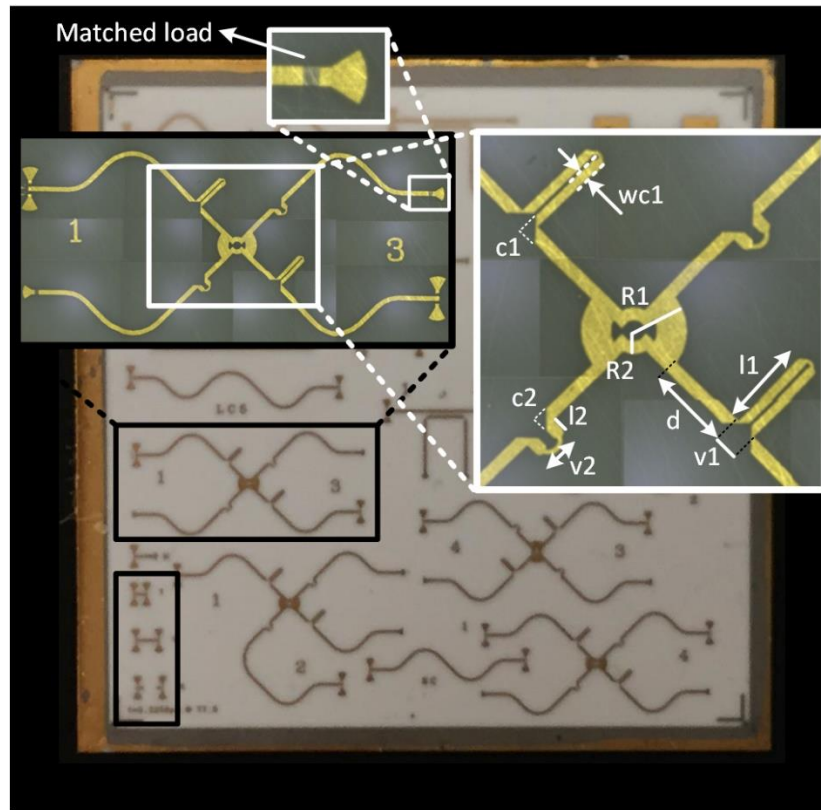


Figure 6-13: Prototyped hybrid on ceramic die; The ports #1, #2 , #3, #4 in layout correspond to the ports #1, #3, #4, #2 in standard port definition in Fig. 3 respectively). $R1=393.7 \text{ } \mu\text{m}$. $R2=172.7 \text{ } \mu\text{m}$, $d=624.8 \text{ } \mu\text{m}$, $v1=162.6 \text{ } \mu\text{m}$, $l1=1.46 \text{ mm}$, $l2=94 \text{ } \mu\text{m}$, $v2=647.7 \text{ } \mu\text{m}$, $C1=142.24 \text{ } \mu\text{m}$, $C2=114.3 \text{ } \mu\text{m}$, $wc1=68.6 \text{ } \mu\text{m}$.

To assess the performance of the prototyped hybrid, two-port on-wafer S -parameter measurement was carried out using the probe station (Karl Suss) with VNA (Agilent Technologies PNA-X, N5247A) shown in Figure 6-14. To preserve the repeatability of amplitude and phase

measurements, the Ground-Signal-Ground (GSG) probe (Picoprobe by GGB Industries-Model 120) with pitch size of 150 μm was positioned on the same place over the coplanar adaptors with the same amount of pressure using high accuracy controllers. To de-embed the effect of transitions from the probe to the input ports of the designed hybrid, a standard Through-Reflect-Line (TRL) calibration kit was also designed on the same die for calibration purposes.

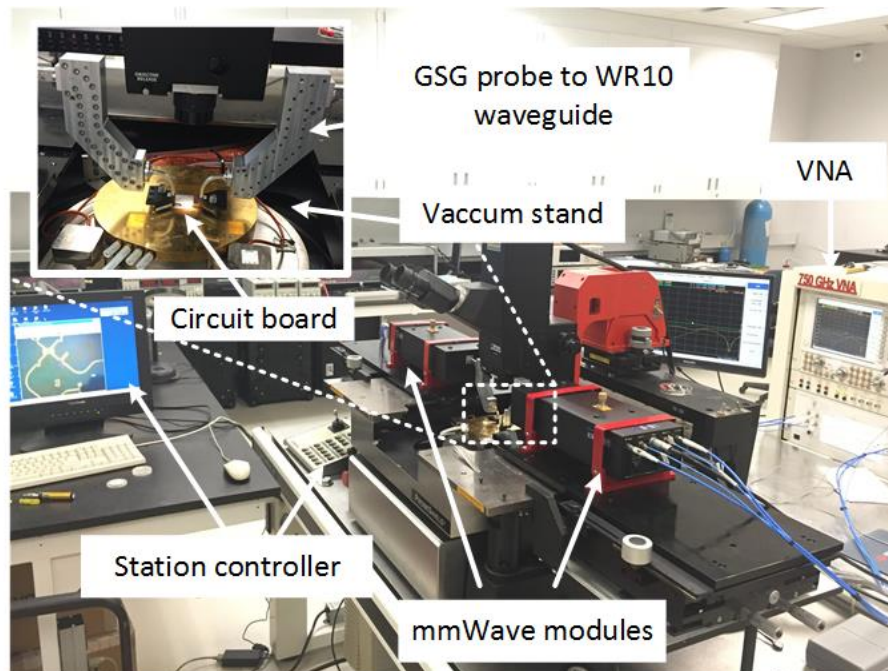


Figure 6-14: Measurement setup which is hold on mmWave probing station

The phase and amplitude measurement results are shown in Figure 6-16, and Figure 6-15. It should be noted that, ports #1, #2, #3, #4 in layout correspond to ports #1, #3, #4, #2, respectively within the standard port definition in Figure 6-6. It can be seen that the designed 180° hybrid is very well matched (return loss > 10 dB) over 10 GHz bandwidth with excellent isolation at the center frequency. The measured phase difference shown in Figure 6-16 agree well with the simulation values.

The performance of the prototyped device is compared with the recently reported 180° hybrids in Table II based on the measurement results. One can observe that with the tight condition of 5° deviation from phase differences of the output signals it covers a fractional bandwidth of around 5% which corresponds to roughly 4 GHz bandwidth around 77 GHz. This is sufficient for applications such as automotive radar (i.e. 76 GHz- 77 GHz) or backhaul radios (71 GHz-76 GHz).

In these frequency bands the prototyped hybrid can be matched with return loss values larger than 15 dB and isolation of better than 20 dB.

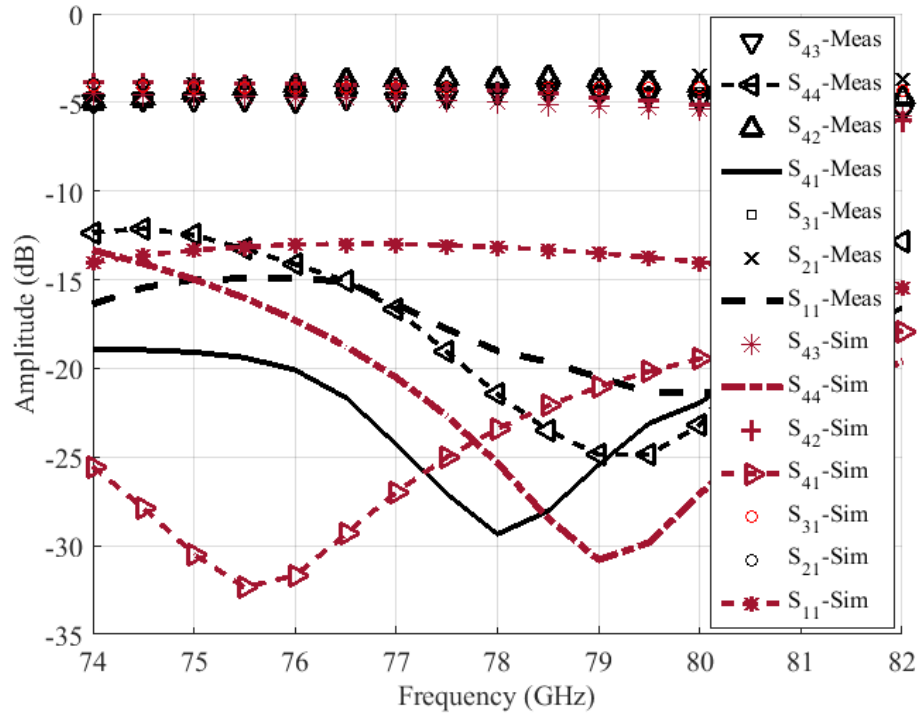


Figure 6-15: Measured and simulated amplitude components of S -parameters.

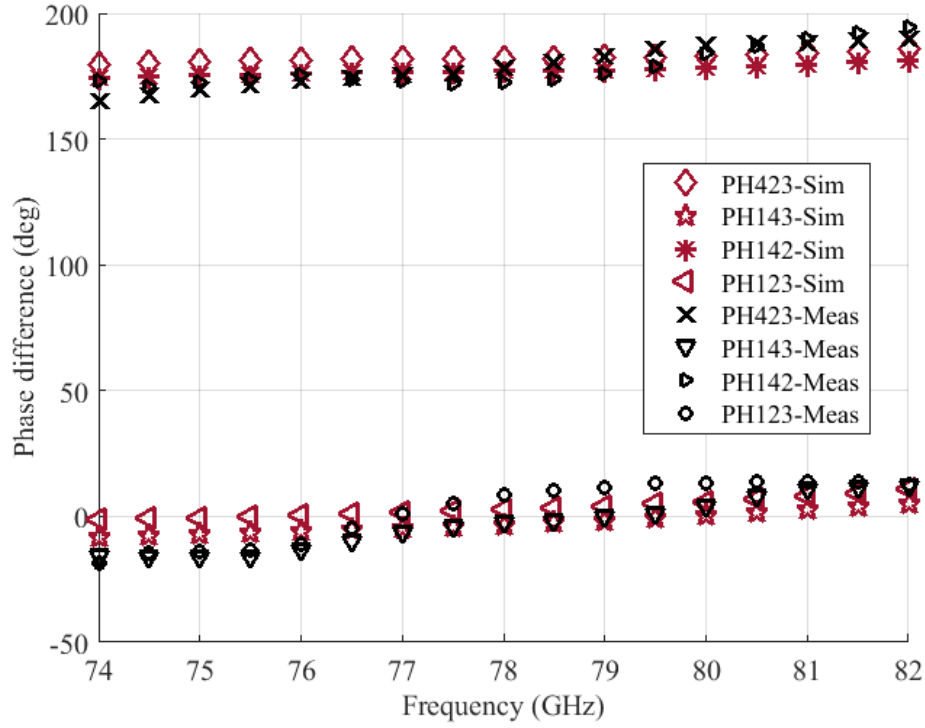


Figure 6-16: Comparison of measured and simulated phase differences. $PH423 = \angle S_{42} - \angle S_{43}$,
 $PH123 = \angle S_{12} - \angle S_{13}$, $PH142 = \angle S_{12} - \angle S_{42}$, $PH143 = \angle S_{13} - \angle S_{43}$.

Table 6-2 shows that the prototype of the proposed hybrid possesses the least fractional bandwidth in terms of matching, isolation or phase differences, in comparison to other works. Nevertheless, it has a sufficient coverage over the application bandwidth. It should be highlighted that none of the previously reported works were implemented in millimeter wave frequency bands as this work did. The crossovers across the microstrip traces in [134], multilayer crossing in [119] and [135] to obtain non-interspersed ports or lumped capacitors in [133] can substantially degrade the performance of the device when designed within high frequency regions. A simple and single layer topology of the proposed 180 hybrid with non-interspersed input-outputs is achieved at the expense of a larger size against the compact size of previous works.

Table 6-2: Comparison of measured performances of 180o hybrid couplers

Hybrids	Design frequency (GHz)	Implementation technology	Fractional Bandwidth (%)				Dimensions (Guided wavelength λ_g)
			Return loss > 15 dB	Isolation > 20 dB	Phase imbalance $0 \pm 5^\circ$	Phase difference $180 \pm 5^\circ$	
[134]	2	Single layer PCB with crossover	22.9	37.5	8.3		-
[119]	24	LTCC	14 dB *	14.6 dB*	177° *		0.67×0.54
[135]	8	LTCC	20 **	35 **	12.0 **		0.69×0.59
[133]	2.4	Single layer PCB	26.3	12.7	45.8	12.9	0.64×0.53
This work	77	MHMIC	10.25	6.41	4.5	5.19	1.86×1.86

6.2.5 Conclusion:

A concept of field rotation is proposed to be applied as phase inverter in the development of baluns. The concept is also demonstrated to be realizable via antipodal fin-lines. Since the E-field polarization is actually manipulated through field rotation, there is no dependency on frequency or wavelength. Hence, a favorable phase inversion in a wide bandwidth is expected. In order to make a balun of wideband characteristics, the fin-line phase inverter is also incorporated with SIW-based power divider as SIW among many types of transmission lines is one of the rare ones with reliable performances at very high frequencies. In addition, unlike many of the prior arts on balun design, the proposed architecture does not require a tight line coupling in the phase inverter section and hence it can be implemented via simpler and less expensive fabrication processes than MMICs or MHMICs. The proposed balun is implemented using a simple and low cost PCB process for applications around E-band. Since the topology of the balun is planar, it can be easily integrated

with other components. The proposed architecture of the balun along with the concept of phase inverter may find wide applications in circuits and systems operating at very high frequency ranges

In addition, a topology of 180° hybrid coupler was introduced and analyzed throughout this chapter. The principles of the proposed hybrid were theoretically examined through the S -parameter analysis. The 4-port T -matrix of the proposed hybrid was derived for conversion to S -Matrix. The derived analytical equations help calculate the bandwidth in which the maximum tolerable deviation from 180° phase difference occurs. The theoretical analysis was validated when compared with simulation results with ideal components in commercial software. In addition, the proposed hybrid was compared with previously reported coupled-line 180° hybrids in terms of matching, phase and gain imbalance. The main application of such structure is in circuits operating at the millimeter-wave frequency band where already reported topologies of 180° hybrid couplers with non-interspersed input-output ports could fail due to their structural parasitic effects. Successful implementation of the prototyped hybrid on MHMIC die around 77 GHz makes the proposed topology a comparable candidate for applications in mixer, amplifiers or multiport phasing networks in high frequency integrated circuits.

CHAPTER 7 MILLIMETER-WAVE MULTIFUNCTION MULTI-PORT INTERFEROMETRIC RECEIVER FOR FUTURE WIRELESS SYSTEMS

The variety of applications of six-port interferometric technology that have been reported in the literature are referenced in chapter 1. However, a multiport-based receiver (MPR) that can unify all or some of those system functions has not been reported as it is already mentioned throughout this thesis.

In all these reported applications, the fundamental six-port operation principle, which are explained in chapter 2, remains the same. In fact, the input signals are combined through the output ports upon experiencing specific phase shifts and amplitude distributions. For the common six-port architecture, shown in Figure 2-6, the relative phase differences between two input signals appearing at four output ports are 0 , $\pi/2$, π , and $3\pi/2$ [32]. These relative phase differences can be obtained with a variety of topologies of couplers, dividers and phase shifters, depending on the applications [148]. However, the conventional six-port technique should be further improved if it is to be employed for simultaneously handling several functions. For example, a dual-band six-port receiver (SPR) was developed in [48] that can down-convert two differently modulated signals in two different bands, using only one six-port correlator circuit. Moreover, a dual-function multiport receiver was reported in [105, 149] where an AOA estimation system is integrated with communication signal demodulator within a single SPR. The integration in the scheme proposed by [105] was achieved mostly through a new method of signal processing of the output signals.

We have presented another solution in chapter 5 that unifies six-port based systems, including radars, AOA sensors and data communication receivers that were previously realized within two distinct six-port receivers (SPR). This chapter presents our extended research based on the early concept demonstrated in chapter 5 and [104] and further improved scheme with focus on the capabilities of AOA estimation and data communication.

The unification of two SPRs within our proposed scheme is mainly achieved through a new configuration of signals at input ports, a new phase processing of the input signals within a structured eight-port passive network and a complementary post-processing of the signals at the output of detectors.

Using two RF input ports and two LO input ports that are switched in two consecutive time slots, the proposed multiport receiver (MPR) can estimate the AOA with a simple signal processing algorithm. The plurality of the RF input ports can cause self-interference for the received communication signals. Therefore, a phasing network within the proposed eight-port wave correlator is devised such that the incoming quadrature modulated RF carriers are demodulated in an orthogonal manner at four output ports.

It is found that receiving communication signal from a non-zero AOA makes imbalance between demodulated components. To this end, the proposed MPR can first find the angular position of the other unit and then recover the demodulation components through data fusion and post processing. The mathematical model for the developed MPR is derived which is discussed first in this chapter, and its principal functionality is theoretically analyzed subsequently. Furthermore, an appropriate calibration technique is proposed to deal with the non-idealities in practice.

In addition, a transceiver architecture based on this MPR is implemented, and prototyped for operation around 77 GHz. Technical discussions for implementation of such millimeter-wave sub/system module are discussed in this chapter. Finally, the results of system-level measurements that were carried out to evaluate the proposed system performances are discussed. The limitations of the presented system scheme are also discussed through this chapter. The results of research in this project are published in [150] which are brought here, as well.

7.1 Proposed multiport architecture

Angle detection within the six-port based AOA sensing systems is based on the technique of phase-difference-of-arrival (PDOA) detection that requires two receiving input channels. The same technique can be incorporated with the six-port based radios, for integrating both system functions. Two variants of the conventional six-port network, i.e., either one comprising three 90° hybrids and one power divider [35] or the other with four 90° hybrid couplers and one 90° phase shifter [151] have sufficient ports for this purpose, provided that the usually match-loaded port is made available to form a seven-port interferometer.

However, the quadrature-amplitude-modulated radio signals interfere with each other when received through two input ports, superposed within the conventional six-port phasing network and mixed via power detectors. Figure 7-1 shows the proposed eight-port network through which the input signals experience different relative phase differences in comparison to those through the conventional six-port.

In Figure 7-2 , the relative phase shift that the two signals from ports P2 and P7 experience with respect to that of the signal from port P1 are depicted, (i.e., $q_i = S(i, 2)/S(i, 1)$, $x_i = S(i, 7)/S(i, 1)$). One can observe that with the proposed multiport network, the mixing products of the signals from two input ports (i.e. P2 and P7) with that from port P1 are orthogonal at four outputs, hence a quadrature demodulation of the modulated RF signal without interference is made feasible through the proposed multiport network.

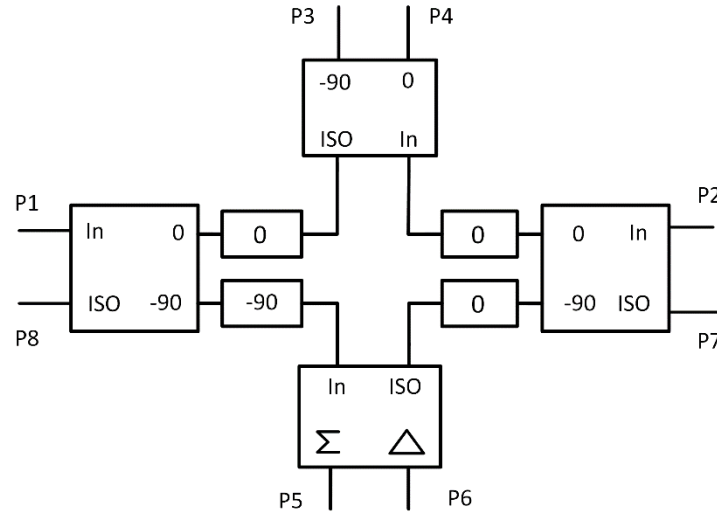


Figure 7-1: The proposed multiport network

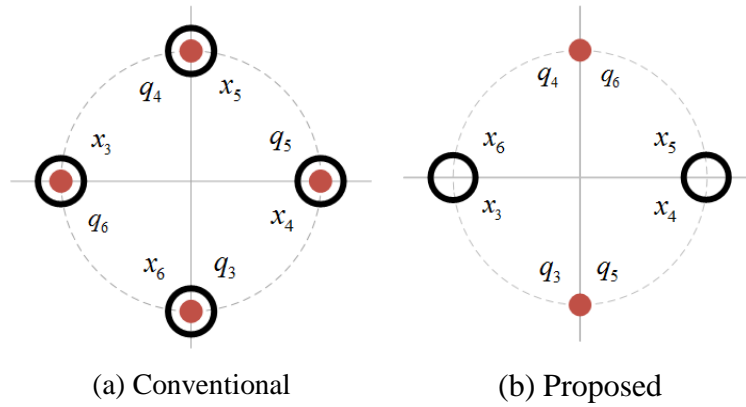


Figure 7-2: The comparison of the scattering matrix relationship between the conventional and proposed multiport. Filled circles are $q_i = S(i, 2)/S(i, 1)$, $i=1, 2, 3, 4$. The empty circles denote $x_i = S(i, 7)/S(i, 1)$. Port P1 is connected to LO source and ports P2 and P7 are the inputs RF ports.

To elaborate the functionality of the proposed multiport interferometer technique in both AOA sensing and radio communication, a mathematical model of such a multiport receiver is derived and presented along with an essential signal processing algorithm as follows.

Let us assume that two Rx antennas, at a distance (d) from each other, are connected to ports P2 and P7 while the LO signal is connected to port P1. The incoming wave from the angle of θ would be received by two Rx antenna elements, with a relative phase difference of $\Delta\varphi = 2\pi f d \sin(\theta)/c$, where c denotes the speed of light and f denotes the carrier frequency.

The input RF signal at port P2 and the LO signal at port 1 can be modeled as $U_2 = A_{RF}(t)\exp(j\theta_R(t))$ and as $U_1 = A_{LO}(t)\exp(j\theta_T(t) + \theta_{LO})$, respectively. With the diode power detectors operating in the square law region, the detected voltages (V_i) at the output port of i th detector can be expressed as

$$\begin{aligned}
V_i &= \text{Re} \left\{ \left(\left| S_{i1} \right| A_{LO} \exp \left(j \left(\Theta_T(t) + \theta_{LO} + \varphi_{i1} \right) \right) + \left| S_{i2} \right| A_{RF} \exp \left(j \left(\Theta_R(t) + \varphi_{i2} \right) \right) + \right. \\
&\quad \left. \left| S_{i7} \right| A_{RF} \exp \left(j \left(\Theta_R(t) + \Delta \varphi + \varphi_{i7} \right) \right) \right)^2 \Bigg\} \\
&= \text{Re} \left\{ \begin{aligned} &\left| S_{i1} \right|^2 A_{LO}^2 + \left| S_{i2} \right|^2 A_{RF}^2 + \left| S_{i7} \right|^2 A_{RF}^2 \\ &+ 2 \left| S_{i1} \right| \left| S_{i2} \right| A_{LO} A_{RF}^* \exp \left(j \left(\Theta_T(t) - \Theta_R(t) + \theta_{LO} + \varphi_{i2}^i \right) \right) \\ &+ 2 \left| S_{i1} \right| \left| S_{i7} \right| A_{LO} A_{RF}^* \exp \left(j \left(\Theta_T(t) - \Theta_R(t) + \theta_{LO} + \varphi_{i7}^i - \Delta \varphi \right) \right) \\ &+ 2 \left| S_{i2} \right| \left| S_{i7} \right| A_{RF}^2 \exp \left(j \left(\varphi_{i2}^i - \Delta \varphi \right) \right) \end{aligned} \right\} \quad (7-1)
\end{aligned}$$

where $|S_{i1,2,7}|$ and $\varphi_{i1,2,7}$ are the amplitude and phase scattering parameters from three input ports to the i th output port and $\varphi_{jl}^i = \varphi_j^i - \varphi_l^i$.

When the LO signal is an unmodulated single frequency carrier and the RF signal is modulated through QAM technique, we can consider $A_{LO}(t) = A_{LO}$ and $A_{RF}(t) = A_{RF}(I(t) + jQ(t))$. Thus, (1) turns out to

$$\begin{aligned}
V_i &= DC + |S_{i1}| |S_{i2}| A_{LO} A_{RF} \left(I \cos(\Delta \omega t + \theta_{LO} + \varphi_{i2}^i) + Q \sin(\Delta \omega t + \theta_{LO} + \varphi_{i2}^i) \right) \\
&\quad + |S_{i1}| |S_{i7}| A_{LO} A_{RF} \left(I \cos(\Delta \omega t + \theta_{LO} + \varphi_{i7}^i - \Delta \varphi) + Q \sin(\Delta \omega t + \theta_{LO} + \varphi_{i7}^i - \Delta \varphi) \right) \cdot \quad (7-2) \\
&\quad + |S_{i2}| |S_{i7}| A_{RF}^2 \left(\cos(\varphi_{i2}^i - \Delta \varphi) \right)
\end{aligned}$$

Given identical transmitting and receiving RF carrier frequencies, (i.e., $\Delta \omega = 0$), the baseband signals at the output of the detectors would be

$$\begin{aligned}
V_i &= DC + K_1 \left(I \cos(\theta_{LO} + \varphi_{i2}^i) + Q \sin(\theta_{LO} + \varphi_{i2}^i) \right) + \\
&\quad K_7 \left(I \cos(\theta_{LO} + \varphi_{i7}^i - \Delta \varphi) + Q \sin(\theta_{LO} + \varphi_{i7}^i - \Delta \varphi) \right) \quad (7-3) \\
&\quad + K_{27} \left(\cos(\varphi_{i2}^i - \Delta \varphi) \right)
\end{aligned}$$

where $K_1 = 2|S_{i1}||S_{i2}|A_{LO}A_{RF}$, $K_7 = 2|S_{i1}||S_{i7}|A_{LO}A_{RF}$, $K_{27} = |S_{i2}||S_{i7}|A_{RF}^2$. Differentiating the signals at the ports i and j yields:

$$\begin{aligned}
V_i - V_j = & K_1 \begin{pmatrix} -I \sin\left(\frac{\delta_{12}^{ij}}{2}\right) \sin\left(\frac{2\theta_{LO} + \sigma_{12}^{ij}}{2}\right) \\ + Q \sin\left(\frac{\delta_{12}^{ij}}{2}\right) \cos\left(\frac{2\theta_{LO} + \sigma_{12}^{ij}}{2}\right) \end{pmatrix} \\
& + K_7 \begin{pmatrix} -I^7 \sin\left(\frac{\delta_{17}^{ij}}{2}\right) \sin\left(\frac{2\theta_{LO} + \sigma_{17}^{ij} - 2\Delta\varphi}{2}\right) \\ + Q^7 \sin\left(\frac{\delta_{17}^{ij}}{2}\right) \cos\left(\frac{2\theta_{LO} + \sigma_{17}^{ij} - 2\Delta\varphi}{2}\right) \end{pmatrix} \\
& - K_{27} \sin\left(\frac{\delta_{27}^{ij}}{2}\right) \sin\left(\frac{\sigma_{27}^{ij} - 2\Delta\varphi}{2}\right)
\end{aligned} \tag{7-4}$$

where $\delta_{12}^{ij} = \varphi_{12}^i - \varphi_{12}^j$ and $\sigma_{12}^{ij} = \varphi_{12}^i + \varphi_{12}^j$. It can be further simplified in accordance with the relative phase differences of the proposed eight-port network and with the assumption that $\theta_{LO} = 0$, into

$$\begin{aligned}
\overline{H1: V_3 - V_4} &= (k_1 + k_7 \sin(\Delta\varphi))Q - (k_7 \cos(\Delta\varphi))I \\
\overline{H2: V_5 - V_6} &= (k_1 - k_7 \sin(\Delta\varphi))Q + (k_7 \cos(\Delta\varphi))I
\end{aligned} \tag{7-5}$$

Obviously, the AOA should be determined first to discriminate I and Q signals in (7-5).

On the other hand, if the incoming signal is an unmodulated carrier oscillating at a frequency with small difference from the frequency of the reference LO signal, the AOA of the incoming signal can be estimated as it is explained in the following. Hence, assuming $A_{LO}(t) = A_{LO}$, $A_{RF}(t) = A_{RF}$ and $\Theta_T = 2\pi f_1 t + \alpha$ for reference signal in (1) and $\Theta_R(t) = 2\pi f_0 t$ for incoming signal from angle θ , one can express the differentiated output products of the detectors as:

$$\begin{aligned}
\overline{H3: V_3 - V_4} &= 2(-k_1^R \sin(\gamma + \alpha) - k_7^R \cos(\gamma + \alpha - \Delta\varphi)) \\
\overline{H4: V_5 - V_6} &= 2(-k_1^R \sin(\gamma + \alpha) + k_7^R \cos(\gamma + \alpha - \Delta\varphi))
\end{aligned} \tag{7-6}$$

where $\gamma = 2\pi(f_1 - f_0)t$.

If the LO is switched to port 8, the input signals would be processed differently in accordance with the different relative phase differences, and hence the output products turn out to be:

$$\begin{aligned}
\overline{H5: V_3 - V_4} &= 2(k_1^R \cos(\gamma + \alpha) - k_7^R \sin(\gamma + \alpha - \Delta\varphi)) \\
\overline{H6: V_5 - V_6} &= 2(-k_1^R \cos(\gamma + \alpha) - k_7^R \sin(\gamma + \alpha - \Delta\varphi))
\end{aligned} \tag{7-7}$$

To solve for I and Q in radio mode and AOA in sensing mode the following signal processing

is proposed.

$$\begin{aligned}
 H_4 + H_3 &= -4k_1^R \sin(\gamma + \alpha) \\
 H_5 - H_6 &= +4k_1^R \cos(\gamma + \alpha) \\
 H_4 - H_3 &= 4k_7^R (\cos(\gamma + \alpha) \cos(\Delta\varphi) + \sin(\gamma + \alpha) \sin(\Delta\varphi))
 \end{aligned} \tag{7-8}$$

In [27] and [104], the phases of beat signals were compared through fast Fourier transform (FFT) that degrades the phase resolution. Within the proposed scheme, the phase difference ($\Delta\varphi$) can be obtained from all the outputs of both cases, i.e., LO at port 1 and LO at port 8, through a simple processing of the signals in time domain without transforming the signal to frequency domain, as it is explained next. Therefore, an excellent phase resolution of the multiport phasing network is preserved.

Reformulating (H_4-H_3) in (7-8) into matrix format and using the technique of deterministic least mean square (LMS), the vector Λ can be estimated as:

$$\begin{aligned}
 \overline{G}_{n \times 1} &= 4k_7^R [\sin(\gamma) \quad \cos(\gamma)]_{n \times 2} \begin{bmatrix} \sin(\Delta\varphi) \\ \cos(\Delta\varphi) \end{bmatrix}_{2 \times 1} = ZM \\
 M &= (Z^* Z)^{-1} Z^* G
 \end{aligned} \tag{7-9}$$

where the superscript (*) denotes the conjugate transpose of the known matrix Z . The obtained vector of M in sensing mode can be readily used to recover the true in-phase (I^r) and (Q^r) in radio mode through:

$$\begin{aligned}
 H_1 + H_2 &= 2k_1 Q \\
 H_1 - H_2 &= 2k_7 (\sin(\Delta\varphi) Q - \cos(\Delta\varphi) I) \\
 \begin{bmatrix} I^r \\ Q^r \end{bmatrix} &= \frac{1}{\cos(\Delta\varphi)} \times \begin{bmatrix} -1 & \sin(\Delta\varphi) \\ 0 & \cos(\Delta\varphi) \end{bmatrix} \begin{bmatrix} H_1 - H_2 \\ H_1 + H_2 \end{bmatrix}
 \end{aligned} \tag{7-10}$$

Furthermore, the AOA (θ) can be readily calculated from the M vector through

$$\theta = \begin{cases} + \sin^{-1} \left(\frac{\cos^{-1}(M(2))}{\frac{2\pi f}{c} d} \right) & \text{if } \sin^{-1} \left(\frac{\sin^{-1}(M(1))}{\frac{2\pi f}{c} d} \right) \geq 0 \\ - \sin^{-1} \left(\frac{\cos^{-1}(M(2))}{\frac{2\pi f}{c} d} \right) & \text{if } \sin^{-1} \left(\frac{\sin^{-1}(M(1))}{\frac{2\pi f}{c} d} \right) \leq 0 \end{cases} \tag{7-11}$$

Indeed, the equations for θ in (7-11) are complementary to each other, which yield the

maximum unambiguous range of angle for a specific distance between antenna elements. This is elaborated further in detail in the following section. The conditions on the phase of transmission coefficients of the wave correlator for functionality of the proposed multiport are:

$$\begin{aligned}
 & \begin{cases} \angle S_{31} - \angle S_{38} = 2n\pi + \pi/2 \\ \angle S_{31} - \angle S_{32} = 2n\pi + \pi/2 \\ \angle S_{31} - \angle S_{37} = 2n\pi + \pi \end{cases} \\
 & \begin{cases} \angle S_{41} - \angle S_{48} = 2n\pi + \pi/2 \\ \angle S_{41} - \angle S_{42} = 2n\pi - \pi/2 \\ \angle S_{41} - \angle S_{47} = 2n\pi \end{cases} \\
 & \begin{cases} \angle S_{51} - \angle S_{58} = 2n\pi - \pi/2 \\ \angle S_{51} - \angle S_{52} = 2n\pi - \pi/2 \\ \angle S_{51} - \angle S_{57} = 2n\pi - \pi \end{cases} \\
 & \begin{cases} \angle S_{61} - \angle S_{68} = 2n\pi - \pi/2 \\ \angle S_{61} - \angle S_{62} = 2n\pi + \pi/2 \\ \angle S_{61} - \angle S_{67} = 2n\pi \end{cases}
 \end{aligned} \tag{7-12}$$

The transmission coefficients in the multiport network should be identical and diode detectors should also operate within their square law region with identical transfer functions. In comparison to the essential conditions within the conventional six-port correlator as listed in [48], the phase difference at one pair of outputs is rotated by 90° which mainly helps discrimination of quadrature components of the radio signal.

7.2 Ambiguity in AOA detection

Angle detection based on the technique of PDOA estimation is subjected to the issue of ambiguity when the phase difference between the incoming signals at two receiver antenna elements exceeds the value of 180° . In other words, the estimated phase difference is bound to the range of -180° to 180° and unwrapped by 360° . However, throughout the proposed technique, $\sin(\Delta\varphi)$ and $\cos(\Delta\varphi)$ are extracted from the signals at the output of detectors whereas within the conventional six-port based AOA detection systems $\Delta\varphi$ is directly obtained from the output signals. Therefore, the phase difference would be limited to the range of -90° to 90° or from 0° to 180° if extracted from $\sin(\Delta\varphi)$ or $\cos(\Delta\varphi)$, respectively. The constrained unambiguous range

of phase detection can yield a limited operational range of angle detection by the system. Figure 7-3 demonstrates the above analysis for ambiguity in AOA estimation. One can observe that AOA estimation through (7-11) within the proposed multiport system is extended to the same unambiguous range associated with the conventional six-port based systems.

It should be remarked that the complete I - Q recovery does not essentially require the AOA, and the obtained M vector is sufficient, which can be obtained without ambiguity.

The main drawback of the proposed multiport-based AOA system is the necessity of using an additional LO source while the conventional six-port based AOA system operates through mixing the received signals at two input ports. However, the DC signals at the output of detectors in the conventional six-port based AOA systems suffer from lower SNR values due to the effect of flicker noise, whereas the AOA is extracted from IF signals within the proposed multiport-based system.

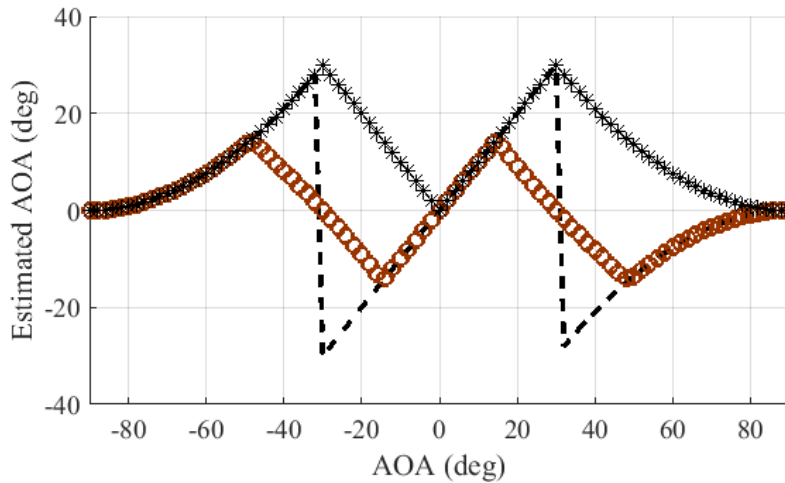


Figure 7-3: The unambiguous range of AOA estimation using the obtained M vector; *: from $\cos^{-1}(M(2))$, O: from $\sin^{-1}(M(1))$, --: combination of both in (7-11).

7.3 Multi-function transceiver architecture

In order to demonstrate the functionality of the proposed multiport receiver, a multifunction transceiver scheme is proposed which is shown in Figure 7-4. The proposed transceiver architecture can operate in accordance with the time domain integrated systems [28] that is capable of AOA detection, when operating in sensing mode, and data communication when operating in radio mode. A typical waveform associated with the proposed transceiver is depicted in Figure 7-5. The operation principles along with the details of this transceiver architecture are explained next.

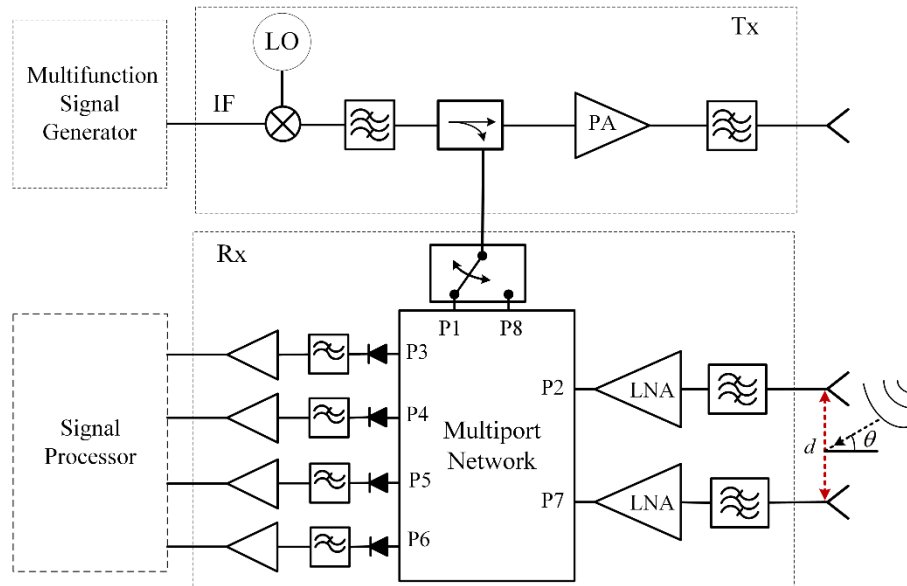


Figure 7-4: The proposed multifunction transceiver architecture

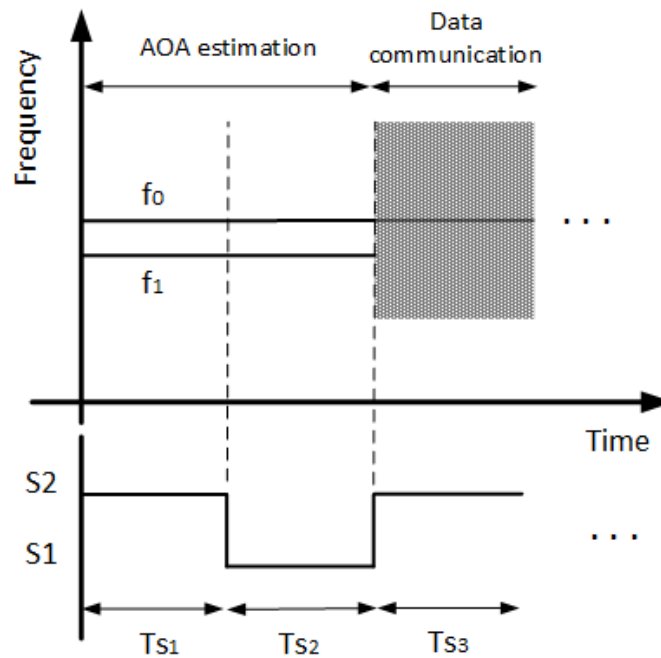


Figure 7-5: Modulation scheme of the Operational waveform

The sensing and radio modes appear in successive time slots. For radio communication, two units can find their relative angular position using two single frequency sinusoidal signals that have a small frequency spacing. Once the AOA of the incoming beam is estimated, it can be used in the

subsequent radio time slots for complete recovery of the demodulated signals. The on-board units operate in time-division-duplexing (TDD) manner and RF carrier in the Tx block is modulated for transmitting data from one unit while it remains unmodulated in the other unit to be used as LO in the Rx block for demodulating the received signal. In addition, the synchronized square wave signal is used for switching the reference signal between two LO ports in the Rx block.

Within the Tx block, the IF signal is up-converted and amplified prior to transmission through the antenna. A small portion of the RF signal is coupled from the Tx block to the Rx one to be used as LO signal for demodulating the received signal. The Tx antenna is separated from the Rx one to increase the isolation. To detect the AOA based on the technique of PDOA detection, two Rx antenna elements capture the signal and deliver it to two RF input ports (i.e. P2 and P7) of the proposed eight-port network through two distinct channels. If the frequency difference between f_0 and f_1 is unknown, the LO signal from the Tx block can be switched between two LO input ports of P1 and P8 in two successive time slots to expedite the AOA estimation, whereas in communication mode the switch remains in single state connecting to port 1.

Moreover, the proposed system scheme is capable of carrying out radar functions and estimating the angular position of an object if the frequency modulated up-chirp signals are incorporated with the waveform in Figure 7-5. Switching the LO signal between two ports of 1 and 8 can help finding the in-phase and quadrature components of beat signal and hence the Z matrix in (7-9) for angle detection. However, this is not demonstrated in this paper and the scope of the presented multifunction system is limited to AOA sensing and data communication.

7.4 Calibration technique

In practice, some inevitable circuit imperfections such as amplitude and phase imbalances within the multiport junction, mismatch or inconsistent conversion-loss values of four detectors can cause errors or misshapes and degrade the system performance in different manners. A variety of calibration and linearization techniques have been reported for six-port based receivers, which are compared and categorized in [50]. However, the conventional six-port calibration technique are not adoptable for the proposed eight-port circuit. Therefore, a new linear calibration technique for our proposed multifunction MPR for two different modes of sensing and communication is developed which is explained in the following.

7.4.1 Calibration in sensing mode

If a continuous wave (CW) signal is transmitted to the multiport receiver and arrives from the known angle of θ , while the reference oscillating signal also features a single frequency having difference Δf with respect to the incoming signal, the received signal at the output of the i th detector can be expressed by

$$\begin{aligned} V_i = & DC + g_2^i \cos(2\pi\Delta ft + \theta_{Lo} + \varphi_{12}^i + e_{12}^i) \\ & + g_7^i \cos(2\pi\Delta ft + \theta_{Lo} + \varphi_{17}^i + e_{17}^i - \Delta\varphi) + g_{27}^i \cos(\varphi_{27}^i + e_{27}^i - \Delta\varphi) \end{aligned} \quad (7-13)$$

where e_{12}^i , e_{17}^i and e_{27}^i are the deviations from the corresponding ideal phase-differences and g_2^i , g_7^i and g_{27}^i denote the gain imbalances. Considering the specific phase difference values in our proposed eight-port network ($\varphi_{12}^3 = 90^\circ, \varphi_{12}^4 = -90^\circ, \varphi_{12}^5 = 90^\circ, \varphi_{12}^6 = -90^\circ$), $\varphi_{17}^3 = 180^\circ, \varphi_{17}^4 = 0^\circ, \varphi_{17}^5 = 0^\circ, \varphi_{17}^6 = -180^\circ$ and denoting $\gamma = 2\pi\Delta ft$, one can simplify (13) upon removing the DC terms and expand them into:

$$\begin{aligned} V_3 &= Z \times \begin{bmatrix} -g_2^3 \cos(e_{12}^3) - g_7^3 \cos(e_{17}^3) \sin(\Delta\varphi) + g_7^3 \sin(e_{17}^3) \cos(\Delta\varphi) \\ -g_2^3 \sin(e_{12}^3) - g_7^3 \cos(e_{17}^3) \cos(\Delta\varphi) - g_7^3 \sin(e_{17}^3) \sin(\Delta\varphi) \end{bmatrix} \\ V_4 &= Z \times \begin{bmatrix} +g_2^4 \cos(e_{12}^4) + g_7^4 \cos(e_{17}^4) \sin(\Delta\varphi) - g_7^4 \sin(e_{17}^4) \cos(\Delta\varphi) \\ +g_2^4 \sin(e_{12}^4) + g_7^4 \cos(e_{17}^4) \cos(\Delta\varphi) + g_7^4 \sin(e_{17}^4) \sin(\Delta\varphi) \end{bmatrix} \\ V_5 &= Z \times \begin{bmatrix} -g_2^5 \cos(e_{12}^5) + g_7^5 \cos(e_{17}^5) \sin(\Delta\varphi) - g_7^5 \sin(e_{17}^5) \cos(\Delta\varphi) \\ -g_2^5 \sin(e_{12}^5) + g_7^5 \cos(e_{17}^5) \cos(\Delta\varphi) + g_7^5 \sin(e_{17}^5) \sin(\Delta\varphi) \end{bmatrix} \\ V_6 &= Z \times \begin{bmatrix} +g_2^6 \cos(e_{12}^6) - g_7^6 \cos(e_{17}^6) \sin(\Delta\varphi) + g_7^6 \sin(e_{17}^6) \cos(\Delta\varphi) \\ +g_2^6 \sin(e_{12}^6) - g_7^6 \cos(e_{17}^6) \cos(\Delta\varphi) - g_7^6 \sin(e_{17}^6) \sin(\Delta\varphi) \end{bmatrix} \end{aligned} \quad (7-14)$$

where Z denotes the matrix of $[\sin(\gamma) \ \cos(\gamma)]_{n \times 2}$ for n samples. Except $\Delta\varphi$ which depends on the incoming wave's AOA, all the expressions in (7-14) remain unchanged. Grouping the output signals (P), one can express (7-14) by:

$$\overline{V_{n \times 4}} = Z_{n \times 2} \times \begin{bmatrix} E_1^3 & E_1^4 & E_1^5 & E_1^6 \\ E_2^3 & E_2^4 & E_2^5 & E_2^6 \end{bmatrix}_{2 \times 4} \quad (7-15)$$

where the terms in matrix E can be estimated through least square technique:

$$E_{2 \times 4} = (Z^* Z)^{-1} \overline{Z V_{n \times 4}} \quad (7-16)$$

Each vector in E includes the constant error terms (b) that can be discriminated from variables of

$\sin(\Delta\varphi)$ and $\cos(\Delta\varphi)$ for each output signal as in:

$$\begin{aligned}
 \begin{bmatrix} E_1^3 \\ E_2^3 \end{bmatrix} &= \begin{bmatrix} -1 & 0 & -\sin(\Delta\varphi) & +\cos(\Delta\varphi) \\ 0 & -1 & -\cos(\Delta\varphi) & -\sin(\Delta\varphi) \end{bmatrix} \begin{bmatrix} b_1^3 & b_2^3 & b_3^3 & b_4^3 \end{bmatrix}^T \\
 \begin{bmatrix} E_1^4 \\ E_2^4 \end{bmatrix} &= \begin{bmatrix} +1 & 0 & +\sin(\Delta\varphi) & -\cos(\Delta\varphi) \\ 0 & +1 & +\cos(\Delta\varphi) & +\sin(\Delta\varphi) \end{bmatrix} \begin{bmatrix} b_1^4 & b_2^4 & b_3^4 & b_4^4 \end{bmatrix}^T \\
 \begin{bmatrix} E_1^5 \\ E_2^5 \end{bmatrix} &= \begin{bmatrix} -1 & 0 & +\sin(\Delta\varphi) & -\cos(\Delta\varphi) \\ 0 & -1 & +\cos(\Delta\varphi) & +\sin(\Delta\varphi) \end{bmatrix} \begin{bmatrix} b_1^5 & b_2^5 & b_3^5 & b_4^5 \end{bmatrix}^T \\
 \begin{bmatrix} E_1^6 \\ E_2^6 \end{bmatrix} &= \begin{bmatrix} +1 & 0 & -\sin(\Delta\varphi) & +\cos(\Delta\varphi) \\ 0 & +1 & -\cos(\Delta\varphi) & -\sin(\Delta\varphi) \end{bmatrix} \begin{bmatrix} b_1^6 & b_2^6 & b_3^6 & b_4^6 \end{bmatrix}^T
 \end{aligned} \tag{7-17}$$

Within the initial calibration process, the error vectors can be estimated by solving the equations in (7-17) for two different known values of $\Delta\varphi$. Thereafter and for other measurements, they can be used for estimating the unknown variables ($\sin(\Delta\varphi)$, $\cos(\Delta\varphi)$) in the system of linear equations in E from (7-16).

7.4.2 Calibration in radio mode

The calibration of the proposed MPR, when operating as radio, can be done through training data sequence. The output of the detectors upon removing the DC terms can be expressed as

$$\begin{aligned}
 \overline{V}_i &= \alpha_i \left(I \cos(\theta_{Lo} + \varphi_{12}^i + e_{12}^i) + Q \sin(\theta_{Lo} + \varphi_{12}^i + e_{12}^i) \right) \\
 &\quad + \beta_i \left(I \cos(\theta_{Lo} + \varphi_{17}^i + e_{17}^i - \Delta\varphi) + Q \sin(\theta_{Lo} + \varphi_{17}^i + e_{17}^i - \Delta\varphi) \right)
 \end{aligned} \tag{7-18}$$

where e_{12}^i is the phase deviation from the ideal value of φ_{12}^i and α_i includes the amplitude imbalance through the multiport network and the detectors' conversion gain. Applying the required phase conditions in our multiport receiver, one can reformulate (7-18) for all four outputs into:

$$\begin{aligned}
 \overline{V}_{n \times 4} &= R_{n \times 2} \times A_{2 \times 4} \\
 \overline{V}_{n \times 4} &= R_{n \times 2} \times \begin{bmatrix} W_1^3 & W_1^4 & W_1^5 & W_1^6 \\ W_2^3 & W_2^4 & W_2^5 & W_2^6 \end{bmatrix}_{2 \times 4}
 \end{aligned} \tag{7-19}$$

where R is the matrix of the n training I and Q symbols, i.e., $R = [I \ Q]_{n \times 2}$. The arguments of the matrix A include both the error terms and phase differences between incoming signals at the input ports which can be expressed from (7-19) as

$$\begin{aligned}
\begin{bmatrix} W_1^3 \\ W_2^3 \end{bmatrix} &= \begin{bmatrix} -1 & 0 & -\cos(\Delta\varphi) & -\sin(\Delta\varphi) \\ 0 & +1 & +\sin(\Delta\varphi) & -\cos(\Delta\varphi) \end{bmatrix} \begin{bmatrix} a_1^3 & a_2^3 & a_3^3 & a_4^3 \end{bmatrix}^T \\
\begin{bmatrix} W_1^4 \\ W_2^4 \end{bmatrix} &= \begin{bmatrix} +1 & 0 & +\cos(\Delta\varphi) & +\sin(\Delta\varphi) \\ 0 & -1 & -\sin(\Delta\varphi) & +\cos(\Delta\varphi) \end{bmatrix} \begin{bmatrix} a_1^4 & a_2^4 & a_3^4 & a_4^4 \end{bmatrix}^T \\
\begin{bmatrix} W_1^5 \\ W_2^5 \end{bmatrix} &= \begin{bmatrix} -1 & 0 & +\cos(\Delta\varphi) & +\sin(\Delta\varphi) \\ 0 & +1 & -\sin(\Delta\varphi) & +\cos(\Delta\varphi) \end{bmatrix} \begin{bmatrix} a_1^5 & a_2^5 & a_3^5 & a_4^5 \end{bmatrix}^T \\
\begin{bmatrix} W_1^6 \\ W_2^6 \end{bmatrix} &= \begin{bmatrix} +1 & 0 & -\cos(\Delta\varphi) & -\sin(\Delta\varphi) \\ 0 & -1 & +\sin(\Delta\varphi) & -\cos(\Delta\varphi) \end{bmatrix} \begin{bmatrix} a_1^6 & a_2^6 & a_3^6 & a_4^6 \end{bmatrix}^T
\end{aligned} \tag{7-20}$$

The matrix (A) can be estimated for any angle through the least square technique:

$$A = \left((R^* R)^{-1} R \right) \overline{V} . \tag{7-21}$$

The error terms of $(a_1^i, a_2^i, a_3^i, a_4^i)$ in each vector of matrix A remain unchanged for all incoming angles and can be obtained through solving the equations associated with two different arbitrary incoming angles for calibration. Thereafter and for any incoming AOA, I and Q components of the demodulated signal can be recovered from the weighted combination of all output signals through:

$$I = \sum_{i=1}^4 \chi_i V_i , \quad Q = \sum_{i=1}^4 \eta_i V_i . \tag{7-22}$$

The coefficients of χ_i and η_i are

$$\begin{aligned}
\chi_1 &= \frac{q_4}{q_4 q_1 - q_2 q_3} & \eta_1 &= \frac{-q_3}{(q_4 q_1 - q_2 q_3)} \\
\chi_2 &= -\chi_1 & \eta_2 &= -\chi_1 \\
\chi_3 &= \frac{-q_2}{q_4 q_1 - q_2 q_3} & \eta_3 &= \frac{1}{q_4} \left(1 + \frac{q_3 q_2}{q_4 q_1 - q_2 q_3} \right) \\
\chi_4 &= -\chi_3 & \eta_4 &= -\eta_3
\end{aligned} \quad \text{and} \tag{7-23}$$

where $q_{1,2,3,4}$ are obtained from the calibration matrix (A) and the phase difference associated with the relative angular position of the second unit. The information about $\Delta\varphi$ is already estimated in

the sensing mode and can be used to calculate $q_{1,2,3,4}$ and accordingly χ and η as:

$$\begin{aligned}
 q_1 &= -(a_1^3 + a_1^4) - (a_3^3 + a_3^4) \cos(\Delta \varphi) - (a_4^3 + a_4^4) \sin(\Delta \varphi) \\
 q_2 &= (a_2^3 + a_2^4) + (a_3^3 + a_3^4) \sin(\Delta \varphi) - (a_4^3 + a_4^4) \cos(\Delta \varphi) \\
 q_3 &= -(a_1^5 + a_1^6) + (a_3^5 + a_3^6) \cos(\Delta \varphi) + (a_4^5 + a_4^6) \sin(\Delta \varphi) \\
 q_4 &= (a_2^5 + a_2^6) - (a_3^5 + a_3^6) \sin(\Delta \varphi) + (a_4^5 + a_4^6) \cos(\Delta \varphi)
 \end{aligned} \tag{7-24}$$

It is worth mentioning that for such least square problems that are used within the proposed calibration technique, the minimum norm least square solution (*pinv function in Matlab*) can yield the best solution in practice [152].

7.5 Prototyped transceiver

Several remarkable features of the multiport interferometric technology, such as simplicity, low required power and wide achievable bandwidth, make it appropriate for applications around millimeter-wave frequency bands including automotive industry and backhaul radio connectivity. Therefore, the proposed multifunctional transceiver architecture is characterized, designed and prototyped for operation around 77 GHz, which is demonstrated in Figure 7-7. Some of the RF components including mixer, amplifier, switch and the Schottky diodes are the commercially available off-the-shelf monolithic microwave integrated circuits (MMICs) dies which are integrated with the designed passive components such as antenna, filter, coupler, and eight-port network using our in-house monolithic hybrid microwave integrated circuits (MHMICs) and PCB processes. The details of the designed transceiver are briefly discussed next.

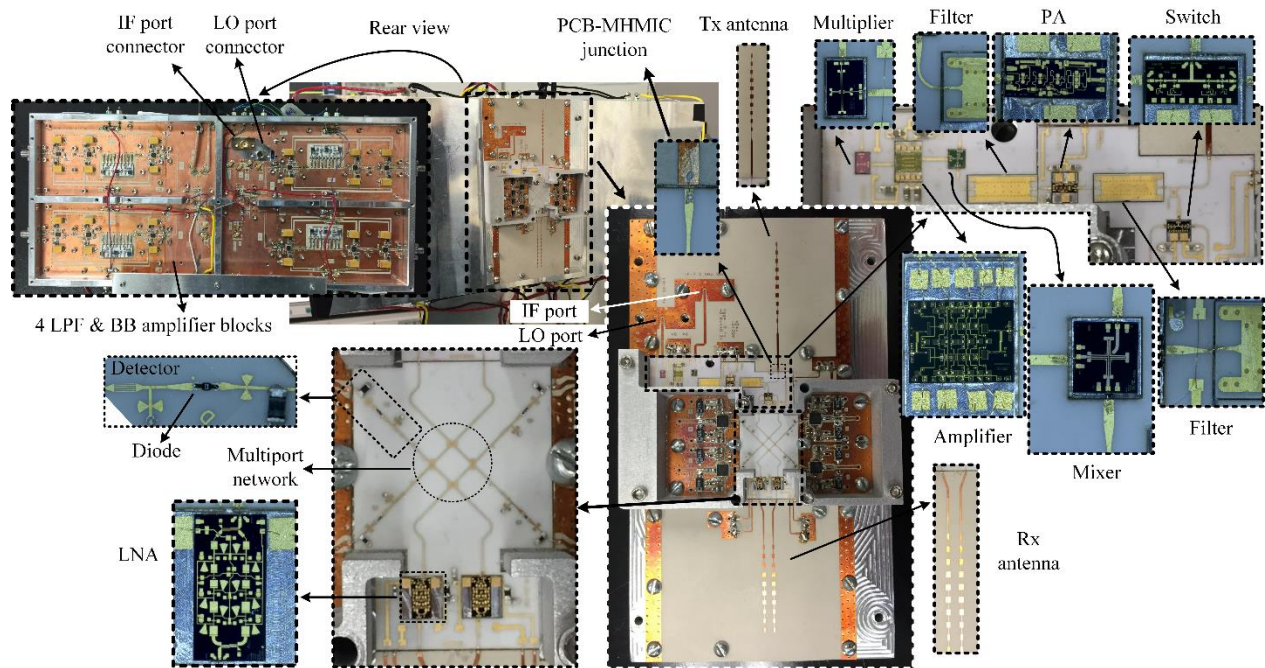


Figure 7-6: The prototyped transceiver

7.5.1 Tx block

The block diagram of the designed Tx unit, along with the part-number of the commercial components are depicted in Figure 7-7. The LO signal at 70 GHz with the required power (15 dBm) at the mixer is generated using a cascade of frequency multiplier (HMC-1105) and an amplifier (HMC-1144). The transmitting IF signal is up-converted by a mixer (MDB-277) and amplified throughout a power amplifier (AUH-320). Two band-pass-filters (BPF) filter out the LO signal which is leaking out to the RF port of the mixer.

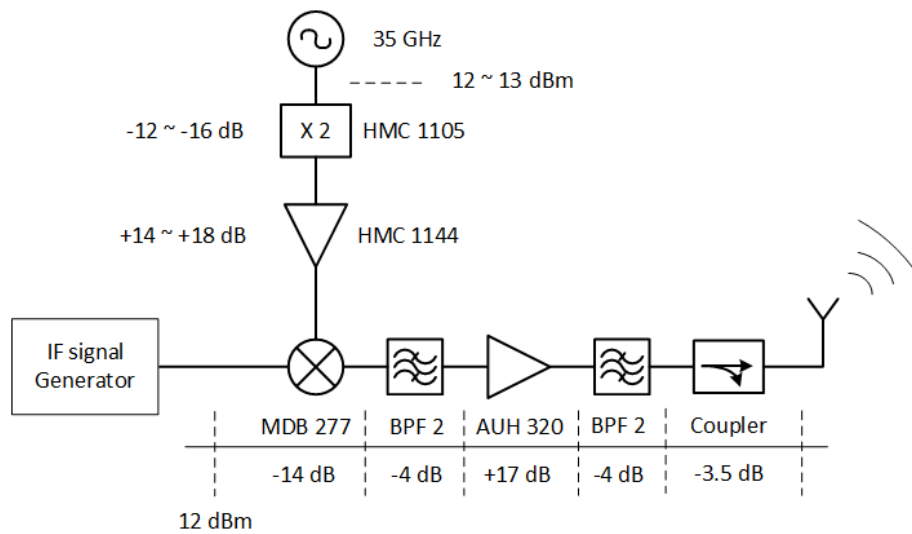


Figure 7-7: The block diagram of the designed Tx block for implementing the proposed transceiver.

A fourth-order substrate-integrated-waveguide (SIW) cavity BPF [153] is designed on alumina substrate which is a ceramic with relative permittivity of 9.9 and thickness of 0.254 mm. Figure 7-8 shows a microscopic photograph of the prototyped filter which is fabricated using our in-house high precision via-filled MHMIC technology. The vias in this filter were filled by gold for metallization purposes. The S-parameter measurement of the filter is carried out on a probing station. The microstrip-to-coplanar adaptor at the input of the filter for modes transition between CPW ground-signal-ground (GSG) probe and microstrip input line.

In Figure 7-9, the measured results of the fabricated filter are compared with those of simulations which were carried out in the commercial full-wave simulation package of HFSS. The metallic and dielectric losses were not considered and therefore a 2 dB difference between measured and simulated insertion losses can be observed. The frequency shift is attributed to the fabrication tolerance and oversize cutting of around 25 μm of the laser beam which was used for drilling the holes on the substrate. This inevitable tolerance that made changes in the dimensions were studied first through experiments and considered in final design.

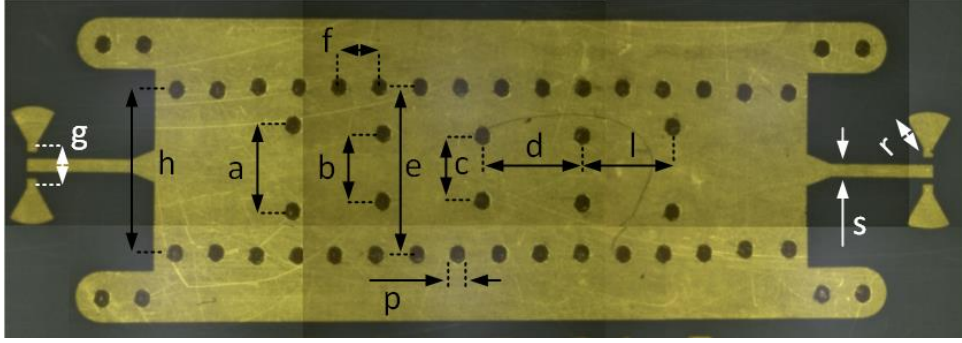


Figure 7-8: Microscopic photograph of the prototyped MHMIC SIW cavity BPF. The dimensions are: $g=275\text{ }\mu\text{m}$, $a=650.2\text{ }\mu\text{m}$, $b=523.2\text{ }\mu\text{m}$, $e=1.2\text{ mm}$, $c=497.8\text{ }\mu\text{m}$, $d=767\text{ }\mu\text{m}$, $l=703.6\text{ }\mu\text{m}$. $h=1.15\text{ mm}$, $s=94\text{ }\mu\text{m}$. $r=254\text{ }\mu\text{m}$, $f=304.8\text{ }\mu\text{m}$, $p=177.8\text{ }\mu\text{m}$.

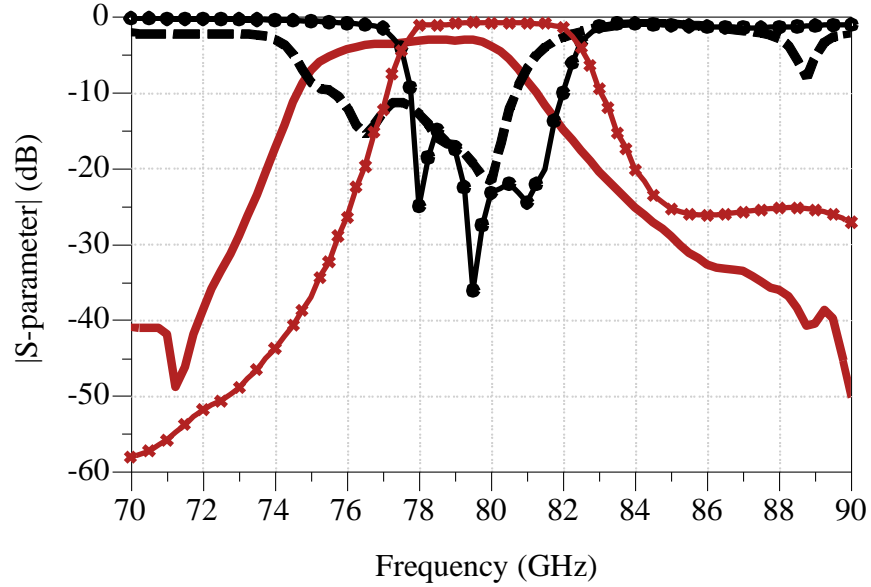


Figure 7-9: Measured and simulated S-parameters of the BPF. -x-: S_{21} simulation, -o-: S_{11} simulation, dashed line: S_{11} measurements, solid line: S_{21} measurements.

7.6 Antenna

Both Tx and Rx antennas are series-fed patch arrays [154, 155] with the gain of 16 dB and side-lobe level of around 18 dB. The prototyped Rx antenna is shown in Figure 7-10. Since WR10 metal waveguides are normally used for measurements around W-band frequencies (75 GHz -110 GHz), microstrip-SIW-WR10 convertor is added to the feed port of the antenna.

Figure 7-11 compares measured and simulated return loss of the antenna with 10 dB bandwidth of 1.5 GHz around center frequency of 77.5 GHz. The antenna pattern is also measured in two planes

and compared with simulations in Figure 7-12.

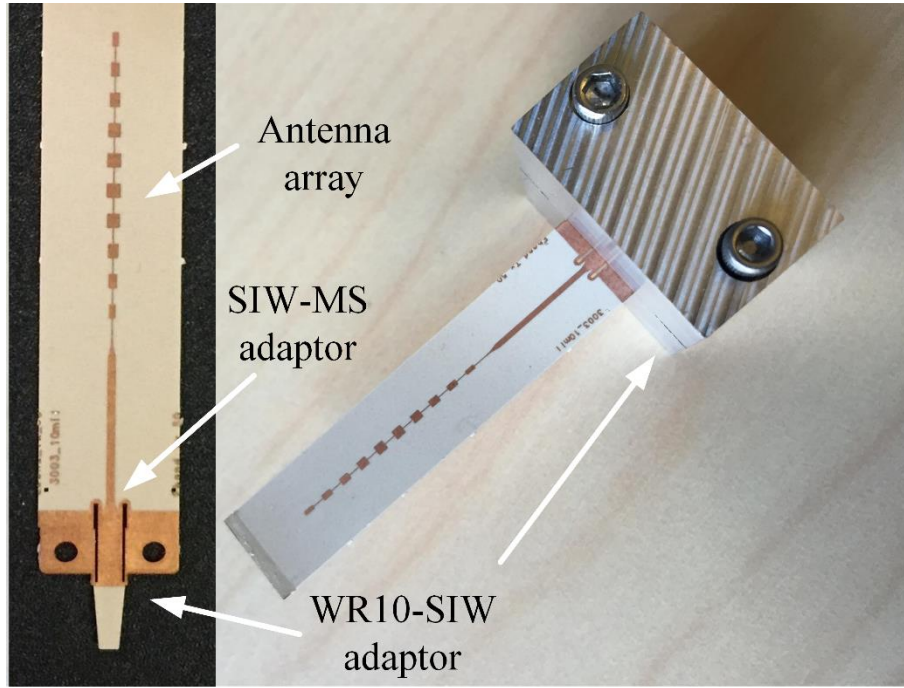


Figure 7-10: The prototyped Tx antenna with the SIW-WR10 adaptor. The edge-to-edge distance between adjacent elements are 1.239 mm; length of all element are 1.082 mm, and the width (W_i) of the i^{th} ($i=1$ to 5) element are 0.432 mm, 0.584 mm, 0.716 mm, 0.858 mm, 0.960 mm, respectively. The same antenna elements are used for Rx antenna. The distance between antenna elements are 0.6λ .

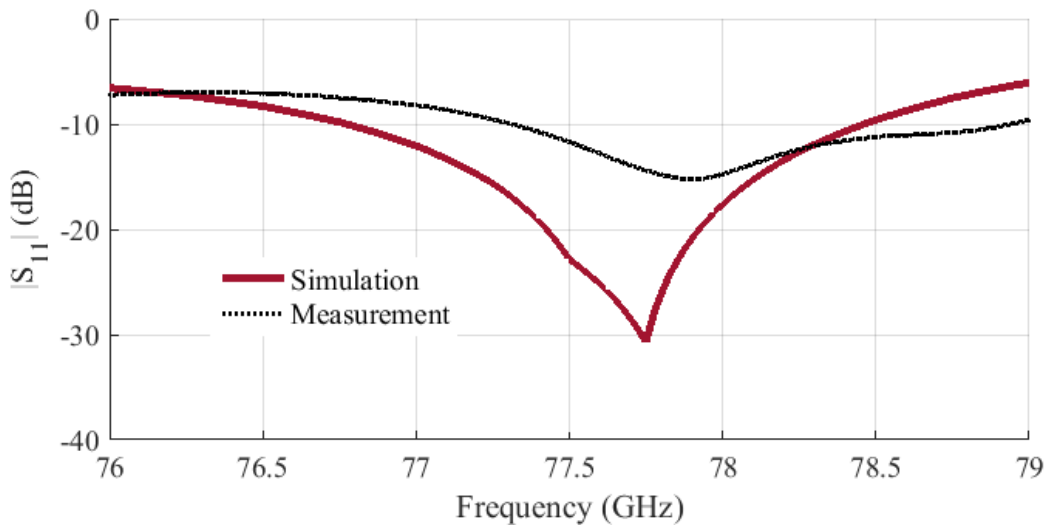


Figure 7-11: Measured and simulated S11 of the antenna.

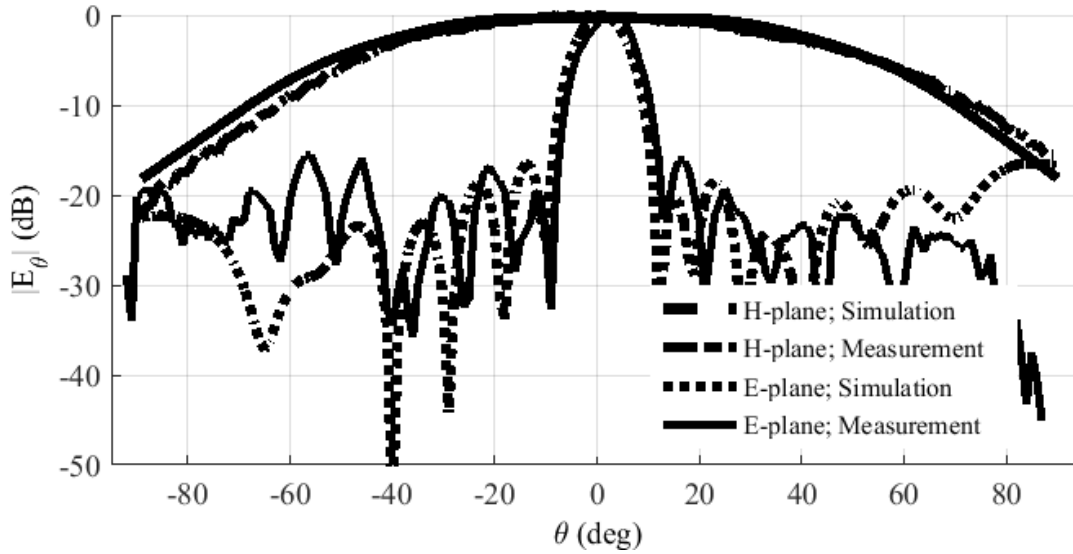


Figure 7-12: Measured and simulated series-fed antenna pattern in two planes.

7.6.1 Rx block

As it is shown in Figure 7-6 the Rx block consists of two LNAs (ALH-509) for two RF paths, eight-port network and the detector circuits with baseband amplifiers.

The 180 hybrid coupler in the first eight-port topology should essentially be a coupler with non-interspersed ports as it is demonstrated in chapter 6 to avoid the routing problems within the eight-port layout. The required phasing condition for the proposed multifunction multiport network in (7-12) can be realized with another configuration of couplers and phase shifter blocks other than the one presented in Figure 7-1. The second topology which is comprised of four 90° hybrid couplers readily satisfies the essential relative phase differences in (7-12) and is implemented on alumina ceramic substrate as it is shown in Figure 7-13. The design rules and considerations of such millimeter-wave quadrature couplers that are also used in our multiport topology were already discussed by [156-158]. Therefore, they are not repeated herein.

The S-parameter of the fabricated eight-port network was measured using the probing station and the results are presented in Figure 7-14, and Figure 7-15. Due to the symmetry within the second topology of the eight-port network, only one pair of ports in two distinct circuits were terminated with a designed microstrip-to-GSG probe adaptor, while other ports were match-loaded. The agreement of the measured phase relationship with the ideal desired values is confirmed in Figure 7-15. The technique of through-reflect-line (TRL) was implemented for calibration using the kit

on the same board. The effect of extra length of the transmission lines at the input/output ports were also considered in phase-difference calculation.

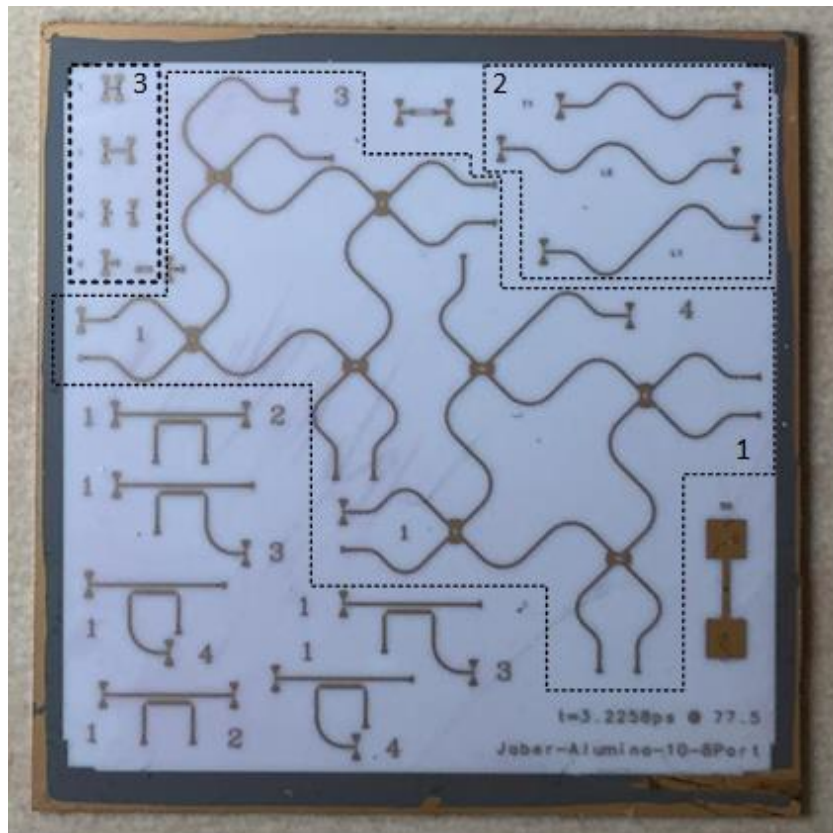


Figure 7-13: Fabricated multiport circuit on ceramic substrate using MHMIC process. Zone 1: two eight-port circuits for measuring S_{13} and S_{14} , Zone 2: Phase compensating lines, Zone 3: TRL calibration kit

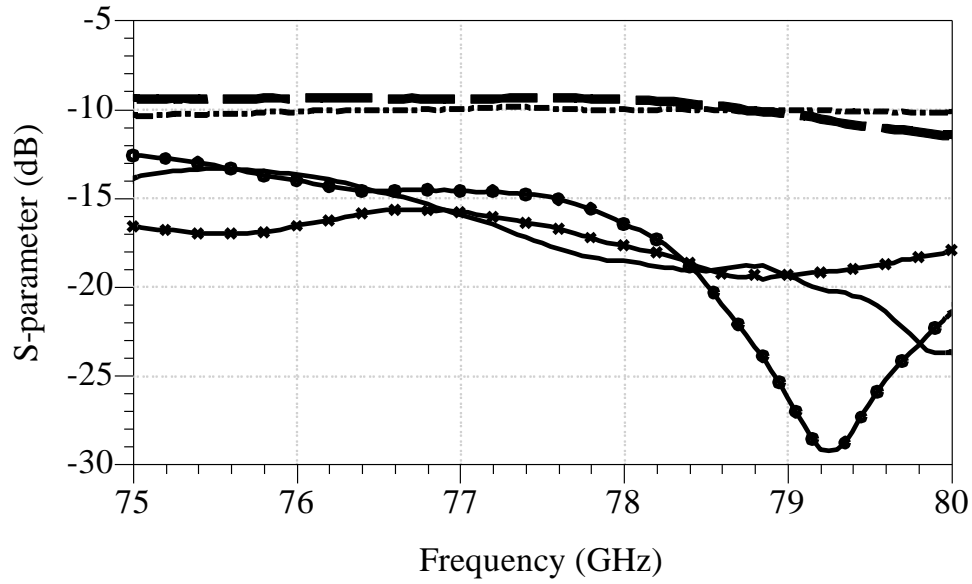


Figure 7-14: Measured S-parameter of the multiport network. —o—: S_{11} , —x—: S_{33} , solid line: S_{44} , dashed line: S_{13} , —.—: S_{14} .

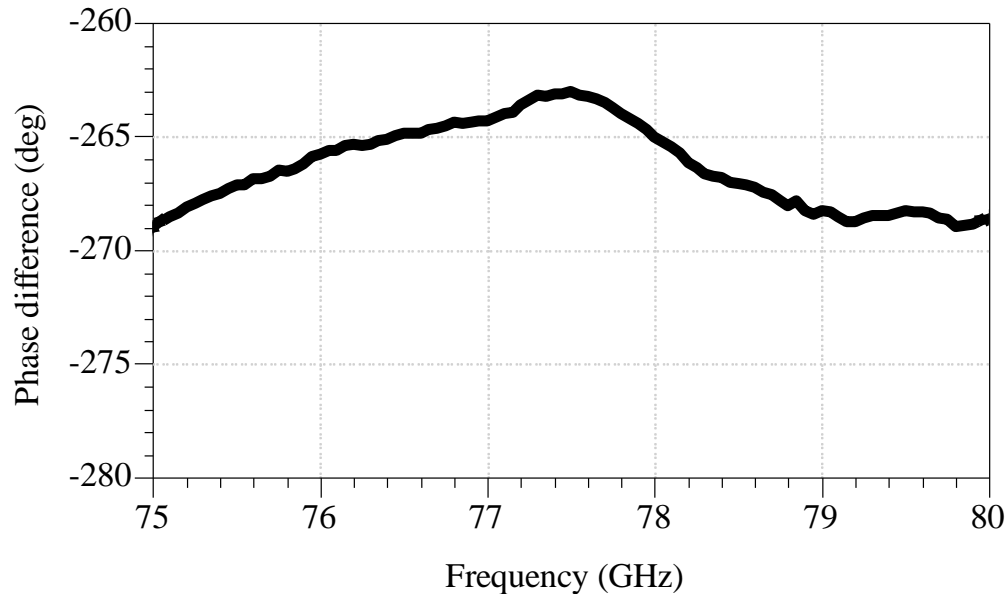


Figure 7-15: Measured phase difference between input and output ports of the prototyped multiport ($\angle S_{13} - \angle S_{14} = 90^\circ$).

The schematic of the diode detector circuit is shown in Figure 7-16 which is designed with the Schottky diode model of MZBD-9161 from Aerolfex and optimized in ADS. The available SPICE model of the diode was first completed based on several sets of large and small signal measurements of one diode on one alumina substrate.

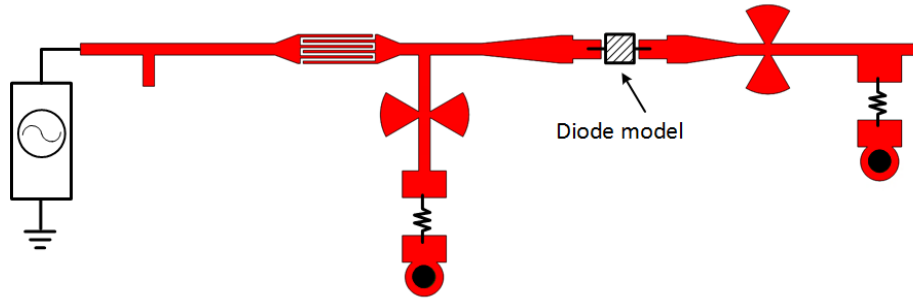


Figure 7-16: Schematic circuit of the Schottky diode for simulation in ADS.

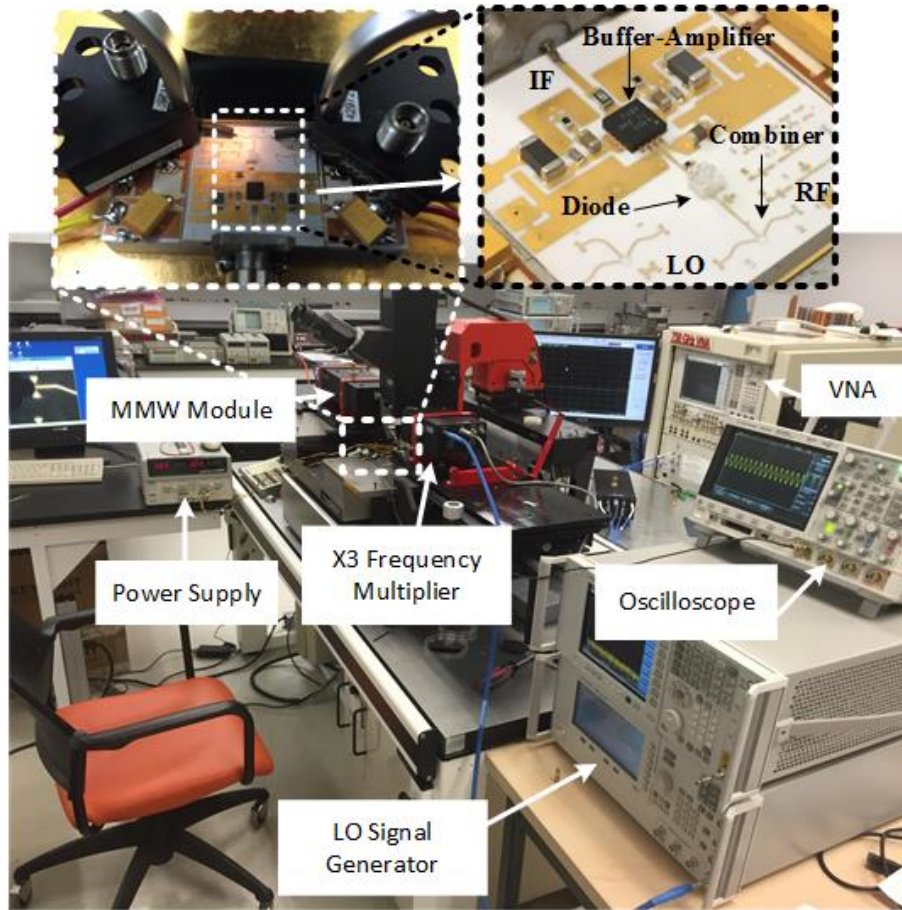


Figure 7-17: Prototyped detector circuit in measurement setup.

Through curve-fitting of I - V diode model ($I = I_s(\exp((q/nkT)(V - R_s I)) - 1)$) with the measured I - V curves, the DC model parameters, including the diode ideality factor (n), saturation current (I_s) and series resistor (R_s) were first obtained. Subsequently, the parasitic effect of the diode package and the I/O signal leads on 50 Ω transmission line were estimated using the

measured complex input impedance and detected voltage over a range of input power.

The designed detector was fabricated through our in-house MHMICs process on alumina substrate and its performance was assessed through measurements. Figure 7-17 shows the prototyped detector in the measurement setup. The Wilkinson power combiner with the topology proposed by [157] at the input of the detector was used for adding the RF and LO signals at the detector input to measure the conversion loss with different LO powers. The RF signal at 77.5 GHz was provided by PNA-X vector network analyzer (N5247A), while a combination of signal generator and frequency multiplier (X3) was used for generating the LO signal at around 77.4 GHz. Both RF and LO signal powers were measured by a power meter (E4419B) and the loss of the WR-10 waveguide, probe and power divider were considered in setting up the desired power level at the diode input port. Figure 7-12 shows the measured RF to IF conversion gain over a range of LO signal power versus different RF signal power.

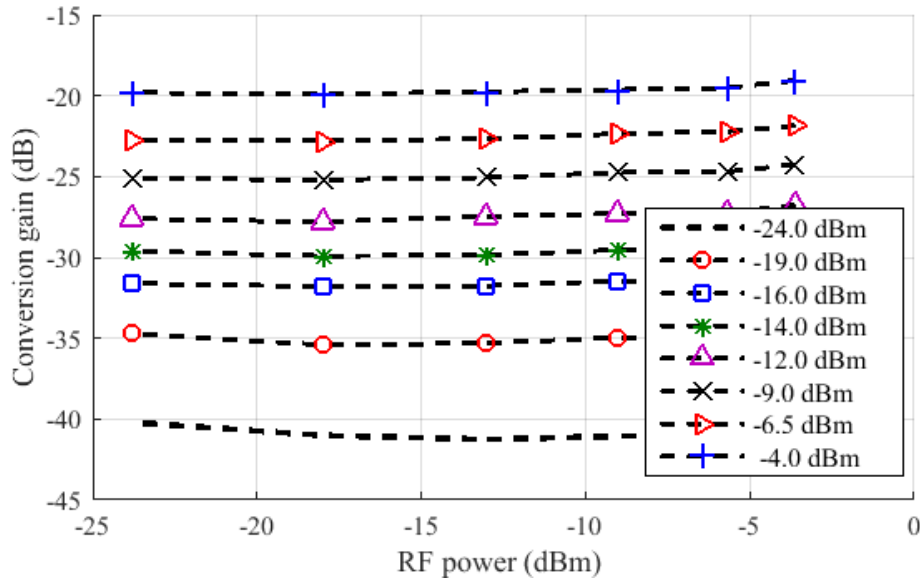


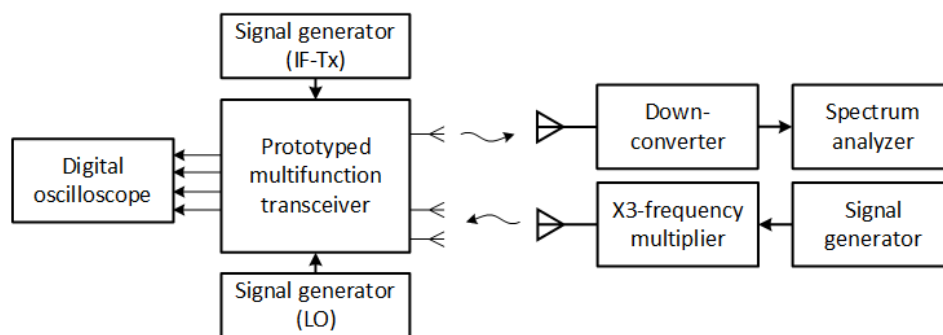
Figure 7-18: Measured RF-IF conversion gain of prototyped detector at different LO powers. RF and LO frequencies were 77.5 GHz and 77.470 GHz, respectively. The load resistor was 100 K Ω .

7.7 System-level measurements

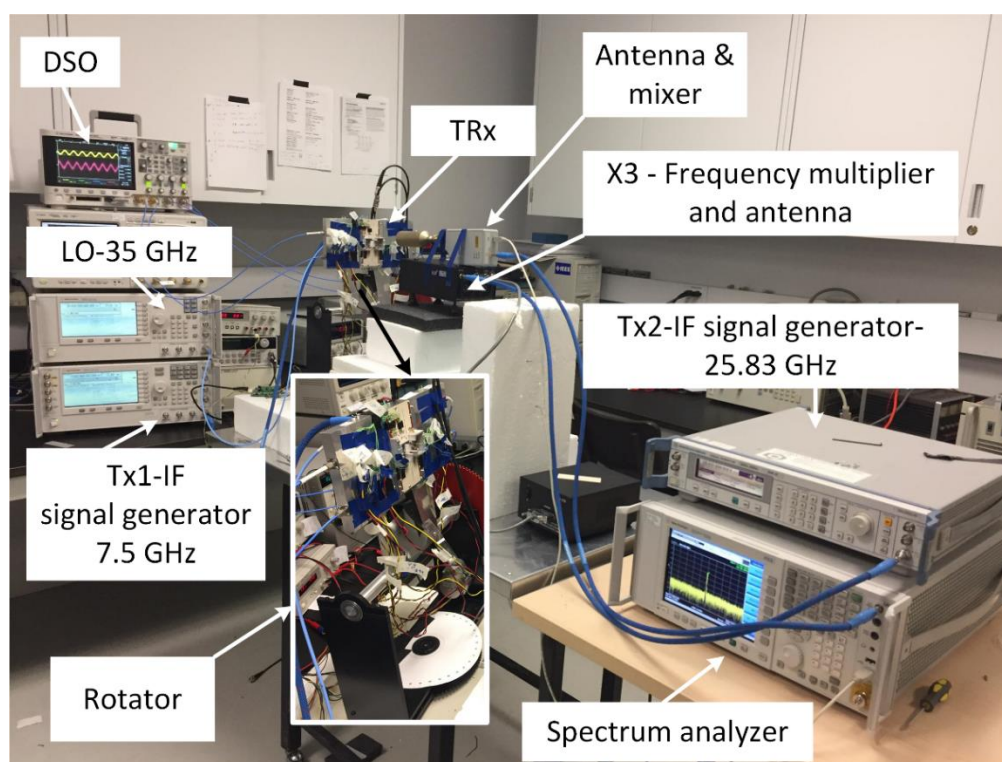
To evaluate the performance of the proposed transceiver, system-level measurements were carried out in our laboratories and the measurement results are presented. Figure 7-19 shows the in-lab measurement setup without the absorbers that were placed sufficiently to reduce the effect

of multi-reflection. The prototyped transceiver module is mounted on a mechanical rotator for its accurate rotation horizontally. This resembles the situation in which the incoming signal is received from different desired angles. The 35 GHz LO and the 7.5 GHz IF signals for the Tx block are generated by PSG (E8257D) analog and (E8267D) vector signal generators, respectively. All signal generators that are used for LO and IF signals were synchronized. The transmitted signal at the frequency of 77.5 GHz from the Tx antenna is received by a horn antenna and down-converted through a waveguide harmonic mixer from Agilent Technologies (M1970W) that was connected to the spectrum analyzer (Keysight-PXA-N9030A). Hence, the signal displayed in the spectrum analyzer shows the signal at the output of the transmitter block, which is travelled through a free-space channel within a distance of around 30 cm.

On the other hand, a single frequency sinusoidal signal at around 77.5 GHz is generated and transmitted toward the prototyped transceiver, using a combination of signal generator (SMR-40), X3-frequency multiplier and a horn antenna. The received down-converted signals at the output of our transceiver are probed by the digital oscilloscope (DSO-X3034A). The spectrum of the transmitted signal is demonstrated in Figure 7-20 which shows the signal peak at 77.5 GHz with power of around -38 dBm. On the other hand, the IF signal at the frequency of 10 MHz can be seen in the oscilloscope that proves the functionality of the full chain.



(a) Block diagram of the test-bed



(b) Picture of the in-lab measurement setup

Figure 7-19: System level measurement setup (without absorbers).

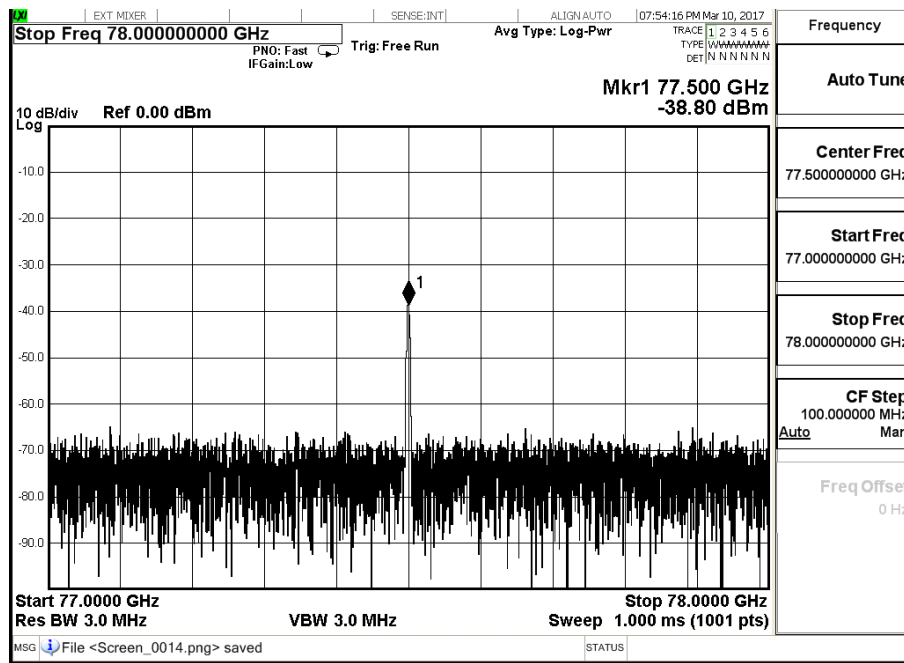


Figure 7-20: Received signal at the spectrum analyzer.

To assess the system performance for different functions including AOA and communication, a few sets of measurements were carried out which are presented in the following.

7.7.1 AOA detection

For system evaluation in terms of AOA estimation, the prototyped transceiver was rotated to different angles, while the position of the other unit as a signal source remained unchanged. Due to some limitation of our rotator, sweeping only a range of angles between -5° to 5° was feasible. The system was initially calibrated through the proposed calibration technique prior to complete measurements for all angles. The measurement results of the M vector, associated with each angle, are compared with the ideal values in Figure 7-21. It can be observed that the measurement results are in close agreement with the ideal values. The existing errors are mainly attributed to a poor signal-to-noise-ratio (SNR) of the probed signals at the output of the detectors which is measured to be around 9 dB. It should be noted that the calibration was carried out at two arbitrary angles of 0° and 3° , and therefore the errors at these two angles are zero. The measured M vector can readily be converted to AOA through (7-11) which is not shown herein.

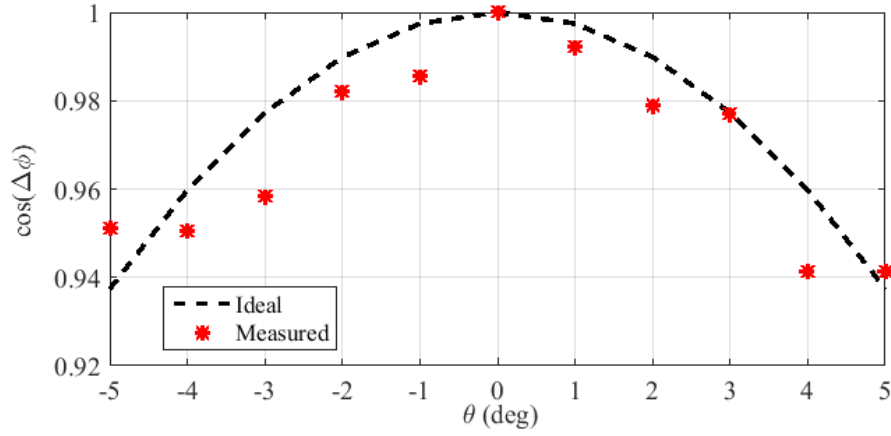
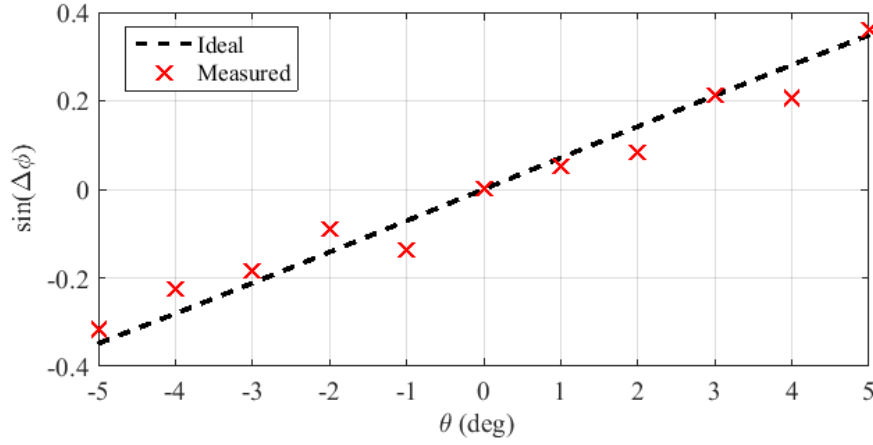
(a) $\cos(\Delta\varphi)$ (b) $\sin(\Delta\varphi)$

Figure 7-21: Measurement result of AOA detection.

7.7.2 Radio communication

The measured S-parameters of the prototyped multiport circuit and the measured detector models were incorporated within the proposed transceiver in the commercial software of ADS for system-level measurements. Therefore, the phase and gain imbalances throughout the prototyped multiport network were taken into account. Imbalances up to 1.5 dB were also considered between conversion losses of different detectors.

Figure 7-22 shows the schematic view of the block-diagram of the platform for this measurement that is conducted through co-simulations of MATLAB and ADS. Random data are generated, modulated and sent to ADS upon root-raised-cosine (RRC) filtering in MATLAB. I and

Q components were used to modulate the RF carrier that goes through AWGN channel to the input of the multiport network. The PDOA between received signals at the output of the antenna elements was stimulated using a phase shifter block. The detected signals at the output of the receiver are processed in MATLAB for calibration, recovery and match-filtering.

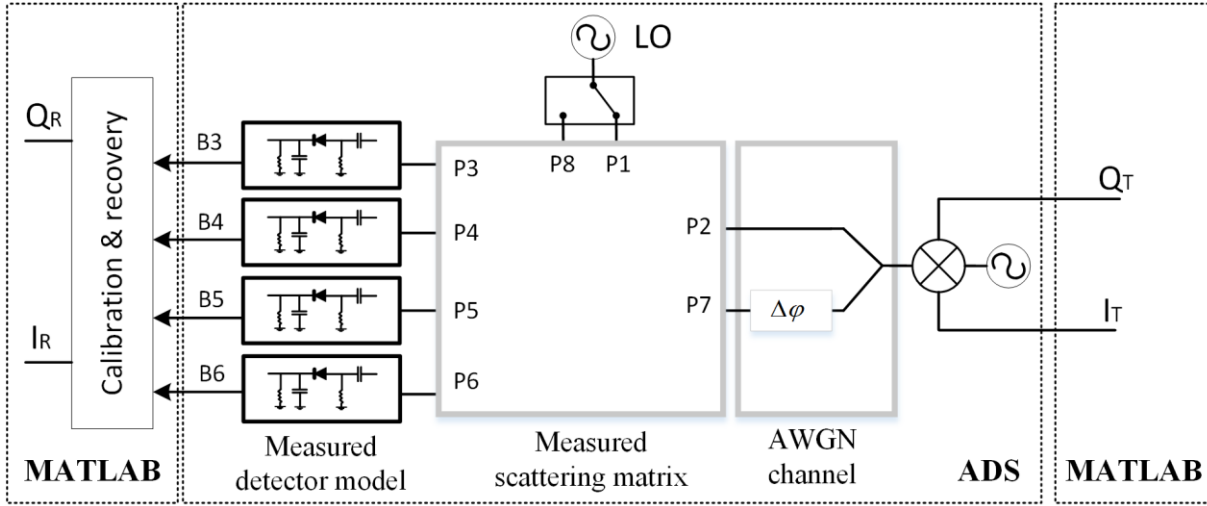


Figure 7-22: The block-diagram of the system-level simulation platform in ADS and MATLAB.

The initial test was carried out with a high value of SNR to evaluate merely the proposed technique of calibration and I - Q recovery in the presence of the practical circuit non-idealities and non-zero AOA. Figure 7-23 compares the constellation diagrams of the received I - Q components of the 16-QAM modulated signals before and after recovery with those of the transmitted signal from the angle $\theta = 5^\circ$. The imbalance in the diagram before recovery is due to the existing non-zero PDOA between the received signals at the terminals of two antenna elements. The phase and gain imbalances within the measured receiver model disturbs the constellation points that can be readily observed. An excellent agreement of the recovered constellation points with the reference ones validates the functionality of the proposed calibration and recovery technique for this multifunction receiver. It is worth mentioning that received signal should be match-filtered after recovery and calibration.

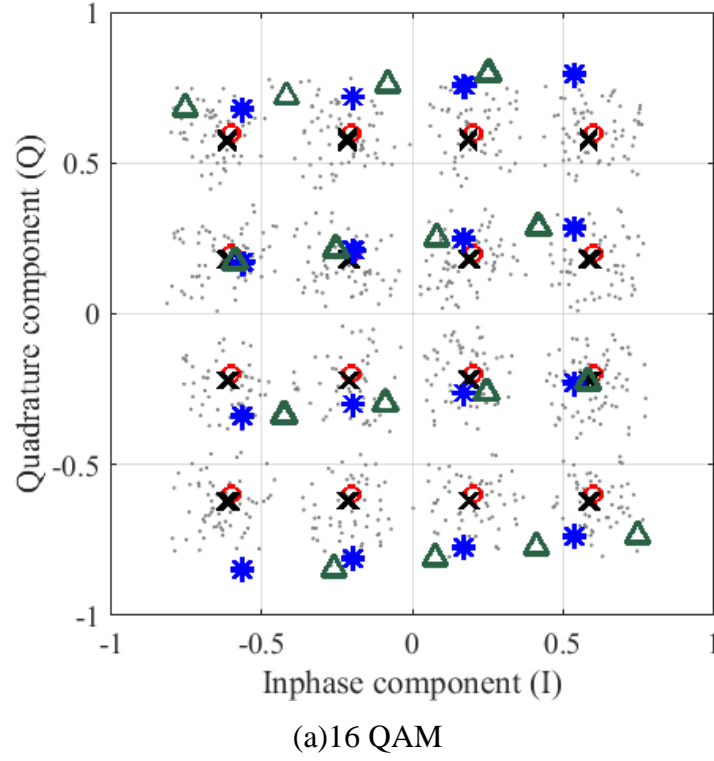


Figure 7-23: The constellation diagram of the simulated receiver with non-idealities. O: reference points, *: recovered directly from (13) without calibration, X: recovered with calibration, triangle: without recovery and without calibration, dots: without match filtering, roll-off factor=0.5; filter span: 8 symbols; 10 samples per symbol, AOA=5°.

In the second set of measurements, the error vector magnitude (EVM) of the received signal for a range of AOA was calculated through (7-23) when calibration was done at two arbitrarily selected angles of 2° and 6°. It should be noted that for I - Q recovery it is assumed the M vector is known for each AOA. In Figure 7-24, the EVM of the received signal before and after recovery are compared versus different AOA. The significant improvement of the EVM proves the impact of the proposed recovery and calibration technique.

$$EVM_{RMS} = \sqrt{\frac{\frac{1}{N} \sum_{k=1}^N (I_k - I_k^r)^2 + (Q_k - Q_k^r)^2}{\frac{1}{N} \sum_{k=1}^N I_k^2 + Q_k^2}} \quad (7-23)$$

The final test was carried out with higher modulation order (i.e. 64 QAM) with different values of SNR of the signal at the input of the receiver. SNR is considered to be $(\log_2 M) \times E_s/N_o$, where

E_s denotes the average symbol energy and N_o is the noise power spectral density (PSD). In this line-of-sight (LOS) radio measurement over additive white Gaussian noise (AWGN) channel, the Gaussian noise model was used to model the thermal noise and the noise in the receiver circuitry that cause signal degradation. Figure 7-25 compares the received constellation diagram before and after recovery with the SNR value of 20 dB and the AOA of 10° . One can observe a successful signal calibration and recovery in the presence of noise and severe signal degradation with large values of AOA. In addition, the EVM was also measured versus different SNR value for two modulation orders of 16 and 64 and the results are plotted in Figure 7-26. In [159], it was shown how the EVM can be theoretically related to SNR. Therefore, the measurement results in Figure 7-26 are compared with the theoretical EVM values that are calculated using equ. (4) in [160]. One can observe that the measured EVM values are in close agreement for SNR larger than 15 dB. It is worth mentioning that the error terms in (7-19) are independent from the modulation order and they are estimated only once with the SNR of 20 dB in connection with the data sequence belonging to one modulation order in these measurements.

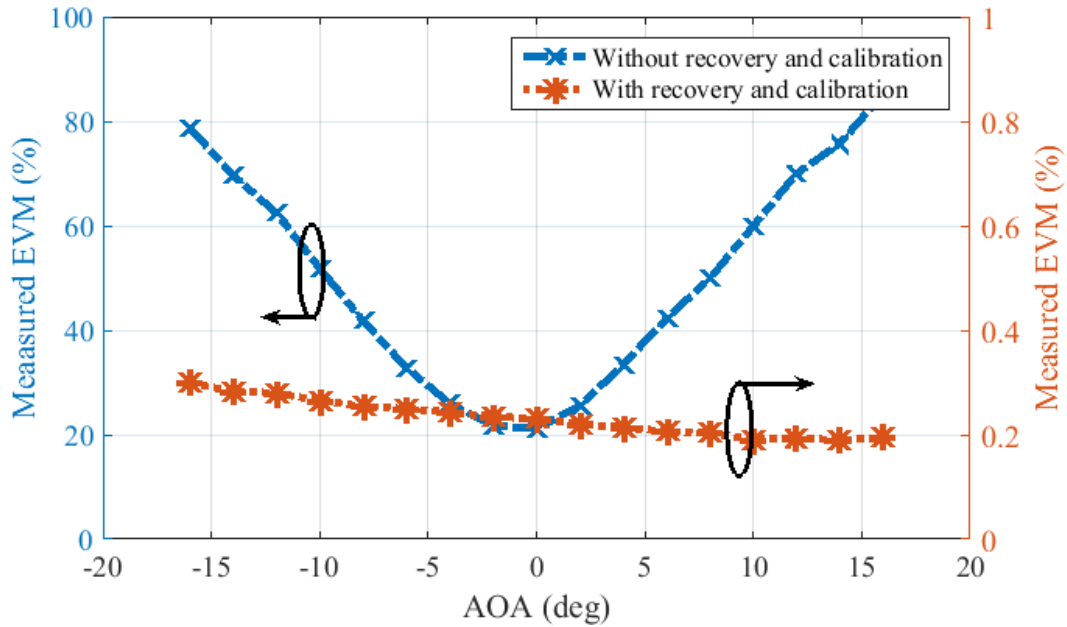


Figure 7-24: The EVM over different AOA. Calibration was done at angles 2 and 6 modulation of 16 QAM.

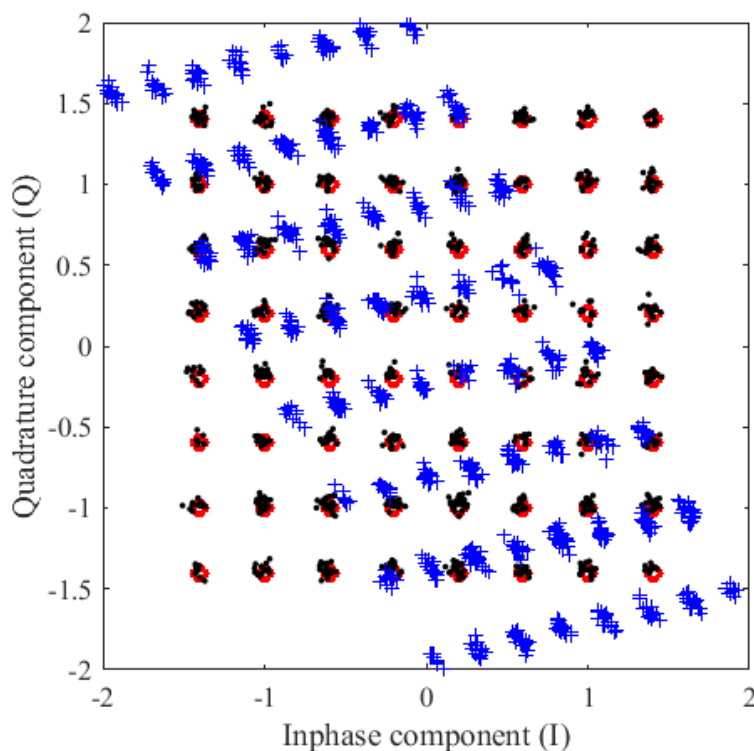


Figure 7-25: Measured constellation diagram when SNR =20 dB, AOA=10°. Calibrated with SNR=20 dB. O: reference points, dot: received after calibration and recovery, +: without recovery and calibration. 64-QAM; 1000 symbols; RRC filter; roll-off factor=0.5; filter span: 8 symbols; 10 samples per symbol and data rate= 4 MHz. AOA=10°.

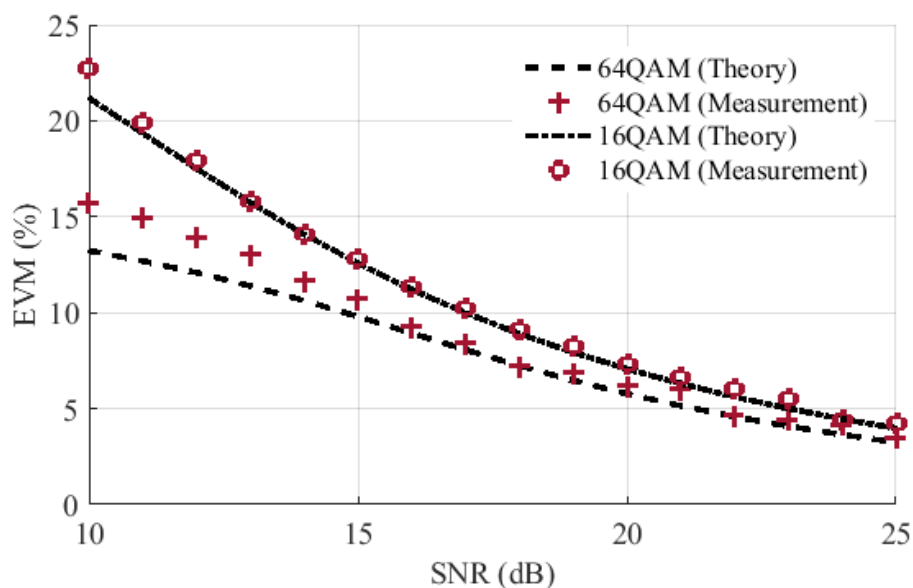


Figure 7-26: The EVM over SNR. Calibration was done when we had noise and SNR=20 dB.

7.8 Conclusion

A multifunction system scheme is proposed, analyzed and implemented in this paper. It is mainly based on the technique of multiport interferometry and integrates two functions of angle detection and data communication through a simple architecture. Furthermore, two formerly distinct six-port receivers with different configuration of input signals are unified within a single multiport interferometric system through the proposed eight-port correlator and configuration of four input ports for RF and LO signals and four output ports for detected signals.

The proposed multiport network features a new phasing condition to deal with the incompatibilities between the distinct system functions. Two different variants of the topology of passive network are also shown that satisfy the required phase condition. The proposed receiver is also mathematically modeled and its operation principles are analyzed theoretically. The AOA parameters of the incoming signal can be estimated through a simple proposed signal processing algorithm. A technique out of data fusion was also proposed for recovering the demodulated signal from the distorted I - Q output signals.

To assess the presented concept, the multifunction eight-port interferometric receiver architecture is employed in a complete transceiver and implemented for applications around millimeter-wave frequency bands along with an appropriate operational waveform scheme. In addition to the discussions for implementation of such integrated transceiver, system-level measurement results are presented for concept validation.

One limitation of such multifunctional multiport based transceiver is the short operational range which is mainly because of the poor dynamic range of such technique. Another limitation can be observed in the proposed calibration technique and if the initial phase difference between two units changes after initial calibration, the calibration should be repeated.

Nevertheless, such Rx topology can find applications in future 5G and future wireless systems including autonomous driving and self-adaptive mobile intelligence with the capability of communication. This would make the future multifunctional transceivers rather compact and low cost alternatives of the tedious assembly of them on one platform.

CHAPTER 8 2-D DIRECTION OF ARRIVAL (DOA) ESTIMATION SYSTEM THROUGH MULTIPORT TECHNOLOGY

As it was already mentioned through the introduction of this thesis in chapter 1, development of multifunction systems can also address the integration of multiple sensors and is not limited to only RadCom systems. Therefore, in continuation of research within the framework of this PhD thesis, we have also developed multifunction system schemes through which multiple sensing functions are integrated in a single unified system. In this chapter, a 2-D AOA sensor is presented that is unifying two AOA estimation systems, indeed.

The demand for accurately estimating an incoming beam's AOA is often encountered in a wide range of application areas such as industrial machinery localization, object positioning or antenna-to-antenna alignment [36, 43, 79, 80]. Moreover, there are certain systems in which fast simultaneous angle detection in both horizontal and vertical planes, i.e., two-dimensional (2D) direction of arrival (DOA) is required. Correction of the antenna beam misalignments over a two dimensional space in point-to-point radio systems [43] is a good example of this kind. This scenario can also be found in highly directive wireless links between ground stations and mobile aircrafts such that transmit antenna is constantly re-oriented in real time toward receiver antenna.

As it is discussed in chapter 2, AOA detection systems were developed which is shown in Figure 2-8 using the classic six-port junction. However, all solutions reported so far can estimate the direction of arrival in merely one dimension, i.e., only azimuth or altitude angle, to our best knowledge. The assembly of two distinct six-port AoA detection modules (i.e. one for horizontal and the other for vertical angle) may present one solution for two dimensional AoA estimation. However, it does not lead to an attractive scheme in terms of cost and size even if practical implementation challenges may be overcome [161].

Other possible solutions for two dimensional DOA were disclosed in [162-167]. In [165], a novel antenna topology is proposed where three antenna elements are arranged in a specific two-dimensional planar fashion with the fourth one in a different plane. The RF received signals are down-converted to IF upon being mixed by coherent local oscillators. The phase of the filtered IF signals is then compared using phase detectors and processed further for angle estimation. In [166], a linear interferometer array of receiving elements is used. In [168], an antenna system is presented

that consists of three elements including a right-handed and a left-handed circular polarized antenna in addition to an omnidirectional bi-conical dipole antenna. It is a hybrid solution by which the desired DOA information is extracted from the difference in phase modes and the interferometric phase difference. However, large size and small operational zone are its main constraints [169].

In this chapter, a holistic system solution is presented that makes use of two main features of multiport technique, i.e., excellent phase resolution and plurality of ports for 2D DOA estimation. The proposed system consists of three main parts, namely an antenna, a multiport wave interferometric receiver or phase discriminator and a signal processor. The antenna is composed of four receiving elements located in the same plane, which is arranged in a diamond-shaped configuration. The received signals manifest relative phase differences that contain information about the beam's direction of arrival. A multiport passive junction is proposed and described in this chapter, which allows the superposition of four input signals with a specific phase relationship. This is different from the conventional six-port design platforms. The tailored multiport scheme yields multiple signal mixing products at the outputs of power detectors that are solvable for obtaining two unknown angle values. In other words, with the proposed eight-port junction topology, the interferometer extracts these informative phase differences and leaves them for a simple signal processing algorithm to estimate the two angles.

In addition, an appropriate calibration technique is formulated and presented herein to deal with non-idealities and consecutive errors in practice. Moreover, the system is implemented over millimeter-wave frequency bands (60 GHz) using a combined design technique of substrate integrated waveguide (SIW) and microstrip line. The work is finally concluded upon the presentation of system-level measurement results. Excellent results are obtained, thus validating the outstanding functionality of the proposed system. The result of our research in this project, which have been reported in [170] and [171], are discussed in this chapter.

8.1 System scheme and analysis

Our proposed 2D DOA detection system consists of an antenna with four receiving elements, a multiport interferometric receiver, and also a signal processing unit. The principles of operation along with the main features of each individual part are discussed in the following.

8.1.1 Antenna topology and plane wave

Figure 8-1 shows the topology of the antenna structure with four independent linearly polarized receiving nodes. The relative distance between the phase centers of each pair in two horizontal and vertical axes is identical, namely L .

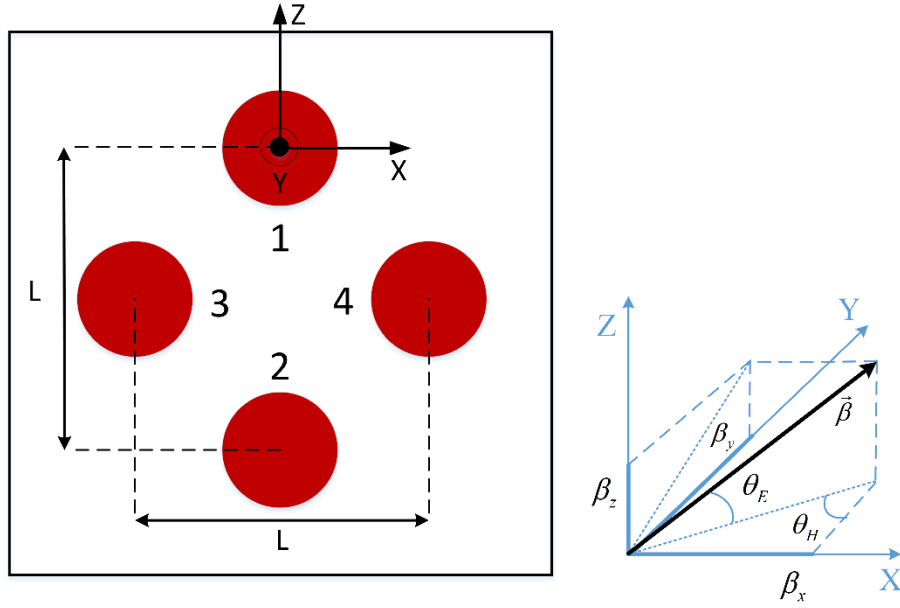


Figure 8-1: Receiver antenna structure with four receiving elements and their interaction with the propagation vector of an incoming plane wave

This configuration of receiving elements allows for capturing signals from the arriving wave-front with phase differences in accordance with its azimuth (θ_H) and altitude (θ_E) AoA.

The plane wave denoted by \vec{e} arriving at the antenna is expressible as:

$$\vec{\varepsilon}(x, y, z, t) = \text{Re} \left\{ \vec{E}(x, y, z) e^{j\omega t} \right\} = \text{Re} \left\{ E_0 e^{-j\vec{\beta} \cdot \vec{r}} e^{j\omega t} \right\} = E_0 \cos(\omega t - \vec{\beta} \cdot \vec{r}) \quad (8-1)$$

where $\vec{r} = \vec{x} + \vec{y} + \vec{z}$ is the position vector and $\vec{\beta} = \beta_x \vec{x} + \beta_y \vec{y} + \beta_z \vec{z}$ is the wave propagation vector. As it is sketched in Figure 8-1, $\vec{\beta}$ may be related to θ_H and θ_E with the antenna's normal vector, i.e. $\vec{n} = 0\vec{x} + 1\vec{y} + 0\vec{z}$. Hence, the components of the propagation vector, projected on Cartesian coordinate system would be:

$$\begin{aligned}
\beta_x &= \beta_o \cos \theta_E \sin \theta_H \\
\beta_y &= \beta_o \cos \theta_H \cos \theta_E \\
\beta_z &= \beta_o \sin \theta_E
\end{aligned} \tag{8-2}$$

Accordingly, the phase of the incoming plane wave ($\vec{\beta} \cdot \vec{r}$) at each receiving element in the coordinate system with its origin located at the center of receiving element 1 are

$$\begin{aligned}
\vec{\beta} \cdot \vec{r}_1 &= 0 \\
\vec{\beta} \cdot \vec{r}_2 &= -\beta_o L \sin \theta_E \\
\vec{\beta} \cdot \vec{r}_3 &= -\beta_o \frac{L}{2} \cos \theta_E \sin \theta_H - \beta_o \frac{L}{2} \sin \theta_E \\
\vec{\beta} \cdot \vec{r}_4 &= \beta_o \frac{L}{2} \cos \theta_E \sin \theta_H - \beta_o \frac{L}{2} \sin \theta_E
\end{aligned} \tag{8-3}$$

Thus, assuming $\varphi_E = \beta_o L \sin \theta_E$ as phase difference between the signals appearing at antenna elements 1 and 2, and $\varphi_H = \beta_o L \cos \theta_E \sin \theta_H$ as phase difference between the signals at antenna elements 3 and 4, (3) can be written as

$$\begin{aligned}
\vec{\beta} \cdot \vec{r}_1 &= 0 & \vec{\beta} \cdot \vec{r}_2 &= -\varphi_E \\
\vec{\beta} \cdot \vec{r}_3 &= -\frac{\varphi_H}{2} - \frac{\varphi_E}{2} & \vec{\beta} \cdot \vec{r}_4 &= \frac{\varphi_H}{2} - \frac{\varphi_E}{2}
\end{aligned} \tag{8-4}$$

Given these phase values, the angles of the incoming electromagnetic beam can be estimated. To extract the phase differences of φ_E and φ_H out of the received signals, a topological architecture of multiport interferometer is proposed in this work, which is explained as follows.

8.2 Multiport interferometer topology

Figure 8-2 shows the proposed topology of the multiport network with four 90°-hybrid couplers and three phase shifters. P1, P2, P7 and P8 are input ports expectedly connected to receiving antenna elements of 1, 2, 3 and 4, respectively. The proposed multiport architecture is different from the classical six-port junction not only in the number of available ports but also in the relative phase shifts that the input signals would experience throughout multiport interference. This critical interferometric phase relationship helps extract the phase differences of the incoming wave at four antenna elements from the superimposed and mixed signals at the output of detectors, and consequently the DOA information can be obtained. The most popular topologies of six-port

junction is formed by three 90°-hybrid couplers and one power divider [35] or four 90°-hybrid couplers with one 90° phase shifter [151] to superimpose the two input signals with relative phase differences of multiple of $\pi/2$ at four output ports.

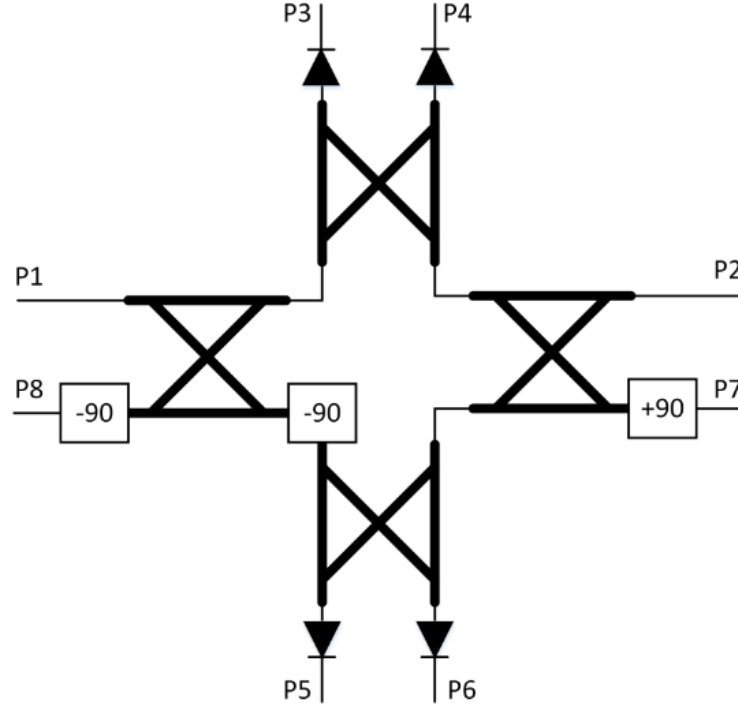


Figure 8-2: Proposed multiport interferometer topology for 2D DOA parameter extraction

Considering the scattering matrix of this passive interferometric junction, one can express the specific phase relationship of the four input signals that appear at the four output ports as:

$$\begin{cases} \angle S_{31} - \angle S_{38} = 2n\pi - \pi \\ \angle S_{31} - \angle S_{32} = 2n\pi + \pi/2 \\ \angle S_{31} - \angle S_{37} = 2n\pi + \pi/2 \end{cases} ; \begin{cases} \angle S_{41} - \angle S_{48} = 2n\pi + \pi \\ \angle S_{41} - \angle S_{42} = 2n\pi - \pi/2 \\ \angle S_{41} - \angle S_{47} = 2n\pi - \pi/2 \end{cases}$$

$$\begin{cases} \angle S_{51} - \angle S_{58} = 2n\pi \\ \angle S_{51} - \angle S_{52} = 2n\pi \\ \angle S_{51} - \angle S_{57} = 2n\pi + \pi \end{cases} ; \begin{cases} \angle S_{61} - \angle S_{68} = 2n\pi \\ \angle S_{61} - \angle S_{62} = 2n\pi - \pi \\ \angle S_{61} - \angle S_{67} = 2n\pi \end{cases} \quad (8-5)$$

where n is an integer number, and $\angle S_{ij} - \angle S_{il}$ denotes the phase difference of input signals from input ports j and l at the i^{th} output port. The rest of phase relationship between all incoming signals can be obtained through a linear manipulation of the equations in (8-5). This essential phase relation

makes the proposed multiport junction different from previously reported ones, being capable of carrying out 2D AoA detections. Other possible topologies of passive interferometric networks which satisfy this phase condition can also be used in the proposed system. Within such a multiport system, the phase differences between the incoming signals can be extracted as follows.

Taking the received signal at port 1 as the reference signal, the input signals to the interferometer can be expressed as

$$\begin{aligned}
 I_1 &= A \cos(\omega t) = A \cos(\gamma_1) \\
 I_7 &= A \cos(\omega t + \frac{\varphi_H}{2} + \frac{\varphi_E}{2}) = A \cos(\gamma_7) \\
 I_2 &= A \cos(\omega t + \varphi_E) = A \cos(\gamma_2) \\
 I_8 &= A \cos(\omega t - \frac{\varphi_H}{2} + \frac{\varphi_E}{2}) = A \cos(\gamma_8)
 \end{aligned} \tag{8-6}$$

The output signals of the multiport are a combination of these input signals that experience specific phase shifts. These signals can be written as

$$\begin{aligned}
 O_3 &= \frac{A}{2} (-\cos(\gamma_1) + \cos(\gamma_8) - \sin(\gamma_2) - \sin(\gamma_7)) \\
 O_4 &= \frac{A}{2} (-\sin(\gamma_1) + \sin(\gamma_8) - \cos(\gamma_2) - \cos(\gamma_7)) \\
 O_5 &= \frac{A}{2} (+\cos(\gamma_1) + \cos(\gamma_8) + \cos(\gamma_2) - \cos(\gamma_7)) \\
 O_6 &= \frac{A}{2} (+\sin(\gamma_1) + \sin(\gamma_8) - \sin(\gamma_2) + \sin(\gamma_7))
 \end{aligned} \tag{8-7}$$

which are mixed together, passing through the output power detectors. The mixing products, after low pass filtering, are expressed in (8-8) at the bottom of this page. K is the detector's voltage gain and is also assumed to be identical for all detectors at the output ports. The mixing products of all the input signals with identical frequencies would be a DC signal that can be sampled using analog-to-digital converters (ADC) for further processing

$$\begin{aligned}
B_3 &= K \frac{A^2}{4} (1 + 1 + 1 + 1 - \cos(\gamma_1 - \gamma_8) - \sin(\gamma_1 - \gamma_2) - \sin(\gamma_1 - \gamma_7) + \sin(\gamma_8 - \gamma_2) + \sin(\gamma_8 - \gamma_7) + \cos(\gamma_2 - \gamma_7)) \\
B_4 &= K \frac{A^2}{4} (1 + 1 + 1 + 1 - \cos(\gamma_1 - \gamma_8) + \sin(\gamma_1 - \gamma_2) + \sin(\gamma_1 - \gamma_7) - \sin(\gamma_8 - \gamma_2) - \sin(\gamma_8 - \gamma_7) + \cos(\gamma_2 - \gamma_7)) \\
B_5 &= K \frac{A^2}{4} (1 + 1 + 1 + 1 + \cos(\gamma_1 - \gamma_8) + \cos(\gamma_1 - \gamma_2) - \cos(\gamma_1 - \gamma_7) + \cos(\gamma_8 - \gamma_2) - \cos(\gamma_8 - \gamma_7) - \cos(\gamma_2 - \gamma_7)) \\
B_6 &= K \frac{A^2}{4} (1 + 1 + 1 + 1 + \cos(\gamma_1 - \gamma_8) - \cos(\gamma_1 - \gamma_2) + \cos(\gamma_1 - \gamma_7) - \cos(\gamma_8 - \gamma_2) + \cos(\gamma_8 - \gamma_7) - \cos(\gamma_2 - \gamma_7))
\end{aligned} \tag{8-8}$$

8.3 Signal processing algorithm

To estimate the azimuth and elevation angles, the following signal processing algorithm is proposed and formulated. Subtracting the two pairs of signals from each other helps remove the unwanted DC signals and yields

$$\begin{aligned}
BB_{34} &= B_3 - B_4 = K \frac{A^2}{2} (\sin(\varphi_E) - \sin(\varphi_H)) \\
BB_{56} &= B_5 - B_6 = K \frac{A^2}{2} (\cos(\varphi_E) - \cos(\varphi_H))
\end{aligned} \tag{8-9}$$

that can be rearranged into

$$\begin{aligned}
BB_{34} &= K \frac{A^2}{2} \left(\cos\left(\frac{\varphi_E + \varphi_H}{2}\right) \sin\left(\frac{\varphi_E - \varphi_H}{2}\right) \right) \\
BB_{56} &= -K \frac{A^2}{2} \left(\sin\left(\frac{\varphi_E + \varphi_H}{2}\right) \sin\left(\frac{\varphi_E - \varphi_H}{2}\right) \right)
\end{aligned} \tag{8-10}$$

Assuming $x = \varphi_E + \varphi_H$ and $y = \varphi_E - \varphi_H$, (8) can be readily solved for θ_E and θ_H as in the following

$$\begin{aligned}
\theta_E &= \sin^{-1} \left(\frac{x + y}{2\beta_0 L} \right) \\
\theta_H &= \sin^{-1} \left(\frac{x - y}{2\beta_0 L \cos \theta_E} \right)
\end{aligned} \tag{8-11}$$

8.4 Plane wave simulations

In order to validate the phase equations in (4) and evaluate the performance of the designed antenna system in terms of received phase difference, a simulation is conducted using commercial

software of HFSS and the obtained phase values are compared with the theoretical ones. Figure 8-3 shows the simulation setup. The two relative angles between the plane wave pointing vector and the antenna normal vector are desirably set through rotating the antenna over the two axes. Simulation results are compared with theoretical values in Figure 8-4. The phase deviation from the ideal values can be attributed to the effect of imperfect radiation pattern and can differ for different types of antenna, e.g., dipole, patch and dielectric resonator antenna.

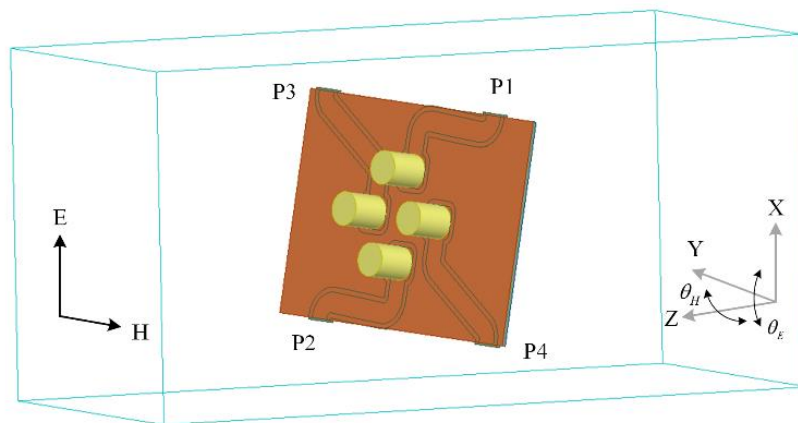


Figure 8-3: Plane wave simulation scenario in HFSS; Top and bottom plane boundary conditions are defined as PEC and at the side walls as PMC. The wave port is defined in the front plane and the back plane is with the radiation condition

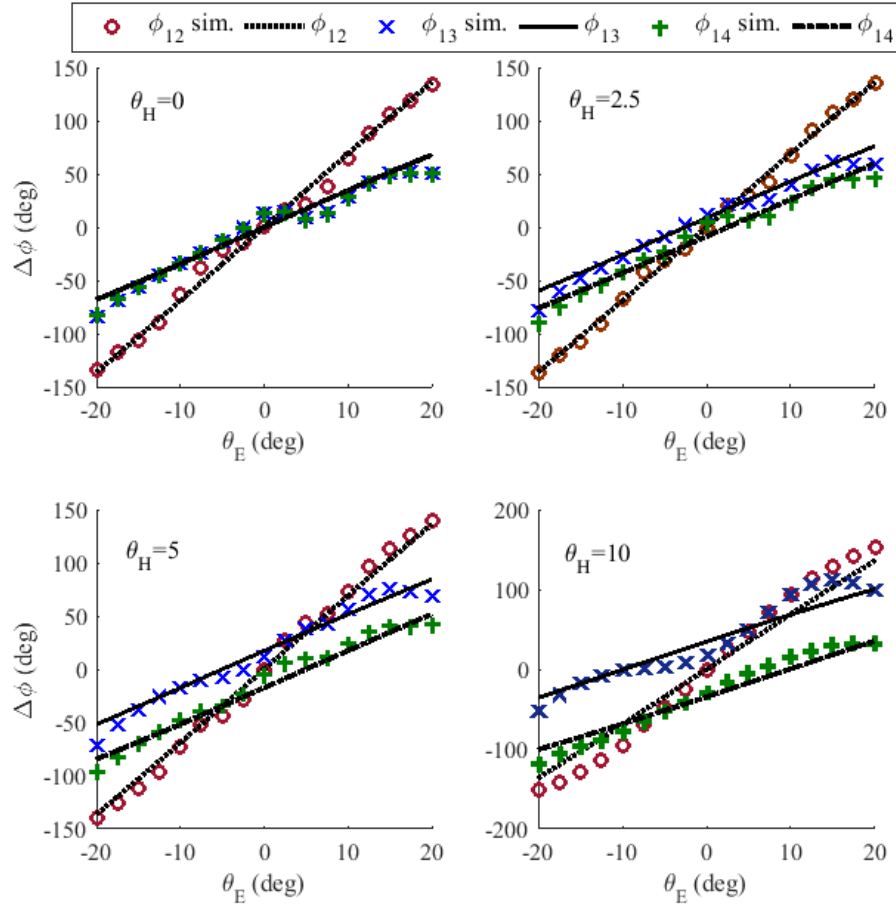


Figure 8-4: Plane wave simulation results at 60 GHz in HFSS; The inherent 180° phase difference due to different slot orientations are compensated in simulation results

8.5 Ambiguity issue and required distance between antenna elements

The unambiguous range of detection in one plane is not independent of AoA in the other plane, and both angles contribute to the phase ambiguity that basically limits the detection range. Moreover, the distance between antenna elements determines the unambiguous range of detection. In the case of one dimensional angle detection with two antenna elements, a wider range of detection can be obtained with a shorter distance, i.e., a half of wavelength. However, mutual coupling between those antenna elements could be undesirably high with short distances, hence large distances can make the design procedure easier. The unambiguous detection range of angles should satisfy the following condition

$$\begin{aligned} \left| \beta_0 L (\sin \theta_E + \cos \theta_E \sin \theta_H) \right| &< \pi \\ \left| \beta_0 L (\sin \theta_E - \cos \theta_E \sin \theta_H) \right| &< \pi \end{aligned} \quad (8-12)$$

From this condition and considering the desired range of operation, the maximum value of distance between the antenna elements (L_{max}) can be determined as shown in Figure 8-5. One can readily observe the coupling between θ_E and θ_H . From the resulting diamond shaped area for any value of L , it can be concluded that the unambiguous range of θ_E (θ_H) is larger with smaller one of θ_H (θ_E). Moreover, the dashed line rectangles show the limited range of detection for two values of L when an identical unambiguous range is desired. This information is helpful when designing the antenna in practice.

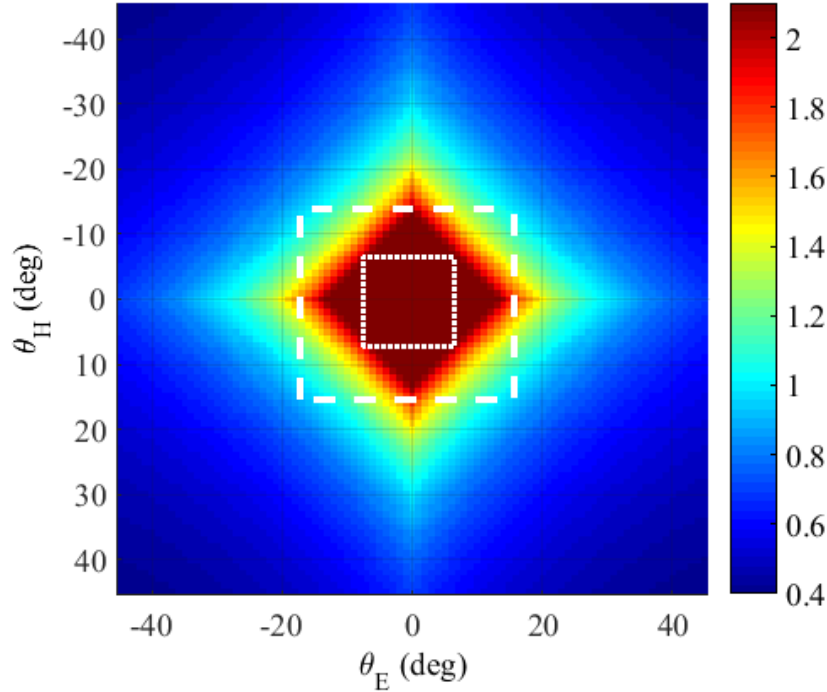


Figure 8-5: L_{max} values as a multiplication of free space wavelength. The corresponding range of angle detection obtained from the common areas of L_{max} in (8-10).

This analysis is validated via system-level simulations in ADS and part of simulation results are shown in Figure 8-6 for two different values of distance between antenna elements, i.e., 1.6λ and 0.95λ . It can be seen that with smaller values of θ_H larger unambiguous detection range of θ_E can be obtained. The details of this system-level simulations are explained next.

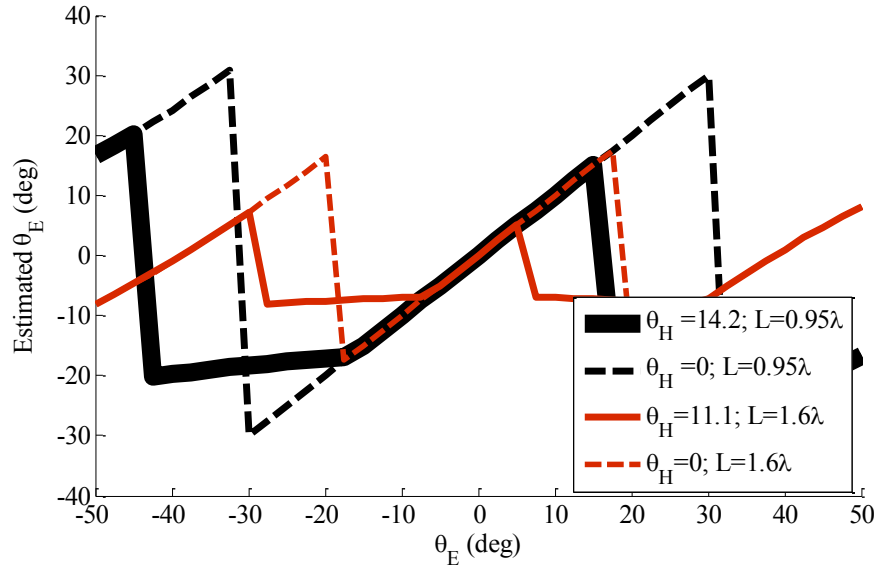


Figure 8-6: AOA detection system level simulation results from ADS. The unambiguous detection range of angle in one dimension depends on both the distance between antenna elements and the incoming angle in the other dimension.

8.6 System-level simulations

To assess the proposed system analysis, a set of system-level simulations is carried out using commercial software package of Ptolemy in ADS. Figure 8-7 shows the simulation schematic where the received plane wave at four output ports of the antenna is modeled by one single frequency sinusoidal source and four phase shifters. The phase difference between input signals to multiport DOA receiver is determined in accordance with the incoming θ_E and θ_H . The power detector is designed using the Spice model of Schottky diode and the multiport block is made with the built-in hybrid coupler and phase shifter components. In fact, it is a co-simulation of Circuit-Envelope simulator for RF parts and Data-Flow simulator for signal processing. The output of the detectors are processed through the proposed signal processing to estimate the angles in two dimensions.

Figure 8-8 shows excellent simulation results under ideal conditions with respect to different distances between antenna elements.

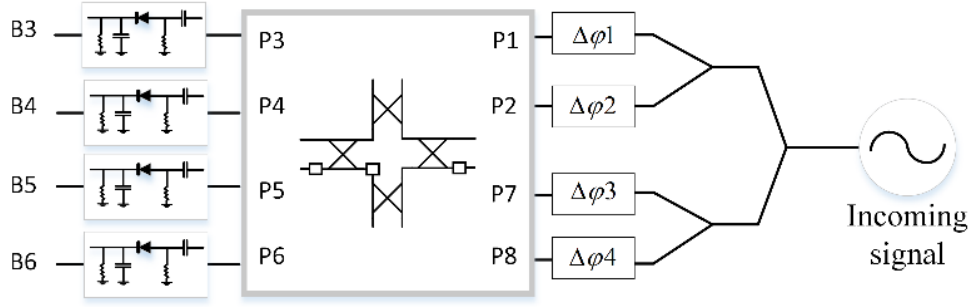
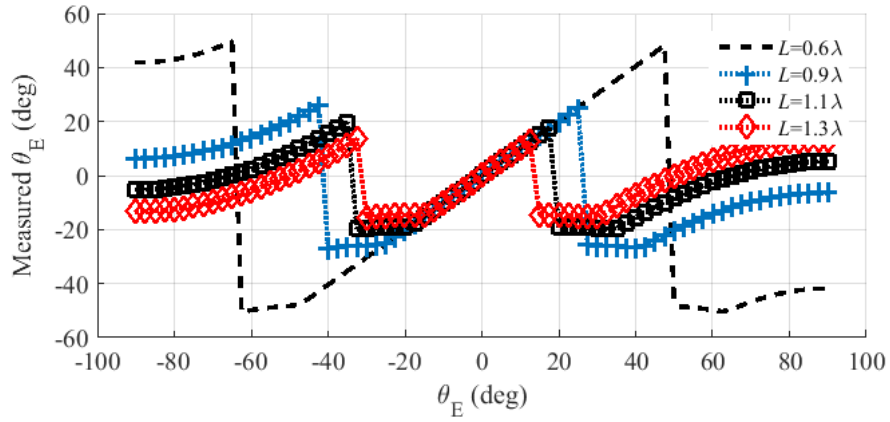
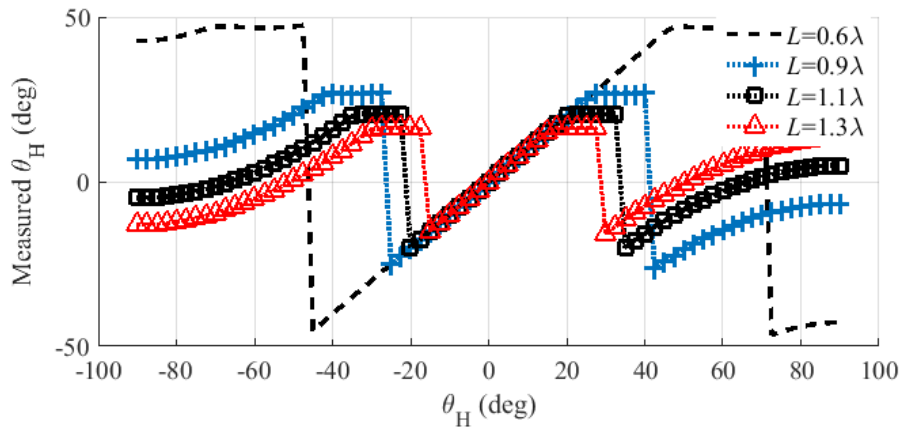


Figure 8-7: Ptolemy Co-simulation panel of Circuit Envelop (for RF portions) and DF (data flow for DSP) simulators in ADS; The RF source represents the incoming plane wave to the receiving antenna and the phase shifters represent the phase difference of the received signals at the output of each receiving element, i.e., $\Delta\phi_1 = 0$, $\Delta\phi_2 = \varphi_E$, $\Delta\phi_3 = \varphi_H/2 + \varphi_E/2$, $\Delta\phi_4 = -\varphi_H/2 + \varphi_E/2$.



(a) Altitude



(b) Azimuth

Figure 8-8: System level simulation results from ADS for angle detection in two dimensions for different distances between antenna elements; (a) $\theta_H = 8^\circ$ when sweeping θ_E , (b) $\theta_E = -6^\circ$ when sweeping θ_H .

8.7 Calibration technique

There may be several sources of non-ideal behavior throughout the proposed detection system that may cause erroneous estimations of DOA. Discrepancy in phase and gain of antenna elements and low-noise amplifier (LNA) blocks, coupling ratios of interferometer and conversion gain of diode detectors can be the contributing sources of error. Equation (8), which describes the relationship between the outputs of the interferometer (i.e., B_3 , B_4 , B_5 , B_6) and the incoming signals, has been developed under an assumption of ideal phase and equal gain conditions, which may not be realistic in practice. Considering all of the sources of non-ideal behavior, it is possible to express each pair of detected signals B_3 and B_4 and B_5 and B_6 as follows:

$$\begin{aligned}
\frac{-}{B_3} &= kq_3 \frac{A^2}{4} \begin{bmatrix} g_{13}g_{83}\alpha_1\alpha_8 \\ g_{13}g_{23}\alpha_1\alpha_2 \\ g_{13}g_{73}\alpha_1\alpha_7 \\ g_{83}g_{23}\alpha_8\alpha_2 \\ g_{83}g_{73}\alpha_8\alpha_7 \\ g_{23}g_{73}\alpha_2\alpha_7 \end{bmatrix} \begin{bmatrix} -\cos(\gamma_1 - \gamma_8 - (\zeta_{13} - \zeta_{83})) \\ -\sin(\gamma_1 - \gamma_2 - (\zeta_{13} - \zeta_{23})) \\ -\sin(\gamma_1 - \gamma_7 - (\zeta_{13} - \zeta_{73})) \\ +\sin(\gamma_8 - \gamma_2 - (\zeta_{83} - \zeta_{23})) \\ +\sin(\gamma_8 - \gamma_7 - (\zeta_{83} - \zeta_{73})) \\ +\cos(\gamma_2 - \gamma_7 - (\zeta_{23} - \zeta_{73})) \end{bmatrix} \\
\frac{-}{B_4} &= kq_4 \frac{A^2}{4} \begin{bmatrix} g_{14}g_{84}\alpha_1\alpha_8 \\ g_{14}g_{24}\alpha_1\alpha_2 \\ g_{14}g_{74}\alpha_1\alpha_7 \\ g_{84}g_{24}\alpha_8\alpha_2 \\ g_{84}g_{74}\alpha_8\alpha_7 \\ g_{24}g_{74}\alpha_2\alpha_7 \end{bmatrix} \begin{bmatrix} -\cos(\gamma_1 - \gamma_8 - (\zeta_{14} - \zeta_{84})) \\ +\sin(\gamma_1 - \gamma_2 - (\zeta_{14} - \zeta_{24})) \\ +\sin(\gamma_1 - \gamma_7 - (\zeta_{14} - \zeta_{74})) \\ -\sin(\gamma_8 - \gamma_2 - (\zeta_{84} - \zeta_{24})) \\ -\sin(\gamma_8 - \gamma_7 - (\zeta_{84} - \zeta_{74})) \\ +\cos(\gamma_2 - \gamma_7 - (\zeta_{24} - \zeta_{74})) \end{bmatrix} \\
\frac{-}{B_5} &= kq_5 \frac{A^2}{4} \begin{bmatrix} g_{15}g_{85}\alpha_1\alpha_8 \\ g_{15}g_{25}\alpha_1\alpha_2 \\ g_{15}g_{75}\alpha_1\alpha_7 \\ g_{85}g_{25}\alpha_8\alpha_2 \\ g_{85}g_{75}\alpha_8\alpha_7 \\ g_{25}g_{75}\alpha_2\alpha_7 \end{bmatrix} \begin{bmatrix} +\cos(\gamma_1 - \gamma_8 - (\zeta_{15} - \zeta_{85})) \\ +\cos(\gamma_1 - \gamma_2 - (\zeta_{15} - \zeta_{25})) \\ -\cos(\gamma_1 - \gamma_7 - (\zeta_{15} - \zeta_{75})) \\ +\cos(\gamma_8 - \gamma_2 - (\zeta_{85} - \zeta_{25})) \\ -\cos(\gamma_8 - \gamma_7 - (\zeta_{85} - \zeta_{75})) \\ -\cos(\gamma_2 - \gamma_7 - (\zeta_{25} - \zeta_{75})) \end{bmatrix} \\
\frac{-}{B_6} &= kq_6 \frac{A^2}{4} \begin{bmatrix} g_{16}g_{86}\alpha_1\alpha_8 \\ g_{16}g_{26}\alpha_1\alpha_2 \\ g_{16}g_{76}\alpha_1\alpha_7 \\ g_{86}g_{26}\alpha_8\alpha_2 \\ g_{86}g_{76}\alpha_8\alpha_7 \\ g_{26}g_{76}\alpha_2\alpha_7 \end{bmatrix} \begin{bmatrix} +\cos(\gamma_1 - \gamma_8 - (\zeta_{16} - \zeta_{86})) \\ -\cos(\gamma_1 - \gamma_2 - (\zeta_{16} - \zeta_{26})) \\ +\cos(\gamma_1 - \gamma_7 - (\zeta_{16} - \zeta_{76})) \\ -\cos(\gamma_8 - \gamma_2 - (\zeta_{86} - \zeta_{26})) \\ +\cos(\gamma_8 - \gamma_7 - (\zeta_{86} - \zeta_{76})) \\ -\cos(\gamma_2 - \gamma_7 - (\zeta_{26} - \zeta_{76})) \end{bmatrix}
\end{aligned} \tag{8-13}$$

where q is the relative difference of each detector's voltage loss with respect to the identical value of k . The difference in multi-port's coupling ratio with respect to an ideal coupling (i.e., 0.5) is denoted by g , and α is the gain difference of the LNAs and the antenna elements between 4 different channels. Finally, $\zeta_{i,j}$ denotes the deviation from the ideal desired phase difference in the multiport interferometric network from port i to port j . Note that constant terms of $(kA^2/4)(1 + 1 + 1 + 1)$ in (8) are not shown in the above matrices to simplify their presentation. Since the mentioned sources of errors are constant and typically do not vary randomly, one-time calibration is sufficient.

Under a close look into (11), some of the presented terms may be trimmed or merged together, i.e., $\gamma_1 - \gamma_8 = -(\gamma_2 - \gamma_7)$ and $\gamma_1 - \gamma_7 = (\gamma_8 - \gamma_2)$. Therefore, the equation for B_3 for example may be re-formulated as:

$$\begin{aligned} B_3 = & -a_1 \cos(\phi_1 + \Delta \zeta_1) - a_2 \sin(\phi_2 + \Delta \zeta_2) - a_3 \sin(\phi_3 + \Delta \zeta_3) \\ & + a_4 \sin(\phi_3 + \Delta \zeta_4) + a_5 \sin(\phi_4 + \Delta \zeta_5) + a_6 \cos(-\phi_1 + \Delta \zeta_6) \end{aligned} \quad (8-14)$$

where $\phi_1 = \gamma_1 - \gamma_8$, $\phi_2 = (\gamma_1 - \gamma_2)$, $\phi_3 = \gamma_1 - \gamma_7$, $\phi_4 = \gamma_8 - \gamma_7$ and a_1 to a_6 . Equation (13) can be expanded into:

$$\begin{aligned} B_3 = & \begin{bmatrix} (a_6 \cos(\Delta \zeta_6) - a_1 \cos(\Delta \zeta_1)) \cos(\phi_1) + \\ (a_1 \sin(\Delta \zeta_1) - a_6 \sin(\Delta \zeta_6)) \sin(\phi_1) \end{bmatrix} + \begin{bmatrix} (a_4 \cos(\Delta \zeta_4) - a_3 \cos(\Delta \zeta_3)) \sin(\phi_3) + \\ (a_4 \sin(\Delta \zeta_4) - a_3 \sin(\Delta \zeta_3)) \cos(\phi_3) \end{bmatrix} \\ & + [-a_2 \cos(\Delta \zeta_2) \sin(\phi_2) - a_2 \sin(\Delta \zeta_2) \cos(\phi_2)] + [a_5 \cos(\Delta \zeta_5) \sin(\phi_4) + a_5 \sin(\Delta \zeta_5) \cos(\phi_4)] \end{aligned} \quad (8-15)$$

which may be simplified into $\bar{B}_3 = H_3 E_3$, where H_3 is a calibrated model and E_3 is a constant error vector for channel 3 and are respectively expressible as:

$$H_3 = \begin{bmatrix} \cos(\phi_1) \\ \sin(\phi_1) \\ \sin(\phi_3) \\ \cos(\phi_3) \\ \sin(\phi_2) \\ \cos(\phi_2) \\ \sin(\phi_4) \\ \cos(\phi_4) \end{bmatrix} \quad E_3 = \begin{bmatrix} a_6 \cos(\Delta \zeta_6) - a_1 \cos(\Delta \zeta_1) \\ a_1 \sin(\Delta \zeta_1) - a_6 \sin(\Delta \zeta_6) \\ a_4 \cos(\Delta \zeta_4) - a_3 \cos(\Delta \zeta_3) \\ a_4 \sin(\Delta \zeta_4) - a_3 \sin(\Delta \zeta_3) \\ -a_2 \cos(\Delta \zeta_2) \\ -a_2 \sin(\Delta \zeta_2) \\ +a_5 \cos(\Delta \zeta_5) \\ +a_5 \sin(\Delta \zeta_5) \end{bmatrix} \quad (8-16)$$

Likewise, the model and error vectors of 4, 5 and 6 can be derived: (H_i) are all the same, but E_i would be different.

Error vectors (E_3, E_4, E_5, E_6) include all error terms and should be estimated only once. As mentioned previously, the errors are constant in nature since they all originate from practical non-varying non-idealities in RF front-end circuitry. If the deviations of the captured phases by antenna elements from the ideal ones are negligible, the error terms would be autonomous from the incoming angles. Therefore, the error vectors can be estimated by one-time measurement with incoming wave at a known angle using least square (LS) technique as in the following.

The desired operational range of angles in both dimensions may be partitioned into a plurality

of cells with predetermined elevation and azimuth angles. Hence, for a given DOA, there is a corresponding cell. Figure 8-9 illustrates an example partitioning the operational range of angles into a plurality of cells, where each cell represents a range of angles.

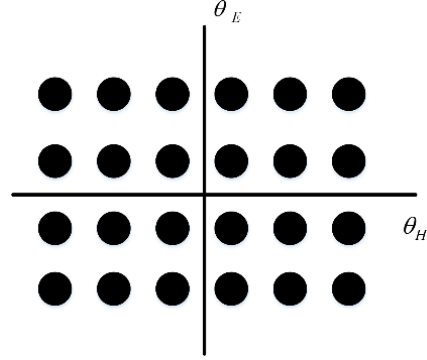


Figure 8-9: Partitioning cells for calibration; for each row (θ_E) n samples at n angles of θ_H are measured to calculate the error vectors

A small number of measurement samples (n) may be used to obtain vectors of \vec{B}_3 for each row of n cells. The error vector E_3 is obtained from the vector of \vec{B}_3 , using the LS technique. For each cell, there is a vector of H_3 and the corresponding scalar value of the vector of \vec{B}_3 , where \vec{B}_3 includes scalar values for an entire row of cells. E_3 is a vector (with size of 8×1). When measurement is done for n nodes at n different angles in one dimension (e.g., vertical) but identical in the other angle (e.g., horizontal), one vector of \vec{B}_3 (with the size of $n \times 1$) and a matrix of \vec{H}_3 (with the size of $n \times 8$) which includes n vectors of H_3 would be obtained. The operations may be expressed

$$\vec{B}_i = \vec{H}_i E_i; E_i = \left(\vec{H}_i^T \vec{H}_i \right)^{-1} \vec{H}_i^T \vec{B}_i \quad i = 3 \dots 6 \quad (8-17)$$

It is worth mentioning that for such rank deficient least square problems, the minimum norm least square solution (*pinv function in Matlab*) can yield the best solution in practice [152]. As an illustrative example, the measurements for calibration are conducted with a fixed θ_E and sweeping θ_H over the entire operational range. Therefore, for each row, one vector of \vec{B}_3 may be obtained and hence one error vector of E_3 . At the same time, measurements and error vectors for other channels (e.g., 4, 5, and 6) may be obtained.

Thereafter, the stored error vectors (E_3, E_4, E_5 , and E_6) and ideal models (H_3, H_4, H_5 , and

H6) may be used for solving the system of nonlinear equations in (8-11) to estimate two unknown variables of φ_E and φ_H

8.8 Implementation

For system implementation, a second configuration of the proposed multiport architecture with input ports at the center is depicted in Figure 8-10. This configuration makes connection to the antenna ports easier while satisfying the phase condition in (8-5). A crossover is essentially placed at the signal path from ports 2 and 7, and in order to maintain the desired phase relationships the phase difference made by the crossover is compensated by two additional transmission lines. Furthermore, the transmission lines between antenna terminals to the input ports of the multiport component should be designed such that the phase shifts that the captured signals experience would be identical.

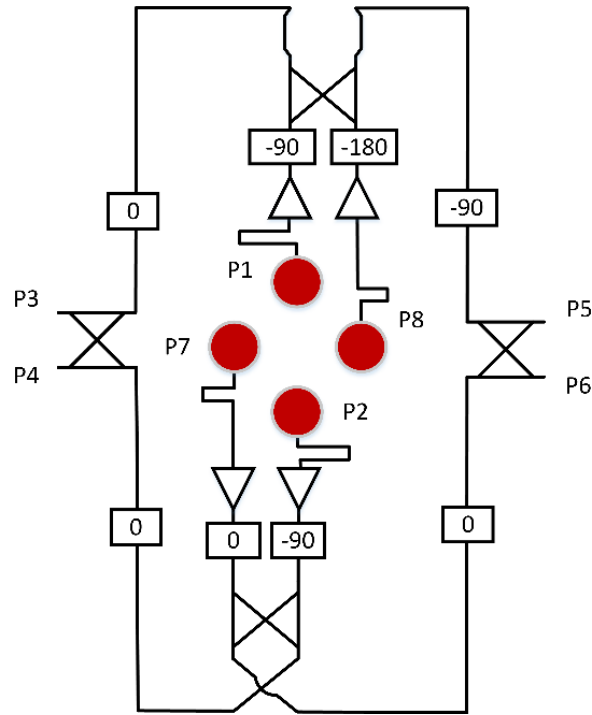


Figure 8-10: Second configuration of the multiport interferometric architecture with relocated ports. The internal input ports provide easier connections to the antenna terminals.

SIW technology can be a preferred choice at millimeter-waves for realizing the multiport passive network because it is quite immune against unwanted radiation. This network can be built upon a combination of the already developed passive components with this technology, i.e.,

couplers, phase shifters and crossovers [24, 172-174]. The multiport junction with the topology shown in Figure 8-10 was designed with SIW building blocks on the substrate of RO/6002 with the thickness of 0.254 mm and simulated in HFSS. Figure 8-11 and Figure 8-12 show the simulation results of amplitude and phase components of the scattering matrix. One can see that the phase differences around 58 GHz agree very well with the essential phase relationship requirements.

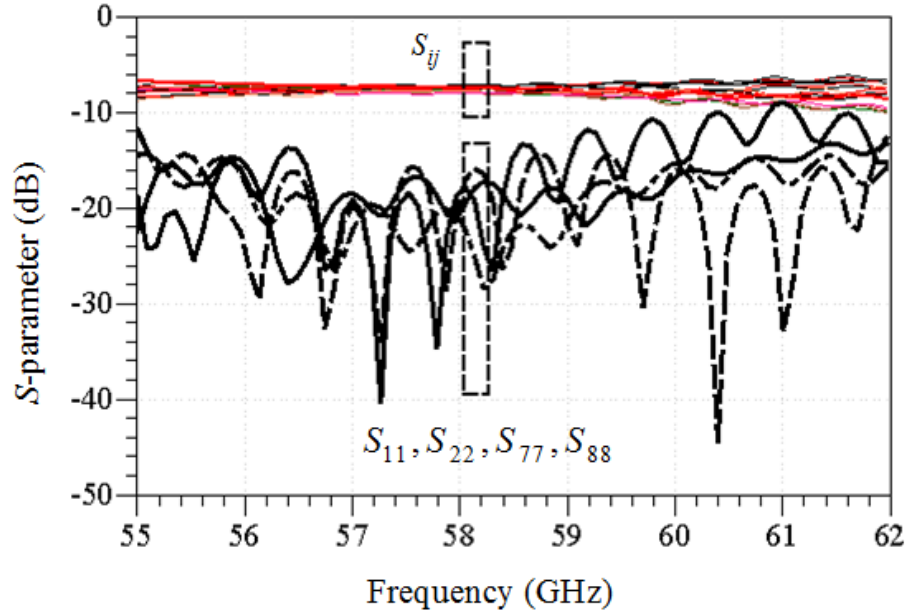


Figure 8-11: Simulation results of amplitude component of the S-parameters of the designed eight-port interferometric network. The simulation is carried out in commercial software of HFSS

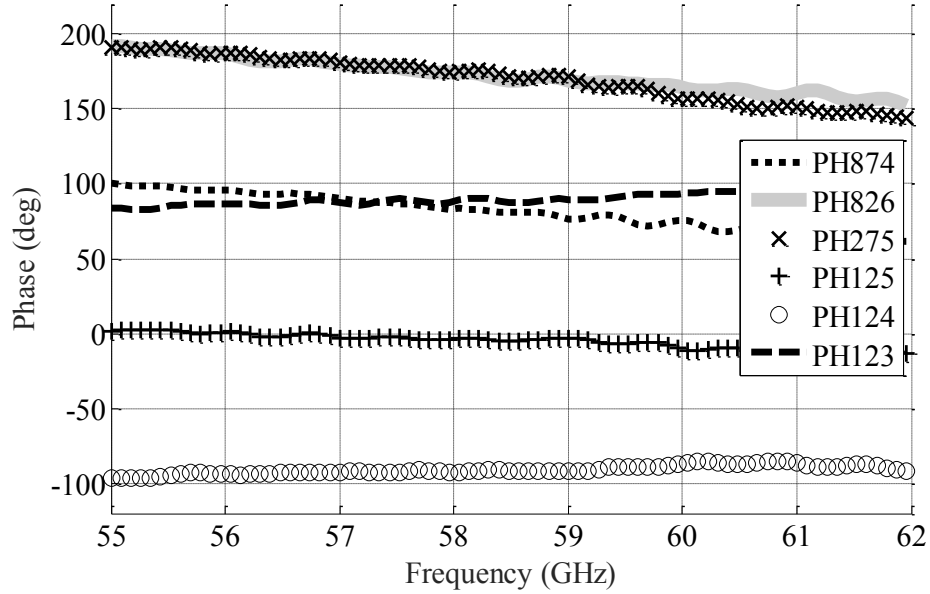


Figure 8-12: Simulation results of the phase differences (PH_{mkn}) between different pairs of input signals (m and k) at four output ports (n) ; The desired phase differences in accordance with the essential conditions listed in (8-5) occurs around 58 GHz

8.9 Experimental prototyping

In order to assess the performance of the proposed 2D AoA detection system, it is prototyped around V frequency band for antenna alignment applications in point-to-point radio systems. Techniques for this implementation along with measurement results are briefly discussed next.

Since measuring the eight-port was not feasible due to the ports locations, the used phase shifters as the critical part were fabricated which is shown in Figure 8-13. The measured phase differences are shown in Figure 8-14. The different-length-different width phase shifters can provide the desired phase shifts in wider bandwidth and are suitable for wideband systems.

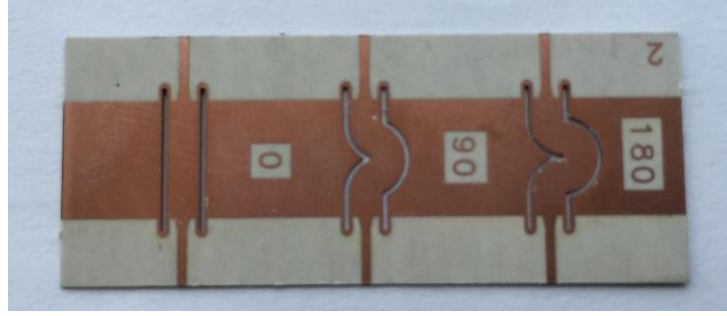


Figure 8-13: Fabricated phase shifters

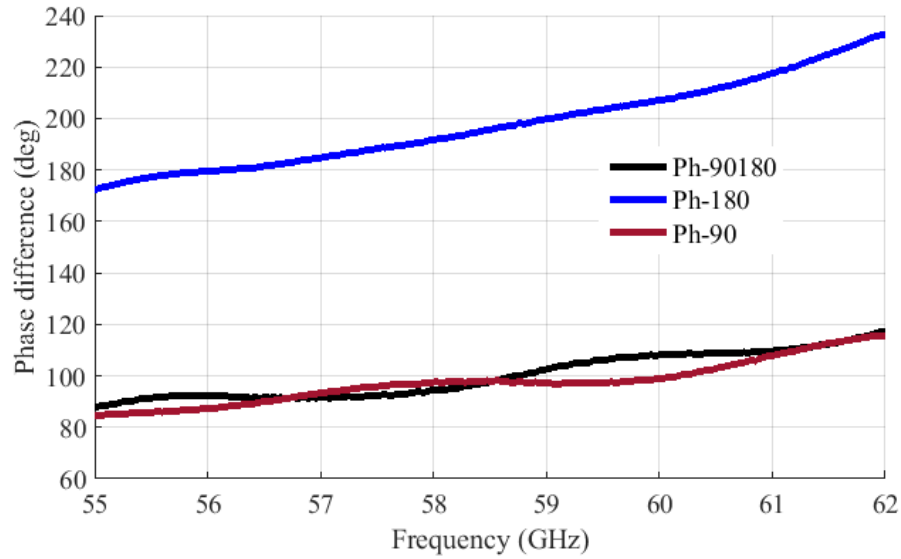


Figure 8-14: Measured phase difference; the desired phase difference occurs around 57.5 GHz

8.9.1 Antenna structure

At millimeter-wave frequencies, low gain and low efficiency are mainly caused by surface waves and conductor losses. To eliminate substrate modes, slot antenna backed by SIW cavity can be used to avoid the substrate mode over the millimeter-wave range of interest. Since various SIW antennas have been proposed and studied for 60-GHz applications in the past years, our implementation can be made in a straightforward manner.

A wide-bandwidth aperture-coupled microstrip patch antenna (MPA) fed by SIW was presented in [175]. The antenna designed using transverse and longitudinal slot configurations achieve simulated impedance bandwidth of 22% and gain up to 6.8 dBi. A wide slot antenna backed by SIW cavity is investigated in [176]. Dual-resonance operation mechanism increases the

impedance bandwidth of antenna from 3% to 11.6%. SIW dielectric resonator (DR) mounted on the conducting back plane of an HMSIW was proposed in [177]. A 60 GHz linearly polarized HWSIW-fed DRA was first designed by applying a transverse rectangular slot to feed a dielectric cylinder. The prototype shows a gain higher than 5.5 dBi over the whole operation band of 24%. Experimental data for SIW-DRA, based on two different slot orientations are developed in [177]. The measured gain for SIW-DRA single element showed a broadside gain of 5.51 dBi.

The DRA is used for the proposed system as it offers high radiation efficiency and more flexibility in terms of gain and compatibility with integrated circuits. Figure 8-15 shows the geometry of the proposed hybrid structure (DRA and SIW cavity) within the desired arrangement. Each element consists of a dielectric cylinder with diameter d and height h made of Rogers 6010 with relative permittivity of 10.1 and loss tangent of 0.002. The slot backed rectangular cavity is also designed on a RG/6010 substrate, but with a different thickness of 0.254 mm. The slot antenna is backed by a resonant cavity with length L and width W , and a centered half wavelength slot is etched on the top wide wall of the cavity for coupling. The dielectric cylinder is glued over the slot on the SIW cavity using 5-15 μm of thickness of glue layer with a permittivity of 3.5 and an estimated loss tangent of 0.05. The slot and the HEM₁₁ δ mode of the cylindrical DRA radiate as horizontal magnetic dipoles.

The antenna elements are analyzed in the presence of other elements through the proposed arrangement using the full-wave electromagnetic solver, i.e., Ansoft HFSS. The designed antenna is then fabricated using our low cost in-house PCB process. The prototyped antenna board with four V-connectors at the input ports is shown in Figure 8-16. It should be noted that four SIW feed lines are designed such that the received signals experience identical phase differences from the antenna to the output ports.

Figure 8-17 demonstrates simulated and measured S-parameters of the proposed antenna. The achieved -10 dB bandwidth is from 58 to 61 GHz (5%) and a good agreement between simulations and measurements is observed. The degradation in the measurements is principally attributed to the influence of SIW-microstrip adaptor and also the transition from microstrip lines to test-fixtures which were not considered in the simulations. The isolation between two couples of input ports (S_{12} , S_{17}) are also presented in the same figure. One can observe the isolation level around -30 dB over the entire operating frequency band. The accomplished level of isolation limits the impact

of coupling on the global system performance. The 3D radiation pattern of the proposed antenna is shown in Figure 8-15 at 59 GHz. The peak gain of the proposed antenna is achieved at the broadside direction of axis. The radiation in the E-plane (yz plane) is larger than that in the H-plane (xz plane)

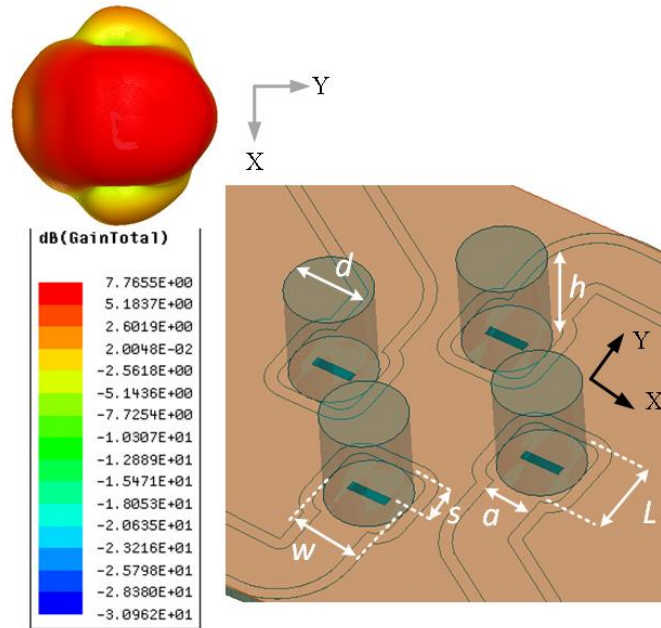


Figure 8-15: Designed antenna configuration; $h=2.54$ mm, $d=0.75$ mm, $L=2.3$ mm, $w=2$ mm, $s=1$ mm, slot width=0.229 mm, slot length= 1 mm; distance between elements=5.53 mm; Simulation pattern of the antenna when only one port is radiating and other ports are terminated with

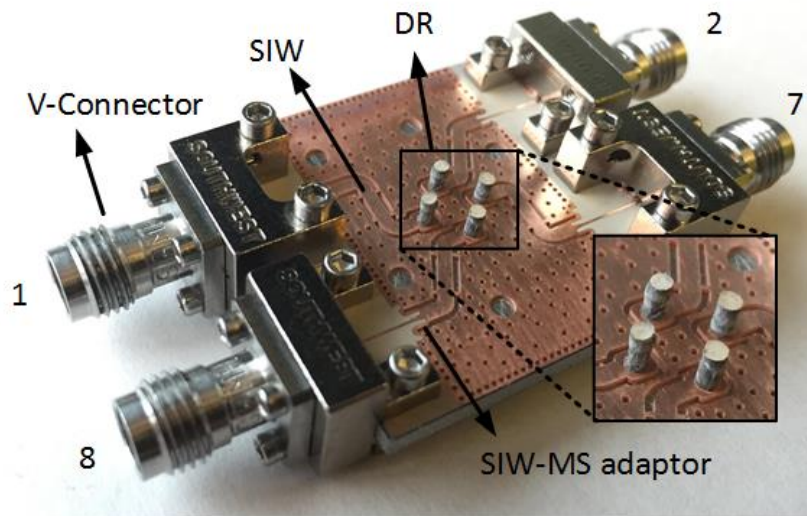


Figure 8-16: Fabricated antenna with input transmission lines and V-Launchers; The dielectric cylinders are deformed during fabrication within the laser cutting process

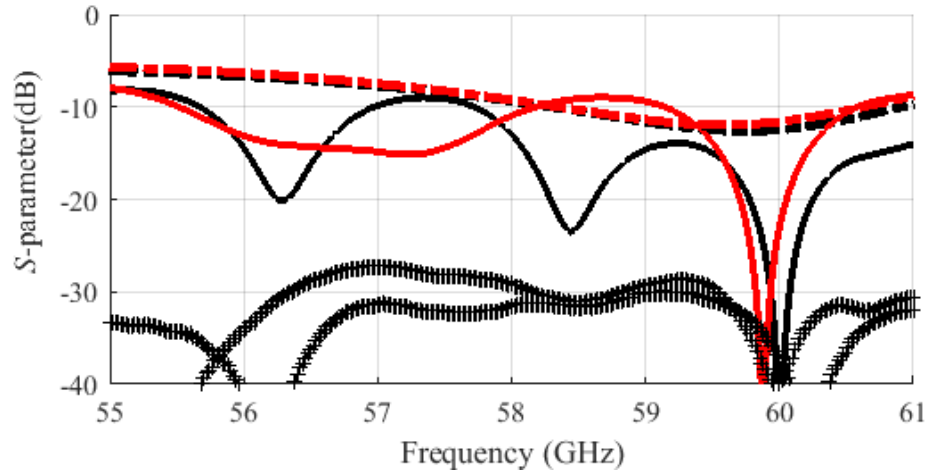


Figure 8-17: Measured and simulated S-parameters of the two elements of the antenna; solid line: measurement; dashed line: simulation; square and +: measured coupling. The reference plane in measurements is calibrated at the test-fixture coaxial input port

The achieved gain of 7.8 dBi is higher than the previously reported gain of the antenna in [175-177] . The radiation pattern of the prototyped antenna was also measured in the anechoic chamber and the results of measurements in both E and H planes are plotted in Figure 8-18, and Figure 8-19.

It can be seen that the antenna has a symmetric broadside radiation pattern. The discrepancy could be due to the tolerance in fabrication and the presence of metal connectors, which would not be used in the final integrated system.

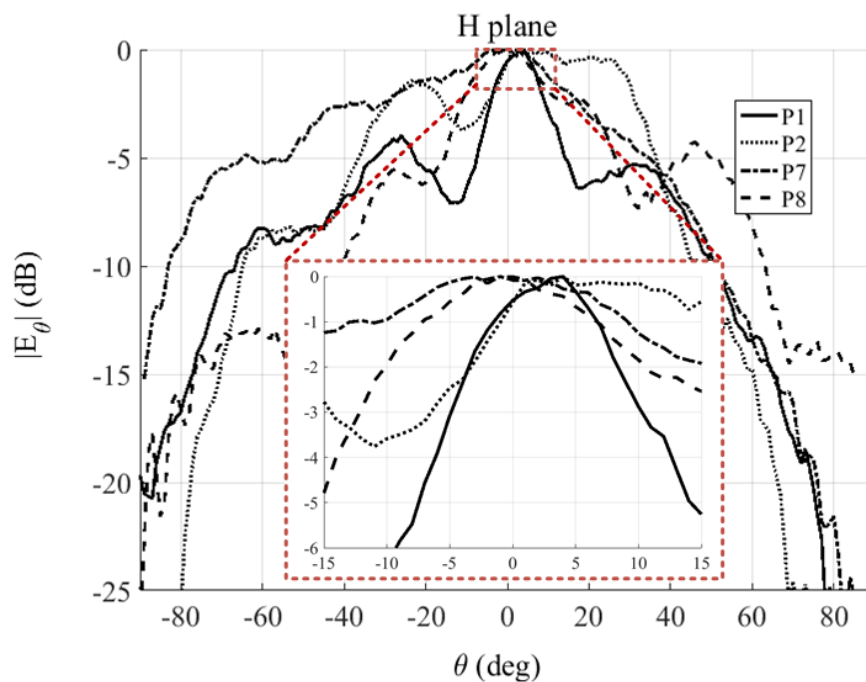


Figure 8-18: Measured antenna pattern in H plane; solid line: P7, -.- : P8, dashed line: P1, dots: P2; when zoomed in the range of -15 to 15; H planes

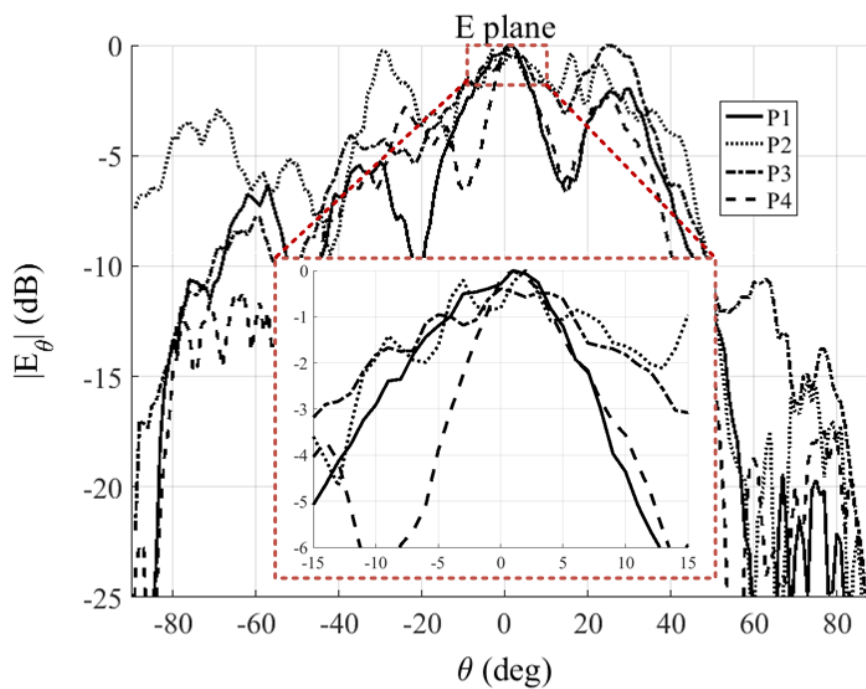


Figure 8-19: Measured antenna pattern in E plane; solid line: P7, -.- : P8, dashed line: P1, dots: P2; when zoomed in the range of -15 to 15; E plane

Measured gain values at 59 GHz for ports P1, P2, P7 and P8 are 4.4 dBi, 5.0 dBi, 4.98 dBi and 5.38 dBi, respectively. It should be noted that the differences between simulated and measured gains can be due to the loss in the feedline and the connector as well the deviation of the considered dielectric loss in the simulation from the real value in the prototyped antenna. The cross-polarization level of the antenna is below -19 dB, showing that the antenna has a good polarization purity. The above data suggests that the proposed antenna has a required performance to cover angular range from -5 to +5.

8.9.2 Detector circuit

The detector circuit with the schematic shown in Figure 8-20 was designed using the zero bias Schottky diode (MZBD-9161) from Aeroflex. Large and small signal models of the diode were derived through several in-lab measurements and using the technique of curve fitting.

The DC model parameters, including diode ideality factor (n), saturation current (I_s) and series resistor (R_s) are obtained from measured I-V curves when fitted with the diode model, i.e., $I = I_s(\exp((q/nkT)(V - R_s I)) - 1)$. The rest of the diode Spice model parameters are taken from diode datasheet. To obtain the parasitic elements of the diode package and the input/output leads on a $50\ \Omega$ transmission line, the measured complex input impedance or the return loss (small signal) and the detected voltage (large signal) over a range of input power were fitted with the model.

Subsequently, the derived diode model was utilized for detector circuit design. The detector layout for Momentum/HB simulations in ADS is depicted in Figure 8-20.

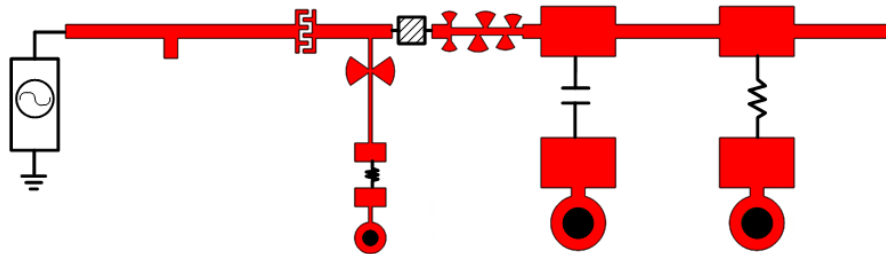


Figure 8-20: Detector layout with components for simulation in ADS

The interdigital capacitor at the input blocks the DC current and isolates the DC grounded SIW eight-port from detector input. The butterfly stubs filter out the RF signal at the video detected voltage and the low pass filter with close to zero cut-off frequency suppresses the noise to increase signal to noise ratio at the output. The single stub before the capacitor matches the detector input impedance to 50 Ohm. This detector is prototyped on Rogers 6010 with permittivity of around 10.1 through low cost printed circuit board (PCB) technology. The populated detector board with off-the-shelf components is shown in Figure 8-21.

From the S11 measurement results which are shown in Figure 8-22, one can observe the detector is matched at 58 GHz. In addition, the measurement detected voltage for a range of input powers is compared with simulation results in Figure 8-23. An excellent agreement between simulation and measurement results at 58 GHz validates the presented design technique and also the acceptable performance of the detector to be used in the proposed system.

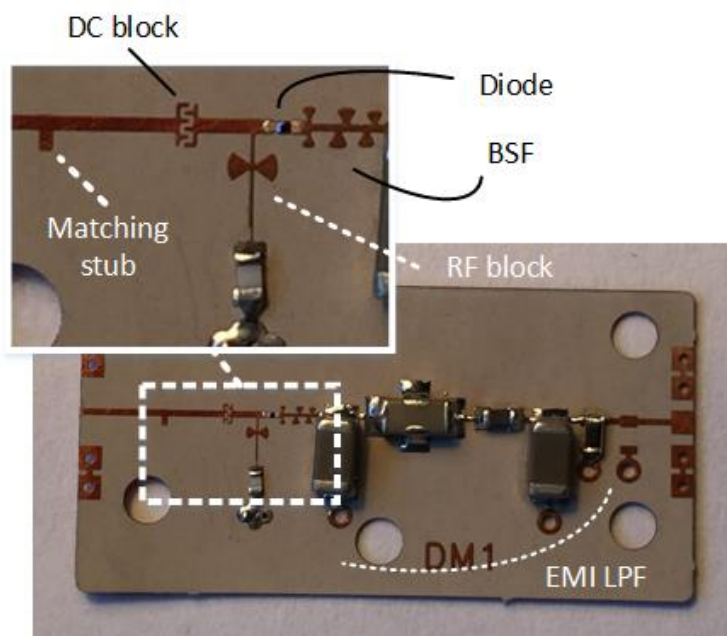


Figure 8-21: Detector circuit with EMI filter with zero-bias Schottkey diode (MZBD-9161)

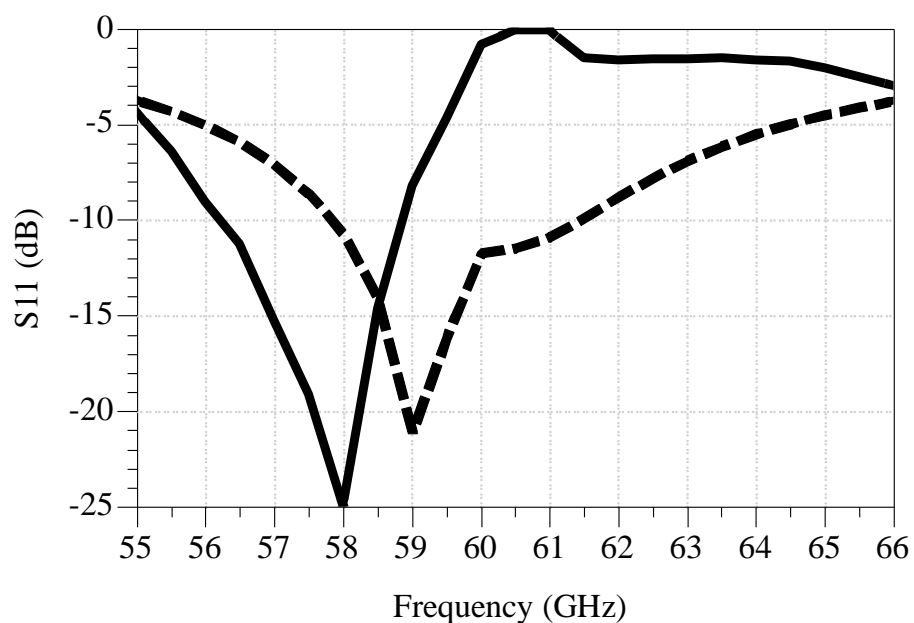


Figure 8-22: Return loss of the detector; solid line: measurement, dashed line: simulation, diode placement affects the return loss and makes a shift.

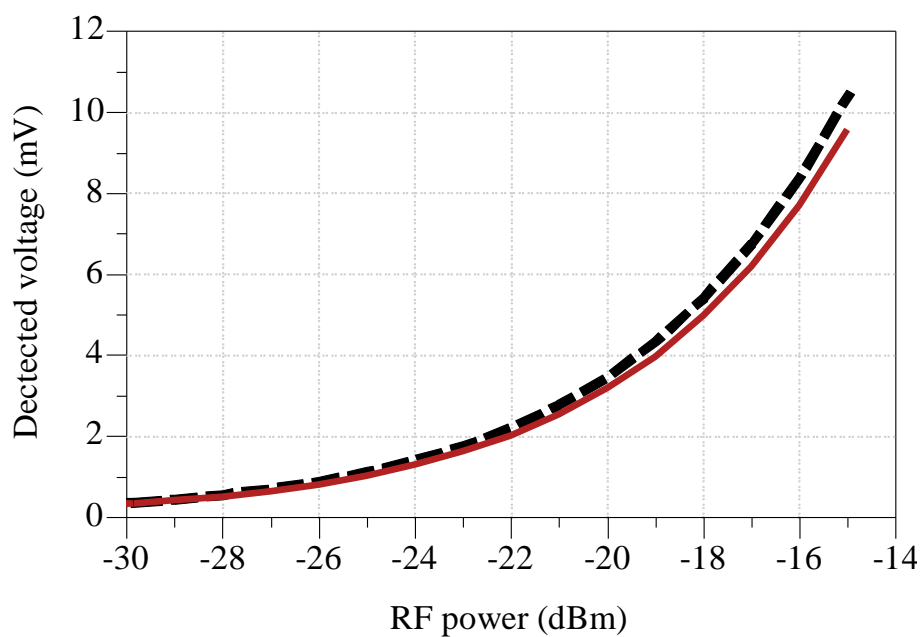


Figure 8-23: Detected voltage vs input RF power at 58 GHz; dashed line: simulation, solid line: measurement

8.9.3 System Assembly

Upon prototyping and testing all distinct parts, the whole DOA detection system is assembled within a metal box as it is shown in Figure 8-24. In order to prevent the undesired electromagnetic interference, different parts are placed in separate cavities. The antenna unit, the eight LNA dies (TGA4600) and the multiport interferometric passive network are located in the central cavity. Two cascaded LNA dies amplify the received signal from each antenna element with typical gain value of around 22 dBi. The band stop filter (BSF) after the second amplifier guarantees the suppression of intermodulation products. The building components of multiport with SIW technology, including phase shifter, Riblet hybrid, crossover and phase-compensator are highlighted in the same figure. Long transmission lines within the SIW multiport circuit inevitably increases the insertion loss and subsequently the sensitivity of the receiver. Even though SIW in thicker substrates suffers from less insertion loss, the thickness of 0.254 mm was selected due to our in-house PCB fabrication limitations and also to make it compatible with the detector circuit for interconnects between two circuits. It should also be mentioned that signals travelling the 50 ohm microstrip transmission lines which are used at the input and output of the cascaded amplifiers may interfere with the signal in the adjacent channels and degrade the system performance. Therefore, four LNA channels are isolated from each other via metallic shields that are not shown in the figure. However, the signal guided through SIW is fully confined internally and is therefore completely immune against undesired radiation and interference. Active low pass filters with very small cut-off frequency are designed within the baseband amplifier blocks for noise suppression.

8.9.4 System level measurements

Before measuring the system performance, the phase difference between the received signals through the prototyped antenna is measured within a test-bed which is shown in Figure 8-25. One of the four ports of the PNA-X vector network analyzer (N5247A) is connected to the transmitting horn antenna and three others to three input ports of our proposed antenna, i.e., P1, P3 and P4 in Figure 8-2. The phase differences were obtained by comparing S-parameters of the four ports. The measurements were independent of the distance between Tx and Rx antennas since the phase difference between the received signals in three antenna elements were calculated with reference to the signal of the port connected to the Tx horn antenna, e.g., $\varphi_{13} = \angle S_{Rx1,Tx} - \angle S_{Rx3,Tx}$. A rotator system that was able to rotate in both dimensions of azimuth and elevation was used in this test. One set of measurement results in which the rotator was set to be at $\theta_E = 5^\circ$ and θ_H was swept from -10° to $+10^\circ$ is plotted and compared with the theoretical values in Figure 8-26. One can observe a very good agreement between the measured results and the theoretical values within the range of -5° to 5° . The deviation that occurs beyond this range can pertain to the difference

between the radiation patterns of the antenna elements and the environmental effects of the antenna surrounding in the measurement setup. Hence, the operational range of the prototyped system should be limited within this range.

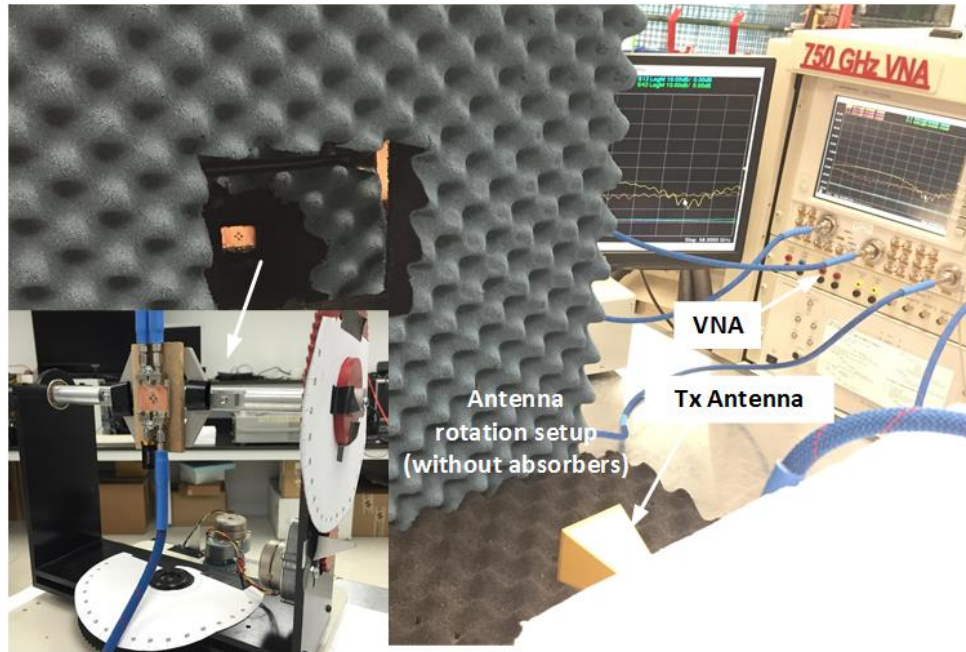


Figure 8-25: Measurement setup for phase difference of arrival measurement using the prototyped antenna

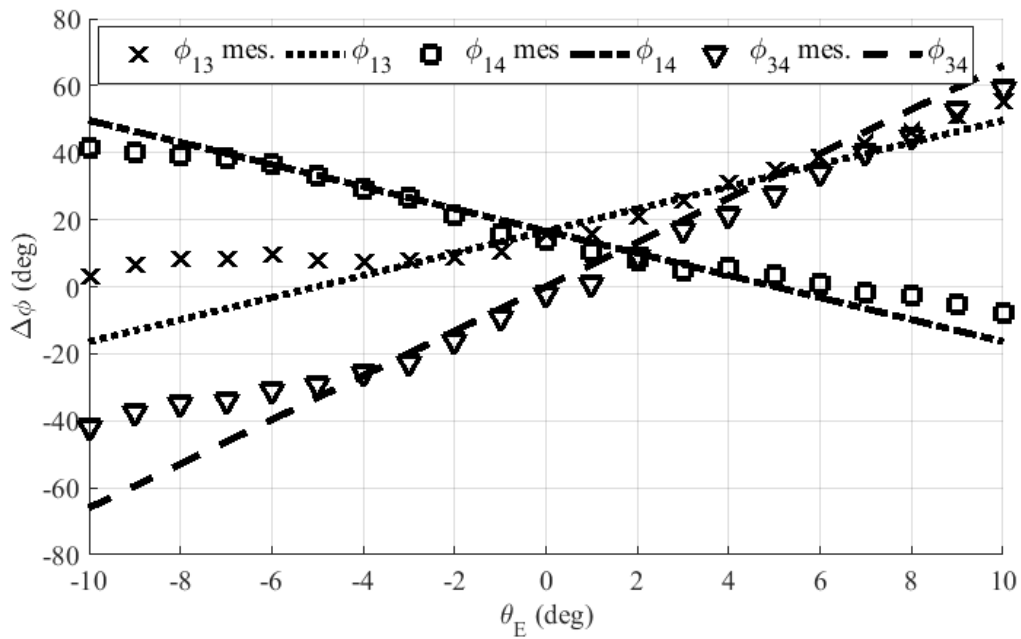


Figure 8-26: Measurement results for phase difference of arrival between received signals at three of the prototyped antenna elements when oriented at $\theta_E = 5^\circ$ at 57 GHz.

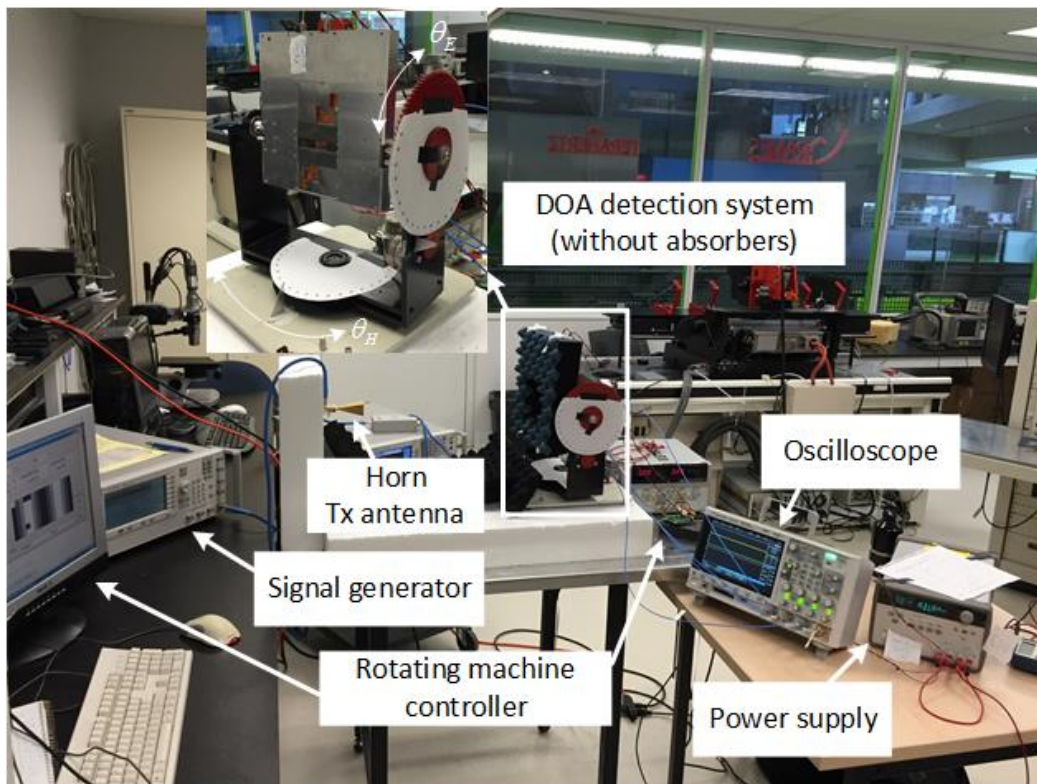


Figure 8-27: Test bed for system level measurements

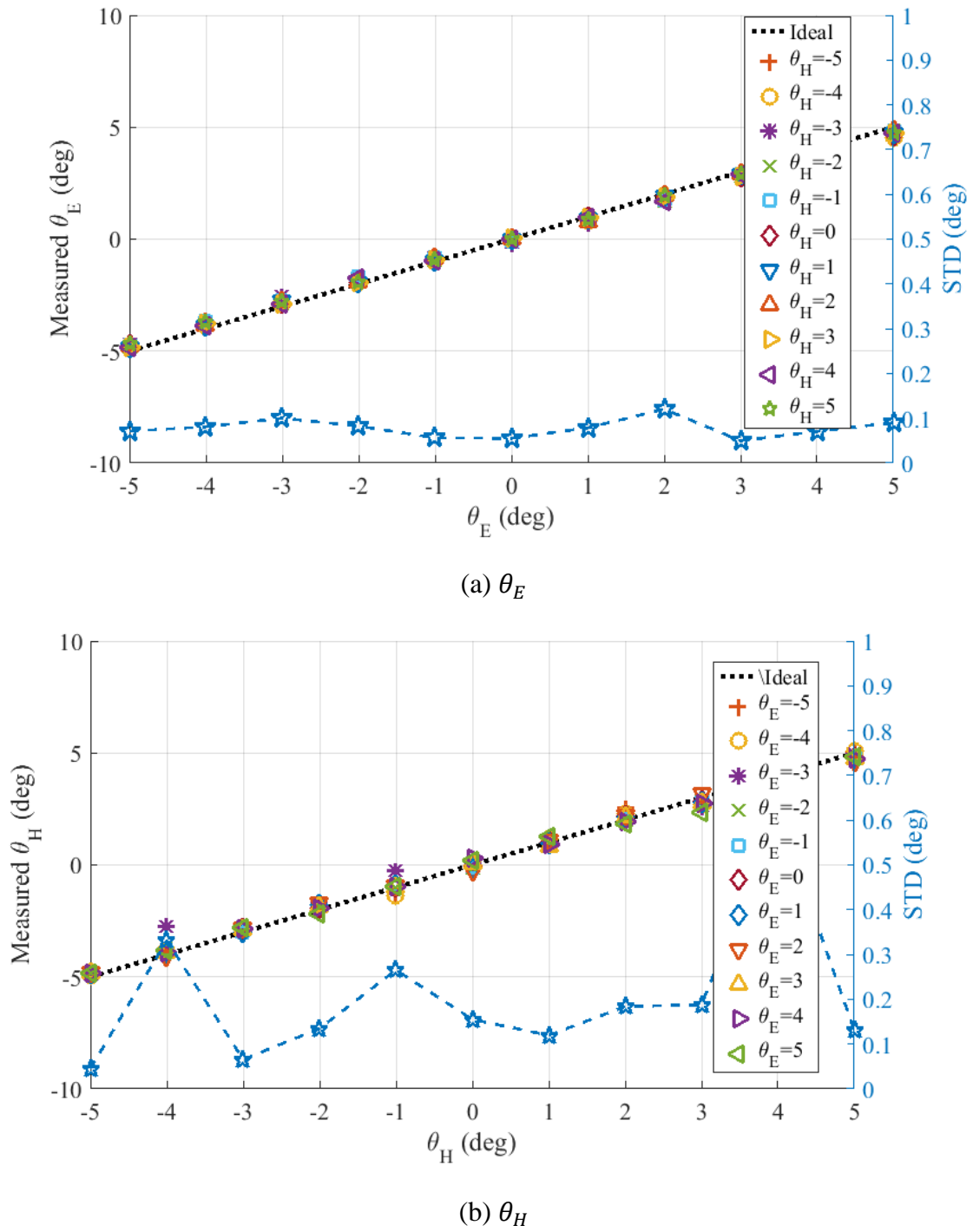


Figure 8-28: System level measurement results at 58 GHz

Subsequently, the whole system performance was evaluated in another test-bed which is shown in Figure 8-27. A PSG analog signal generator (E8257D) is used for generating a single frequency reference signal with the power of around 6 dBm. With the gain of around 22 dBi of the standard horn antenna, the emitting power was 28 dBm. The DOA detection system was placed at a distance of around 70 cm from the Tx antenna, hence in the Fairfield region.

The DoA system output signals were probed using the digital storage oscilloscope (DSO-X 3034A). The measurements were conducted for the whole range of -5° to $+5^\circ$ with the step of 1° for both angles in three different frequencies of 57 GHz, 58 GHz and 59 GHz. The best system performance upon calibration was obtained at 58 GHz. Therefore, the measurement results at this frequency along with the STD (*i.e.*, $\sqrt{(1/n) \sum_{i=1}^n (x_i - \mu)^2}$) at each angle are plotted in Figure 8-28. The measurement results are highly linear, and the excellent agreement of the estimated angles of arrival in both dimensions with the ideal values proves reliable functionality of the proposed system.

8.10 Conclusion

A multiport interferometry technique-enabled 2D DOA detection system is proposed, studied, developed and demonstrated through both simulations and experiments in this work. The original six-port based AOA detection system is organically expanded to an eight-port system with four input ports and specific relative phase differences between input signals throughout the proposed passive wave correlator. In other words, the incoming signals are processed differently in terms of the experiencing phase shift in the interferometric passive network prior to additively mixing in the detectors. The essential relative phase shifts in the multiport network are devised in a manner that helps extract the relative phase differences between the four received signals. Furthermore, with the arranged diamond shaped configuration of four receiving antenna elements, the incoming wave is received by the four antenna elements with relative phase differences that carry information about incoming DOA. The system is theoretically analyzed and the required conditions that the proposed eight-port network should satisfy are also presented and discussed. Based upon the theoretical analysis, the operation principles of the proposed system are evaluated via system-level simulations. Moreover, the techniques for implementing the proposed concept at selected millimeter wave frequency band are examined and the whole system is then prototyped to

experimentally assess the system performance in practice. Excellent results are obtained with the STD value of around 0.2° . The main drawbacks of the prototyped system are related to narrow operational frequency band and poor sensitivity that limits the operational distance between Tx antenna and Rx antenna. Nevertheless, the system bandwidth can be increased using wideband phase shifters, which have been reported in the literature. Use of LNA blocks with larger gain values or SIW transmission lines within substrates with larger thickness and thus lower loss can help improve the sensitivity.

CHAPTER 9 DUAL-MODE COMMUNICATION TRANSCEIVER ARCHITECTURE FOR BACKHAUL SMALL CELL APPLICATIONS

From chapter 4 throughout chapter 7 of this thesis, integration of sensing and communicating related functions were subjected for research and further development, while our contributions in developing a dual sensing-function in a single unified system was discussed in chapter 8. Afterwards, our focus was drawn into developing advanced radio architectures with versatile functionality of operating in multiple frequency bands and essentially in multiple modes. Such radio transceivers that can be usefully deployed into different platforms within 5G and future wireless systems. In this chapter, a transceiver architecture is presented that may utilize three frequency bands to operate in two modes of FDD and TDD for data communication. It can also sense signal traffics in a specific spectrum in order to monitor the whole band and generate the awareness of free channels.

The main problem is addressed in several key parts of the proposed transceiver. In the Tx block, a hybrid Heterodyne-Homodyne topology is proposed so that it can use only one LO with variable frequency for up-conversion to RF frequency at two bands in two modes. Using a novel filter-switch bank the transmitting and receiving signals over different frequency bands in two modes are routed to and from single Rx and single Tx blocks. This yields unified blocks of each mode of TDD and FDD over different bands, and also allows for a single antenna to be shared between both Tx and Rx. Direct down conversion in Rx lets the single LO to be shared with the Rx for both modes because the carrier frequency of transmitting and receiving signals is identical in TDD mode and the fixed difference of those in FDD mode is already considered in Tx through Heterodyne up conversion.

Spectrum sensing is also proposed to be done either independently or in a combined manner before or after the down-converter block, respectively. Indeed, the specific arrangement in the proposed architecture allows for sharing the components for multi-functions and hence making the transceiver rather compact, low cost and simple.

The proposed scheme is filed through a US patent application [178], and only the main features of the developed transceiver is concisely elaborated next.

9.1 Multiple band/mode radio

With the advent of backhaul technology in small cells for wireless communication with extremely high data throughput, millimeter wave frequency bands have been considered as the preferred spectrum for developing multifunction transceivers for such purposes. The spectrum at around 60 GHz and also 70 GHz and 80 GHz offers enough bandwidth for high data rate links. However, the channels are structured differently through these bands. Therefore, a combined V/E-band radio architecture in one reconfigurable system would be the ideal solution to address their needs.

Radio communication systems operating in V or E bands have some functional differences or incompatibilities that makes integration of these front-end modules in a single transceiver difficult. In fact, the system which is able to operate in both bands in a cognitive manner should essentially have the following features:

- 1) It should operate in V (57 GHz – 66 GHz), E (71 GHz – 76 GHz) and E (81 GHz – 86 GHz) bands. So, all RF components employed in the RF front-end must support this wide range of frequency or should be reconfigurable.
- 2) The V-band is an ISM band in Europe and therefore open for license-free uses. To mitigate interference, the system should be able to sense the spectrum and recognize the free available in-band channels at the same time of using at least one channel for data communication.
- 3) E-bands feature structured channels while the channels in V-band are not structured. The system should operate within TDD mode in V-band while the operational mode in E-bands is FDD.
- 4) All these multi-functionalities must be realized in an integrated scheme through unification of typical architectures of transceiver in two bands in support of lower cost and smaller size of the final system.

In the literature, some schemes for multi-band and/or multimode radio applications have been reported that can address some of the above-mentioned requirements. The previously reported schemes are concisely reviewed in the following:

Several simple radio transceiver architectures which are able to handle two different modes of TDD and FDD are presented in [179]. Furthermore, the RF front-end of the system comprises two distinct blocks, one block as a transceiver with a diplexer at the terminal of the antenna that may transmit signals at the first band (F1) and receive signals at the second band (F2). This may enable the transceiver to operate in FDD mode completely but only function as a transmitter in TDD mode which is assumed to be the mode for the first band only. The other block with a separate Rx antenna functions merely as a receiver that can receive signals in both bands of F1 in TDD mode and F2 in FDD mode. The additional signal which is received through the second Rx block in FDD mode may improve the system performance through maximal ratio combining when space diversity technique is employed. Since the main application scenario is assumed to be wireless mobile data communication cells, the use of a spatial diversity technique helps mitigate the effect of fading.

In order to implement this concept, three different embodiments for the frequency band multiplexing at the antenna feeding ports in both blocks are described in [179]. The antenna at the transceiver block is proposed to be connected to a diplexer or a combination of a diplexer and two switches, whilst the antenna at the second block which is used only for receiving can be connected to either a tunable filter or a combination of two filters and a switch. With these possible arrangements, three configurations of the overall system transceiver were presented in [179].

In all those configurations, the FDD and TDD modes must share at least one frequency band for receiving or transmitting signals and therefore it is not applicable to systems which must use a separate unlicensed band for TDD mode. Also, it is not appropriate for point-to-point communication systems with line of sight links and the additional Rx block unnecessarily adds up the complexity and the cost of the whole system.

In [180], a filtering method is proposed that can be used for dual mode transceivers that operate in an unlicensed band in TDD mode and two licensed bands in FDD mode. Even though the concept is limited to merely filtering technique, it is explained briefly next.

The architecture comprises three BPFs including FDD forward band (F1) and reverse band (F2) and also TDD unlicensed band (F3), which are all connected to a single antenna at a common point, and appropriate signal paths are selected via four switches. Two switches (S1 and S2) are located at the Tx and Rx terminals and FDD forward and reverse BPFs are interposed between

these switches (S1 and S2) and the antenna terminal. The second port of the third BPF (F3) is routed to the signal paths between these switches (S1 and S2) and the filters (F1 and F2) through two additional switches (S3 and S4) in between.

Any system that utilizes this configuration of filter bank may operate in FDD mode when using forward and reverse filters as main signal path to and from antenna, and the third filter would be shared for either transmission or reception in a timely manner of TDD mode. But, the signal path to FDD filters may not be closed in this mode and the signal path to at least one of them is open in each time slot. This unnecessarily opens the Rx input to the interference from other bands or may let the spurious products of the Tx be transmitted out.

A transceiver is proposed in [181] which supports two mobile communication standards, e.g. global system for mobile communications (GSM) or digital cellular system (DCS) at two different bands of operation. In comparison to its prior work, the proposed scheme brought up advantages when two separate signal paths in either transmitter or receiver which were essentially allocated to each band were replaced by single path in both Tx and Rx blocks using tunable filters at the antenna terminal and reconfigurable frequency divider in the LO synthesizer. This would make the system more compact and low cost. The solutions based on the embodiments in [181] may not operate in both modes of TDD and FDD.

In [182] a dual mode transceiver architecture is proposed that uses two separate frequency bands in order to operate both in TDD and FDD modes. The system may use either upper or lower frequency band for operation in TDD mode, and is able to swap between two bands for operation in FDD mode. This is made feasible by employing a diplexer at the antenna terminal and a switch bank, comprising four independent switches between the diplexer and the Tx and Rx output and input ports, respectively. This configuration allows the system to select the appropriate signal path in each mode. At the back-end and signal processor output, the signal to be transmitted is converted directly to IF and therefore a single stage up-conversion to RF is employed at the Tx block. The received RF frequency is also down converted to IF and then sampled to be converted to digital domain for further IF processing. Two LOs oscillate in two different bands and are mixed with either transmitting IF or received RF signals. The appropriate LO signals may be connected to mixers, using two independent switches.

For systems where there is a fixed frequency offset between the upper frequency range and the lower frequency range, the structure can be simplified further. In the second embodiment of the same scheme, two IF stages is considered and one variable LO is replaced with a fixed tuned LO which is shared between two image rejection mixer in both Tx and Rx blocks. The IF frequency of the signal at the back-end terminal is selected to be half of the frequency offset value. The RF filters are replaced with two IF BPFs in each Tx and Rx blocks. The difference between the center frequencies of the filters is exactly the fixed difference between two bands and the correct signal path for upper or lower bands are selected via two switches at the filter ports. The second IF signal is up-converted using a mixer and tunable LO and the switch bank and the diplexer configuration is remained unchanged.

However, the architecture reported in [182] is only capable of operating in FDD or TDD modes using only two bands and is not functional when the system has to use a different band in TDD mode. Therefore, it is not functional for our dual band and dual mode system. Also, it is not suitable for millimeter wave architectures when the frequency difference between two bands for FDD mode is very large. For example, over E-band (71-76 GHz and 81-86 GHz), this distance is 10 GHz and selecting first IF half of this difference, i.e. 5 GHz as proposed in the second embodiment may demand for very high sampling frequency in ADC blocks.

9.2 Proposed architecture

Figure 9-1 shows the proposed transceiver architecture. It consists of a digital signal processing (DSP) unit, transmitter (Tx) and receiver (Rx) blocks, filter bank and a single antenna. The operation principles of each of them are explained in detail, next.

DSP unit forms symbols out of the transmitting data in accordance with the selected modulation scheme. Then the symbols would be shaped using raised cosine filters and then the digital in-phase and quadrature components would be converted to analog signals to be sent to the transmitter for up-conversion. The signal in the Tx block is low-pass filtered first and then depending on the operational mode, i.e. TDD in V-band or FDD in E-band, it would be switched over to two different signal paths for up-conversion. If the system operates in V-band with TDD mode, the signal would be directly up-converted to the desired channel through quadrature modulation. The LO signal originates from a VCO which is then multiplied by a factor of 3.

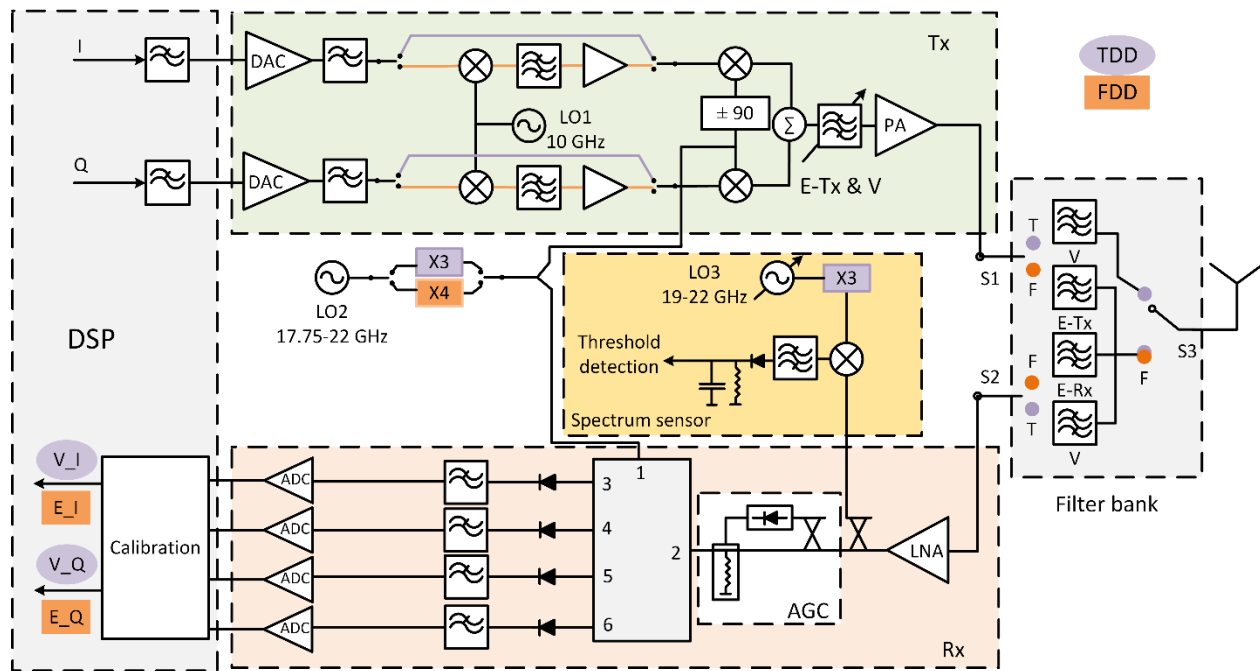


Figure 9-1: Proposed dual-band dual-mode radio architecture

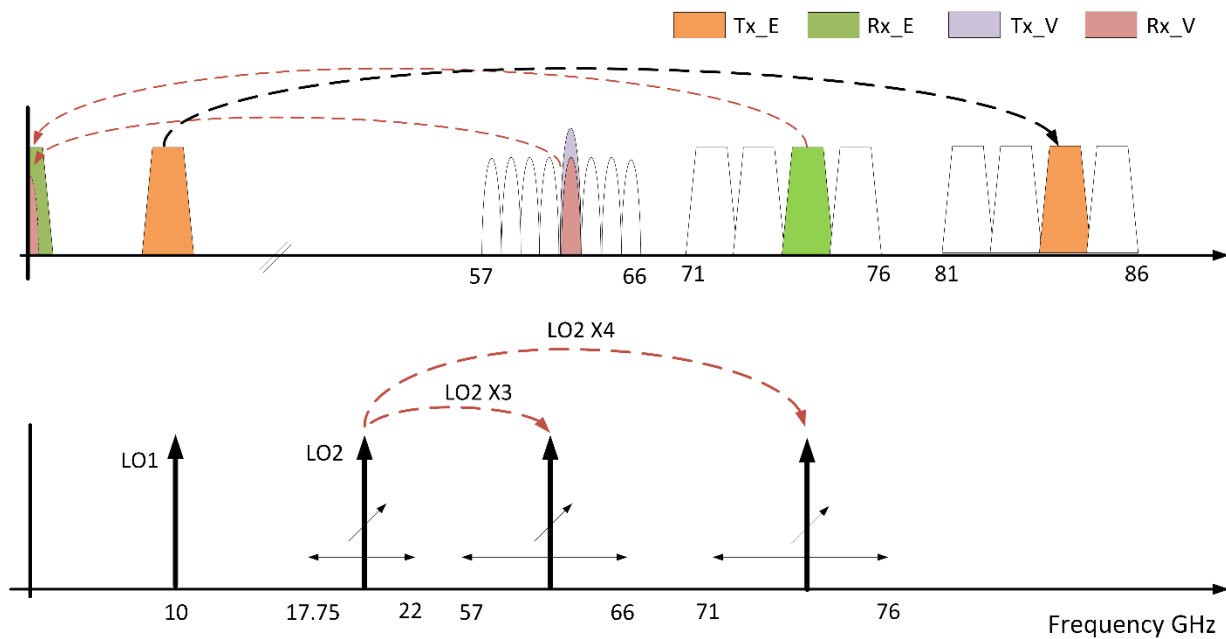


Figure 9-2: Proposed frequency planning diagram

On another hand, if the system operates in E-band with FDD mode, both I and Q components of baseband signal are first converted to intermediate frequency (IF) using an LO oscillating at a

constant frequency which should equal the frequency difference between FDD lower and higher bands, i.e. 10 GHz for E-bands, and then IF signals are up-converted using a quadrature mixer. The second LO signal is originating from the same VCO but its frequency is multiplied by a factor of four so that the up-converted signal locates at E-band. Note that the quadrature mixing of I and Q signals forms a single side-band (SSB) mixer, implying that it should up-convert to E-Low (71 GHz – 76 GHz) by suppressing the upper-side band (USB) or to E-High (81 GHz - 86 GHz) by suppressing the lower-side band (LSB). The selection of either USB or LSB depends on which band is selected for up-link communication.

The RF signal is then filtered in the tunable BPF. This BPF is wideband and also tunable between both bands of V and E-Tx. The filtered signal is transmitted upon being amplified by a power amplifier. Then the signal goes through a filter-switch bank before being transmitted by an antenna.

The filter-switch bank comprises a triplexer, a single BPF with center frequency at the TDD unlicensed band (V-band) and three two-state switches. The triplexer includes a BPF with a center frequency at TDD band, and two other BPFs with center frequency at FDD forward and reverse bands (71-76 GHz and 81-86 GHz). In TDD mode of operation, switches S1 and S2 are in state-T and the switch S3 alternates between two states within the TDD time slots. Thereby, the transmitting and received signals go through the BPFs of the TDD mode. On the other hand, and in FDD mode, all three switches stop in state F so that the transmitting and receiving signals may go through the forward and reverse BPFs, respectively.

In the receiver block, this signal is first amplified using a low noise amplifier (LNA) and then enters the six-port mixer. The initial gain at the receiver input is controlled by automatic gain control (AGC) loop which consists of a directional coupler, a log detector and a variable attenuator. A portion of the amplified input signal enters a separate block through a directional coupler for the purposed of spectrum sensing. As it is already mentioned, the channels in V spectrum band should be observed continuously to keep the system aware of their occupancy by other users. This sensing function takes part in the spectrum sensing block which is comprised of a down converter, an IF BPF with the bandwidth of a single channel, and diode detector. The detected DC signal that is a larger from a specified threshold value can notify the system about the usage of a specific channel

by other users. It should be noted that LO signal in the downvoter is made tunable through the whole V band in order to discriminate existing signal detection in different channels.

A six-port mixer is used as it is capable of down-converting the RF signal through mixing it with very low power LO. The LO signal which is used in the Tx block would be shared with the Rx block to be used in six-port mixer which operates as a direct down converter for both V and E bands.

In V-band, since both up-link and down-link signals are sharing identical frequency channels the frequency up-conversion in Tx and down-conversion in Rx can be done with the same LO through direct conversion or homodyne manner. However, in E-band there is a difference between the carrier frequencies of up and down link signals (i.e. 10 GHz). Therefore, up-conversion is done through two-times mixing or heterodyne scheme which allows sharing the millimeter wave LO between RF mixer in Tx and six-port mixer in Rx. Since the diodes in six-port mixer operate in square-law region, the required LO power is very low which is a significant advantage in comparison to the conventional mixers, because generating high power LO is expensive.

The signals at the output of the six-port mixer are low-pass filtered and then differentiated using operational amplifiers in order to form I and Q signals.

The performance of the proposed dual-band and dual-mode transceiver is evaluated through system-level simulations in ADS. The schematic view of the simulation platform is demonstrated in Figure 9-3. The parameters of SPICE model of the Schottky diode are imported from datasheet and the detector circuit is made using ideal lumped elements. The six-port circuit is also made up of ideal passive components. The RF BPFs which are used in both Tx and Rx blocks are the 4th order Chebyshev filter from simulator. Figure 9-4 shows the simulation results of the communication in FDD mode. In order to evaluate the functionality of the proposed architecture the AWGN channel noise is excluded in this set of simulations. Excellent agreement of the received signal with the transmitted one in Figure 9-3 validates the performance of the proposed transceiver. It should be noted that similar test was successfully carried out for operation in TDD mode which is not brought here.

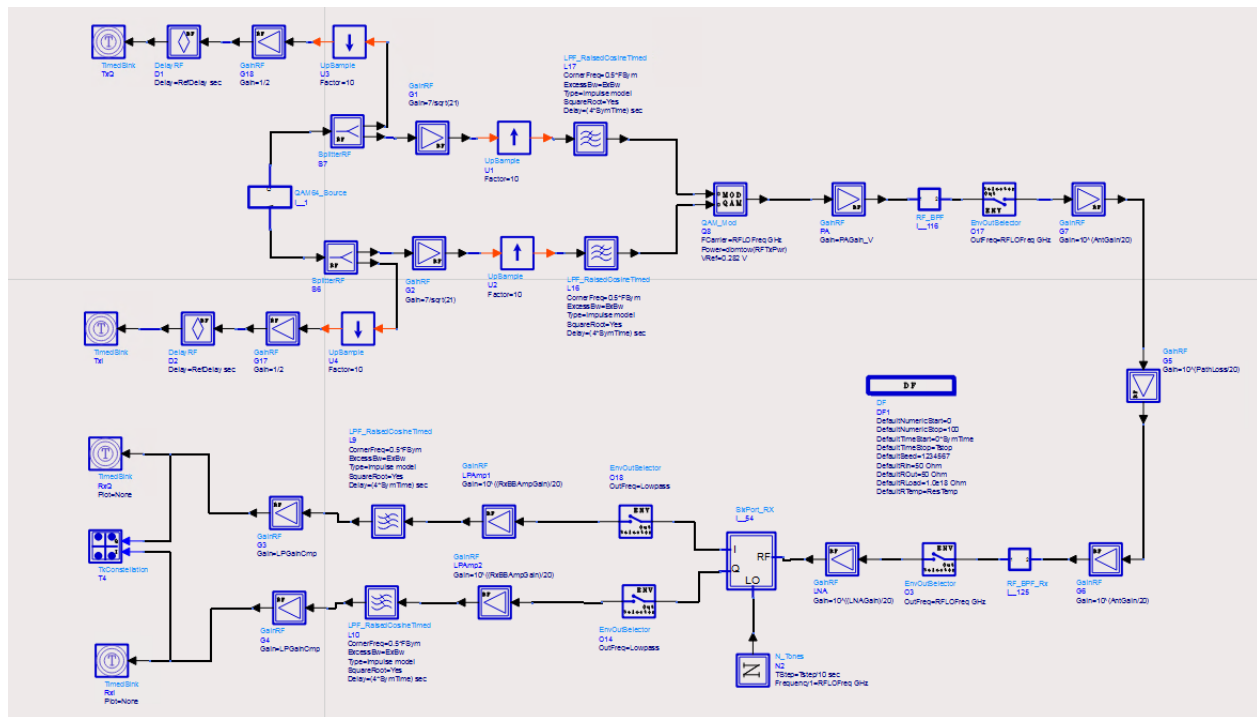
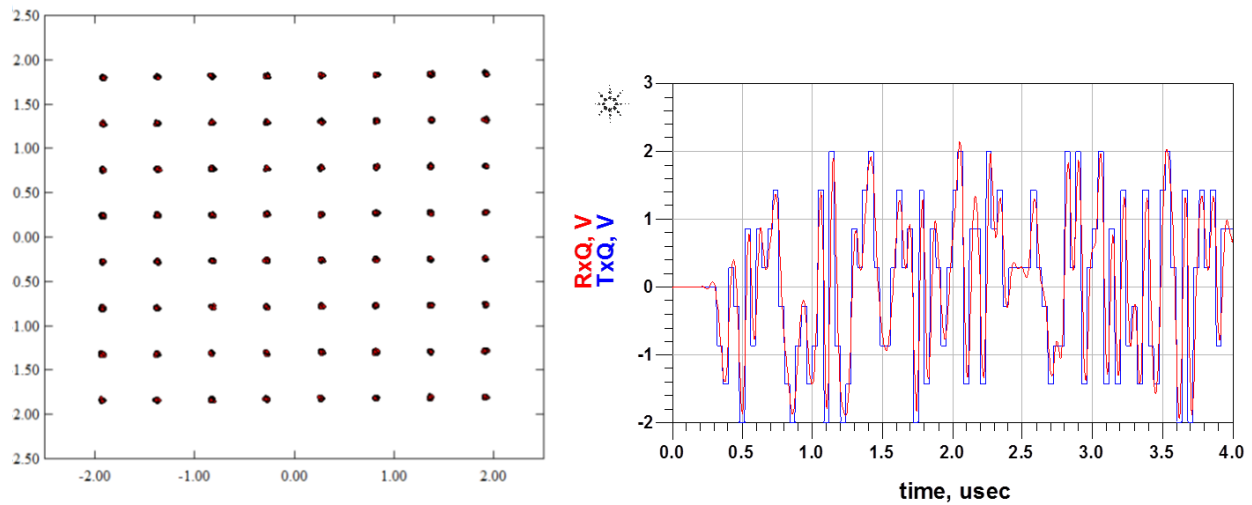


Figure 9-3: Schematic view of the simulation in ADS



(a) Constellation diagram

(b) Quadrature component

Figure 9-4: Simulation results in FDD mode

9.3 Conclusion

Our proposed transceiver architecture has some features that may not be found in previously proposed techniques:

- 1) It is able to function in two modes of TDD and FDD within two different bands. This is made feasible through the proposed filter-switch bank, frequency plan and the novel configuration in Tx and Rx blocks.
- 2) It is able to monitor the all in-band channels by sensing the whole spectrum of the band which is being used for communication by the system itself.
- 3) In Tx block, a hybrid heterodyne and homodyne topology is proposed in order to minimize the number of required variable LO while the direct conversion in Rx allows for the same LO to be shared between Tx and Rx blocks. This makes the architecture simple, compact and low cost.
- 4) The use of six-port-mixer is proposed in Rx as it can operate with very low LO powers. This helps reducing the system power consumption especially for the systems operating at the millimeter wave frequency bands.

CHAPTER 10 CONCLUSION AND FUTURE WORK

10.1 Conclusion

This PhD thesis work was generally developed within a top-down approach, starting from a system concept down to the development of innovative passive components. It has presented comprehensive techniques for realizing multifunctional systems within a set of unified transceiver architectures. Sensing and communicating as the two indispensable applications of wireless technology have been selected for integration with the purpose of cost and size reduction through the development of time agile multifunctional RadCom systems. Based upon an extensive literature review, the time-domain integration schemes of RadCom systems have been improved in a few aspects, i.e., incorporating the additional function of AOA detection and enhancing the range resolution in radar mode of the state-of-art transceiver. The new RadCom scheme was also characterized in terms of required SNR to achieve a desirable accuracy in parameter estimation. The capability of the system was also improved for multiple target detection using the proposed algorithm. Subsequent to system analysis through circuit and system simulations, a complete system demonstrator was prototyped around 5.9 GHz ISM band to prove the developed concept. The component- and system-level measurements that were conducted in our lab, thereby validating the proposed system functionality.

In order to further reduce the size and complexity of the proposed multifunctional transceiver, multiport-based receivers were studied and a passive multiport network was proposed and applied to the receiver block design. The new concept was first validated by system-level measurements of the first prototype of around 5.9 GHz. The unified RadCom transceiver was subsequently improved further by simplifying the function of AOA estimation through parameter estimation in the time domain rather than the FFT-based angle estimation. This was achieved by processing the received signals within the proposed passive 8-port network and switching the LO signals at two input ports in two subsequent time slots. The whole transceiver was analyzed and implemented for operation around 77 GHz. A calibration algorithm was proposed and employed to the experimental measurements in order to prove the functionality of the proposed scheme.

In addition to developing schemes for integrating distinct radar and radio functions, a solution has been put forward for simultaneous 2D DOA detection systems and also the multi-band and

multi-mode radios. To enable the conventional six-port based AOA detection receiver, a new eight-port network with specific relative phasing of the incoming signals was proposed to extract the desired information from the phase differences of the received signals at the antenna terminals. The proposed system was characterized, designed and implemented around 60 GHz (V-band).

Developing new transceivers with versatile functionality in very high frequency band demands for innovative passive components with optimum performance in high frequencies. Within this thesis, a frequency independent balun topology was proposed and validated through measurements. Moreover, a simple and new 180° hybrid coupler with non-interspersed input-output ports was proposed. It was analytically characterized and validated throughout in-lab measurements.

Additionally, a transceiver scheme based on the multiport technique in its receiver block was developed and characterized for next generation dual-band and dual-mode radios for application around V-band and E-band that helps rapid evolution of millimeter-wave technology for backhaul radios.

So far, through this PhD project, various research outcomes were produced including 4 journal articles, 5 conference papers as well as 3 US patents. The main scientific contribution of this thesis are listed in the following:

- 1) The time agile TFMCW operation signal of the RadCom system was generated via a combination of FPGA and DDS with the purpose of realizing a reconfigurable source for such integrated systems.
- 2) The heterodyne based transceiver architecture was developed for a robust RadCom system with the ability of complete positioning of either mobile or stationary objects (i.e. range, velocity and angle estimation) as well as communicating with other unites. The intrinsic incompatibilities of the radar and radio systems were addressed when implementing a 5.9 GHz prototype of the system. A complete implementation flow of the proposed system, starting from system specification in accordance with FCC rules around ISM band to link budget analysis as well as system simulations based on the existing off-the-shelf RF components was examined. The proposed approach was validated through system level in-lab measurements.

- 3) The multiport based technique was developed for unification of the radar and radio transceivers with all functionalities of the already developed heterodyne-based multifunction system. This unification was accomplished, because of analog processing (different from the conventional one) of the input signals throughout the passive multiport network. The new architecture was more compact, and much simpler than the previously reported ones. A low-frequency prototype of the proposed architecture was tested through in-lab measurements.
- 4) The multiport interferometric receiver was analyzed in terms of noise figure, conversion loss, and intermodulation products. A parametric model of the six-port receiver in connection with mixer model was also developed. The derived analytical equations were validated when compared with harmonic balance simulation results.
- 5) The multiport RadCom transceiver was further improved, designed and demonstrated around 77 GHz.
- 6) To cancel out the effect of non-idealities that occur in practice, a comprehensive calibration technique for both radar and radio mode was proposed for application in the unified RadCom transceiver. The proposed calibration technique was assessed within in-lab measurements
- 7) A multiport-based system for simultaneous 2D DOA detection was proposed, studied and, characterized and implemented for operation around 60 GHz.
- 8) The specific calibration method and algorithm for the proposed 2D DOA detection system was also proposed for use in practice.
- 9) A dual-band and dual-mode multiport based transceiver scheme was studied and characterized via system level simulations to be employed in future unlicensed V-band and also E-band backhaul systems.
- 10) With the purpose of application in very high frequency band, a wideband structure based balun was proposed, in which phase inversion can be achieved through wave rotation in a combined configuration of SIW and antipodal fin-line transmission line.

- 11) A simple topology of 180° hybrid coupler was proposed whose input-output ports are non-interspersed. The proposed hybrid was theoretically analyzed and its performance around millimetre-wave frequency bands was assessed through experimental measurements.

10.2 Outlook and future work

The scientific contributions made throughout this thesis can be extended in the following aspects:

- 1) With the existing time-agile joint radar-radio waveform scheme, simultaneous operation of the radar related functions with those related to radio communication is not feasible. In the scenarios with congested sensory targets and essential long time slots for sensing mode, a considerable latency between the communicating units should be expected. The RadCom systems can be interestingly improved if enabled for continuous and non-stop sensing mode as well as communicating within TDD manner. This can be achieved through interleaving the radio channel into the radar one. One possible solution could be QAM modulation of the radar FMCW chirp signals and discriminate them upon de-chirping the received signal into different IF signals. Such concept can be employed for the development of cooperative radars [19, 95, 183-185] with the purpose of incorporating the communication function with their principal function of radar sensing.

Figure 10-1 proposes a frequency-time diagram of the operational signals of a pair of onboard cooperative units. The chirp with the starting frequency of f_0 is the reference chirp that is used for de-chirping and is identical in all units. The second and third chirps with the starting frequency of $f_0 + f_2$ and $f_0 + f_3$ are the ones transmitted from the first and second radar units, respectively. Note that the frequencies of f_1 and f_2 should be selected very small in comparison to the total chirp bandwidth and the sketched diagram should not be scaled for real implementation. T_c denotes the one-way time-of-flight between two radar units and T_0 pertains to the two-way delay time between first sensor and a typical object located at a closer distance. If the radar unit tend to transmit data, the reference chirp signal can also be modulated by a QAM signal at an intermediate frequency of f_c . Using this modulation scheme for the operational signal is justified further in detail with the next paragraphs.

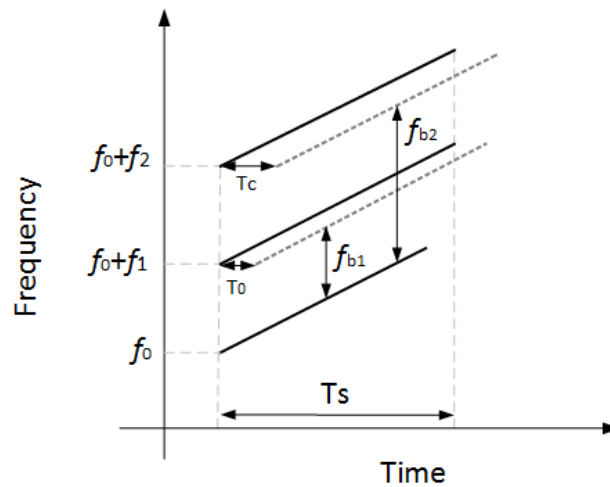


Figure 10-1: Frequency-time diagram of the chirp in two units (radar mode)

Figure 10-2 shows the proposed transceiver architecture for the cooperative radar units. A chirp generator which can be a DDS module or a VCO with a phase lock loop (PLL) or a combination of both can generate the reference chirp signal. This reference signal is then split into two signals to be shared with receiver (Rx) block passing through a power divider. The single IF (i.e., f_i) and the QAM signals (at f_c) are combined through a power combiner and then up-converted when modulating the reference chirp.

Consequently, the transmitting signal contains a pure chirp as well as an interleaved data-modulated chirp if the system intends to transmit information data. In that case, it may not receive any data modulated chirp but only a pure chirp from the other unit. In other words, the data communication should be done in a time division duplex (TDD) manner whereas sensing can be done continuously.

In the Rx block, the incoming chirp signals that include pure or data modulated chirps, coming from other units, and its own transmitted one which is reflected back from surrounding objects are de-chirped by the reference signal in mixer. Interestingly, the mixing products fall in three different IF bands around three IF frequencies of f_1 , f_2 , f_c . In other words, different chirps which are not easily distinguishable in RF band are now separated into adjacent IF bands which can be either analog or digital filtered considering all implementation issues. If the radar beat frequencies are much smaller than the desired data modulation bandwidth, two analog bandpass filters should be sufficient for initial filtering before further digital processing.

Figure 10-3 shows the received IF spectra at the output of the Rx block when the unit is receiving information data as well as detecting its distance to the other unit and a typical object existing nearby. The QAM signal at the IF frequency can be demodulated in the digital domain.

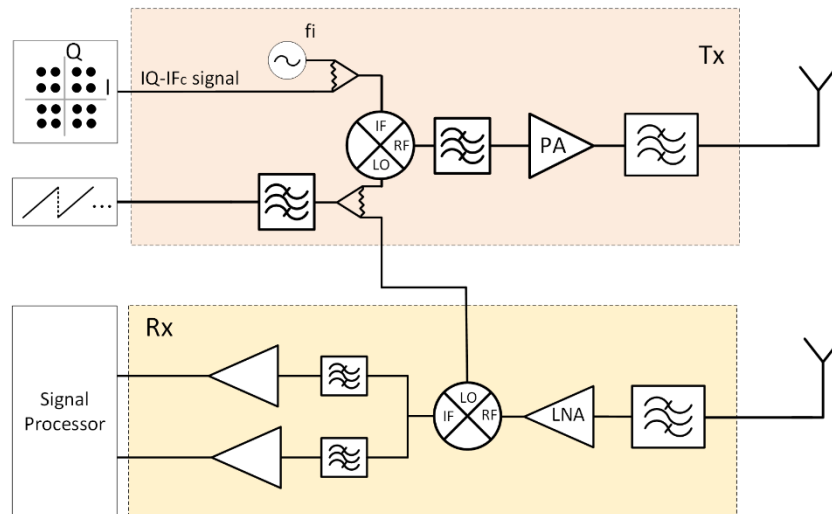


Figure 10-2: Proposed transceiver architecture

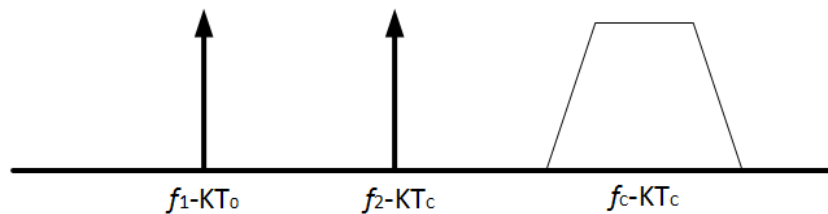


Figure 10-3: Spectra of the de-chirped radar and communication signals

- 2) The time-agile integration scheme suffers from the absolute necessity of synchronization if it is to be employed in future transportation systems with multiple on-board units. The existing scheme can be improved to relax this requirement.
- 3) The multiport-interferometric based receivers suffer from low sensitivity and a short dynamic range. This would consequently limit the maximum and minimum operational range of the multifunctional system. The diode linearization techniques can be incorporated with the appropriate calibration algorithms to improve the dynamic range of the RadCom unified receivers.

- 4) Radar systems use high-gain antennas to compensate for the path loss and focus the eliminating area to the limited desired range, whereas radios essentially are desired to utilize low gain antennas with omnidirectional radiation pattern. A dual mode antenna with reconfigurable pattern can be developed to be incorporated with the RadCom transceivers at the front-end.

BIBLIOGRAPHY

- [1] R. Bishop, *Intelligent vehicle technology and trends*, 2005.
- [2] R. H. Rasshofer and K. Naab, "77 GHz long range radar systems status, ongoing developments and future challenges," in *European Radar Conference, 2005. EURAD 2005.*, 2005, pp. 161-164.
- [3] B. Fleming, "Recent advancement in automotive radar systems [Automotive Electronics]," *IEEE Vehicular Technology Magazine*, vol. 7, pp. 4-9, 2012.
- [4] R. Cager, D. LaFlame, and L. Parode, "Orbiter Ku-band integrated radar and communications subsystem," *IEEE Transactions on Communications*, vol. 26, pp. 1604-1619, 1978.
- [5] E. Cianca and B. Gupta, "FM-UWB for communications and radar in medical applications," *Wireless Personal Communications*, vol. 51, p. 793, 2009.
- [6] M. Jamil, H.-J. Zepernick, and M. I. Pettersson, "On integrated radar and communication systems using oppermann sequences," in *Military Communications Conference, 2008. MILCOM 2008. IEEE*, 2008, pp. 1-6.
- [7] Z. Lin and P. Wei, "Pulse amplitude modulation direct sequence ultra wideband sharing signal for communication and radar systems," in *Antennas, Propagation & EM Theory, 2006. ISAPE'06. 7th International Symposium on*, 2006, pp. 1-5.
- [8] Z. Lin and P. Wei, "Pulse position modulation time hopping ultra wideband sharing signal for radar and communication system," in *Radar, 2006. CIE'06. International Conference on*, 2006, pp. 1-4.
- [9] S. Lindenmeier, K. Boehm, and J. F. Luy, "A wireless data link for mobile applications," *IEEE microwave and wireless components letters*, vol. 13, pp. 326-328, 2003.
- [10] K. Mizui, M. Uchida, and M. Nakagawa, "Vehicle-to-vehicle communications and ranging system using spread spectrum techniques," *Electronics and Communications in Japan (Part I: Communications)*, vol. 79, pp. 106-115, 1996.
- [11] G. N. Saddik, R. S. Singh, and E. R. Brown, "Ultra-wideband multifunctional communications/radar system," *IEEE Transactions on Microwave Theory and Techniques*, vol. 55, pp. 1431-1437, 2007.
- [12] S. Xu, Y. Chen, and P. Zhang, "Integrated radar and communication based on DS-UWB," in *Ultrawideband and Ultrashort Impulse Signals, The Third International Conference*, 2006, pp. 142-144.
- [13] X. Yin, J. Bauwelinck, G. Torfs, P. Demuytere, J. Vandewege, H. Tubbax, *et al.*, "Embedded ranging system in ISM band," *Electronics Letters*, vol. 44, pp. 1043-1045, 2008.
- [14] L. Han and K. Wu, "Multifunctional transceiver for future intelligent transportation systems," *IEEE Transactions on Microwave Theory and Techniques*, vol. 59, pp. 1879-1892, 2011.

- [15] L. Han and K. Wu, "24-GHz joint radar and radio system capable of time-agile wireless sensing and communication," in *Microwave Symposium Digest (MTT), 2011 IEEE MTT-S International*, 2011, pp. 1-4.
- [16] K. Konno and S. Koshikawa, "Millimeter-wave dual mode radar for headway control in IVHS," in *Microwave Symposium Digest, 1997., IEEE MTT-S International*, 1997, pp. 1261-1264.
- [17] V. Winkler and J. Detlefsen, "Automotive 24 GHz pulse radar extended by a DQPSK communication channel," in *Radar Conference, 2007. EuRAD 2007. European*, 2007, pp. 138-141.
- [18] P. Barrenechea, F. Elferink, and J. Janssen, "FMCW radar with broadband communication capability," in *Radar Conference, 2007. EuRAD 2007. European*, 2007, pp. 130-133.
- [19] A. Stelzer, M. Jahn, and S. Scheiblhofer, "Precise distance measurement with cooperative FMCW radar units," in *Radio and Wireless Symposium, 2008 IEEE*, 2008, pp. 771-774.
- [20] H. Zhang, L. Li, and K. Wu, "24GHz software-defined radar system for automotive applications," in *Wireless Technologies, 2007 European Conference on*, 2007, pp. 138-141.
- [21] M. Braun, C. Sturm, A. Niethammer, and F. K. Jondral, "Parametrization of joint OFDM-based radar and communication systems for vehicular applications," in *Personal, Indoor and Mobile Radio Communications, 2009 IEEE 20th International Symposium on*, 2009, pp. 3020-3024.
- [22] D. Garmatyuk and K. Kauffman, "Radar and data communication fusion with UWB-OFDM software-defined system," in *Ultra-Wideband, 2009. ICUWB 2009. IEEE International Conference on*, 2009, pp. 454-458.
- [23] L. Han and K. Wu, "24-GHz integrated radio and radar system capable of time-agile wireless communication and sensing," *IEEE Transactions on Microwave Theory and Techniques*, vol. 60, pp. 619-631, 2012.
- [24] L. Cheng, B. E. Henty, D. D. Stancil, F. Bai, and P. Mudalige, "Mobile vehicle-to-vehicle narrow-band channel measurement and characterization of the 5.9 GHz dedicated short range communication (DSRC) frequency band," *IEEE Journal on Selected Areas in Communications*, vol. 25, 2007.
- [25] M. Bocquet, C. Loyez, C. Lethien, N. Deparis, M. Heddebaut, A. Rivenq, *et al.*, "A multifunctional 60-GHz system for automotive applications with communication and positioning abilities based on time reversal," in *Radar Conference (EuRAD), 2010 European*, 2010, pp. 61-64.
- [26] Y. L. Sit, C. Sturm, J. Baier, and T. Zwick, "Direction of arrival estimation using the MUSIC algorithm for a MIMO OFDM radar," in *Radar Conference (RADAR), 2012 IEEE*, 2012, pp. 0226-0229.
- [27] J. Moghaddasi and K. Wu, "Improved joint radar-radio (RadCom) transceiver for future intelligent transportation platforms and highly mobile high-speed communication systems," in *Wireless Symposium (IWS), 2013 IEEE International*, 2013, pp. 1-4.
- [28] J. Moghaddasi and K. Wu, "Multifunctional Transceiver for Future Radar Sensing and Radio Communicating Data-Fusion Platform," *IEEE Access*, vol. 4, pp. 818-838, 2016.

- [29] J. Östh, M. Karlsson, A. Serban, and S. Gong, "Schottky diode as high-speed variable impedance load in six-port modulators," in *Ultra-Wideband (ICUWB), 2011 IEEE International Conference on*, 2011, pp. 68-71.
- [30] J. Östh, M. Karlsson, A. Serban, and S. Gong, "A comparative study of single-ended vs. differential six-port modulators for wireless communications," *IEEE Transactions on Circuits and Systems I: Regular Papers*, vol. 62, pp. 564-570, 2015.
- [31] R. G. Bosisio, Y. Y. Zhao, X. Y. Xu, S. Abielmona, E. Moldovan, Y. S. Xu, *et al.*, "New-Wave Radio," *IEEE Microwave Magazine*, vol. 9, pp. 89-100, 2008.
- [32] T. Hentschel, "The six-port as a communications receiver," *IEEE Transactions on Microwave Theory and Techniques*, vol. 53, pp. 1039-1047, 2005.
- [33] S. O. Tatu, E. Moldovan, K. Wu, and R. G. Bosisio, "A new direct millimeter-wave six-port receiver," *IEEE Transactions on microwave theory and techniques*, vol. 49, pp. 2517-2522, 2001.
- [34] A. Koelpin, G. Vinci, B. Laemmle, D. Kissinger, and R. Weigel, "The six-port in modern society," *IEEE Microwave Magazine*, vol. 11, pp. 35-43, 2010.
- [35] S. O. Tatu, A. Serban, M. Helaoui, and A. Koelpin, "Multiport technology: The new rise of an old concept," *IEEE Microwave Magazine*, vol. 15, pp. S34-S44, 2014.
- [36] G. Vinci, S. Lindner, F. Barbon, R. Weigel, and A. Koelpin, "Promise of a better position," *IEEE Microwave Magazine*, vol. 13, pp. S41-S49, 2012.
- [37] G. F. Engen, "The six-port reflectometer: An alternative network analyzer," *IEEE Transactions on Microwave Theory and Techniques*, vol. 25, pp. 1075-1080, 1977.
- [38] G. F. Engen, "An improved circuit for implementing the six-port technique of microwave measurements," *IEEE Transactions on microwave theory and techniques*, vol. 25, pp. 1080-1083, 1977.
- [39] G. F. Engen and C. A. Hoer, "Application of an arbitrary 6-port junction to power-measurement problems," *IEEE transactions on Instrumentation and Measurement*, vol. 21, pp. 470-474, 1972.
- [40] J. Li, R. Bosisio, and K. Wu, "A six-port direct digital millimeter wave receiver," in *Microwave Symposium Digest, 1994., IEEE MTT-S International*, 1994, pp. 1659-1662.
- [41] J. Li, R. G. Bosisio, and K. Wu, "A collision avoidance radar using six-port phase/frequency discriminator (SPFD)," in *Telesystems Conference, 1994. Conference Proceedings., 1994 IEEE National*, 1994, pp. 55-58.
- [42] E. Moldovan, S. O. Tatu, T. Gaman, W. Ke, and R. G. Bosisio, "A new 94-GHz six-port collision-avoidance radar sensor," *IEEE Transactions on Microwave Theory and Techniques*, vol. 52, pp. 751-759, 2004.
- [43] G. Vinci, F. Barbon, R. Weigel, and A. Koelpin, "A high accuracy direction-of-arrival and misalignment angle detector," in *Microwave Conference (GeMIC), 2011 German*, 2011, pp. 1-3.

- [44] G. Vinci, A. Koelpin, and R. Weigel, "Employing six-port technology for phase-measurement-based calibration of automotive radar," in *Microwave Conference, 2009. APMC 2009. Asia Pacific*, 2009, pp. 329-332.
- [45] G. Vinci, B. Laemmle, F. Barbon, R. Weigel, and A. Koelpin, "A 77 GHz direction of arrival detector system with SiGe integrated six-port receiver," in *Radio and Wireless Symposium (RWS), 2012 IEEE*, 2012, pp. 247-250.
- [46] A. Koelpin and R. Weigel, "Six-Port based direction finding and ranging," in *2014 20th International Conference on Microwaves, Radar and Wireless Communications (MIKON)*, 2014, pp. 1-5.
- [47] G. Vinci, S. Lindner, F. Barbon, S. Mann, M. Hofmann, A. Duda, *et al.*, "Six-port radar sensor for remote respiration rate and heartbeat vital-sign monitoring," *IEEE Transactions on Microwave Theory and Techniques*, vol. 61, pp. 2093-2100, 2013.
- [48] A. O. Olopade, A. Hasan, and M. Helaoui, "Concurrent Dual-Band Six-Port Receiver for Multi-Standard and Software Defined Radio Applications," *Microwave Theory and Techniques, IEEE Transactions on*, vol. 61, pp. 4252-4261, 2013.
- [49] A. Hasan and M. Helaoui, "Novel modeling and calibration approach for multiport receivers mitigating system imperfections and hardware impairments," *IEEE Transactions on Microwave Theory and Techniques*, vol. 60, pp. 2644-2653, 2012.
- [50] A. Hasan and M. Helaoui, "Comparative analysis of linear six-port receiver calibration techniques," in *Microwave Conference (EuMC), 2013 European*, 2013, pp. 64-67.
- [51] L. Han, "Integrated Communication and Radar Scheme for Future Intelligent Transportation Systems," École Polytechnique de Montréal, 2011.
- [52] D. G. C. Luck, *Frequency Modulated Radar*: Literary Licensing, LLC, 2012.
- [53] H. Rohling and E. Lissel, "77 GHz radar sensor for car application," in *Radar Conference, 1995., Record of the IEEE 1995 International*, 1995, pp. 373-379.
- [54] A. G. Stove, "Linear FMCW radar techniques," in *IEE Proceedings F (Radar and Signal Processing)*, 1992, pp. 343-350.
- [55] B. Razavi, "Design considerations for direct-conversion receivers," *IEEE Transactions on Circuits and Systems II: Analog and Digital Signal Processing*, vol. 44, pp. 428-435, 1997.
- [56] V. D. Min Zou, James Wong, "Quad Demodulators Arm Direct-Conversion Receivers," *Microwaves and RF*, 1998.
- [57] W. Namgoong and T. H. Meng, "Direct-conversion RF receiver design," *IEEE Transactions on Communications*, vol. 49, pp. 518-529, 2001.
- [58] U. L. Rohde and M. Rudolph, *RF/microwave circuit design for wireless applications*: John Wiley & Sons, 2013.
- [59] T. Eireiner and T. Müller, "Six-port receiver for mm-wave-concept, evaluation and implementation," *Proc. IST Mobile and Wireless Communications Summit, Dresden*, vol. 19, p. 23, 2005.
- [60] F. M. Ghannouchi and A. Mohammadi, *The six-port technique with microwave and wireless applications*: Artech House, 2009.

- [61] D. M. Pozar, "Microwave Engineering 3e," *Transmission Lines and Waveguides*, pp. 143-149, 2005.
- [62] M. Golio, *The RF and microwave handbook*: CRC press, 2000.
- [63] C. de la Morena-Álvarez-Palencia and M. Burgos-Garcia, "Four-octave six-port receiver and its calibration for broadband communications and software defined radios," *Progress In Electromagnetics Research*, vol. 116, pp. 1-21, 2011.
- [64] F. Lan, C. Akyel, F. Ghannouchi, J. Gauthier, and S. Khouaja, "A six-port based on-line measurement system using special probe with conical open end to determine relative complex permittivity at radio and microwave frequencies," in *Instrumentation and Measurement Technology Conference, 1999. IMTC/99. Proceedings of the 16th IEEE*, 1999, pp. 42-47.
- [65] G. Luff, P. Probert, and J. Carroll, "Real-time six-port reflectometer," in *IEE Proceedings H (Microwaves, Optics and Antennas)*, 1984, pp. 186-190.
- [66] A. Hasan and M. Helaoui, "Performance driven six-port receiver and its advantages over low-IF receiver architecture," *Journal of Electrical and Computer Engineering*, vol. 2014, p. 1, 2014.
- [67] N. Khaddaj Mallat, E. Moldovan, and S. O. Tatu, "Comparative demodulation results for six-port and conventional 60 GHz direct conversion receivers," *Progress In Electromagnetics Research*, vol. 84, pp. 437-449, 2008.
- [68] Y. Demers, R. Bosisio, and F. Ghannouchi, "Repetitive and single shot pulse microwave six-port reflectometer," *IEEE transactions on instrumentation and measurement*, vol. 39, pp. 195-200, 1990.
- [69] J. Jürgensen, D. Krupezevic, M. Ratni, and Z. Wang, "Baseband Aspects of a Direct Conversion Receiver Concept using Five-Port Technology," in *2nd Karlsruhe Workshop on Software Radio, Karlsruhe, March 2002 Proc*, 2002.
- [70] A. Technologies, "Agilent low barrier Schottky diode detectors," *8472B datasheet*, 2009.
- [71] Z. Chen, G. Gokeda, and Y. Yu, *Introduction to Direction-of-arrival Estimation*: Artech House, 2010.
- [72] S. Chandran, *Advances in Direction-of-arrival Estimation*: Artech House, 2005.
- [73] T. E. Tuncer and B. Friedlander, *Classical and modern direction-of-arrival estimation*: Academic Press, 2009.
- [74] D. A. De Wolf, *Essentials of electromagnetics for engineering*: Cambridge University Press, 2001.
- [75] R. E. Collin, *Foundations for microwave engineering*: John Wiley & Sons, 2007.
- [76] D. K. Barton and S. A. Leonov, *Radar technology encyclopedia*: Artech house, 1998.
- [77] W. Deng, R. Mahmoudi, and A. H. van Roermund, *Time multiplexed beam-forming with space-frequency transformation*: Springer Science & Business Media, 2012.
- [78] N. Levanon and E. Mozeson, *Radar signals*: John Wiley & Sons, 2004.

- [79] A. Lin and H. Ling, "Doppler and direction-of-arrival (DDOA) radar for multiple-mover sensing," *IEEE transactions on aerospace and electronic systems*, vol. 43, 2007.
- [80] J. Hasch, E. Topak, R. Schnabel, T. Zwick, R. Weigel, and C. Waldschmidt, "Millimeter-wave technology for automotive radar sensors in the 77 GHz frequency band," *IEEE Transactions on Microwave Theory and Techniques*, vol. 60, pp. 845-860, 2012.
- [81] V. Winkler, "Range Doppler detection for automotive FMCW radars," in *Microwave Conference, 2007. European*, 2007, pp. 1445-1448.
- [82] A. Bazzi, C. Kärnfelt, A. Peden, T. Chonavel, P. Galaup, and F. Bodereau, "Estimation techniques and simulation platforms for 77 GHz FMCW ACC radars," *The European Physical Journal Applied Physics*, vol. 57, p. 11001, 2012.
- [83] G. Heinzel, A. Rüdiger, and R. Schilling, "Spectrum and spectral density estimation by the Discrete Fourier transform (DFT), including a comprehensive list of window functions and some new at-top windows," 2002.
- [84] H. Rohling, "Some radar topics: waveform design, range CFAR and target recognition," in *Advances in Sensing with Security Applications*, ed: Springer, 2006, pp. 293-322.
- [85] H. Rohling, "Radar CFAR thresholding in clutter and multiple target situations," *IEEE transactions on aerospace and electronic systems*, pp. 608-621, 1983.
- [86] T. Long, Y. Wang, and T. Zeng, "Signal-to-noise ratio in stretch processing," *Electronics Letters*, vol. 46, pp. 720-722, 2010.
- [87] R. Ebelt, B. Waldmann, G. Bauer, A. Aleksieieva, A. Esswein, R. Weigel, *et al.*, "On the performance of pulsed frequency modulated UWB local positioning systems," in *Microwave Symposium Digest (MTT), 2011 IEEE MTT-S International*, 2011, pp. 1-4.
- [88] J. G. Poroakis, "Digital Communications," *McGraw-Hill*, pp. 556-561, 2001.
- [89] F. C. C. (FCC), "Amendment of Parts 2 and 90 of the Commission's Rules to Allocate the 5.850-5.925 GHz Band to Mobile Service for Dedicated Short Range Communications of Intelligent Transportation Services," *WT Docket No. 01-90, ET Docket No. 98-95, Report and Order 19 FCC Rcd-2458 (FCC 03-324)*, 2004.
- [90] A. Technologies, "8 hint for making and interpreting EVM measurements," 2005.
- [91] I. Rosu, "Automatic Gain Control (AGC) in Receivers."
- [92] D. Withlow, "Design and operation of automatic gain control loops for receivers in modern communication systems."
- [93] R. A. Shafik, M. S. Rahman, and A. R. Islam, "On the extended relationships among EVM, BER and SNR as performance metrics," in *Electrical and Computer Engineering, 2006. ICECE'06. International Conference on*, 2006, pp. 408-411.
- [94] Z. Zhen-Yu, W. Ying Rao, and W. Ke, "Broadband Millimeter-Wave Single Balanced Mixer and Its Applications to Substrate Integrated Wireless Systems," *Microwave Theory and Techniques, IEEE Transactions on*, vol. 60, pp. 660-669, 2012.
- [95] R. Feger, C. Pfeffer, W. Scheiblhofer, C. M. Schmid, M. J. Lang, and A. Stelzer, "A 77-GHz Cooperative Radar System Based on Multi-Channel FMCW Stations for Local

- Positioning Applications," *Microwave Theory and Techniques, IEEE Transactions on*, vol. 61, pp. 676-684, 2013.
- [96] B.-H. Ku, P. Schmalenberg, O. Inac, O. D. Gurbuz, J. S. Lee, K. Shiozaki, *et al.*, "A 77–81-GHz 16-Element Phased-Array Receiver With $\pm 50^\circ$ Beam Scanning for Advanced Automotive Radars," *IEEE Transactions on Microwave Theory and Techniques*, vol. 62, pp. 2823-2832, 2014.
 - [97] M. Steinhauer, H.-O. Ruob, H. Irion, and W. Menzel, "Millimeter-wave-radar sensor based on a transceiver array for automotive applications," *IEEE transactions on microwave theory and techniques*, vol. 56, pp. 261-269, 2008.
 - [98] L. Reichardt, C. Sturm, F. Grünhaupt, and T. Zwick, "Demonstrating the use of the IEEE 802.11 P Car-to-Car communication standard for automotive radar," in *Antennas and Propagation (EUCAP), 2012 6th European Conference on*, 2012, pp. 1576-1580.
 - [99] D. Garmatyuk, J. Schuerger, and K. Kauffman, "Multifunctional software-defined radar sensor and data communication system," *IEEE Sensors Journal*, vol. 11, pp. 99-106, 2011.
 - [100] L. Xie, X. Yin, L. Yang, C. Lu, and H. Zhao, "Multifunctional communication transceiver with distance measurement capability," in *Microwave Conference (APMC), 2014 Asia-Pacific*, 2014, pp. 405-407.
 - [101] C. de la Morena-Álvarez-Palencia and M. Burgos-Garcia, "Experimental performance comparison of six-port and conventional zero-IF/low-IF receivers for software defined radio," *Progress In Electromagnetics Research B*, vol. 42, pp. 311-333, 2012.
 - [102] S. M. Winter, H. J. Ehm, A. Koelpin, and R. Weigel, "Six-port receiver local oscillator power selection for maximum output SNR," in *Radio and Wireless Symposium, 2008 IEEE*, 2008, pp. 151-154.
 - [103] I. J. Bahl and P. Bhartia, *Microwave solid state circuit design*: John Wiley & Sons, 2003.
 - [104] J. Moghaddasi and K. Wu, "Unified radar-communication (RadCom) multi-port interferometer transceiver," in *Microwave Conference (EuMC), 2013 European*, 2013, pp. 1791-1794.
 - [105] A. Koelpin, G. Vinci, B. Laemmle, and R. Weigel, "The enhanced six-port receiver: A new concept for simultaneous data reception and direction of arrival detection," in *Microwave Symposium Digest (MTT), 2011 IEEE MTT-S International*, 2011, pp. 1-4.
 - [106] J. Moghaddasi and K. Wu, "Hybrid structure-based broadband field-rotation balun for millimeter-wave applications," in *2015 IEEE MTT-S International Microwave Symposium*, 2015, pp. 1-3.
 - [107] J. Moghaddasi and K. Wu, "Wideband planar 180° hybrid coupler with non-interspersed ports," *IEEE Trans. Microw. Theory Tech.*, vol. (Submitted), 2017.
 - [108] F. S. I. Motorella, "Three balun designs for push-pull amplifiers."
 - [109] R. Sturdivant, "Balun Designs for Wireless: Mixers, Amplifiers and Antennas," *Practical Filters and Couplers: A Collection from Applied Microwave & Wireless*, vol. 5, p. 25, 2001.

- [110] X. Lan, F. Fong, M. Kintis, K. Kono, D. Yamauchi, W.-B. Luo, *et al.*, "An ultra-wideband balun using multi-metal GaAs MMIC technology," *IEEE Microwave and Wireless Components Letters*, vol. 20, pp. 474-476, 2010.
- [111] H.-M. Lee and C.-M. Tsai, "Exact synthesis of broadband three-line baluns," *IEEE Transactions on Microwave Theory and Techniques*, vol. 57, pp. 140-148, 2009.
- [112] F. Zhu, W. Hong, J.-X. Chen, and K. Wu, "Ultra-wideband single and dual baluns based on substrate integrated coaxial line technology," *IEEE Transactions on Microwave theory and techniques*, vol. 60, pp. 3062-3070, 2012.
- [113] K. S. Ang and I. D. Robertson, "Analysis and design of impedance-transforming planar Marchand baluns," *IEEE Transactions on Microwave Theory and Techniques*, vol. 49, pp. 402-406, 2001.
- [114] P.-S. Wu, C.-S. Lin, T.-W. Huang, H. Wang, Y.-C. Wang, and C.-S. Wu, "A millimeter-wave ultra-compact broadband diode mixer using modified Marchand balun," in *Gallium Arsenide and Other Semiconductor Application Symposium, 2005. EGAAS 2005. European*, 2005, pp. 349-352.
- [115] Z.-Y. Zhang and K. Wu, "A broadband substrate integrated waveguide (SIW) planar balun," *IEEE Microwave and Wireless Components Letters*, vol. 17, pp. 843-845, 2007.
- [116] Z. C. Hao, W. Hong, J. X. Chen, X. P. Chen, and K. Wu, "A novel feeding technique for antipodal linearly tapered slot antenna array," in *Microwave Symposium Digest, 2005 IEEE MTT-S International*, 2005, p. 3 pp.
- [117] A. Mozharovskiy, A. Artemenko, V. Ssorin, R. Maslennikov, and A. Sevastyanov, "Wideband tapered antipodal fin-line waveguide-to-microstrip transition for E-band applications," in *Microwave Conference (EuMC), 2013 European*, 2013, pp. 1187-1190.
- [118] S. A. Maas, "Microwave mixers," Norwood, MA, Artech House, Inc., 1986, 368 p., 1986.
- [119] V. Napijalo and B. Kearns, "Multilayer 180° Coupled Line Hybrid Coupler," *IEEE Transactions on Microwave Theory and Techniques*, vol. 56, pp. 2525-2535, 2008.
- [120] S. March, "A wide-band stripline hybrid ring," *IEEE Trans. Microw. Theory Tech.*, vol. 16, p. 361, 1968.
- [121] C.-Y. Chang and C.-C. Yang, "A novel broad-band Chebyshev-response rat-race ring coupler," *IEEE transactions on microwave theory and techniques*, vol. 47, pp. 455-462, 1999.
- [122] B. R. Heimer, L. Fan, and K. Chang, "Uniplanar hybrid couplers using asymmetrical coplanar striplines," *IEEE transactions on microwave theory and techniques*, vol. 45, pp. 2234-2240, 1997.
- [123] C.-H. Ho, L. Fan, and K. Chang, "New uniplanar coplanar waveguide hybrid-ring couplers and magic-T's," *IEEE Transactions on Microwave Theory and Techniques*, vol. 42, pp. 2440-2448, 1994.
- [124] T. T. Mo, Q. Xue, and C. H. Chan, "A broadband compact microstrip rat-race hybrid using a novel CPW inverter," *IEEE transactions on microwave theory and techniques*, vol. 55, pp. 161-167, 2007.

- [125] S. Rehnmark, "Wide-band balanced line microwave hybrids," *IEEE Transactions on Microwave Theory and Techniques*, vol. 25, pp. 825-830, 1977.
- [126] T. Wang and K. Wu, "Size-reduction and band-broadening design technique of uniplanar hybrid ring coupler using phase inverter for M (H) MIC's," *IEEE transactions on microwave theory and techniques*, vol. 47, pp. 198-206, 1999.
- [127] M.-L. Chuang, "Miniaturized ring coupler of arbitrary reduced size," *IEEE microwave and wireless components letters*, vol. 15, pp. 16-18, 2005.
- [128] K. W. Eccleston and S. H. Ong, "Compact planar microstripline branch-line and rat-race couplers," *IEEE Transactions on microwave theory and techniques*, vol. 51, pp. 2119-2125, 2003.
- [129] J.-T. Kuo, J.-S. Wu, and Y.-C. Chiou, "Miniaturized rat race coupler with suppression of spurious passband," *IEEE microwave and wireless components letters*, vol. 17, pp. 46-48, 2007.
- [130] K.-K. M. Cheng and M.-C. J. Chik, "A frequency-compensated rat-race coupler with wide bandwidth and tunable power dividing ratio," *IEEE Transactions on Microwave Theory and Techniques*, vol. 61, pp. 2841-2847, 2013.
- [131] K.-K. M. Cheng and S. Yeung, "A novel rat-race coupler with tunable power dividing ratio, ideal port isolation, and return loss performance," *IEEE Transactions on Microwave Theory and Techniques*, vol. 61, pp. 55-60, 2013.
- [132] M. J. Park and B. Lee, "Coupled-line 180° hybrid coupler," *Microwave and optical technology letters*, vol. 45, pp. 173-176, 2005.
- [133] H. Liu, S. Fang, Z. Wang, and S. Fu, "Novel Coupled Line 180° Hybrid With Non-Interspersed Input and Output Ports," *IEEE Transactions on Microwave Theory and Techniques*, vol. 62, pp. 2641-2649, 2014.
- [134] K. S. Ang, Y. C. Leong, and C. H. Lee, "A new class of multisection 180° hybrids based on cascable hybrid-ring couplers," *IEEE transactions on microwave theory and techniques*, vol. 50, pp. 2147-2152, 2002.
- [135] V. Napijalo, "Coupled Line 180° Hybrids With Lange Couplers," *IEEE Transactions on Microwave Theory and Techniques*, vol. 60, pp. 3674-3682, 2012.
- [136] B. Schiffman, "A new class of broad-band microwave 90-degree phase shifters," *IRE Transactions on Microwave Theory and Techniques*, vol. 6, pp. 232-237, 1958.
- [137] J. R. Quirarte and J. P. Starski, "Synthesis of Schiffman phase shifters," *IEEE Transactions on Microwave Theory and Techniques*, vol. 39, pp. 1885-1889, 1991.
- [138] J. R. Quirarte and J. P. Starski, "Novel Schiffman phase shifters," *IEEE transactions on microwave theory and techniques*, vol. 41, pp. 9-14, 1993.
- [139] B. Schiffman, "Multisection microwave phase-shift network (Correspondence)," *IEEE Transactions on Microwave Theory and Techniques*, vol. 14, pp. 209-209, 1966.
- [140] Y.-X. Guo, Z.-Y. Zhang, and L. C. Ong, "Improved wide-band Schiffman phase shifter," *IEEE Transactions on Microwave Theory and Techniques*, vol. 54, pp. 1196-1200, 2006.

- [141] H. Oraizi and A. Shamsafar, "Optimum design of modified Schiffman multi-section wide band differential phase shifter with impedance matching," *Progress In Electromagnetics Research C*, vol. 29, pp. 1-16, 2012.
- [142] B. Schiek and J. Kohler, "A method for broad-band matching of microstrip differential phase shifters," *IEEE Transactions on Microwave Theory and Techniques*, vol. 25, pp. 666-671, 1977.
- [143] W. Zhang, Y. Liu, Y. Wu, W. Wang, M. Su, and J. Gao, "A modified coupled-line Schiffman phase shifter with short reference line," *Progress In Electromagnetics Research C*, vol. 54, pp. 17-27, 2014.
- [144] J. Dobrowolski, *Introduction to computer methods for microwave circuit analysis and design*: Artech House on Demand, 1991.
- [145] J. Frei, X.-D. Cai, and S. Muller, "Multiport S -parameter and T -parameter conversion with symmetry extension," *IEEE Transactions on Microwave Theory and Techniques*, vol. 56, pp. 2493-2504, 2008.
- [146] G. I. Zysman and A. K. Johnson, "Coupled transmission line networks in an inhomogeneous dielectric medium," *IEEE Transactions on Microwave Theory and Techniques*, vol. 17, pp. 753-759, 1969.
- [147] D. A. Frickey, "Conversions between S , Z , Y , H , $ABCD$, and T parameters which are valid for complex source and load impedances," *IEEE Transactions on microwave theory and techniques*, vol. 42, pp. 205-211, 1994.
- [148] A. Koelpin, G. Vinci, B. Laemmle, D. Kissinger, and R. Weigel, "The Six-Port in Modern Society," *Microwave Magazine, IEEE*, vol. 11, pp. 35-43, 2010.
- [149] A. Koelpin, S. Lindner, G. Vinci, B. Laemmle, and R. Weigel, "The enhanced six-port architecture: A measurement based proof of concept," in *Wireless Sensors and Sensor Networks (WiSNet), 2012 IEEE Topical Conference on*, 2012, pp. 29-32.
- [150] J. Moghaddasi and K. Wu, "Millimeter-Wave Multifunction Multiport Interferometric Receiver for Future Wireless Systems," *IEEE Trans. Microw. Theory Tech.*, vol. (In Press), 2017.
- [151] S. Mann, G. Vinci, S. Lindner, S. Linz, F. Barbon, R. Weigel, *et al.*, "61 GHz six-port radar frontend for high accuracy range detection applications," in *Antennas and Propagation in Wireless Communications (APWC), 2013 IEEE-APS Topical Conference on*, 2013, pp. 818-821.
- [152] J. W. Demmel, *Applied numerical linear algebra*: SIAM, 1997.
- [153] X.-P. Chen, K. Wu, and D. Drolet, "Substrate integrated waveguide filter with improved stopband performance for satellite ground terminal," *IEEE Transactions on Microwave Theory and Techniques*, vol. 57, pp. 674-683, 2009.
- [154] C. A. Balanis, *Antenna theory: analysis and design*: John Wiley & Sons, 2016.
- [155] R. A. Sainati, *CAD of microstrip antennas for wireless applications*: Artech House, Inc., 1996.

- [156] D. Hammou, T. Djerafi, M. Nedil, and S. O. Tatu, "Considerations for On-Wafer Millimeter-Wave Measurements on Thin Ceramic Substrate," *IEEE Transactions on Instrumentation and Measurement*, vol. 65, pp. 441-447, 2016.
- [157] C. Hannachi, D. Hammou, T. Djerafi, Z. Ouairhi, and S. O. Tatu, "Complete Characterization of Novel MHMICs for V-Band Communication Systems," *Journal of Electrical and Computer Engineering*, vol. 2013, p. 9, 2013.
- [158] C. Hannachi, E. Moldovan, S. O. Tatu, and Z. Ouairhi, "V-band six-port quadrature demodulator : Error Vector Magnitude analysis," in *Millimeter Waves (GSMM), 2015 Global Symposium On*, 2015, pp. 1-3.
- [159] H. A. Mahmoud and H. Arslan, "Error vector magnitude to SNR conversion for nondata-aided receivers," *IEEE Transactions on Wireless Communications*, vol. 8, 2009.
- [160] Z.-Y. Zhang, Y. R. Wei, and K. Wu, "Broadband millimeter-wave single balanced mixer and its applications to substrate integrated wireless systems," *IEEE Transactions on Microwave Theory and Techniques*, vol. 60, pp. 660-669, 2012.
- [161] G. Vinci, A. Koelpin, F. Barbon, and R. Weigel, "Six-port-based direction-of-arrival detection system," in *Microwave Conference Proceedings (APMC), 2010 Asia-Pacific*, 2010, pp. 1817-1820.
- [162] M. de La Chapelle, C. McLain, and D. S. Parkman, "Beam alignment system and method for an antenna," ed: Google Patents, 2002.
- [163] R. B. Dybdal and D. D. Pidhayny, "Main beam alignment verification for tracking antennas," ed: Google Patents, 2005.
- [164] D. J. Eggert, C. E. Hendrix, and B. Krinsky, "Direction finding interferometer," ed: Google Patents, 1987.
- [165] J. A. Kaiser Jr, "Scannable beam forming interferometer antenna array system," ed: Google Patents, 1980.
- [166] R. J. Lioio, G. E. Clayton, and R. A. Deaton, "Phase and time-difference precision direction finding system," ed: Google Patents, 1998.
- [167] C. M. Rose, "Emitter azimuth and elevation direction finding using only linear interferometer arrays," ed: Google Patents, 1995.
- [168] J. Remez and E. Ben-Ari, "Direction finding antenna system and method," ed: Google Patents, 2012.
- [169] J. Remez and E. Ben-Ari, "Low-loss wideband multimodal interferometric antenna for DOA in azimuth and elevation," *IEEE antennas and wireless propagation letters*, vol. 8, pp. 898-902, 2009.
- [170] J. Moghaddasi and K. Wu, "System and method for estimating the direction of arrival," *US Patent (91026694US01)*, 2015.
- [171] J. Moghaddasi, T. Djerafi, and K. Wu, "Multiport Interferometer-Enabled 2-D Angle of Arrival (AOA) Estimation System," *IEEE Transactions on Microwave Theory and Techniques*, vol. 65, pp. 1767-1779, 2017.

- [172] T. Djerafi and K. Wu, "60 GHz substrate integrated waveguide crossover structure," in *Microwave Conference, 2009. EuMC 2009. European*, 2009, pp. 1014-1017.
- [173] L. Han, K. Wu, X.-P. Chen, and F. He, "Accurate analysis of finite periodic substrate integrated waveguide structures and its applications," in *Microwave Symposium Digest (MTT), 2010 IEEE MTT-S International*, 2010, pp. 864-867.
- [174] Z.-Y. Zhang, K. Wu, and Y. R. Wei, "Broadband delay compensation phase shifter using slotted substrate integrated waveguide structure," in *Microwave Symposium Digest (MTT), 2011 IEEE MTT-S International*, 2011, pp. 1-4.
- [175] W. M. Abdel-Wahab and S. Safavi-Naeini, "Wide-bandwidth 60-GHz aperture-coupled microstrip patch antennas (MPAs) fed by substrate integrated waveguide (SIW)," *IEEE Antennas and Wireless Propagation Letters*, vol. 10, pp. 1003-1005, 2011.
- [176] K. Gong, Z. N. Chen, X. Qing, P. Chen, and W. Hong, "Substrate integrated waveguide cavity-backed wide slot antenna for 60-GHz bands," *IEEE Transactions on antennas and propagation*, vol. 60, pp. 6023-6026, 2012.
- [177] Q. Lai, C. Fumeaux, W. Hong, and R. Vahldieck, "60 GHz aperture-coupled dielectric resonator antennas fed by a half-mode substrate integrated waveguide," *IEEE Transactions on Antennas and Propagation*, vol. 58, pp. 1856-1864, 2010.
- [178] J. Moghaddasi, L. Li, K. Wang, and K. Wu, "Reconfigurable Multi-mode and Multi-bands Radio Architecture and Transceiver," *US Patent (14/967, 652)*, December, 14 2015.
- [179] J. Vuorio and H. Lilja, "Wireless communication transceiver having a dual mode of operation," ed: Google Patents, 2003.
- [180] D. W. Barabash and R. A. Morris, "Filtering method to allow FDD and TDD operations in PCS transreceivers," ed: Google Patents, 2008.
- [181] R. Vaisanen and K. Kaltiokallio, "Method and arrangement for transmitting and receiving RF signals through various radio interfaces of communication systems," ed: Google Patents, 2014.
- [182] S. J. Dean and D. W. Park, "Dual mode transceiver," ed: Google Patents, 1999.
- [183] R. Ebelt, A. Hamidian, D. Shmakov, Z. Tao, V. Subramanian, G. Boeck, *et al.*, "Cooperative Indoor Localization Using 24-GHz CMOS Radar Transceivers," *Microwave Theory and Techniques, IEEE Transactions on*, vol. 62, pp. 2193-2203, 2014.
- [184] R. Feger, C. Pfeffer, W. Scheiblhofery, C. M. Schmid, M. J. Langz, and A. Stelzer, "A 77-GHz cooperative secondary radar system for local positioning applications," in *Microwave Symposium Digest (MTT), 2012 IEEE MTT-S International*, 2012, pp. 1-3.
- [185] S. Roehr, P. Gulden, and M. Vossiek, "Precise Distance and Velocity Measurement for Real Time Locating in Multipath Environments Using a Frequency-Modulated Continuous-Wave Secondary Radar Approach," *Microwave Theory and Techniques, IEEE Transactions on*, vol. 56, pp. 2329-2339, 2008.

Appendix A – LIST of Publications & Awards

1. Patents

- [P1] **J. Moghaddasi**, and K. Wu, “System and Method for Estimating the Direction of Arrival,” *US Patent Application*, 91026694US01, August 2015.
- [P2] **J. Moghaddasi**, L. Li, K. Wang, and K. Wu, “Reconfigurable Multi-mode and Multi-Bands Radio Architecture and Transceiver,” *US Patent Application*, 91030206US01, December 2015.
- [P3] **J. Moghaddasi**, K. Wu, “A Positioning System with Communication Capability for Future Highly-Mobile Vehicular Platforms,” *US Patent Application*, 60979170, August 2013.

2. Peer-reviewed journal publications

- [J1] **J. Moghaddasi** and K. Wu, "Multifunctional Transceiver for Future Radar Sensing and Radio Communicating Data-Fusion Platform," in *IEEE Access*, vol. 4, no. , pp. 818-838, 2016.
- [J2] **J. Moghaddasi**, T. Djerafi, and K. Wu, “Multiport Interferometer-Enabled 2-D Angle of Arrival (AOA) Estimation System,” *IEEE Transactions on Microwave Theory and Techniques*, vol. 65, pp. 1767-1779, 2017.
- [J3] **J. Moghaddasi**, and K. Wu, “Millimeter-Wave Multifunction Multiport Interferometric Receiver for Future Wireless Systems,” *IEEE Transaction on Microwave Theory and Techniques*, (Accepted and to be published).
- [J3] **J. Moghaddasi**, and K. Wu, “Planar 180deg Hybrid Coupler with Non-Interspersed Ports,” *IEEE Transactions on Microwave Theory and Techniques*, (Submitted).

3. Conference papers

- [C1] **J. Moghaddasi** and K. Wu, "Improved joint radar-radio (RadCom) transceiver for future intelligent transportation platforms and highly mobile high-speed communication systems," *2013 IEEE International Wireless Symposium (IWS)*, Beijing, 2013, pp. 1-4

- [C2] **J. Moghaddasi** and K. Wu, "Unified radar-communication (RadCom) multi-port interferometer transceiver," *2013 European Microwave Conference*, Nuremberg, 2013, pp. 1791-1794.
- [C3] **J. Moghaddasi**, K. Wang and K. Wu, "Parametric characterization of six-port interferometer demodulator through mixer modeling," *2015 European Microwave Conference (EuMC)*, Paris, 2015, pp. 526-529
- [C4] **J. Moghaddasi** and K. Wu, "Hybrid structure-based broadband field-rotation balun for millimeter-wave applications," *2015 IEEE MTT-S International Microwave Symposium*, Phoenix, AZ, 2015, pp. 1-3.
- [C5] J. F. Gu, **J. Moghaddasi** and K. Wu, "Delay and Doppler shift estimation for OFDM-based radar-radio (RadCom) system," *2015 IEEE International Wireless Symposium (IWS 2015)*, Shenzhen, 2015, pp. 1-4.

4. Awards

- [A1] Best Paper Award in IEEE MTT-S International Wireless Symposium (IWS), Beijing, China, April 2013
- [A2] Student Challenge Prize in European Microwave Week (EuMW) 2013, Nuremberg, Germany, October 2013
- [A3] Best Research Poster Award, CREER 2013 Symposium, Montreal, Canada, September 2013
- [A4] IEEE MTT- AdCom Ph.D. Initiative Award, June 2012
- [A5] Best Research Poster Award, CREER 2011 Symposium, Montreal, Canada, September 2011
- [A6] 2nd Place of Research Poster Award, CREER 2015 Symposium, Montreal, Canada, September 2015
- [A7] Canada NSERC-PERSWADE Fellowship Award, January 2015
- [A8] Best Research Poster Award, CREER 2016 Symposium, Montreal, Canada, November 2016

[A9] Travel Grant, European Radar Conference (EuRad 2013), Nuremberg, Germany,
October 2013